THEORETICAL AND EXPERIMENTAL ANALYSIS

OF DYNAMIC CHARACTERISTICS IN LINEAR COMPRESSORS

A Dissertation

Submitted to the Faculty

of

Purdue University

by

Xinye Zhang

In Partial Fulfillment of the

Requirements for the Degree

of

Doctor of Philosophy

May 2020

Purdue University

West Lafayette, Indiana

THE PURDUE UNIVERSITY GRADUATE SCHOOL
STATEMENT OF DISSERTATION APPROVAL

Dr. Eckhard A. Groll, Chair

    School of Mechanical Engineering

Dr. James E. Braun

    School of Mechanical Engineering

Dr. Neera Jain

    School of Mechanical Engineering

Dr. William Travis Horton

    School of Civil Engineering

Approved by:

    Dr. Nicole Key

        Head of the School Graduate Program

To everyone who wants to know about compressors

To my families and friends

To myself in the future

ACKNOWLEDGMENTS

I would like to express my deep appreciation for my major advisor, Professor Eckhard Groll for his instruction, guidance and support during my graduate career. There is a Chinese old saying that "one day as a teacher, all life as a father". I learned a lot from you, not only knowledge of engineering, but also dedication to my work and life. I would also like to thank Professor James Braun for providing a lot of invaluable comments and insights on my papers and research and all weekly meeting with you were the precious in my life. For their time and interest, I would like to thank Professor Neera Jain and Professor William Travis Horton, who served on my advisory and examining committees and thanks for all your feedback, comments and support on my prelim and my defense.

I also would not have completed this journey without the help from Dr. Davide Ziviani, who is my supervisor, colleague and friend. Thanks for all your inputs, efforts and instructions on all my research and papers, in particular, during the study documented in this thesis. I was so lucky to meet you and work with you. I am also very thankful to Dr. Yangfan Liu and Dr. Bin Yang, who gave me many helpful guidance to the world of mathematics, compressors and programming. The scientific mind, personality and optimistic from both of you inspired me in many ways.

Certainly, I would like to thank all my colleagues in our group, Orkan, Riley, Vatsal, Cai, Domenique, Xueyang, Nick, Leon, Danielle, Parveen. It is a great experience to work with all of you and share our research ideas. To my friends in Herrick, Rui, Li, Jie Ma, Yingying, Jie Cai, Xiaoqi, Tongyang, Wenshan, Yutong, Xu, I really enjoyed working with you, chatting with you and having many lunch boxes with you all. I would like to give a special thank you to Haotian, who was always around with me, willing to help and support his senior brother all the time. I would also like to acknowledge all my roommates for last six years, Yatong, Gang, Xing, Xiaodi, thank

you all for accompanying me during my daily life and supporting me in many ways. Wuwei, Xiao, Yuchen, Mingjie, co-founders of LRSGGG club for werewolf games, all the games in the weekend were fantastic memories to me. Jie Xiong, Ran, Doupi, my best family members at Purdue, appreciate all the happiness and memory you gave to me.

Jiajun, Sida, Fuxiang, Yang, my best brothers in my whole life. Thank you all for your unconditionally support and love, although we have 12-hour time difference and seven-thousand miles away. To my best, Yuyang, I would not have finished my study without your inspiring and support from your world. I miss you so much, RIP.

Last but not least, I wish to thank my parents and my families, whose encouragement and support make graduate school possible and a positive experience. In particular, I would like to express my special thanks to my girlfriend, Zhengtian, who always encourages me by all means and supports me unconditionally. You were so qualified as a master of compressor before you graduated as a scientist. All my presentations could not have been better without your detailed comments.

TABLE OF CONTENTS

LIST OF TABLES

LIST OF FIGURES

Figure   Page

SYMBOLS

a	Anchor distance	(m)
A	Area	(m^2)
B	Magnetic density	(N/(Am))
c	Damping coefficient	(kg/s)
C	Capacity	(μF)
C_D	Drag force coefficient	(-)
c_p	Specific heat	(kJ/(kg $-$ K))
C_p	Capacitance	(kJ/(K))
E	Young's modulus	(kJ)
f_F	Fanning friction factor	($-$)
f	friction	(Hz)
F	Gas force on valve	(N)
g	Clearance gap	(μm)
G	Mass flux	(kg/(m^2 $-$ s))
L	Length	(mm)
I	Current	(A)
I	Inductance	(mH)
I_m	Moment of inertia	(kg $-$ m^2)
h	Specific enthalpy	(kJ/kg)
h	Variable clearance gap	(m)
Gr	Grashof number	(-)
k_s	Spring stiffness	(N/m)
k	Thermal conductivity	(W/(m K))
k_v	Spring stiffness	(N/m)

l	Length of valve plate	(m)
L	Length	(m)
$\dot{m}$	Mass flow rate	(kg/s)
m_{eff}	Effective mass	(kg)
m	Mass	(kg)
M	Mass	(kg)
Nu	Nusselt number	(-)
P	Pressure	(kPa)
PR	Pressure ratio	(-)
Pr	Prandtl number	(-)
q	Specific heat transfer	(kJ/kg)
$\dot{Q}$	Heat rate	(kW)
Re	Reynolds number	(-)
Ra	Rayleigh number	(-)
ρ	Density	(m^3/kg)
R	Piston radius	(m)
t	Time	(s)
T	Temperature	(K)
Tr	Transmissibility	(-)
u	Specific internal energy	(kJ/kg)
u_{emf}	Back electromotive force	(V)
v	Specific volume	(m^3/kg)
v	velocity	(m/s)
V	Volume	(m^3)
V_e	Voltage	(V)
V_{gas}	Gas velocity	(m/s)
$\dot{W}$	Power	(W)

$\dot{x}_p$	Piston velocity	(m/s)
X_m	Piston equilibrium position	(m)
X_0	Piston initial position	(m)
y	Valve displacement	(m)
α	Motor factor	(N/A)
α	Heat transfer coefficient	(W/(m^2 − K))
β	Radius of curvature at the peak	(m)
δ	Valve lift	(K)
μ	Viscosity	(Pa s)
η	Efficiency	(-)
ϵ	Eccentricity	(-)
σ	Surface roughness	(μm)
θ	Angle	(deg)
ζ	Damping ratio	(-)
ω_n	Natural frequency	(-)
Ω	Driving frequency	(-)

ABBREVIATIONS

amb	ambient
cl	clearance
cv	control volume
cyl	cylinder
dis	discharge
down	downstream
e	exit
eff	effective
fri	friction
is	isentropic
in	inlet
leak	leakage
m	motor
meas	measured
md	mass-flux domain
out	outlet
o	overall
p	piston
pis	piston
pl	plate
s	spring

tr	transition
pl	plate
re	reed
s	spring
suc	suction
up	upstream
v	valve
w	wall

NOMENCLATURE

BDC	Bottom dead center
EMF	Electromotive force
EMR	Energetic macroscopic representation
FEM	Finite element method
HEOS	Helmholtz equation of state
HVAC	Heating, ventilation, and air conditioning
MAPE	Mean absolute percentage error
KVL	Kirchhoff's voltage Law
OEB	Overall energy balance
RMS	Root mean square
TDC	Top dead center
VCR	Vapor compression refrigeration

ABSTRACT

Zhang, Xinye PhD, Purdue University, May 2020. Theoretical and Experimental Analysis of Dynamic Characteristics in Linear Compressors. Major Professor: Eckhard Groll.

Linear compressor technology is characterized by the absence of a crank mechanism, which has gained increasing attention in vapor compression systems due to its compactness and lower friction losses in comparison to conventional reciprocating compressors. Limited work was found in the open literature related to the development and in-depth validation of a comprehensive linear compressor dynamic model that couples thermodynamic aspects with both mechanical and electrical sub-models. The current thesis presents a comprehensive and generalized simulation model that is used to simulate the dynamic performance of a linear compressor. The model is based on mass and energy balance equations applied to open control volumes. The overall model is composed of several sub-models including the piston dynamics, electrical motor, valve dynamics, and leakage flows. The thermodynamic model and the sub-models are integrated into a compressor overall energy balance that describes the different heat flows and losses. The linear compressor model is able to predict both transient and steady-state behaviors of the piston movement, internal pressure and temperatures as well as the overall performance. Moreover, the simulated compressor was characterized experimentally by using a hot-gas bypass test stand over its operating envelope and the experimental data (*i.e.*, measured mass flow rate, motor power and overall isentropic efficiencies), was used to validate the developed linear compressor model. The validated model was then used to investigate and quantify major sources of losses, analyze the system vibration as well as eccentricity caused by the spring assembly. The validated comprehensive model is a powerful tool that

can be used to improve the prototype linear compressor design as well as explore alternative designs.

In addition, the comprehensive compressor model has been exercised to design and 3-D print novel liner compressor component with the goal of evaluating their potential to approach an quasi-isothermal compression process. The concept of design has been integrated into a refrigeration system and a system simulation model was developed and used to analyze the system performance and to assess its potential for approaching a quasi-isothermal compression process through the utilization of refrigerant economizing and regeneration technology. Moreover, the scalability analysis is conducted in terms of heat pump and air compression application, which provides a guidance to design a scale-up linear compressor as well as the selection of components.

1. INTRODUCTION

1.1 Background

Linear compressor technology is characterized by the absence of a crank mechanism, which has gained increasing attention in vapor compression systems due to its compactness and lower friction losses in comparison to conventional reciprocating compressors. Historically, he first linear compressor concepts were proposed in Europe and Japan in the 1950s for refrigeration applications [1], but limited theoretical work was conducted at that time, and no commercial products were available for years to come. Since the 1960s, the linear compressor underwent continuous development. In particular, Cadman [2] conducted experimental studies related to the design of an electrodynamic oscillating linear compressor over the expected range of operating conditions. The work included comparisons of weight and operating efficiency to conventional technology in order to understand their potential economic benefits. It was concluded that the performance of linear compressors would be superior to that of conventional rotary motor driven compressors in many applications with less frictional losses, but with higher manufacturing cost. That work can be regarded as one of the pioneering studies on oscillating linear compressors. In 1969, Cohen [3] proposed a simulation model with the purpose of assessing the performance of possible designs of electrodynamic oscillating gas compressors that feature a linear spring-sampler load. It was noted that the springs were often required to resonate the oscillating movement, which increased the cost of the linear motor design. As a consequence, it was particularly challenging to compete with conventional rotary motors in the short term. However, the study highlighted the importance of the spring system design and resonance aspects in oscillating compressors creating a path for future developments.

One of the first mathematical models of a single oscillating compressor was developed by Pollak et al. [4] in 1979. In particular, the model was able to identify the characteristics of the linear compressor including the piston stroke and the electric current amplitude. Furthermore, the model accounted for both mechanical and electrical losses. A validation was carried out by using experimental data from an existing compressor. The results showed that the piston movement was shifting from the equilibrium position during the gas compression process, which is a peculiar aspect of the linear compressor. One of the main contributions of the study was the introduction of the concept of a gas spring where a gas pressure force replaces a mechanical spring in establishing the harmonic motion of the piston. The modeling results from these early studies were limited by the computational resources and a lack of thermo-physical property libraries.

In 1992, Van and Unger from Sunpower, Inc. [5] developed a simulation model of a linear compressor in order to design a prototype and replace an existing reciprocating compressor for domestic refrigeration. The simulation model was used to predict all stable operating conditions of the design and the model was validated by the prototype design. The results showed that the linear compressor power consumption was 253 W for an evaporating temperature of -23 °C and a piston stroke of 7.3 mm. Successively, the same research group from Sunpower Inc. [6] designed five different linear compressor prototypes in 1994 and characterized their performance over a range of operating conditions and modulated capacities. Results showed that the efficiency of the compressors improved in the rage of 15% and 25% compared to a conventional reciprocating compressor. Their work contributed significantly to the development of the linear compressor technology. Since then, the research on linear compressors has flourished.

Hasegawa et al. [7] presented a linear compressor prototype with featuring a self-compensated mechanism with gas springs in 2002. The experimental results indicated that the fabricated design could achieve the equivalent performance to that of the conventional linear compressor with a mechanical spring. Therefore, this study provided

a better understanding of the design of spring systems in addition to the previous work conducted by Pollak et al. [4]. At the same time, Koh et al. [8] analyzed the performance of the linear compressor experimentally in cryogenic and miniature systems in 2002. This analysis dealt with quantifying the effect of resonance on the piston stroke under different operating conditions. The relationship between force on piston and amplitude of stroke were also investigated.

In recent years, LG Inc. patented and commercialized several versions of linear compressors since 2002 [9, 10] by utilizing the linear motor technology developed by Sunpower Inc. Their linear compressors were installed in household refrigerators with the use of refrigerant R134a and R600a. The LG linear compressors were all oil-lubricated and designed with the special multiple spring and damping systems [11]. It has been advertised that LG linear compressors show better performance than conventional compressors in terms of compressor thermodynamic and motor efficiencies. Another commercialized linear compressor, i.e., Wisemotion compressor technology, was developed by Embraco in 2008 [12]. The Wisemotion linear compressor was also designed for domestic refrigeration systems using the same two refrigerants as for the LG linear compressor. The Wisemotion linear compressor is an oil-free technology and the lubrication is guaranteed by the refrigerant itself. Furthermore, special surface gas bearings are employed.

Additional research efforts focused on developing linear compressor prototypes. Bradshaw [13] presented a prototype linear compressor for miniature electronics cooling applications. It was hoped that linear compressor is a promising solution for electronic cooling applications. A comprehensive compressor model was also developed to improve the design and understand the effects of several parameters. A novel linear electromagnetic-drive oil-free linear compressor using R134a has been designed by Liang [14], which was incorporated into vapor compression refrigeration (VCR) system. Both modeling and experimental work were conducted to evaluate the influence of resonant frequencies on the compressor as well as the overall system performance. From the analyses, it was concluded that the linear compressor should

be operated at resonance for a high efficiency based on the testing results. A solenoid based linear compressor for household refrigerator was built by Bijanzad [15] and its dynamic characteristics were evaluated with the concept of the gas spring. Finite element method (FEM) was used to simulate the magnetic field density with specific stroke position and current amplitude.

A number of designs have been proposed throughout the years, which ultimately led to commercialized linear compressors. In order to have a better understanding of the linear compressor technology, the main design characteristics are outlined in following section.

1.2 Linear Compressor Characteristics

Aforementioned, linear compressors present unique features in comparison to conventional reciprocating compressors. In particular, the absence of a crank-mechanism enables the possibility of oil-free operation, which is highly desirable from a compressor design stand-point. The absence of oil eliminates refrigerant compatibility issues and opens up more options for environmentally-friendly working fluids. Furthermore, working fluids can be selected to operate at higher temperatures and pressures without issues related to oil degradation. In addition, oil free design significantly reduces the costs associated with filter replacement and oil condensate treatment. Due to its compactness and scalability, the linear compressor is an appealing technology for domestic and miniature-scale refrigeration systems, which have space constraints. Besides, the reduction of the internal space also widens the possibilities of the designs and inside configurations of the linear compressors as well as the refrigerator.

A traditional reciprocating compressor with a crank mechanism has a fixed stroke length. In contrast, the piston stroke of a linear compressor is variable with the stroke depending on a dynamic force balance between an electrical driving force, a gas compression force and a spring force. The variable length of stroke enables the capacity modulation of the refrigeration system with the use of linear compressors. By

adjusting the input frequency (or alternatively the excitation voltage), the electrical driving force affects the stroke length and, consequently, modulates the capacity of the system. It follows that the linear compressor can run on a wider range of capacity modulation instead of switching on and off which results in the minimum temperature variation and smaller vibration.

In order to describe the typical operating principal of the linear compressor, a general schematic of a commercially available hermetic linear compressor is shown in Figure 1.1. The compressor operates with a low-pressure shell and the suction gas flows into the compressor shell directly after the suction tube. Some gas movement is generated within the shell to cool down the internal components. The suction gas travels from the shell of the compressor into the suction muffler, then into the center of the piston. The gas pushes open the suction reed valve at the end of the piston, entering into the compression chamber. Once the chamber pressure reaches the pressure in the discharge muffler, the gas pushes the discharge plate valve away from its seat during the discharging process, entering the muffler and discharge line. There are two opposing sets of four compression springs for a total of eight compression springs in parallel to provide the spring force as well as to keep the piston moving steadily.

In a harmonic vibration system, a non-linear force, $i.e.$, gas spring force, will result in unsteady oscillations, which will be very challenging in terms of controlling compressor operation. Therefore, a large spring stiffness is adopted that dictates a small variation in resonance frequency to avoid the effects of the non-linear gas spring and can minimize piston drift issues, which could become especially significant for larger pressure ratio applications. In order to minimize the piston eccentricity in a linear compressor, the spring assembly should be selected wisely, including choosing suitable spring stiffness, concentric confirmation, suitable free length. Unlike using the piston-ring in a reciprocating compressor, there are two approaches to solve the leakage and friction issues in an oil-free linear compressor. One is to use high pressurized return flow as a gas bearing to seal the leakage and reduce the friction loss at the same time.

Another is to design the piston with extra length, which allows for choked flow in the leakage path, which can also reduce the leakage flow, discussed by Zhang et al. [16]. A moving magnet linear motor assembly is employed and the copper coils are covered by laminations. The piston is connected directly to a moving magnet assembly and the piston movement is driven by an alternating axial force generated by a magnetic field from the linear motor. Continuous capacity modulation of a refrigeration system can be achieved with the use of linear compressors by adjusting the input frequency (or alternatively the excitation voltage), which directly changes the electrical driving force and consequently the piston stroke length. Compared to on/off control, the continuous capacity regulation of a linear compressor provides improved cabinet temperature regulation, lower vibration/noise, and better energy efficiency. In order to maximize motor efficiency and minimize motor size, the piston in a linear compressor is always controlled close to/at operate at resonance frequency.

Due to complexity of the dynamic interactions within a linear compressor, a comprehensive dynamic simulation model and an in-depth experimentally analysis are extremely helpful for understanding the behavior and operation of linear compressors, their control strategies, as well as for exploring performance improvements and future prototype designs.

1.3 State-of-Art of Research on Linear Compressors

This section summaries the state-of-art on the studies of linear compressors in terms of theoretical and experimental work, respectively. In addition, literature relating to the prototypes of linear compressor is also introduced.

1.3.1 Theoretical and experimental analysis of linear compressors

In 1969, Cohen et al. [17] proposed a simulation model with the purpose of assessing the performance of possible designs of electrodynamic oscillating gas compressors featuring a linear spring-damper load over the expected range of operating conditions.
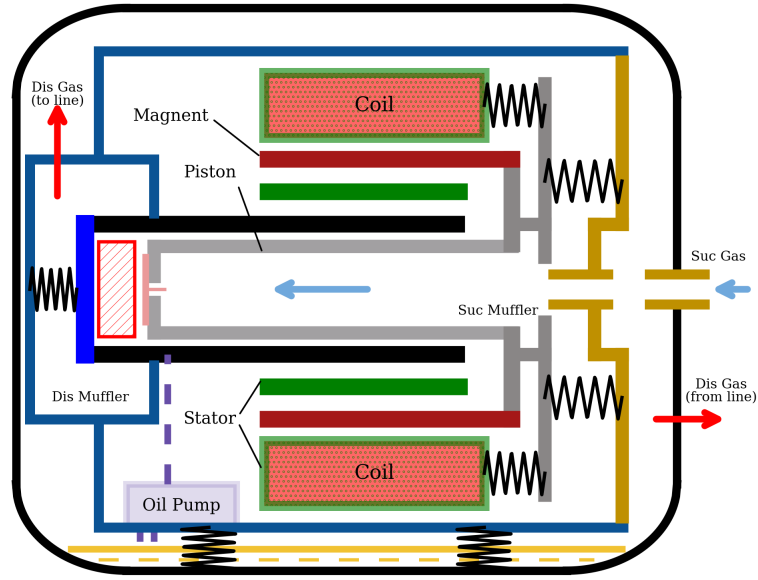
Fig. 1.1. Schematic diagram of a linear compressor from LG Inc.

After almost a decade, one mathematical model of a single oscillating compressor was developed by Pollak et al. [4] in 1979, a cyclic system was used to treat losses as integration over the cycle and consider all forces on the coil-piston combination. One framework for modeling linear compressor was established, considering equivalent damping coefficient, equivalent spring force and oscillating modeling. The preliminary results are shown in Figure 1.2 in terms of the typical response for the power and mass flow rate as functions of frequency. It can be found that the peak shows up at a driving frequency at the resonance frequency of the system where the minimum power is required. However, the modeling results from two studies above were limited by the computational speed and the thermo-physical property evaluation libraries. Therefore, the thermodynamic models presented in these two studies were not able to provide accurate information inside the compression chamber.

(a)

(b)
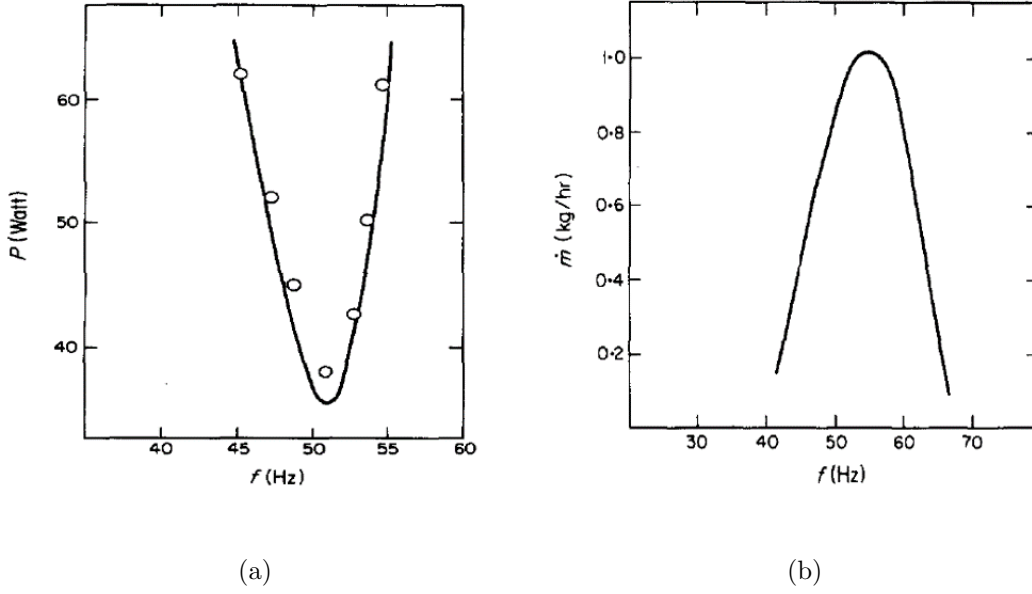
Fig. 1.2. Simulation results obtained by Pollak et al. [4]: (a) Input power as a function of driving frequency. (The experimental data is overlaid as circular markers.); (b) Mass flow rate as a function of frequency.

In 1994, C. Minas [18] proposed two modeling methodologies of the dynamics of a motor-compressor system in terms of a sinusoidal input force associated with pressure force and a mathematical model that was based on electromagnetic and thermodynamic equations on the piston movement. The transient as well as steady-state results were presented. Chen at al. [19] investigated the static and dynamic characteristics of a moving magnet linear motor for compressor. The model was incorporated with both an equivalent magnetic circuit and finite element approaches. Howe et al. [20] proposed a design of a single-phase linear drive with a tubular, moving-magnet motor in 2008. The piston in this design could be controlled by regulating the input current and the compressor will work at resonant frequency accordingly. Experimental work demonstrated the reliabilities of the prototype drive incorporated with the compressor system. Zhang et al. [21] presented a mathematical model with hammering effect for a tubular linear permanent magnet machine with gas spring to predict

the dynamic characteristics of oscillatory motion in 2009. Ibrahim [22] and Wang et al. [23] focused a design methodology to achieve optimal performance for a short-stroke, single phase tubular permanent magnet motor for linear compressor as well. A mathematical model was developed by Tsai at al. [24] for the magnetically levitated linear compressor. A pair of active magnet bearings was employed to regulate the piston deviation as well as to reduce the noise. A significant amount of the research works discussed above dealt with the control analysis of the linear motor in the linear compressor. However, the gap among them is that there was little work done in terms of the thermodynamic process inside the linear compressor and the compressor model was either neglected or simplified for computational consideration.

The resonant frequency of the moving magnet linear compressors of a Stirling cryocooler was presented in Ming Xia [25] and both CFD and Finite Element Method (FEM) methods were applied but the thermodynamic process was not analyzed thoroughly. Dang et al. [26,27] has provided analytic models and experimental validations on dynamic and thermodynamic characteristics of the moving-coil linear compressor. But two compressors in the studies above were used in Stirling-type pulse tube cryocooler with lower temperature and small pressure ratio as operating conditions. Limited results were presented in terms of refrigeration applications. Reported by Kim et al. [28], an inherent capacity modulation method was proposed for a linear compressor capacity control. The performance and capacity modulation capability were validated by numerical and experimental data. The comparison was made between the inherent capacity-modulated and electric resonance compressors.

The novel approach called energetic macroscopic representation (EMR), shown in Figure 1.3, was introduced by Heidari at al. [29] in 2015.The simulation results were verified by both FEM and the experimental data. It allows the further analysis in terms of electromechanical, heat transfer and fluid dynamics in an air linear compressor. Lamantia et al. [30] presented a virtual simulation system with respect to a new linear compressor for household appliances on the basis of Simulink and Adams. One prototype compressor has been built based on the optimized simulation model

to achieve high performance. The works above are either based on the new concept which needs to be proven for reproducibility or generated from the commercial software, which does not provide detailed information behind the simulation results.
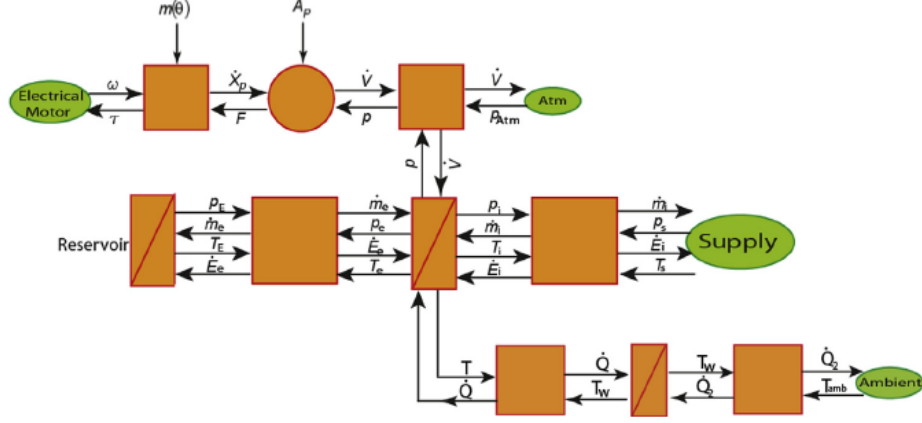
Fig. 1.3. Complete system EMR (excluding reservoir) [29].

More recently, You et al. [31] theoretically and experimentally investigated the electrical and mechanical characteristics of a linear compressor in order to reduce input power and improve efficiency. An expression for the stroke amplitude based on easily obtainable parameters was derived. It was shown that the model can be used to identify resonance frequency of a linear compressor and investigate the variation of stroke in terms of different intrinsic parameters.

The majority of the cited literature focused primarily on the control analysis of linear motors to effectively drive the compressors. Only limited work has been done in terms of analyzing the thermodynamic process inside the linear compressor. In fact, in most of the cases, the compression process was either neglected or simplified for computational purposes. As a result, there is a gap in the literature related to modeling and understanding the dynamics associated with the compression process. Additionally, some of the analyzed compressors were employed in Stirling-type and pulse-tube-type cryocoolers with significantly lower temperature and pressure ratio

operating conditions and only limited results have been reported for refrigeration applications.

Experimental and numerical results concerning the dynamic characteristics of a linear compressor in a refrigeration system were presented by Kim et al. [32]. In this study, a mathematical motor model was included but not coupled with a model of the compression process. Also, no detailed compressor performance data was reported. The research group at the University of Oxford did a lot of research on linear compressor analysis [33], which includes a review of the development of linear compressors and outlines their future potential. One of the research members, Davies et al. [34] described the design and construction of a linear compressor and a corresponding model. Based on this model, dynamic characteristics of linear compressor were analyzed, as shown in Figure 1.5. Liang et al. [35] showed a comparison between a crank-drive reciprocating compressor and a novel oil-free linear compressor. The experimental results showed that the linear motor had better performance than the regular induction motor. In addition, a new type of oil-free magnet linear compressor with clearance seals and flexure springs was designed and incorporated into a vapor compression system which was developed by Liang et al. [14] and the preliminary simulation results are shown in Figure 1.6. Besides, the authors also carried out many studies in terms of the effect of clearance on the performance of oil-free linear compressor, [36–38]. Steady-state performance of the oil-free linear compressor was measured and compared with results from a model that predicts resonant frequency. The resonance frequency for each operating condition was predicted using the discharge pressure, suction pressure and stroke with an accuracy of 1.5 %. During testing, the system achieved a COP of approximately 3.0 for a pressure ratio of 2.5. However, the mathematical model predicts resonance frequency and not thermodynamic performance. Furthermore, a detailed valve model and flow model were not included in the studies above, which may attenuate the accuracy of the calculation of mass flow rate during the compressor simulation.
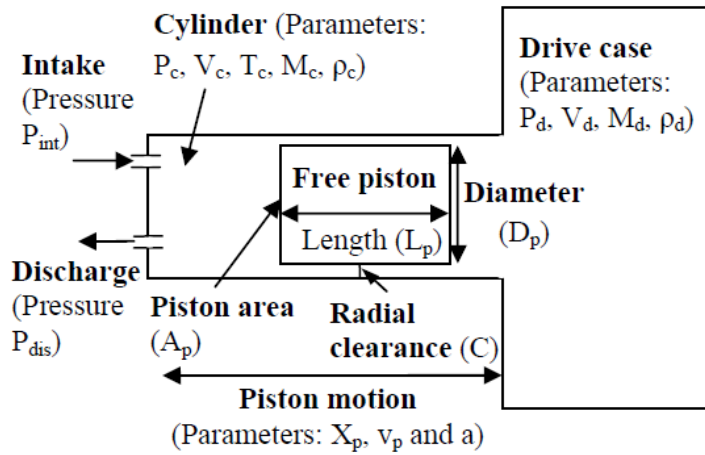
Fig. 1.4. Schematic for free-piston compressor model [34].
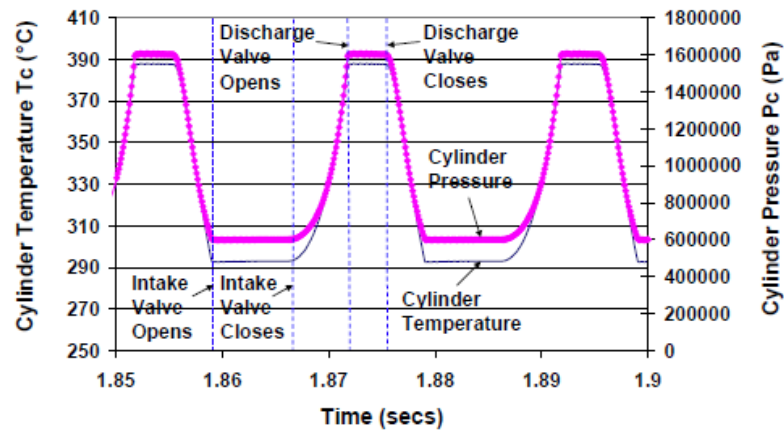
Fig. 1.5. Cylinder Temperature and Cylinder Pressure [34].

In these studies, a number of simplifications were introduced in the models. For example, detailed valve and leakage flow sub-models were not included which limit the capabilities of the models in accurately predicting compressor mass flow rate and considering the effects of design changes on performance. To address this deficiency, Bradshaw [13] developed a detailed mechanistic model of a prototype miniature linear compressor for electronics cooling that includes valve and leakage flow models. Ex-

(a)   (b)
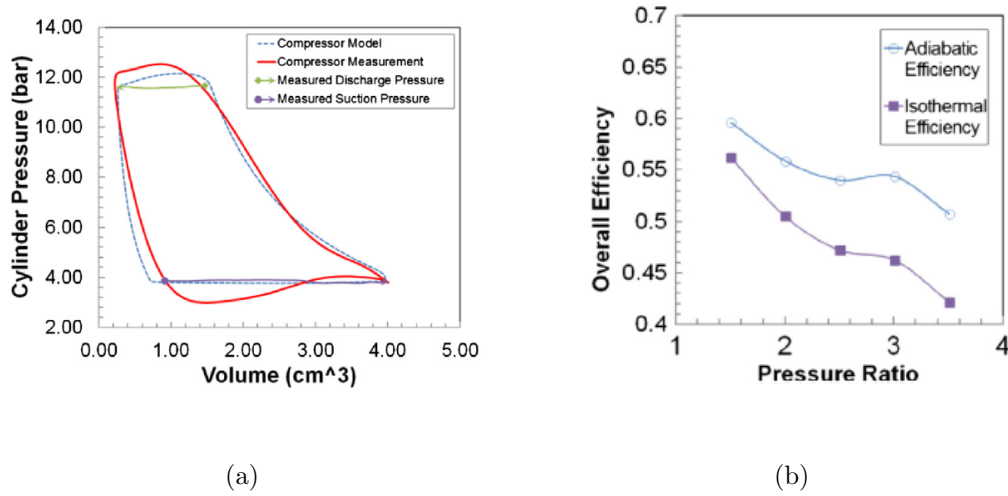
Fig. 1.6. Simulation results of a moving magnet linear compressor: (a) Derived P-V loop compared with the compressor model at the design point; (b) Overall efficiency as a function of pressure ratio for an operating stroke of 13 mm [39].

perimental data was used to validate the model and parametric studies were carried out to evaluate design improvements. The model includes a one degree of freedom valve model and simplified leakage flow and frictional losses. However, the dynamics associated with the mechanical and thermodynamic processes were not fully coupled. As a consequence, the model doesn't capture the fully transient behavior of a linear compressor where the variable stroke is linked to the spring system, gas system, and magnetic field that drives the linear motion.

In 2019, Jiang et al. [40] investigated the characteristics of a novel moving magnet linear motor for a linear compressor and a Finite Element Analysis (FEA) approach was applied to analyze the motor current and armature positions. Moreover, a series of tests were conducted to validate the theoretical results and it was found that the system resonance frequency increases as a function of pressure ratio and the matching motor capacitance varies in a large range of stroke. Dang et al. [41] provided a 3-D analytic model to design a motor for a micro moving-coil linear compressor and the magnetic field and configuration were analyzed and optimized. Experiments were

carried out to characterize the performance of a 500 g linear compressor with a pulse tube cold finger and a motor efficiency of 78.6% was reported for a cooling capacity of 1.2 W at 77 K. Both theoretical and experimental work were conducted by Li et al. [42] and R1234yf was used as a low global warming potential (GWP) refrigerant for an automobile air conditioner. The tested compressor had a motor efficiency of 86% and the maximum system COP was 3.

By surveying the literature, it is apparent that from the theoretical aspect, most previous researchers focused on simplified models that do not fully reflect the dynamic behavior of linear compressors. No previous publication has presented a comprehensive dynamic linear compressor model that couples mechanical, thermodynamic, and electrical sub-models. It is necessary to develop a comprehensive and generalized simulation model that considers these couplings and that can be used to predict both transient start-up and steady-periodic behaviors of linear compressors. In terms of the experimental studies, the majority of the cited literature focused primarily on prototyping linear compressors, which were designed for a specific application, and reported their unique features. Those designs contributed significantly to the development of linear compressor technology, which ultimately led to commercialized linear compressors. The commercialized compressors perform better and more reliable compared to earlier prototypes mentioned in the literature. However, relatively limited information has been published that involves modeling of commercial linear compressors and no experimental validation of models has been presented. It will be interesting to validate the proposed simulation model against the experimental data obtained for two commercially available linear compressors. In addition to assessing the accuracy of the model, targets for model improvement are identified. Furthermore, the model can be also used to identify key parameters affecting system performance based on the sensitivity study.

1.3.2 Prototype design of linear compressors

There were several prototyping linear compressors investigated in the literature along with the development of linear compressor analysis. Some of the typical designs are reviewed and analyzed in this section.

A prototyped oscillating electrodynamic compressor was presented firstly by Pollak et al. [4] in 1979 and the schematic drawing can be seen in Figure 1.7. One thick spring supports the movable coil, which is connected to the piston. The driving force is yielded from the interaction of the alternating coil current with a steady magnetic field, which is produced by a permanent magnet. The suction reed valve is located at the end of the piston and one discharge plate valve opens at another end of the cylinder during the discharging process which is very similar to the design of LG linear compressor, shown in Figure 1.1.
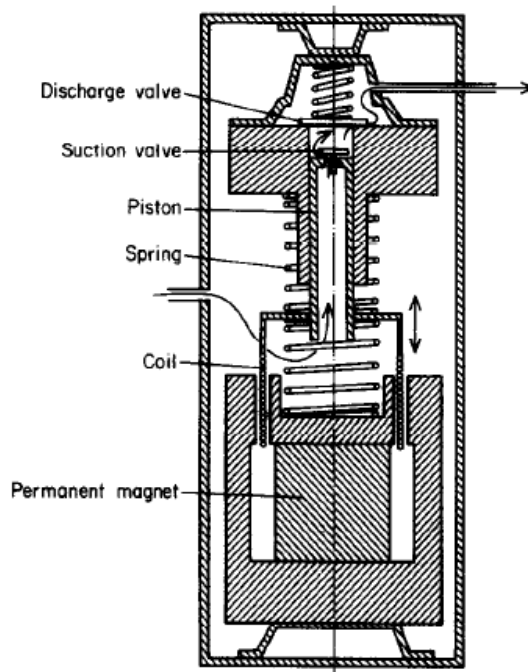
Fig. 1.7. Schematic drawing of oscillating electrodynamic compressor [4].

Sunpower Inc. has been conducting research on linear compressor technology for a long time and they developed and built several genetic linear compressors [5]. One of their designs is shown in Figure 1.8. The entire assembly consists of a linear motor with inner and outer pole pieces, a coil, and one tubular permanent magnet which is connected to the piston as a whole unit during the movement. The piston is supported by non-contact gas bearings, which provide a floating force for the piston and reduces the friction while promising the alignment.
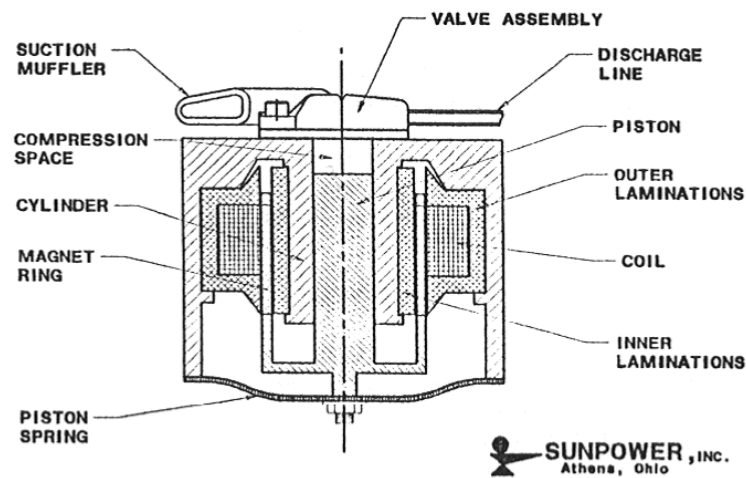
Fig. 1.8. Schematic diagram of linear compressor from Sunpower Inc. [5].

A prototype of a linear compressor was fabricated for miniature scale electronics cooling system and several additional revised designs are reported by Bradshaw et al. [13]. A sectional view diagram of the compressor is seen in Figure 1.9. The motor served as a central hub of assembly and the very thick compression spring is around the surface outside of the motor to stabilize the piston movement at resonant frequency. The motor selected for the prototype design was manufactured by H2W Technologies Inc. and the compressor was designed for a cooling capacity of at least 400 W. The conclusion obtained from this work was that the latest version of the linear

compressor design meets the increasing capacity for electronic cooling and could be a solution for the future commercial development.
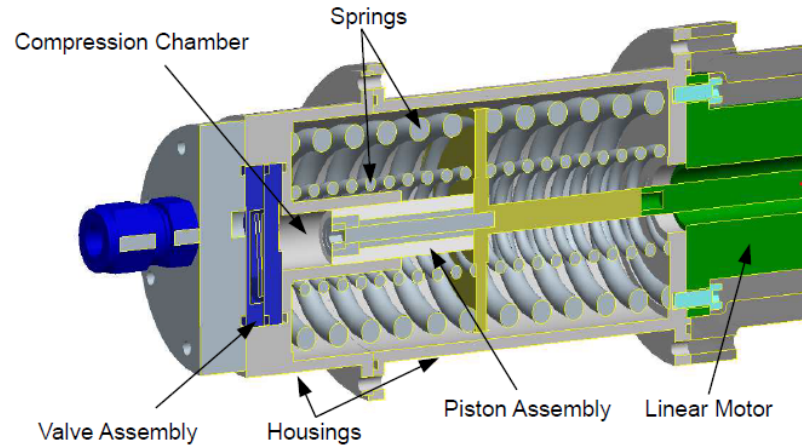
Fig. 1.9. Sectional view of the prototype linear compressor [13].

The University of Oxford built one linear compressor with a new magnetic motor reported by Liang et al. [39]. The design applies a magnet assembly that is supported at both ends, so that a suspension system can be created with greater radial stiffness. As shown in Figure 1.10, the compressor piston is directly attached to the moving magnet assembly and therefore reciprocates at the same frequency. Two sets of spiral springs with high radial stiffness were used to constrain the system movement to act as a linear bearing. It is also reported that the piston and cylinder for this compressor are made from stainless steel and the piston has a polymeric coating that was finished by turning. Recently, Bijanzad at al. [?] reported a performance evaluation of an oil-free linear compressor prototype. The motor is composed of two circular wound coils around the central axis. The coils are encapsulated in the three-legged structure. The plate valves were installed for suction and discharge line. Four different working fluids were analyzed and the motor and overall isentropic efficiency were discussed, which were reported up to 89 % and 67 % at the resonance excitation, respectively.
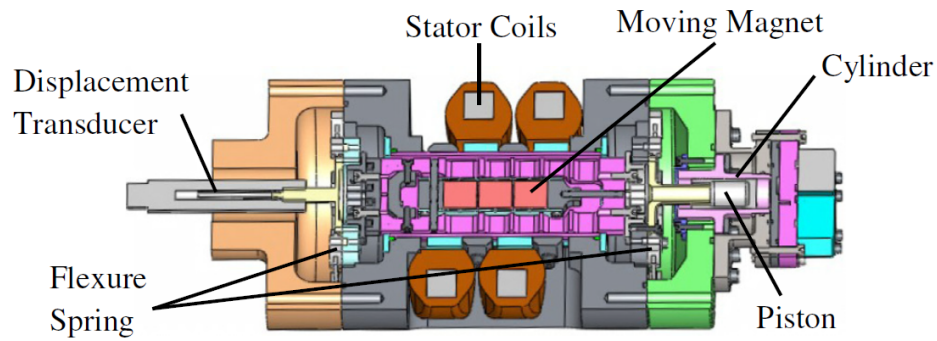
Fig. 1.10. Cross-section view of design of the 100W Oxford moving magnet compressor [39].

In summary, the following conclusions can be obtained from the linear compressor examples reviewed above:

- A high stiffness spring should be applied to ensure the compressor works at resonant frequency without the effect of the non-linearity gas spring force.

- The piston can be connected to the moving magnet, which helps the piston and motor reciprocate at the same frequency. Moreover, tubular is favorable as its design saves the internal space inside the compressor housing and also minimize the eccentricity of the piston.

- The valve assembly can be located on either sides of the piston or both valves can be installed at the end of the cylinder.

- Using a gas bearing is very beneficial for oil-free linear compressor design and the piston can be lubricated by the refrigerant itself.

However, all of these studies are focused on the performance characterization of a conventional reciprocating compressor driven by a linear motor. There was little work reported in the open literature in terms of the modifications of the compressor internal configurations to increase the removal of the heat flux during the compression

process and if it is possible to modify the geometry of the cylinder/piston by adding cooling channel to enhance the heat transfer process inside the linear compressor since there is more saved space due to the lack of the crank mechanism.

1.4 Objectives

Based on the literature review, a number of potential contributions to advance the research on linear compressors has been identified. In particular, the following efforts will be addressed within the present work:

- Develop a fundamental understanding of the dynamic characteristics of linear compressors.

  A comprehensive linear compressor simulation model has been developed to describe the entire dynamic compression process and associated energy flows. The model is based on mass and energy balance equations applied to open control volumes. To that end, the overall model is composed of several sub-models that include a piston dynamic model, an electrical motor model, a valve dynamic model, and a heat transfer model. When integrated together with an overall energy flow model for the compressor, it is possible to predict piston vibration, temperatures, and pressures within the compressor as well as overall performance. The dynamic characteristics of the linear compressor are analyzed and frequency response functions of the stroke are obtained to evaluate the effect of excitation frequency on the compressor performance and motor efficiency. The proposed formulation has been implemented within an open-source software package entitled PDSim written in the Python language by Bell et al. [43] and further enhanced by Ziviani [44]. The results of the compressor simulation model are being validated using experimental data from two commercially linear compressors used in domestic refrigerator/freezers. There is currently no other simulation modeling work available in open literature that considers all aspects.

- Conduct experimental analyses for two commercial linear compressors.

Limited work was found in the open literature related to comprehensive compressor modeling and model validation of commercially available linear compressors. Currently, there are two commercial linear compressors available that are used in residential refrigerator/freezers. One of them uses synthetic POE oil while the other is oil-free. An experimental characterization of the two compressors will be conducted using a hot-gas bypass test stand. Using these measurements, the two compressors will be characterized and compared in terms of dimensionless performance parameters. The conclusion from the comparison will be used to improve the compressor design via parametric studies and to identify key parameters affecting the compressor transients.

- Linear Compressor model validation and sensitivity analyses.

The experimental data collected from the two commercial linear compressors will be used to validate the developed comprehensive compressor model. The validated model will be validated against experimental data obtained for two commercially available linear compressors. In addition to assessing the accuracy of the model, targets for model improvement will be also identified. Additionally, the model will be exercised to identify key parameters affecting system performance and used to quantify the major sources of losses and analyze system vibration as well as piston eccentricity, which ultimately could be used to design the next generation of linear compressors.

- Develop alternative linear compressor prototype designs in terms of their potential for approaching an isothermal compression process.

In addition to the model development and analyses of existing commercial linear compressors, the feasibility of approaching an isothermal compression process is also evaluated from both component and system aspect. Different cooling methods can be applied to enhance the heat transfer process during the compression process. Larger heat exchange surfaces can be integrated into the piston-cylinder design by adding internal cooling paths with different geome-

tries. In particular, several designs have been proposed for performance investigations. A range of unique internal cooling geometries are enabled through the use of 3D printing. The key parameters governing compressor performance, such as leakage gap, piston geometry and internal cooling path configuration, are analyzed and the performance of the best designs are presented along with an assessment of the benefits of compressor cooling. Moreover, the scalability analysis is conducted in terms of heat pump and air compression application, which provides a guidance to design a scale-up linear compressor as well as the component selections.

1.5   Overview

The structure of the thesis follows the aforementioned objectives.

In **Chapter** **2**, a comprehensive mathematical modeling approach is introduced and the solution algorithm is explained. In **Chapter** **3**, the two commercial linear compressors are described along with the hot-gas by-pass test bench utilized for conducting their experimental characterizations. In-depth analyses of their performance are also carried out. A detailed model validation is reported in **Chapter** **4** and the simulation results based on the theoretical model described in Chapter 2 including transient and periodical steady state results are also discussed. In addition, the overall predicted compressor performance is also reported. **Chapter** **5** reports the sensitivity study by using the validated model, including leakage and frictional loss, gas bearing analysis and piston vibration and eccentricity analysis. In **Chapter** **6**, the feasibility of achieving isothermal compression is discussed from the theoretical component and overall system aspect. Moreover, the scalability of linear compressor for two applications, *i.e.,* heat pump and air compression, is also reported. Lastly, **Chapter** **7** summarized the research work conducted and provides both conclusions and recommendations for future work.

2. MATHEMATICAL MODELING

The mathematical approach that is applied to investigate the dynamic characteristics of linear compressor is laid out in this chapter. The aim is to develop a detailed mechanistic simulation model to predict the performance and describe the entire dynamic compression process and associated energy flows. The following aspects are included in this model:

1. Dynamic compression chamber model to predict the behavior of the gas within the working chamber (see Section 2.2).

2. Tube model to simulate a component which the flow goes through. The effects of the pressure drop and heat transfer process have been taken into account (see Section 2.3).

3. Flow path model to simulate the flow path connecting any two components/control volumes. It includes the leakage path and mass flow across the valve assembly (see Section 2.4).

4. Frictional model to simulate the frictional loss between piston and cylinder surface. Two type of friction forces were considered (see Section 2.5).

5. Since the stroke in linear compressor is not fixed by a crank mechanism, the stroke model is used to predict the dynamic movement of the piston by means of an overall force balance and dynamic equation of motion (see Section 2.6).

6. Motor model to determine the driving force on the piston as well as the power consumption during the compression process (see Section 2.7).

7. Heat transfer model to calculate the heat transfer rate inside the compression chamber (see Section 2.8).

8. Transient multi-lumped temperature model to simulate the overall energy balance on each main component of the compressor (see Section 2.9).

2.1 Comprehensive Dynamic Modeling

A comprehensive and generalized simulation model has been developed to simulate the dynamic performance of a linear compressor. The proposed formulation has been implemented within an open-source software package entitled PDSim initially developed by Bell et al. [43] and further enhanced by Ziviani [44], which simulates the performance of reciprocating, scroll, rotary, and screw machines. The package was written in the Python programming language [45] with the core model structure compiled in Cython [46] to increase the computational speed and the whole model is based on an object-oriented programming method. All elements in the various compression and expansion machines were created as objects, which are treated as the instances of a given class or library. Since a multitude of compressors and expanders have similar geometries, mass flow, heat transfer models in their simulation programs, it is be very helpful to plug and play with each component library from PDSim to generate a new local model accordingly. The general structure of a compressor or expander simulation model in PDSim is shown in Figure 2.1. Different modules have been added to the entire structure, which covers most types of compressors and expanders used in different applications. However, it is not necessary to use them all to generate a new model and the complexity can be modified according to the machine type. The optional modules are marked as grey boxes [47].

Generally, in the case of positive displacement machines having a crank-motion, the steady-periodic solution is of particular interest and the working cycle is identified as a function of the rotation angle. However, the real compression and expansion process in compressor are transient thermodynamic processes and a system of dynamic governing equations is necessary to be studied. Due to the fact that linear compressors do not have crank mechanism and the piston stroke is not fixed but determined
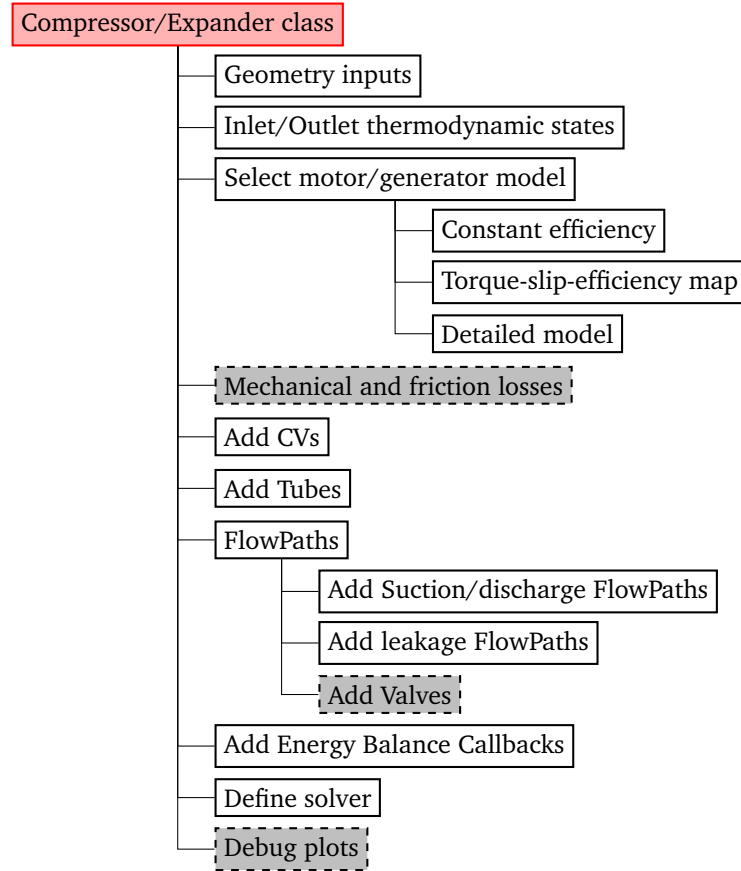
Fig. 2.1. General structure of a compressor/expander model in PDSim (Obtained from [47]).

by electro-mechanical forces instead, the work reported in this thesis extends the previous model to investigate the dynamic thermodynamic characteristics of linear compressors. The system of equations developed needs to be integrated over time. Therefore, the updated structure is general and flexible. It accounts for both transient and steady-periodic solutions.

2.2 Compression Chamber Governing Equations

Mass and energy conservation are applied to the working chamber during the compression process in a linear compressor. A control volume is the fundamental

element in the compressor model, which can be represented as Figure 2.2 and the element is used to connect the neighboring components via different flow paths, which allows to account for all the thermodynamic processes within the compressor. In order to improve the computational efficiency, all thermodynamic properties are assumed to be uniform within each control volume at any time such that the working fluid follows quasi-equilibrium processes. The overall compressor system is modeled by employing the following fundamental components, which can be identified from Figure 1.1.
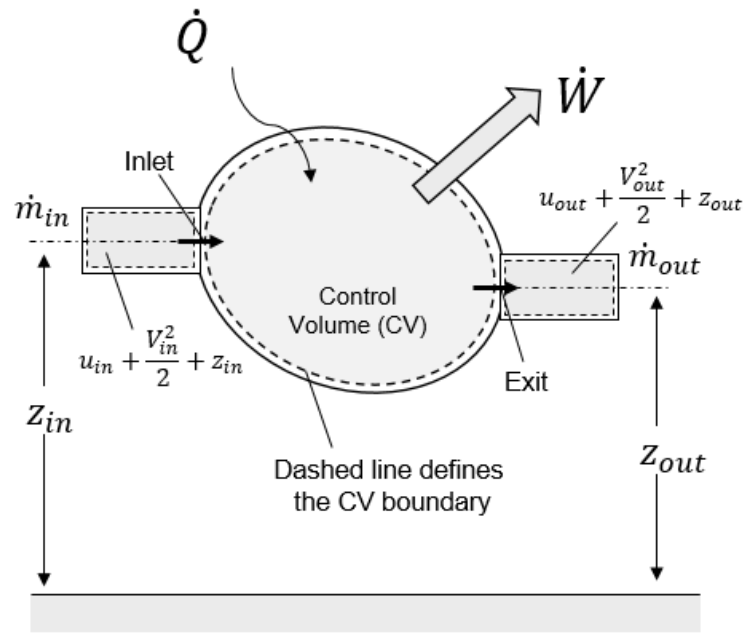
Fig. 2.2. Diagram of a control volume for 1st law analysis (Adapted from [47]).

- **Control Volume (CV):** working chamber, *i.e.*, compression chamber and shell chamber.

- **Tube:** suction and discharge connection tubing that contain flow paths where pressure drop and heat transfer processes associated with the working fluid are considered.

- **Flow Path:** connect each component of the entire model with a connected element that could either be a control volume or a tube, *i.e.*, valve flows, leakage flows.
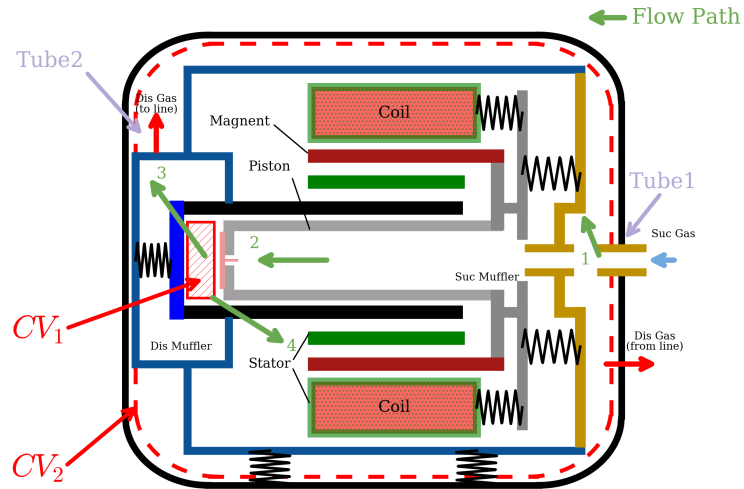
Fig. 2.3. Schematic diagram of a commercial linear compressor.

Table 2.1.
Description of the nomenclature and symbols used in Figure 2.3.

Component	Description
CV_1	compressor chamber
CV_2	shell chamber
Tube1	suction tube
Tube2	discharge tube
Flow Path 1	suction flow
Flow Path 2	suction valve flow
Flow Path 3	discharge valve flow
Flow Path 4	leakage flow

Since there is no crank mechanism inside a linear compressor, the governing equations developed in this study are time dependent and not rotating-angle dependent as typically utilized when modeling positive displacement compressors. The time-dependent model is well suited for predicting performance for both transient start-up after steady-periodic dynamic behavior has been achieved for a given set of boundary conditions. For a one-dimensional one-inlet, one-outlet control volume flow, the energy rate balance is shown in Equation 2.1:

$$\frac{dE_{cv}}{dt} = \dot{Q} - \dot{W} + \dot{m}_i \left(u_i + \frac{V_i^2}{2} + gz_i \right) - \dot{m}_e \left(u_e + \frac{V_e^2}{2} + gz_e \right) \qquad (2.1)$$

where E_{cv} denotes the energy of the control volume at time t. The terms $\dot{Q}$ and $\dot{W}$ account, respectively, for the net rate of energy transfer rate by heat and work across the boundary of the control volume at t. The other two terms inside the bracket represent the rates of transfer of internal, kinetic and potential energy of the entering and exiting flow.

Generally, there are two contributions for the work shown as terms $\dot{W}$ in Equation 2.1: one is the work associated with the liquid pressure for flowing and the other is shown as $\dot{W}_{cv}$, which consists of the other work effects on the control volume, including rotating shafts, movement of the boundary and electrical effects and so on and it is named as boundary work. Therefore, the work term $\dot{W}$ is divided and written as Equation 2.2:

$$\dot{W} = \dot{W}_{cv} + \dot{m}_e(P_e v_e) - \dot{m}_i(P_i v_i) \qquad (2.2)$$

where $\dot{m}_e$ and $\dot{m}_i$ are the mass flow rates and v_e and v_i are the specific volumes evaluated at the exit and inlet, respectively.

Substituting Equation 2.1 and Equation 2.2, the new expression of the control volume energy rate balance can be derived as Equation 2.3 and with the definition of specific enthalpy $h = u + pv$, the simplified form can be obtained as Equation 2.4:

$$\frac{dE_{cv}}{dt} = \dot{Q}_{cv} - \dot{W}_{cv} + \dot{m}_i \left(u_i + P_i v_i + \frac{V_i^2}{2} + gz_i \right) - \dot{m}_e \left(u_e + P_e v_e + \frac{V_e^2}{2} + gz_e \right) \quad (2.3)$$

$$\frac{dE_{cv}}{dt} = \dot{Q}_{cv} - \dot{W}_{cv} + \dot{m}_i \left(h_i + \frac{V_i^2}{2} + gz_i \right) - \dot{m}_e \left(h_e + \frac{V_e^2}{2} + gz_e \right) \quad (2.4)$$

By selecting a proper control volume to describe the compression process, further assumptions can be made to simplify Equation 2.4. In particular, the net change in potential and kinetic energies associated with the mass of fluid flowing across the boundary of the control control volume can be neglected due to their small contributions. Therefore, the energy conversation equation applied to a specific control volume of a compression chamber can be reduced to:

$$\frac{dE_{cv}}{dt} = \dot{Q}_{cv} - \dot{W}_{cv} + \sum_j \dot{m}_j h_j \quad (2.5)$$

where $\dot{m}_j h_j$ is enthalpy flow rate corresponding to the product of the upstream enthalpy and the mass flow rate for the j-th flow path , since there can be multiple flow paths connected to one control volume that allow mass flow in and out the control volume (*e.g.*, valves, leakage flows).

In order to expand Equation 2.5 to include the definitions of boundary work for a positive displacement machine and the specific internal energy, Equation 2.6 and Equation 2.7 can be derived.

$$\dot{W}_{cv} = -P_{cv} \frac{dV}{dt} \quad (2.6)$$

$$\frac{dE_{cv}}{dt} = \frac{d(u_{cv} m_{cv})}{dt} = m_{cv} \frac{du_{cv}}{dt} + u_{cv} \frac{dm_{cv}}{dt} \quad (2.7)$$

From the fundamentals of thermodynamics, it can be recalled that the exact differential of the specific internal energy and the specific internal energy can be expressed as:

$$du = C_v dT + \left[T \left(\frac{\partial P}{\partial T} \right)_v - P \right] dv \tag{2.8}$$

$$u = h - Pv \tag{2.9}$$

By substituting Equations 2.6 to 2.9 to Equation 2.5, the governing differential equation for transient behavior of the gas within the chamber is as follows:

$$m_{cv} c_{\text{p,cv}} \frac{dT}{dt} = T \left(\frac{\partial P}{\partial T} \right)_v \left[\frac{dV}{dt} - \frac{1}{\rho} \frac{dm_{cv}}{dt} \right] + h_{cv} \frac{dm_{cv}}{dt} + \frac{dQ}{dt} + \sum \frac{dm_{in}}{dt} h_{in} - \sum \frac{dm_{out}}{dt} h_{out} \tag{2.10}$$

where m_{cv} and $c_{p,CV}$ denotes the mass and the specific heat of the control volume; $\dot{m}_{out}$ and $\dot{m}_{in}$ represent the mass flow rates at the outlet and inlet. All the time derivative terms, *i.e.*, dT/dt, dV/dt, dQ/dt account, respectively, for the net change rate across the boundary of the control volume at time t.

With respect to the conservation of mass flow for the control volume, multiple flow paths are considered and the derivative of the mass is given by:

$$\frac{dm_{\text{cv}}}{dt} = \frac{dm_{\text{in}}}{dt} + \frac{dm_{\text{leak,in}}}{dt} - \frac{dm_{\text{out}}}{dt} - \frac{dm_{\text{leak,out}}}{dt} \tag{2.11}$$

where $dm_{\text{leak,in}}/dt$ and $dm_{\text{leak,out}}/dt$ are the leakage mass flow rates at the exit and inlet, respectively.

In order to carry on the thermodynamic calculations at each time step, the thermo-physical properties of the working fluid are retrieved from the open-source library CoolProp v6.1 developed by Bell. [48]. The CoolProp library employs the high-accuracy Helmholtz Equation of State (HEOS) explicit in temperature and density. A more detailed discussion on the selection of the independent variables used to carry on the integration of the governing equations can be found in Ziviani. [44]. The conservation equations are solved at a particular time step and coupled through the stroke control, valve, motor, heat transfer sub-models which will be presented later.

2.3 Tube Model

The tube mode is used to simulate flow through connection tubing and predicts the pressure drop and heat transfer process inside. The turbulent flow regime is applied in the model with some prerequisites as follows [49]:

- Quasi-steady flow through the tube
- Either the outlet or the inlet state is fixed in terms of the flow inside the tube
- Viscous effects are taken into account
- Single-phase flow

To understand the flow regime in the tube, the relationship between the Fanning friction factor and the Reynolds number is complex and is governed by Colebrook equation [50] where f is used as implicit form:

$$\frac{1}{\sqrt{f}} = -2.0 log_{10} \left(\frac{\frac{\epsilon}{d}}{3.7} + \frac{2.51}{\text{Re}\sqrt{\text{f}}} \right) \qquad (2.12)$$

Another formula was developed by Stuart W. Churchill [51] to analyze friction factor in the flow regime of laminar and turbulent flow both. This was originally derived to demonstrate the curves in the Moody chart, which shows the Darcy-Weisbach Friction factor versus Reynolds number. The Darcy Weisbach Formula f_D is 4 times the Fanning friction factor f and so a factor of $\frac{1}{4}$ has been applied to produce the formula given below:

$$f = 8 \left[(8/\text{Re})^{12} + (A + B)^{-1.5} \right]^{\frac{1}{12}} \qquad (2.13)$$

$$A = \left(2.457 \ln \left[(7/\text{Re})^{0.9} + 0.27 \left(\epsilon/D \right) \right]^{-1} \right)^{16} \qquad (2.14)$$

$$B = (37530/\text{Re})^{16} . \qquad (2.15)$$

where Reynolds number is given by Re $= GD/\mu$ and G is the mass flux given by $G = \dot{m}_{\text{tube}}/A_{\text{tube}}$ and A_{tube} is the cross-sectional flow area of the tube given by $A_{\text{tube}} = \pi D^2/4$.

2.3.1 Heat transfer

To calculate the heat transfer rate for turbulent fluid flow in the tubes, the Nusselt number (Nu) is determined by Gnielinski correlation as Equation 2.16, reported by Taler [52] and the heat transfer coefficient α is derived accordingly with Equation 2.17.

$$\text{Nu} = \frac{(f/8)(\text{Re} - 1000)\text{Pr}}{1 + 12.7\sqrt{f/8}(\text{Pr}^{2/3} - 1)}. \tag{2.16}$$

where $4 \times 10^3 \leq \text{Re} \geq 10^6, 0.5 \leq \text{Pr} \geq 200$ and f denotes the friction factor for smooth tubes which is calculated by Equation 2.13.

$$\alpha = \frac{k\text{Nu}}{D} \tag{2.17}$$

If the inlet state of the tube is fixed and the wall temperature is known, the outlet temperature can be obtained from Equation 2.18, otherwise Equation 2.19 and Equation 2.20 together yield the inlet temperature backwards with the given additional heat input to revise the outlet temperature.

$$T_{\text{out}} = T_{\text{wall}} - (T_{\text{wall}} - T_{\text{in}})\exp\left(-\frac{\pi DL\alpha}{\dot{m}_{\text{tube}}c_{\text{p}}}\right) \tag{2.18}$$

$$T_{\text{out}}^* = T_{\text{out}} - \frac{\dot{Q}_{add}}{\dot{m}c_p} \tag{2.19}$$

$$T_{\text{in}} = T_{\text{wall}} - \frac{T_{\text{wall}} - T_{\text{out}}^*}{\exp\left(-\frac{\pi DL\alpha}{\dot{m}_{\text{tube}}c_{\text{p}}}\right)} \tag{2.20}$$

2.3.2 Pressure drop

The head loss through the tubes can be calculated using the Darcy Weisbach equation [53] combined with the Fanning friction factor:

$$h_f = 4f\frac{L}{D}\frac{V^2}{2g}, \tag{2.21}$$

where V is the averaged flow velocity in the tubes

The pressure drop through the tubes can then be evaluated as:

$$\Delta P = \rho g h_f \tag{2.22}$$

The mass flux is determined with a form in terms of the average velocity in the tubes:

$$G = \rho A_{tube} V \tag{2.23}$$

Substituting Equation 2.21 and Equation 2.23 to Equation 2.22 , it yields the change of pressure through the tubes

$$\Delta P = -\frac{fG^2 L}{2\rho D} \tag{2.24}$$

With given the pressure drop across the tube, the pressure difference can be calculated based on Equation 2.25.

$$\Delta P = |P_{in} - P_{out}|, \tag{2.25}$$

2.4 Flow Path Model

Flow paths are used to connect each component of the entire model and the connected element could either be a control volume, as defined in Section 2.2, or a tube, as defined in Section 2.3. In each flow path, the model uses the input as inlet operating conditions to pursue the unknown pressure at the outlet. In addition, the mass flow rate through the flow path is determined accordingly in terms of different flow coefficients. In general, there are two types of flow path existing in the linear compressors: leakage flow valve flow path, which are presented in the following sections.

2.4.1 Leakage flow path

One of the mass leakage paths in linear compressors generally happens between the compression chamber and the compressor case through the gap, *i.e.*, radial clearance, which is located between the outer surface of the piston and the inner surface of cylinder wall. The leakage is a result of pressure differences between the compression chamber and compressor shell. Instead of using a piston ring or oil film that are commonly used to seal the leakage path in a conventional reciprocating compressor, an oil-free linear compressor uses the refrigerant with a small clearance gap to seal the leakage path and lubricate the piston motion. Some of the previous researchers adopted simplified leakage models, such as an isentropic flow model [13] or a simplified Couette flow model [34]. However, these approaches may not be adequate for estimating leakage flow in oil-free linear compressors. The leakage flow through the clearance gap between the piston and cylinder surfaces is governed by the Navier-Strokes (N-S) equations, in which inertia, body, pressure and viscous terms are included.

Based on lubrication theory [54], the leakage flow condition within the gap between the piston and cylinder is generally considered as "slow viscous motion", where the pressure and viscous terms are predominant. This allows simplification of the N-S equations. In this study, the leakage flow is modeled as a 1-D lubrication film with constant clearance gap, *i.e.*, no eccentricity, and the modified governing equation is given by Equation 2.26. This model was used to determine the pressure distribution inside the gas film, which was needed for calculating the leakage rate and frictional loss.

$$\frac{d}{dx}\left(\frac{\rho g^3}{12\mu}\frac{dP}{dx}\right) = \frac{\dot{x}_p}{2}\frac{d}{dx}(\rho g) + \frac{d}{dt}(\rho g) \tag{2.26}$$

where g is the clearance gap thickness, ρ is the gas density, μ is the viscosity of the gas. $\dot{x}_p(t)$ denotes piston movement velocity obtained from the linear compressor model, respectively.

The left-hand side (LHS) of Equation 2.26 represents the Poiseuille term and describes the net flow rates due to pressure gradients within the leakage path. The first term on the right-hand side (RHS) is the Couette term representing the net entraining flow rates due to surface velocity, *i.e.* piston velocity. The second term in the RHS denotes the transient change of the flow rate, coupled with the pressure change profile. Consequently, the integral form of the leakage mass flow rate can be determined by the integral through the flow path area at the end of the piston.

2.4.2   Valve model

It is assumed that the gas flow through the valve port is isentropic and compressible flow. One isentropic nozzle model is utilized to calculate the mass flow with the assumption that the flow is compressible without friction and heat transfer. The absence of heat transfer and friction means the flow will be reversible and adiabatic. The thermodynamic parameters in upstream condition, *i.e.*, temperature and pressure, are the inputs to this nozzle model. Within the isentropic nozzle, the local pressure ratio and the critical pressure ratio are needed and calculated by Equation 2.27 and Equation 2.28. The comparison between these two pressures are used to determine if the maximum flow rate occurs when sonic condition happens at the exit of the flow path, which is called a "choked flow", where the flow rate is maximum.

$$PR = \frac{P_{down}}{P_{up}}, \tag{2.27}$$

$$PR_{cri} = \left(\frac{2}{k+1}\right)^{k/(k-1)}, \tag{2.28}$$

where k is heat capacity ratio of the flow, subscript "up" means the upstream and *down* means the downstream of the leakage path.

Therefore, flow through the leakage path is divided into two sections based on the comparison as follows:

- Section I, $1 \geq PR \geq PR_{cri}$, flow is not choked and mass flow rate is calculated by:

$$\dot{m} = \frac{AP_u}{\sqrt{RT_u}}\sqrt{\frac{2k}{k-1}\text{PR}^{\frac{1}{k}}(1-\text{PR}^{\frac{k-1}{k}})} \tag{2.29}$$

where subscript u denotes the parameters in upstream condition

- Section II, $PR \leq PR_{cri}$, flow is choked

$$\dot{m} = \frac{A\rho_u}{\sqrt{kRT_u}}\left(1+\frac{k-1}{2}\right)^{\frac{1+k}{2(1-k)}} \tag{2.30}$$

The mass flow rate through the valve calculated by Equation 2.29 and Equation 2.30. However, the flow area changes along with the valve opening process, illustrated in Figure 2.4. Valve motion can be characterized as pressure dominant or mass dominant based on the lift of the valve opening with different flow area. This categorization was first suggested by Soedel [55] and improved by Kim et al. [56]. It can be noted that flow area in pressure-dominant region is a function of the valve lift and is equal to the valve circumference area, calculated by Equation 2.31. When the valve lifts high enough over one traditional point, the flow area begins to be independent of the valve lift and is equal to the port area, given by Equation 2.32. Theoretically, there is a critical valve lift between the mass-flux-dominant and pressure dominant modes and this critical value can be determined by assuming that the mass flow rate in two domains are consistent at this height, represented by Equation 2.33.

$$A_p = \pi D_v y_v \tag{2.31}$$

$$A_m = \frac{\pi}{4}D_{port}^2 \tag{2.32}$$

$$\rho_p V_p A_p = \rho_m V_m A_m \tag{2.33}$$
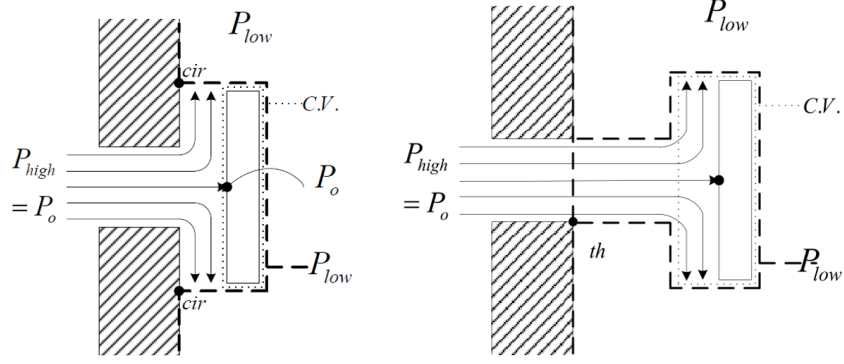
Fig. 2.4. Two dominant modes of valve opening (adapted from Bell et al. [43]).

Thus, substituting Equation 2.31 and Equation 2.32 to Equation 2.33, it yields the transitional displacement, as shown in Equation 2.34.

$$y_{\text{tr}} = \frac{1}{4}\frac{D_{\text{port}}^2}{D_{\text{valve}}} \tag{2.34}$$

where D_{port} denotes the diameter of the valve port and D_{valve} represents the valve plate diameter.

In addition, the valve displacement is investigated by dynamic modeling of the valve plate. The free body diagrams of the valve plate in terms of the two modes are shown in Figure 2.5. The summation of the forces in the y direction yields the equations of motion of the valve in terms of the two modes. For the pressure-dominant region, the pressure from upstream drops through the flow path to the downstream with lower pressure and the differential pressure force is dominant force on the valve movement. When the valve lift is beyond the transitional height, the pressure forces on the two sides of the valve plate are canceled and the mass flux force is added in the mass flux dominant condition. The governing equations for these two valve dominant modes are shown in Equation 2.35 and Equation 2.36:

$$m_{\text{eff,v}}\ddot{y}_v = \frac{1}{2}C_D\rho_v A_v v_{\text{gas}}^2(t)A_v - k_v y_v + (P_{\text{up}}(t) - P_{\text{down}}(t))A_v \tag{2.35}$$
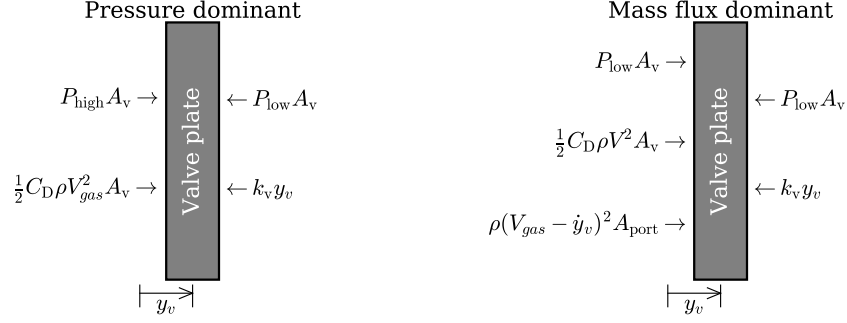
Fig. 2.5. Free body diagram of valve plate (Adapted from Bell et al. [43]).

$$m_{\text{eff,v}}\ddot{y}_v = \frac{1}{2}C_D\rho_v A_v v^2_{\text{gas}}(t)A_v + \rho(v_{\text{gas}}(t) - \dot{y}_v)^2 A_{\text{po}} - k_v y_v(t) \qquad (2.36)$$

where $m_{\text{eff,v}}$ is the valve effective mass, C_D is the drag force coefficient, ρ_v is the density of valve material, $v_{\text{gas}}(t)$ is the gas velocity, and y_v is the valve instantaneous transverse displacement. P_{up} and P_{down} represent the upstream and down stream pressure on valve, A_v and A_{po} denote the flow area on valve plate and valve port, respectively.

Figure 2.6 and Figure 2.7 depict the two valve types employed for suction and discharge in the linear compressor. Modeling approaches from Kim et al. [56] and Bell et al. [43] are employed. A reed valve is used on the suction side and is modeled as a one-degree-of-freedom, lumped element, vibrational system considering the natural frequency. A plate valve is used for discharge and is treated with a mass-spring model. The stiffness of the reed valve is calculated using Equation 2.37. The equivalent masses for the reed and plate values are estimated using the approach of Wood et al. [57] and given in Equation 2.39 and Equation 2.40, where the natural frequency of reed valve is determined from Equation 2.38.

$$k_s = \frac{F}{\delta_s} = \frac{3EI_m}{a^3} \qquad (2.37)$$

$$\omega_n = \frac{1.875^2}{2\pi l^2}\left(\frac{EI_m}{m_L}\right)^{0.5} \qquad (2.38)$$
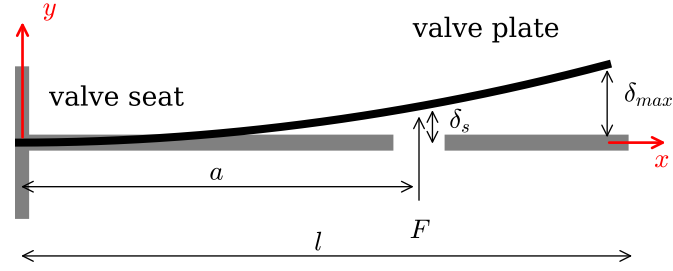
Fig. 2.6. Schematic of a reed valve.
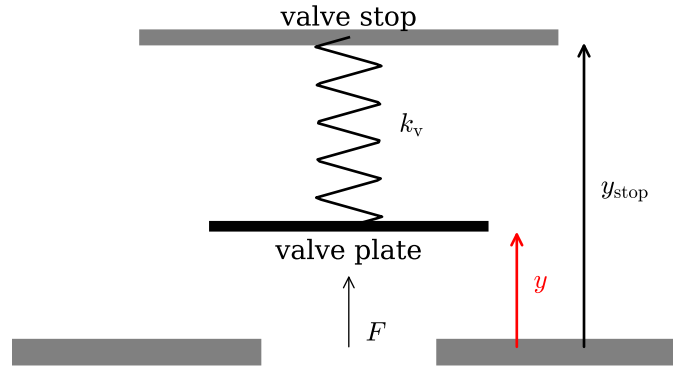
Fig. 2.7. Schematic of a plate valve.

$$m_{\text{eff,re}} = \frac{k_s}{\omega_n^2} \tag{2.39}$$

$$m_{\text{eff,pl}} = m_v + \frac{1}{3}m_s \tag{2.40}$$

where ω_n is the natural frequency, m_L is the mass of valve per unit of length, m_s is the spring mass, E is Young's modulus and I_m is the moment of inertia of the beam cross section. Regarding the geometry parameters in the valve, a is the distance between the anchor and valve port, and l the valve reed length.

2.5   Friction Model

The friction force between the cylinder wall and piston surface is the sum of the asperity contact force and gas viscous friction force of the gas flow. The viscous friction contribution is obtained by Equation 2.41, which is determined by the pressure distribution within the clearance gap and the gas viscosity. For an oil lubricated compressor, the effect of this term should be limited given the low viscosity of gas compared with that of the oil lubricant.

$$F_{\text{vis}} = \int_0^{L_p} \left[\frac{g}{2} \frac{dP}{dx} + \frac{\mu}{g} \dot{x}_p \right] dx \tag{2.41}$$

Another term contributing to the frictional loss is due to the surface roughness, which can be determined by the model proposed by Greenwood and Tripp [58] that is shown in Equation 2.42. The friction force due to the surface roughness, called the asperity contact force, depends on the relative ratio between the clearance gap and surface roughness. It can be concluded from this equation that when the clearance gap is so small that the gas film thickness is below the limit of surface roughness, the asperity force will increase dramatically. After obtaining the transient friction work variation along the piston length, the root mean square (RMS) value of the friction loss is obtained from Equation 2.44.

$$F_{asp} = \int_0^{L_p} C_f \frac{16\sqrt{2}}{15} \pi (\sigma \beta \eta^\star)^2 E \sqrt{\frac{\sigma}{\beta}} P \left(\frac{g}{\sigma} \right) dx \tag{2.42}$$

where σ is the surface averaged roughness, β denotes the radius of curvature at the peak of asperity, C_f is the dry friction coefficient, $\eta^\star$ represents the surface density of asperity peaks and P(x) is the probability distribution function of asperity height, which is denoted in Equation 2.43.

$$P(x) = \begin{cases} A(\Omega - x)^z & \text{if } x \leq \Omega \\ 0 & \text{if } x > \Omega \end{cases} \tag{2.43}$$

where A and Z are the probability distribution linear and exponent factor, respectively, and Ω is the boundary for asperity force.

$$\dot{W}_{\text{fri}} = \sqrt{\frac{1}{n} \sum \left((F_{\text{vis}} + F_{\text{asp}}) \dot{x}_p \right)^2} \tag{2.44}$$

where n is the number of the calculated values at each time step.

2.6   Piston Model

The stroke length of the linear compressor is not fixed by a crank mechanism but by the geometry, the motor and the dynamic force balance instead. The spring suspension system is used to ensure that the piston is moving linearly. The piston is modeled as a free body with forced, damped and simple harmonic oscillation. Figure 2.8 shows the force balance analysis on the piston assembly. The movement of the piston is affected by the gas pressure differential force, the mechanical spring force and the friction force and the governing equation can be expressed as Equation 2.45. The motor driving force is based on the input current (I) and motor factor (α) as described in Section 2.7. The piston starts from an initial point with some gas inside the compression chamber and is moved between top dead center (TDC) and bottom dead center (BDC). According to the force balance and the frequency of the input power, the piston displacement will oscillate between positive and negative values and the stroke can also be affected.

$$m_{\text{eff,p}} \ddot{x}_p + c_{\text{fri}} \dot{x}_p + k_s x_p + (P(t) - P_{\text{shell}}) A_p = \alpha I(t) \tag{2.45}$$

where $m_{\text{eff,p}}$ is the effective mass of piston and moving magnet, c_{fri} is the friction coefficient, calculated by Equation 2.46, k_s is the mechanical spring stiffness, A_p is the piston cross area, x_p and $\dot{x}_p$ are the piston instantaneous transverse displacement and velocity, respectively.

$$c_{fri} = \frac{\mu A_{p,cir}}{\text{g}} \tag{2.46}$$

where μ is the gas dynamic viscosity, $A_{p,cir}$ is the circumferential area of piston and g is clearance gap.
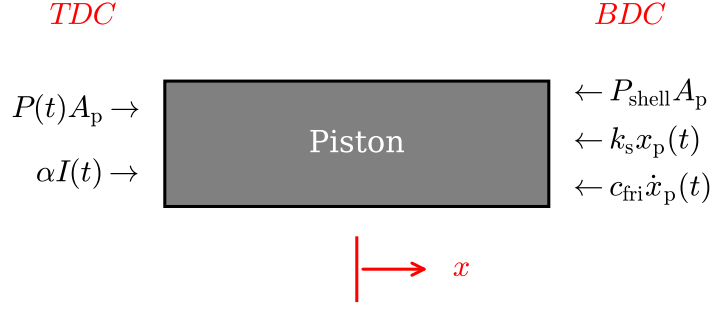
Fig. 2.8. Free body diagram of piston with pressure force term.

In order to determine the resonant frequency of the system, the equation of motion (EOM) is setup as a function of damping and spring term only. Therefore, the gas pressure force term is then divided into an equivalent viscous damping force and an equivalent spring force. The modified governing equation is shown as Equation 2.47 and the new force balance can be represented by the new free body diagram in Figure 2.9.

$$m_{\text{eff,p}}\ddot{x}_p + (c_{\text{fri}} + c_{\text{gas}})\dot{x}_p + (k_s - k_{\text{gas}})x_p = \alpha I(t) \tag{2.47}$$

where c_{gas} is the equivalent viscous damping coefficient and k_{gas} is the equivalent spring stiffness which can be calculated by Equation 2.48 and Equation 2.49 respectively.

$$k_{\text{gas}} = \frac{P_s(PR - 1)A_P}{x_p} \tag{2.48}$$

$$\oint c_{\text{gas}}\dot{x}_p \, ds = \oint P \, dV \tag{2.49}$$

where PR denotes the pressure ratio on the piston and A_p represents the piston across area.
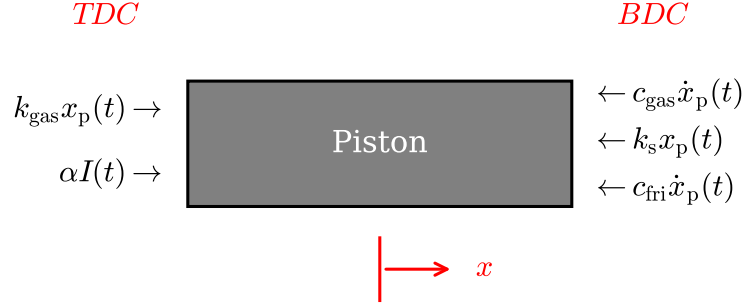
Fig. 2.9. Free body diagram of piston with the equivalent gas spring and damping term.

The total spring stiffness of the system can, therefore, be obtained by the sum of two spring stiffness terms from Equation 2.50 and the resonant frequency is expressed as Equation 2.52 with the natural frequency given by Equation 2.51.

$$k_{\text{tot}} = k_s + k_{\text{gas}} \tag{2.50}$$

$$\omega_n = \sqrt{\frac{k_{\text{tot}}}{m_{\text{eff,p}}}} \tag{2.51}$$

$$f = \frac{1}{2\pi}\omega_n \tag{2.52}$$

2.6.1 Piston bias displacement

Unlike in conventional reciprocating compressor, the stroke in linear compressor is not fixed and is based on the overall force balance in the system. A special characteristic of linear compressors is piston bias displacement where the piston shifts from one initial position X_0 to a new equilibrium position X_m. This concept was briefly reported by Bradshaw [13] as piston drift and was found to be a function of the stroke-to-diameter ratio. Figure 2.10 depicts this behavior of the piston in a linear

compressor. Initially, there is no differential pressure force ($P_{cyl}(t) = P_{shell}(t)$) acting on the piston body at X_0 and the suction pressure is equal to the discharge pressure. This initial equilibrium position is determined by the design/assembly of the compressor, i.e. magnet location, spring system, motor power etc. Once the compressor starts operation and the in-cylinder pressure begins to be established, the pressure difference between the compression chamber and compressor shell is no longer equal to zero, e.g., $P_{cyl}(t) > P_{shell}(t)$, and the bias shift occurs. The bias of the initial position relative to the equilibrium position for a given operating condition is determined using Equation 2.53, where the position is measured from the discharge plate to the TDC position of the piston.
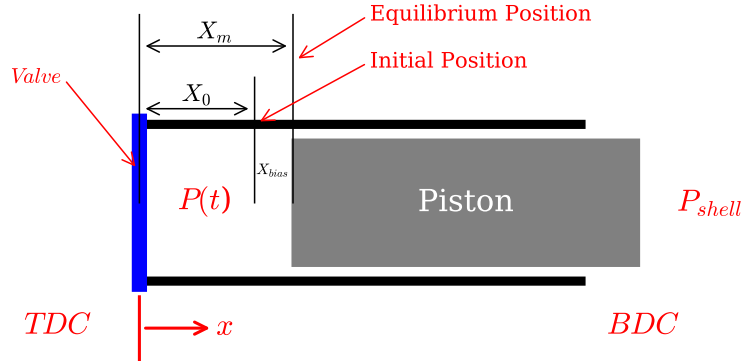
Fig. 2.10. Schematic of piston bias displacement.

$$X_{\text{bias}} = X_m - X_0 \tag{2.53}$$

In order to understand how the piston bias affects compressor design and operation, there are three scenarios to consider as follows:

- $X_0 < X_m$

  The bias displacement is positive, which means the overall pressure force pushes the piston to the direction of BDC until the new equilibrium position has been

reached. In this case, the piston does not make contact with the valve assembly during the discharging process and a clearance volume exists for gas expansion prior to the suction valve opening. In reality, this type of bias displacement is usually more favorable for linear compressor design.

- $X_0 \geq X_m$

  This case results from improper design of the linear compressor, which can result from under-estimation of the piston oscillation amplitude or oversizing the mechanical spring assembly. In this case, metal-to-metal contact may occur when the piston is at TDC during a discharging process. Although the negative effect of gas re-expansion is minimal, this situation is not desirable because of the potential for compressor damage. There are potential solutions to address this issue that don't require changing the original compressor design. For example, the top of the cylinder can be a discharge valve, as discussed for the example of Figure 1.1. As the piston moves close to the discharge valve, the valve can be pushed away from the valve seat simultaneously. Therefore, metallic contact can be avoided if the springs are chosen appropriately. However, there is the potential for high pressure drop and oscillating behavior during the discharging process. Alternatively, the clearance volume can be fixed by adjusting the input excitation voltage based on the transient piston displacement [38]. However, more control and dynamic sensors are required to achieve this solution.

- $X_0 \ll X_m$

  If X_0 is significantly less than X_m, then a large volume change occurs during the re-expansion process prior to suction gas entering the cylinder. This leads to a limited amount of gas in the compressor chamber being compressed and very poor overall performance in terms of mass flow. This situation should be avoided in the compressor design.

In summary, it is important to control piston bias displacement in linear compressor design and the simulation model developed in this study is very useful for that

purpose. The piston diameter, nominal linear motor stroke length, spring forces, *etc.* affect the initial and equilibrium positions and should be considered in sensitivity studies during the design phase.

2.6.2   Spring stiffness

The mechanical spring stiffness, k_s, can be measured experimentally and the method, adopted by Bradshaw et al. [13], is to measure the spring displacement with different load mass weight. The test setup is shown in Figure 2.11. The relationship between the load and the spring displacement can be obtained from the curve based on the experimental data and the curve slope is the calculated spring stiffness respectively.
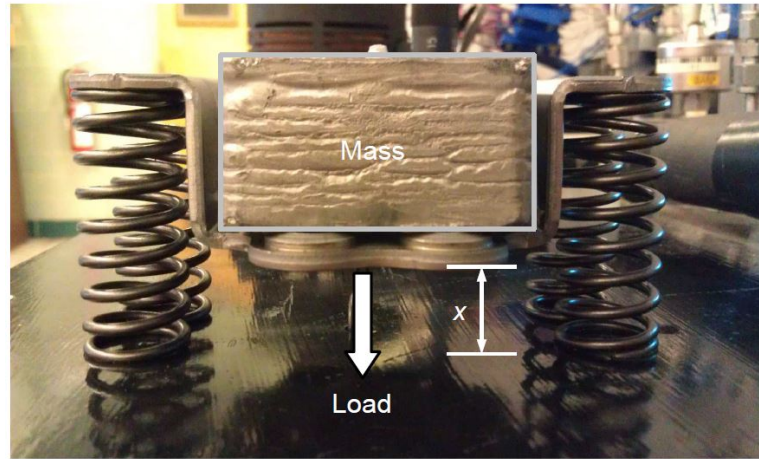
Fig. 2.11.   Measurement of spring stiffness in linear compressor by Bradshaw et al. [13].

As shown in Equation 2.51 and Equation 2.52, the natural frequency as well as the resonant frequency is the function of the sum of the mechanical spring stiffness and the gas spring stiffness. It can be seen in Equation 2.48 that the latter one depends on the pressure ratio (PR), and its value will increase with the increasing pressure ratio. Due to the non-linearity of gas spring stiffness behavior, reported by Liang [59], the

gas spring should be avoided in the design and ensure that the resonant frequency is dominated by mechanical spring stiffness otherwise there may be some numerical instabilities and unexpected compressor movement control issues showing up. A large spring stiffness is adopted that dictates a small variation in resonance frequency to avoid the effects of the non-linear gas spring, shown in Equation 2.54 when $k_s \gg k_{\text{gas}}$ and can minimize piston drift issues, which could become especially significant for larger pressure ratio applications.

$$f = \frac{1}{2\pi} \sqrt{\frac{k_s + k_{gas}}{m_{eff}}} = \frac{1}{2\pi} \sqrt{\frac{k_s}{m_{eff}}} \tag{2.54}$$

2.6.3 Oil viscosity

The dynamic linear compressor model presented in this report is general enough to account for both oil-free and oil-lubricated compressor. In terms of damping coefficients associated with oil film, it is necessary to determine the oil viscosity inside the compressor, which is a function of the local instantaneous temperature and pressure. The correlation of POE oil density and viscosity was derived and reported first by Kauzlarich [60] as shown in Equation 2.55. In this correlation, VG is the ISO-VG number which is given by compressor manufacturer.

$$\mu_o \rho_o = \left\{ 0.0400 \exp\left[\frac{458.4}{T_o + 240.5} \right] \right\} V G^{\left\{ 0.2097 \exp\left[\frac{473.9}{T_o + 123.7} \right] \right\}} \tag{2.55}$$

where ρ_o is the oil density given by:

$$\rho_o = (0.8753 - 0.00062 T_o) V G^{0.0374} \tag{2.56}$$

2.7 Motor Model

Pollak et al. [4] proposed a motor model that utilizes a parallel effective resistance and inductance. This simplified model, adopted by many researchers [13, 14, 34],

assumes that the compressor motion is harmonic and the input power follows sinusoidal voltage and current variations. However, this approach does not consider the dynamic interaction of the current, piston movement, and input voltage. Furthermore, the method was not validated for dynamic and transient analysis. Therefore, a dynamic model for the motor electric circuit that considers these interactions and that includes the input voltage V, inductance L, electric resistance R, capacitance C, and coupling to the piston velocity is proposed in Equation 2.57.
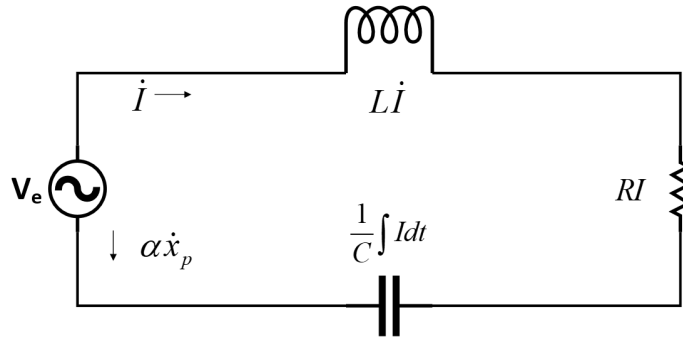
Fig. 2.12. Electric circuit diagram used in linear compressors

$$V_e - u_{\mathrm{emf}}(t) = L\dot{I} + RI + \frac{1}{C} \int I dt \qquad (2.57)$$

where $u_{\mathrm{emf}}(t)$ represents the back Electromotive force (EMF), which is the induced voltage generated in the magnetic field due to relative motion between piston and stator winding, calculated with Faraday's Law as:

$$u_{\mathrm{emf}}(t) = Bl\dot{x}_p \quad = \alpha\dot{x}_p \qquad (2.58)$$

where B is the magnetic density and l is the length of the conductor. However, the motor factor α is always used to calculate EMF, which can be obtained from nameplate of the motor or correlated with experimental data.

Once the input current is determined from the circuit equation, the input and output power are calculated based on Equation 2.59 and Equation 2.60, which is the

square root of the arithmetic mean of the transient power consumption. The motor efficiency is obtained from Equation 2.61, coupled with the piston model presented in Equation 2.45.

$$\dot{W}_{\text{in,RMS}} = \sqrt{\frac{1}{n}\sum \dot{W}_{in}^2(t)} = \sqrt{\frac{1}{n}\sum (V(t)I(t))^2} \qquad (2.59)$$

$$\dot{W}_{\text{out,RMS}} = \sqrt{\frac{1}{n}\sum \dot{W}_{out}^2(t)} = \sqrt{\frac{1}{n}\sum (\alpha I(t)\dot{x}_p(t))^2} \qquad (2.60)$$

$$\eta_m = \frac{\dot{W}_{\text{out,rms}}}{\dot{W}_{\text{in,rms}}} \qquad (2.61)$$

where n is the number of the calculated values at each time step.

2.8 In-cylinder Heat Transfer Model

The instantaneous heat transfer process between cylinder wall and compression chamber is due to the turbulent relative motion of the working fluid. This process is similar to that in conventional reciprocating compressor and is determined by the correlation shown in Equation 2.62 that was proposed by Adair et al. [61]. The heat transfer coefficient h_c is obtained from Nusselt number and used to determine the instantaneous heat transfer rate using Equation 2.64. The instantaneous transient heat transfer rate between cylinder wall and compressor chamber is calculated at each time step and the overall heat transfer rate for each of two control volumes, shown in Figure 2.3, which is integrated in the overall energy balance of the entire compressor.

$$\text{Nu} = \frac{h_c D_p}{k} = 0.053 \text{Re}^{0.8} \text{Pr}^{0.6} \qquad (2.62)$$

$$\text{Re} = \frac{\rho D \dot{x}_p}{\mu} \qquad (2.63)$$

$$\dot{Q} = h_c A_w (T(t) - T_{\text{cyl}}(t)) \tag{2.64}$$

where D_p is the piston diameter, h_c is the convective heat transfer coefficient, k is the thermal conductivity, A_w is heat transfer area of the cylinder wall.

The in-cylinder heat transfer area (A_w) depends on the piston motion and is coupled to the solution of the piston model. This is more complicated than the solution for a conventional crank-driven reciprocating compressor where the surface area variation can be predetermined from the sinusoidal shaped piston movement.

2.9   Overall Energy Balance

In order to close the compressor model, an overall energy balance (OEB) needs to be imposed. In particular, a compressor is characterized by a heat flow network in which heat is transferred between the working fluid and each control volumes within the compressor. Additional heat is generated by friction and motor heat generation. To limit the complexity of the problem, it is assumed that the temperature distributions are uniform within the lumped mass. Such assumption is reasonable given the fact that spatial variations of the temperatures are small with respect to the average temperature of the component. The resulting thermal model is called the lumped capacitance method, as proposed by Bergman [62], and it is used in this study. This concept implies that temperature gradients within solids are negligible. In order to account for the two simulation modes, two formulations of the overall energy balance coupled with the other sub-models have been implemented. From the available literature, Liu [63] and Chen [64] developed dynamic thermal network models to predict transient temperatures for key components in a hermetic rolling piston compressor and a hermetic scroll compressor, respectively. In both studies, dynamic models for the overall energy balances were developed at first, and then simplified to obtain a steady-state system of equations. For instance, Liu [63] used the dynamic model and conducted the validation by using transient temperature

measurements, but ultimately used a steady-state model due to the longer time-scale of the lumped temperatures with respect to the highly-dynamic in-cylinder compression process. Nevertheless, in the case of the linear compressor, it can be beneficial having a dynamic OEB since the simulation starts from time zero.

As shown in Figure 2.13 and Figure 2.14, there are five unknown lumped temperatures: the motor temperature, T_{motor}; the cylinder wall temperature T_{wall}, the shell temperature T_{shell}; two control volume temperatures, T_{com} and T_{gas}. It has to be highlighted that the control volume temperatures are also coupled with the chamber model, discussed in Section 2.2 and can be identified as follows:
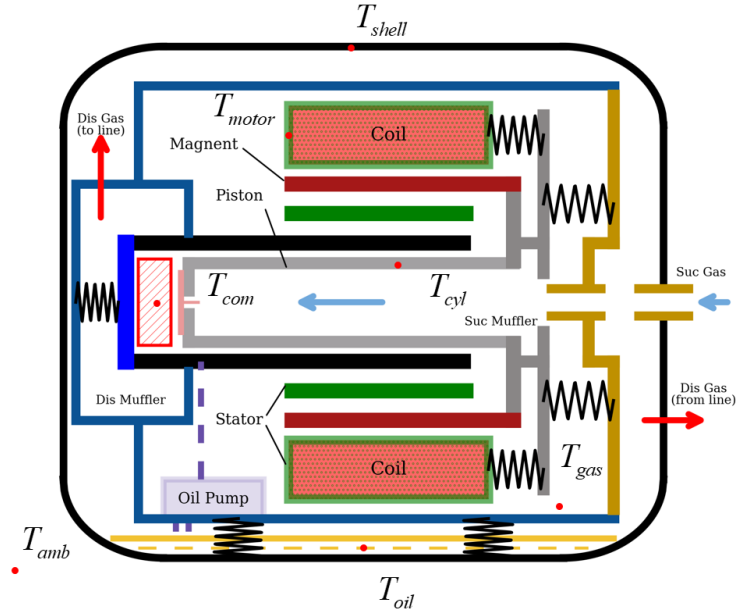
Fig. 2.13. Schematic of the linear compressor with the different lumped temperatures considered.

- T_{amb} : ambient temperature around the compressor;

- T_{com} : lumped temperature of compressor (compression chamber);

- T_{shell} : lumped temperature of compressor shell;

- T_{cyl} : lumped temperature of cylinder wall;
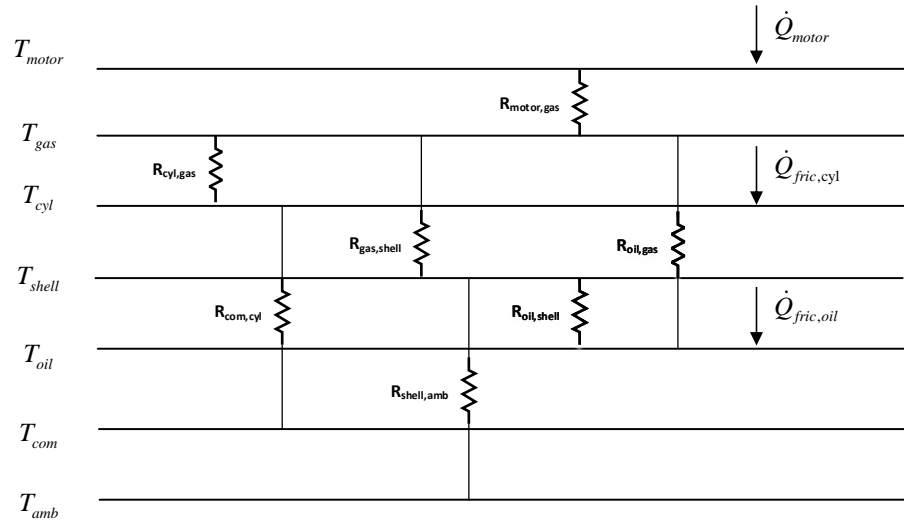
Fig. 2.14. Thermal resistance network of the overall energy balance for the linear compressor.

- T_{gas} : lumped temperature of the gas within the compressor shell;

- T_{motor} : lumped temperature of the motor;

- T_{oil} : lumped temperature of the oil in the oil sump if applicable;

- $R_{\text{cyl,comp}}$: average thermal resistance between cylinder wall and compression chamber;

- $R_{\text{cyl,gas}}$: average thermal resistance between cylinder and gas within the shell;

- $R_{\text{gas,shell}}$: average thermal resistance between gas within the shell and the shell;

- $R_{\text{shell,amb}}$: average thermal resistance between the compressor shell and ambient air;

- $R_{\text{motor,gas}}$: average thermal resistance between motor and gas within the shell;

- $R_{\text{oil,shell}}$: average thermal resistance between oil in oil sump and the shell;

- $R_{\mathrm{oil,gas}}$: average thermal resistance between oil in the oil sump and gas within the shell;

- $\dot{Q}_{\mathrm{motor}}$: rate of heat generated by motor;

- $\dot{Q}_{\mathrm{fric,cyl}}$: rate of heat generated by friction on the cylinder wall (oil-free);

- $\dot{Q}_{\mathrm{fric,oil}}$: rate of heat generated by friction on the oil (if applicable);

All the averaged thermal resistances are based on material properties and different correlations for heat transfer coefficients in this study which are listed in Table 2.2. Once the Nusselt number is obtained, Equation 2.65 and Equation 2.66 are used to calculate the thermal resistance for each component. To this end, the transient overall energy balance is obtained and coupled with the other governing equations to consist a system of ordinary differential equations, shown in Equation 2.67.

$$h_{i,j} = \frac{\mathrm{Nu}k}{D} \tag{2.65}$$

where k is the thermal conductivity coefficient and D is the characteristic length

$$R_{i,j} = \frac{1}{A_{i,j}h_{i,j}} \tag{2.66}$$

Once all the thermal resistances are determined, the temperatures of the main compressor components listed above are solved simultaneously using the system of equations represented by Equation 2.67. These equations are coupled to each other through heat flows across the thermal resistances.

$$\frac{d}{dt}(c_{p,i}T_i) = \sum \frac{T_j - T_i}{R_{ij}} + \dot{Q}_{i,fric} \tag{2.67}$$

where i refers to the analyzed component and j is corresponding component based on thermal resistance network and $\dot{Q}_{i,fric}$ is the friction loss, applicable in motor, cylinder and oil only. In addition, $c_{p,i}$ denotes the lumped thermal capacitance which is usually given by Equation 2.68.

$$C_{p,i} = m_i c_{p,i} \tag{2.68}$$

where m_i denotes the mass of each component and $c_{p,i}$ represents the specific heat of the material of the component.

It is important to notice that most of the masses discussed above are constant except for the gas mass inside the compression chamber which can be obtained from the mass conservation in Equation 2.11. In addition, the specific heat of each component can be assumed as constant value as well. Therefore, the transient temperatures of the compressor system can be predicted from the group of first order of ordinary differential equation which are coupled with other governing equations discussed in previous sections.

Table 2.2.
List of some heat transfer correlations used in this study for energy balance.

Correlation	Resistance	Reference
$\mathrm{Nu} = 0.053 \frac{k}{D_h} \mathrm{Re}^{0.8} \mathrm{Pr}^{0.6}$	$R_{wall,comp}$	[61]
$\mathrm{Nu} = 4.36$	$R_{wall,gas}$	[61]
$\mathrm{Nu} = 0.037(\mathrm{Re}^{4/5} - 871 \mathrm{Pr}^{1/3}$	$R_{shell,gas}$	[65]
$\mathrm{Nu} = 0.825 + \dfrac{0.387 \mathrm{Ra}^{1/6}}{\left[1 + (0.492/\mathrm{Pr})^{9/16}\right]^{8/27}}$	$R_{shell,amb}$	[65]
$\mathrm{Nu} = 0.11(\mathrm{GrPr})^{1/3}$	$R_{motor,gas}$	[66]
$\mathrm{Nu} = 0.818 \mathrm{Pr}^{1/3} \mathrm{Ra}^{0.034}$	$R_{oil,shell}$	[67]
$\mathrm{Nu} = 0.27 \mathrm{Ra}^{0.25}$	$R_{oil,gas}$	[65]

Instead of using capacitance in the thermal network analysis, there is no time-based integration for the overall energy balance for the quasi-steady mode. Therefore, multiple preliminary guess values are made for lumped temperatures, which must be determined iteratively through the cycle. The overall energy balance, shown in

Equation 2.69, is then enforced by solving each of the lumped masses based on a global energy balance over the course of a periodic cycle.

$$\dot{W}_{loss} + \sum \dot{Q}_i(T_{lump}) = 0 \tag{2.69}$$

where $\dot{W}_{loss}$ is the mechanical losses within the compressor and $\dot{Q}_i(T_{lump})$ denotes the heat transfer between each lumped temperature.

2.10 Numerical Solution Approach

As previously outlined, there are two simulation modes, *i.e.*, dynamic start-up and periodical steady-state, in the proposed simulation framework. For a given set of boundary conditions (inlet refrigerant pressure and temperature, refrigerant outlet pressure, and ambient temperature), the dynamic start-up mode tracks the time evolution of the short-term dynamics of the oscillating piston, the longer-term dynamics associated with the thermal inertia of the compressor materials, and the coupling between the two. On the other hand, the steady-periodic mode allows the compressor materials to achieve steady-state conditions for a given set of boundary conditions and outputs the steady-periodic solution for the dynamics associated with a complete cycle of the piston from suction to discharge. The overall solution algorithm of these two simulation modes are show in Figure 2.15 and Figure 2.16, respectively.

Both the dynamic start-up and steady-periodic modes begin with specified compressor geometry data and operating (boundary) conditions as inputs. The model in the dynamic mode, shown in Figure 2.15, also has inputs that define the initial conditions related to the lumped temperatures along with the piston position. At each time step, the governing differential equations and sub-models are coupled and executed to determine derivatives that are integrated by a general solver. An adaptive Runge-Kutta integrator $4^{th}/5^{th}$ (RK45) is used for integration of the system of differential equations with variable step-size that is based on maintaining a required error per step.

For a given set of temperature conditions for the lumped masses, the dynamics associated with the piston motion and compression process are solved for a complete cycle. To reach the periodical steady-state cycle, the compressor must satisfy criteria for mechanical and electrical steady-periodic behavior as well as when the thermal states reach steady-state conditions associated with the specified boundary conditions. For a given set of lumped mass states, periodic steady-state behavior of the piston motion is enforced by checking the cyclic dynamic convergence (r_{cycle}), *i.e.*, the residuals of piston displacement/velocity, in-cylinder pressure/temperature and current variation within the linear motor at the end of every simulated cycle. After this step, the simulation is not terminated until the simulation process reaches the preset ending time (t_{end}). The transient mode of the simulation model can be used to investigate compressor transient behavior in terms of thermodynamic, electric and mechanistic aspects and can also be run to a steady-periodic solution in order to allow the impact of design changes on steady-state performance.

However, the use of the model for steady-state design analysis is challenging because of significant computational requirements. Therefore, a periodical steady-state mode was also developed to more appropriately accommodate design analysis. Figure 2.16 depicts the algorithm flow chart of the periodical steady-state mode. The structure of the flow chart is similar to the dynamic mode but is constructed with more decision symbols and different loops. From the previous analysis, it should be apparent that the piston motion profile, *i.e.*, piston instantaneous displacement and velocity, results from a coupling between the motor and chamber models as well as other sub-models. Given an initial guess for the piston motion profile (X_p), the solution for the piston and motor models is decoupled from the main solver, which covers the energy balance, valve dynamics and some other sub-models. The benefit from this decoupling approach is a faster convergence of the model since the piston and the motor follow the oscillation profile, but the in-cylinder pressure/temperature are more predictable.

Similar to the characteristic of a conventional reciprocating compressor, a sinusoidal shape of piston motion profile is assumed at the beginning of the cycle. Moreover, a random starting time (t_{start}) of the analyzed periodical steady-state cycle is defined. The main solver is then executed until the energy balance convergence criteria have been reached within one cycle and the thermodynamic profiles of each control volume can be obtained. Then, the piston and motor models with some additional initial guess values are coupled with the calculated thermodynamic profiles. At each iteration, a new piston motion profile is obtained, which doesn't necessarily follow a sinusoidal shape. The outer loop's role is to enforce the linkage between mechanics and energy balances for each control volume. In particular, the lumped temperatures that are being adjusted at each step of the loop for energy balances, vibration parameters are iterated at each step of the loop for mechanics loop.

2.11   Summary

In summary, a comprehensive linear compressor simulation model was developed to describe both the transient and periodic-steady behavior of a linear compressor and associated energy flows. The overall model is composed of several sub-models that include a dynamic piston, tube, flow, electrical motor, and heat transfer. The model was used to predict and analyze the performance of a commercial linear compressor. Both transient and periodical state-state simulation results were presented and analyzed. The simulation results based on this model and a detailed model validation will be presented in the following chapters.
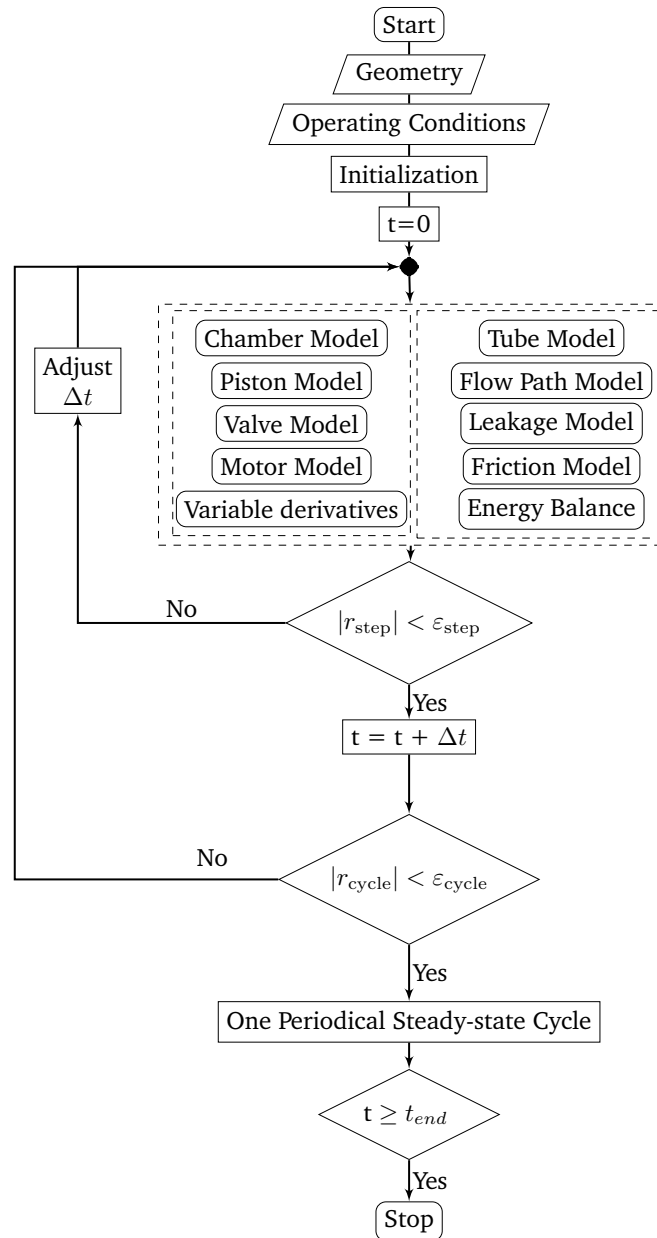
Fig. 2.15. The flow chart of the dynamic start-up mode in the proposed linear compressor simulation model.
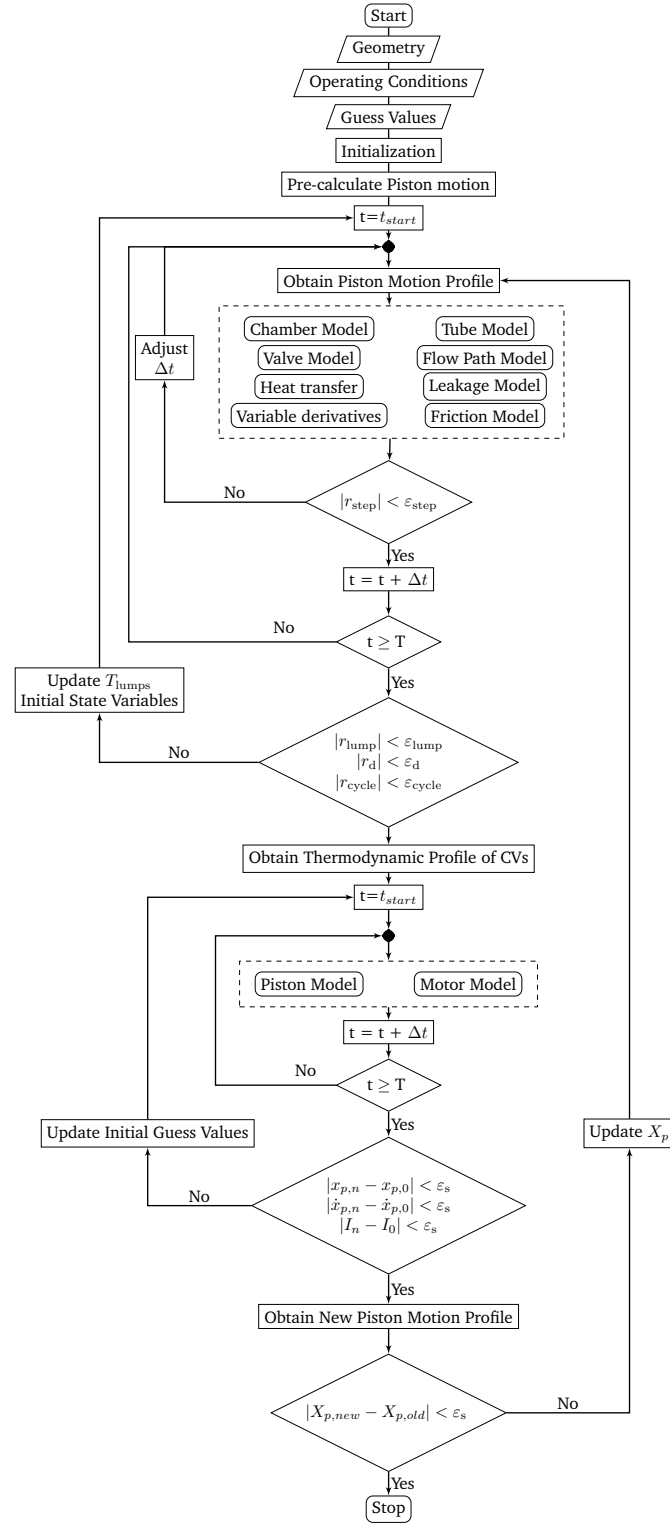
Fig. 2.16. The flow chart of the periodical steady-state mode in the proposed linear compressor simulation model.

3. EXPERIMENTAL TESTING OF COMMERCIAL LINEAR COMPRESSORS

The commercialized compressors showed better and repeatable performance compared to earlier prototypes mentioned in the literature. However, relatively limited information was reported in the literature with respect to the linear compressor modeling work based on the commercial products and experimental validation was totally absent. In this chapter, two commercial linear compressors are used to conduct experimental investigations to better understand the behavior of the linear compressor technology. In particular, the tests are performed by employing a hot-gas by-pass test bench available at the Ray W. Herrick Laboratories. The measurements of the linear compressors include the compressor mass flow rate, suction and discharge pressure and temperatures as well as the electrical power consumption. The objectives are two-fold: (i) characterize and compare the performance of the commercial compressors through their operating envelope; (ii) gather experimental data to be used for model validation in Chapter 4. (iii) conduct two experimental performance comparisons between two compressors.

3.1 Description of Commercial Linear Compressors

A LG and an Embraco linear compressors have been selected to perform an in-depth performance evaluation due to their significantly different designs. Both compressors have been designed to work with either R134a or R600a in domestic refrigerators/freezers [68].

Figure 3.1 and Figure 3.2 show a picture and schematic diagram of Wisemotion oil-free linear compressor from Embraco, respectively. It can be seen that the Wisemotion compressor is more compact than conventional reciprocating compressors. By looking

at the internal structure of the compressor, it can be noted that it has been designed to be independent from the frequency variations during operation. In fact, instead of using multiple set of springs, a single thick spring and two suspension systems are included to stabilize the movement of piston as well as reduce the vibration. Similar to the LG linear compressor, presented in Section 1.2, the suction valve and discharge valve are located at the end of the piston and cylinder, respectively. The Wisemotion linear compressor is an oil-free technology and the refrigerant is employed to lubricate the only bearing of the assembly, which presents a special anti-wear surface coating.

Fig. 3.1. Picture of Embraco linear compressor.

LG has been developing and employing linear compressor in many of their domestic refrigerator/freezers for nearly 10 years. The commercial LG linear compressor is shown in Figure 3.3 and its design resembles that one of a conventional reciprocating compressor [10]. A detailed schematic of the compressor is provided in Figure 3.4. Based on the previous student's work [13], it was determined that 150 mL of a synthetic refrigerant POE oil was added into the compressor system and drained through the oil sump and oil channel for lubrication. One tubular motor was used to provide the driving force for the piston reciprocating movement and several laminations which cover the copper coils were designed to generate the electromagnetic filed.
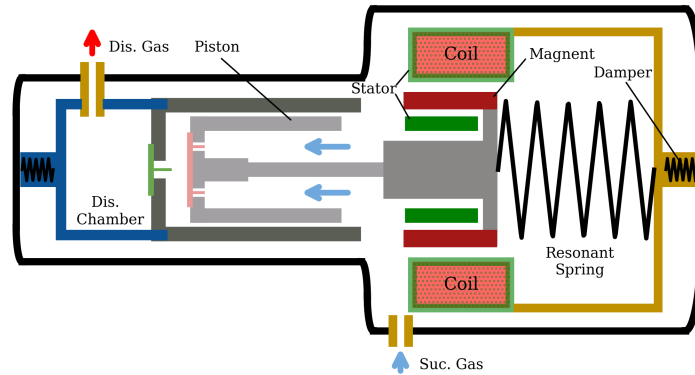
Fig. 3.2. Schematic diagram of Embraco linear compressor.

Fig. 3.3. Picture of LG linear compressor.

Table 3.1 shows a summary of these two linear compressors including basic information and geometry for each of them, respectively. By analyzing the listed features of two compressors, several significant aspects can be concluded as follows:
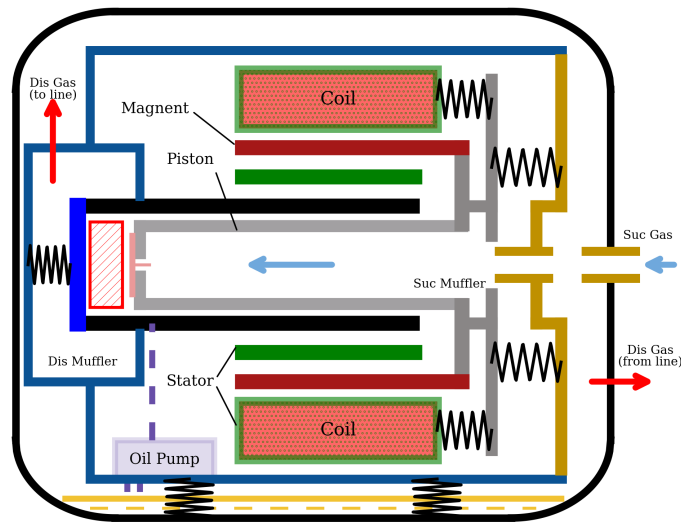
Fig. 3.4. Schematic diagram of LG linear compressor.

- Piston dimension in the Wisemotion compressor is smaller than in LG compressor as well as the piston mass, which requires less power to drive the piston at the same operating condition.

- One thick spring is installed in the Wisemotion compressor while there are a total of 8 springs as a system used in the LG compressor.

- Both suction and discharge valves in the Wisemotion compressor have larger size than the ones in the LG compressor.

- The Wisemotion compressor has a much larger clearance gap than the LG compressor due to its oil-free operation.

- One suspension system was used in the Wisemotion compressor to absorb the vibration as well as the noise from the motor.

Table 3.1.
Summary of two commercial linear compressors.

Manufacturer	LG	Embraco
Basic Information		
No.	FLB075LBNA	WMD 7H
Ref	R134a	R134a
Motor	Tubular linear motor	Separated linear motor
Lubrication	Oil	Refrigerant
Vibration Absorption	No	Yes
Control	Voltage/current control	Impact sensor
Orientation	Verical	Horizontal
Suspension system	No	Yes
Geometry		
Size (cm)	20/18/20	30/13/12
Piston diameter (cm)	2.65	1.95
Piston Length (cm)	7.96	5.17
Piston mass (kg)	0.63	0.04
Total Spring mass (kg)	0.16	0.24
Number of spring (-)	8	1
Clearance gap (μm)	5	9
Suction valve diameter (cm)	0.52	1.80
Discharge valve diameter (cm)	2.95	3.65
Suction valve type	reed valve	reed valve
Discharge valve type	plate valve	reed valve

3.2 Experimental Test Setup

Both linear compressors have been tested in a hot-gas bypass compressor load stand and R134a has been used as the working fluid during the compressor performance testing. Figure 3.5 and Figure 3.6 show the schematic and picture of the test

stand used for the Wisemotion linear compressor testing. In the test bench for the LG linear compressor, shown in Figure 3.7 and Figure 3.8, several modifications were added to accommodate the oil-lubricated aspect. An oil separator having one inlet and two outlets, was used to separate oil that was discharged with the compressed refrigerant by the compressor system. Oil flow was pushed by the high pressure gas in the discharge line back to the suction line when the needle valve is open with high resolution flow orifice. To ensure oil starvation did not occur, a sight glass was added to monitor oil levels in the test system to indicate if the needle valve was needed to open for oil flowing back.

The hot-gas bypass test stand includes three pairs of needle valves, located in the discharge line, bypass line, and liquid line, respectively. Each pair of valves consists of one valve for coarse tuning and one for fine tuning. These valves serve the following control functions:

- The valves in the bypass line are used to control the suction pressure.

- The valves in the liquid line are used to control the superheat at the compressor inlet.

- The valves in the discharge line are used to control the discharge pressure.

During the tests, the following compressor measurements were recorded: compressor mass flow rate, suction and discharge temperatures, suction and discharge pressures, intermediate pressure and temperature, and compressor power. Using these measurements, the overall isentropic efficiency can be calculated to evaluate compressor performance, as defined by Equation 3.1.

$$\eta_{o,is} = \frac{\dot{m}_{meas}(h_{dis,is}(T,P) - h_{suc}(T,P))}{\dot{W}_{meas}} \tag{3.1}$$

where η is compressor efficiency , $\dot{m}$ is the compressor flow rate, h is the enthalpy of the gas. $\dot{W}$ denotes the compressor power.

65
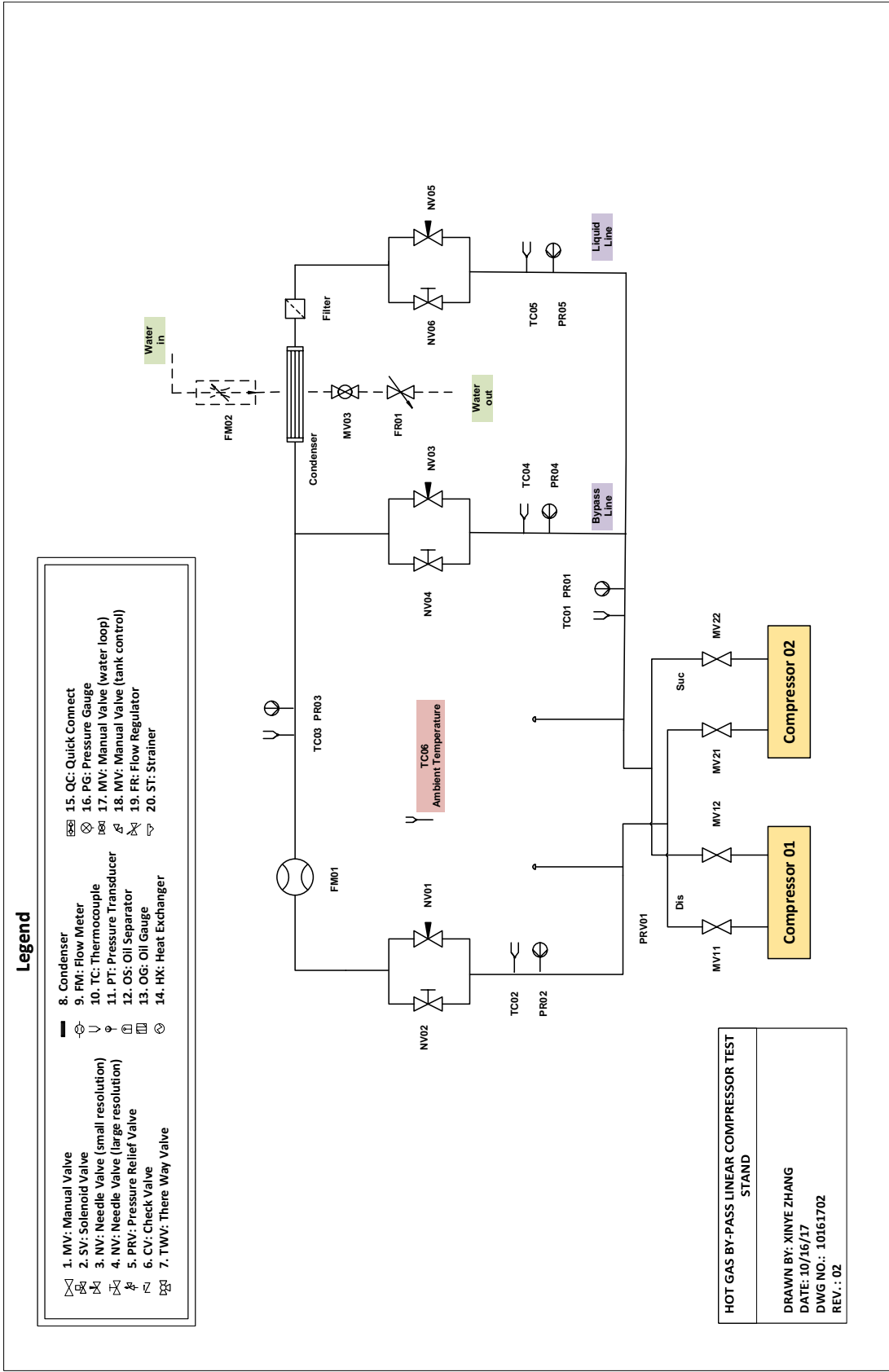
Fig. 3.5. Schematic diagram of hot gas bypass test bench for Embraco linear compressor.
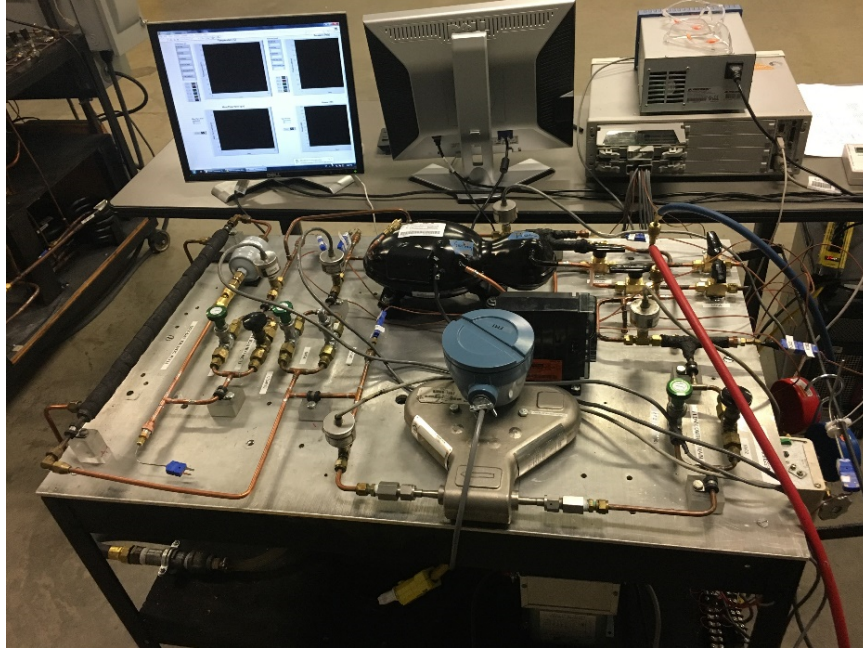
Fig. 3.6. View of test bench for Embraco linear compressor.

In the test stand, temperatures are measured with T-type thermocouples with ±0.25 °C accuracy. All pressures are measured with pressure transducers that have an accuracy of ±0.13% of full scale. A Coriolis-effect mass flow meter with a rated accuracy of ±0.1% has also been installed after the parallel needle valves NV01 and NV02 in the discharge line to measure the mass flow rates of the refrigerant. Electric power consumption of the compressor is measured with a power meter with an accuracy of ±0.1%. One tube-in-tube condenser is installed to condense the refrigerant to the subcooled liquid and one recirculating chiller is used to provide the cooling capacity in the condenser. A data acquisition system is used to convert the incoming voltages from the measuring instrumentation to digital signals for transfer to a personal computer. The computer uses a proper data reduction program for further data analysis. During the tests, the following compressor measurements were recorded: compressor mass flow rate, suction and discharge temperatures, suction and discharge pressures, intermediate pressure and temperature, and compressor power consumption. Using these measurements, the compressor performance was evaluated.
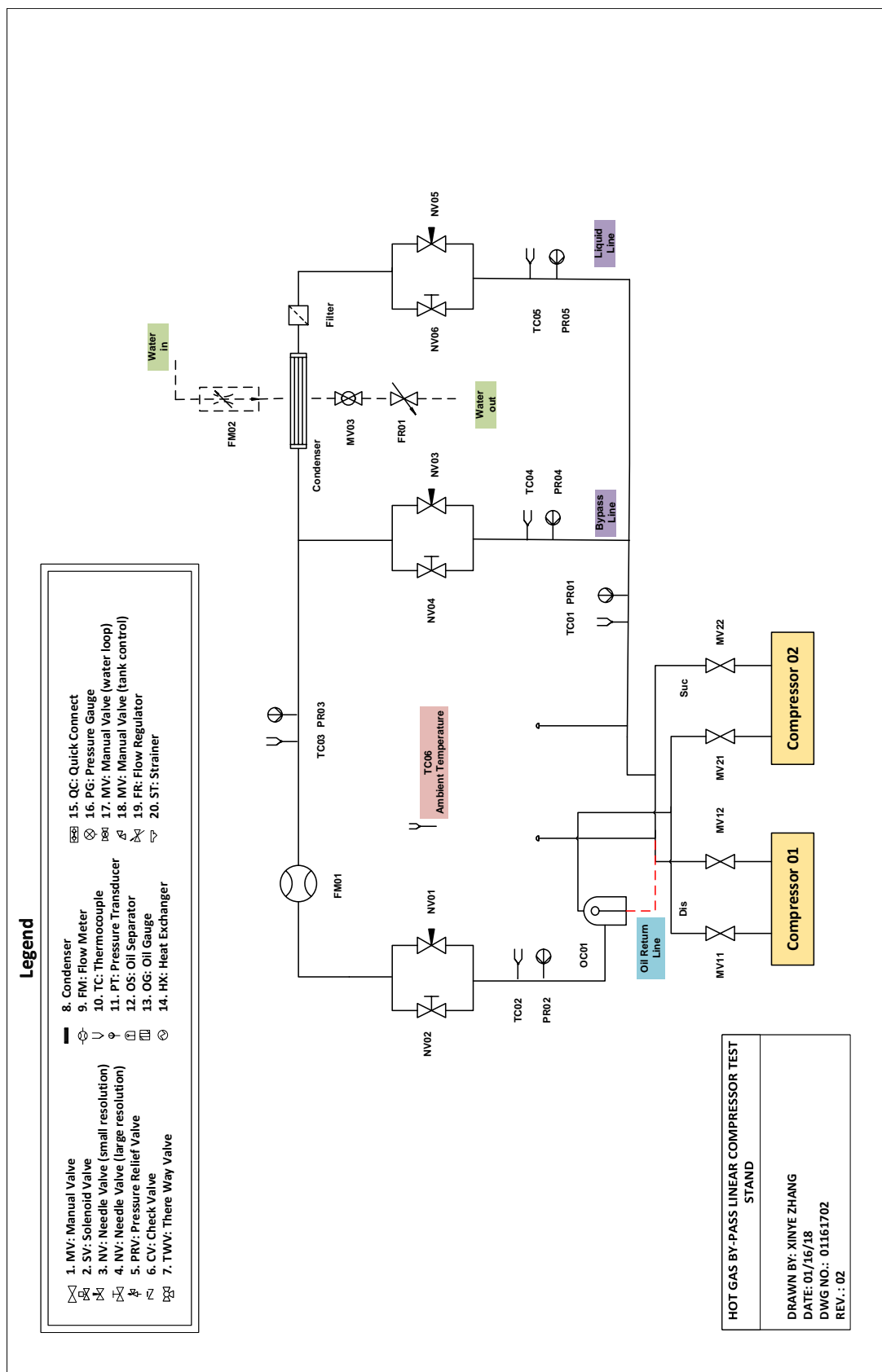
Fig. 3.7. Schematic diagram of hot gas bypass test bench for LG linear compressor.
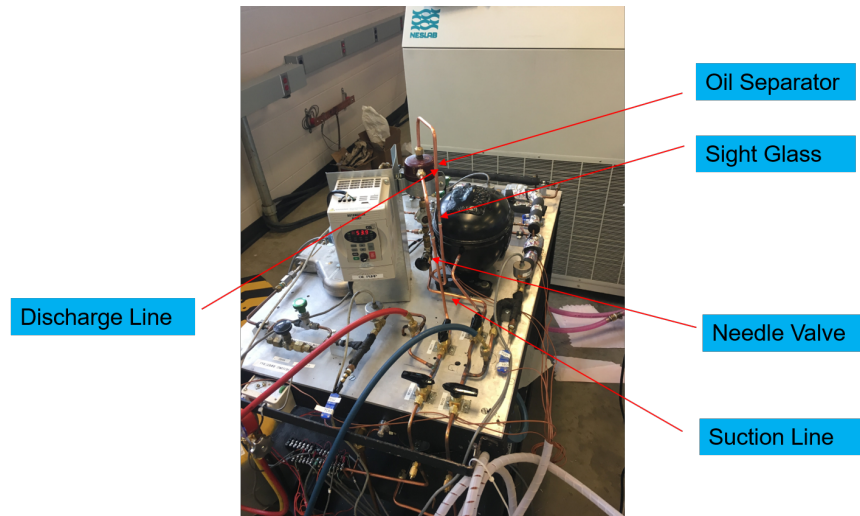
Fig. 3.8. View of test bench for LG linear compressor.

Figure 3.9 shows the P-h diagram of the entire cycle in the hot-gas bypass test stand. The compressor operates between state point 1 and point 2. After that, the high-pressure gas is expanded across a set of parallel valves to an intermediate pressure at state point 3. Then the flow is distributed into two flow lines: hot gas line and liquid line. In the liquid line, the refrigerant flow through one tube-in-tube condenser and is condensed to the subcooled liquid at state point 6 where point 5 is saturated liquid point at intermediate pressure. The subcooled liquid is then isenthalpically throttling to the suction state point 7. In the hot-gas bypass line, two parallel valves are used to reduce the refrigerant pressure to the compressor suction pressure at the state point 9. By controlling the ratio of these two-line flow rates, the suction pressure as well as the superheated suction temperature (difference between point 8 and point 1) can be controlled and adjusted accordingly and the mixed state point is state point 1 as the closure of the cycle.
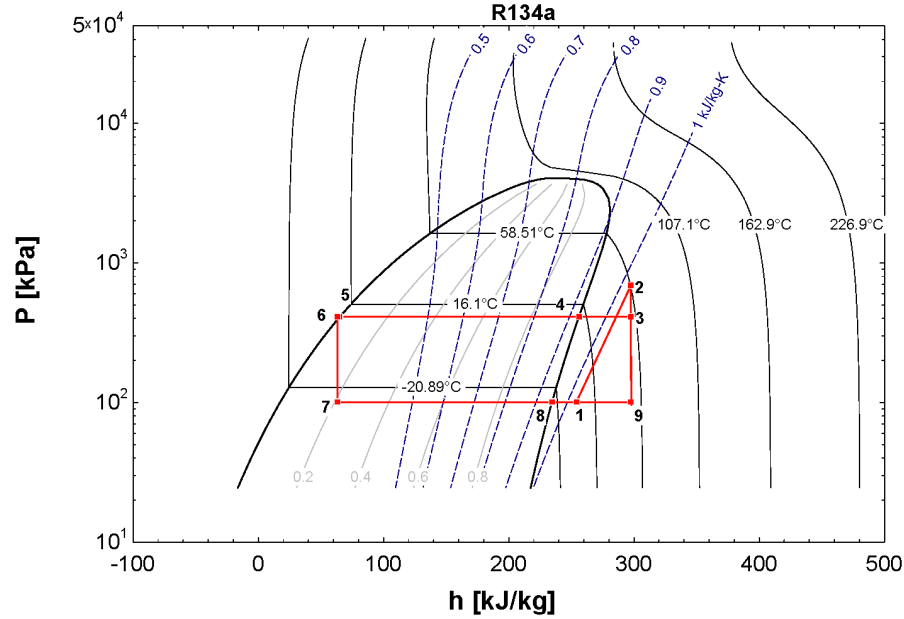
Fig. 3.9. P-h diagram from Embraco linear compressor tested in hot-gas bypass test stand from Embraco.

3.3   Measurement Devices and Uncertainty Analysis

Assuming that the experiment has been setup correctly with good calibration to eliminate the fixed errors, there are still some random errors (non-repeatability) in each experimental reading. An uncertainty analysis is the procedure used to quantify data validity and accuracy. The experiments for the two linear compressors in this work involve the uncertainty of the instrumentation used for all measurements. The goal of this section is to summarize all the uncertainties for each instrument and report the preliminary uncertainty analysis for the tests discussed in this work.

During the experimental data analysis process, there are two parameters associated with each test: direct measured parameters, such as temperature, pressure, mass flow rate, pressure, frequency, etc. and indirect calculated parameters, including efficiency, COP, heat loss, etc. The uncertainty of the direct measurements depends

on the accuracy of the devices used in the tests and the indirect parameters are the function of the direct measured properties, which are determined by:

$$u(x) = \sqrt{\sum_{i=1}^{n} \left(\frac{\partial x}{\partial r_i} u(r_i) \right)^2} \tag{3.2}$$

where $u(x)$ denotes the parameter for uncertainty analysis. n is the number of direct measured parameters. The partial differential $\frac{\partial x}{\partial r_i}$ represents the relative uncertainty in the result due to uncertainty in r_i.

Table 3.2 gives a summary of the devices used for all the tests and the uncertainty of each instrument, including: parameter, device name, manufacturer, model number and the uncertainty associated with each measurement. Due to the different features for two compressors, two different motor diver and power meter were used for each experiment and the superscript [1] denotes the devices used for the Embraco Wisemotion linear compressor and superscript [2] represents the devices used for the LG linear compressor, respectively.

Table 3.2.
Summary of the measurement devices used for testing and the uncertainties.

Parameter	Device	Manufacturer	Model No.	Uncertainty
Temperature	Thermocouple	OMEGA	TMQSS-062	$\pm 0.2K$
Pressure	Pressure Sensor	OMEGA	PX176-015A	$\pm 4kPa$
Mass Flow Rate	MicroMotion	EMERSON	CMF010	$\pm 0.35\%$
Frequency	AC Driver	EMBRACO	WMD7H[1]	-
		tGSX	GS2-10P2[2]	$\pm 5\%$
Coolant Flow Rate	Flow Meter	OMEGA	FL-3207G	$\pm 2\%$
Cooling Capacity	NESLAB	THERMO	HX-500	± 0.1 °C
Power Consumption	Power Meter	AMTEX	XL5C5[1]	$\pm 0.1\%$
		OSI	PC8-005-08E[2]	$\pm 0.1\%$

For example, the evaluation of the overall isentropic efficiency of a linear compressor, shown in Equation 3.3, is a function of mass flow rate, suction/discharge temperatures and pressures, and power consumption. This calculation is associated with the uncertainty of all devices used in this measurement: mass flow meter, pressure transducer, thermocouple, and power transducer. The overall uncertainty of the overall isentropic efficiency would be the combination effects from all these aspects, denoted by the letter A (Temperature), B (Pressure), C (mass flow rate) and D (power consumption) and the overall uncertainty is obtained from the square root of the sum of all four aspects, shown in Equation 3.4, where all the aspects are determined by the Equation 5.7 to Equation 3.8.

$$\eta_{o,is} = \frac{\dot{m}_{meas}(h_{suc}(T,P) - h_{dis}(T,P))}{\dot{W}_{in,meas}} \tag{3.3}$$

$$u(\eta) = \sqrt{A + B + C + D} \tag{3.4}$$

$$A = \left[\left(\frac{\partial\eta}{\partial T_{suc}}\right)u(T_{suc})\right]^2 + \left[\left(\frac{\partial\eta}{\partial T_{dis}}\right)u(T_{dis})\right]^2 \tag{3.5}$$

$$B = \left[\left(\frac{\partial\eta}{\partial T_{dis}}\right)u(T_{dis})\right]^2 \tag{3.6}$$

$$C = \left[\left(\frac{\partial\eta}{\partial \dot{m}}\right)u(\dot{m})\right]^2 + \left[\left(\frac{\partial\eta}{\partial \dot{W}}\right)u(\dot{W})\right]^2 \tag{3.7}$$

$$D = \left[\left(\frac{\partial\eta}{\partial \dot{W}}\right)u(\dot{W})\right]^2 \tag{3.8}$$

Basically, after analyzing the number of direct parameters associated with the measurements, Equation 3.4 to Equation 3.8 can be used to estimate the uncertainties for other parameters as well, like heat loss, system COP, following the similar procedures to the example of the overall isentropic efficiency discussed above.

3.4 Testing Matrix

Two test matrices have been identified to properly test each compressor. Each test matrix is described below.

3.4.1 Embraco Wisemotion linear compressor

It has been reported that Wisemotion linear compressor can run on a wider range of capacity modulation instead of switching on and off, which results in the minimum temperature variation and smaller vibration because the compressor operation is not based on the frequency variation significantly. A linear compressor testing envelope was given by Embraco, which includes steady operation region and transient operation region in terms of different evaporation and condensation temperatures and the test matrix is shown in Figure 3.10. To characterize the performance of the compressor, three sets of tests were chosen as the testing matrix. In particular, twelve regular tests were conducted to evaluate the compressor performance with normal inverter input frequencies: 50Hz, 60Hz, 70Hz. Since Wisemotion compressor is designed with variable capacity, and nine tests were picked up to test the compressor with different inverter input frequencies as well as the power consumption. Finally, one boundary condition was used to check if compressor works functionally with three frequencies.

A total of 28 points were tested and used to characterize the compressor performance and for the future validation of the dynamic model, shown in Table 3.3. During all tests, the following compressor measurements were recorded: compressor mass flow rate, suction and discharge temperatures, suction and discharge pressures, intermediate pressure and temperature, and compressor power consumption. Using these measurements, the compressor performance was analyzed.
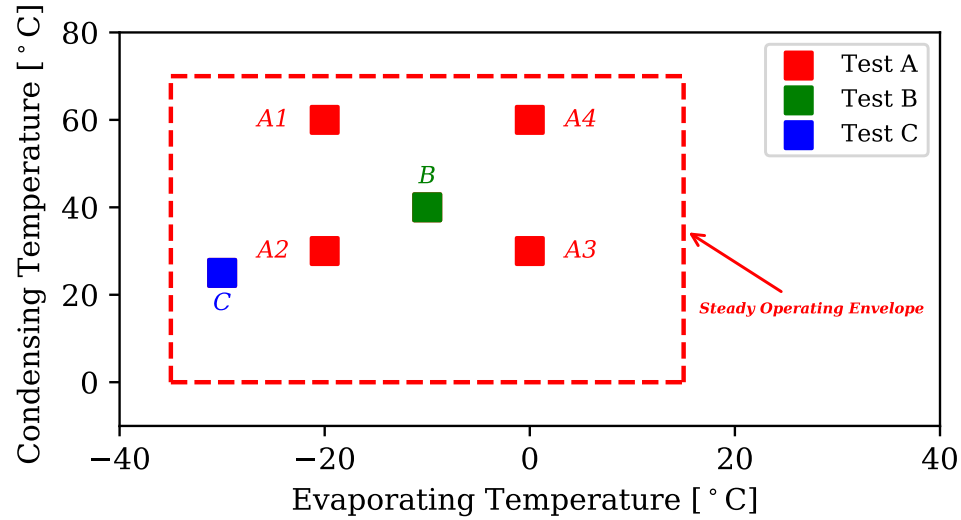
Fig. 3.10. Embraco linear compressor test envelope.

Table 3.3.

Test matrix for Wisemotion linear compressor (with 15 ℃ superheat and f denotes the inverter input frequency)

Test Type	No. of Test	Test Conditions
A1	4	PR = 10; P_{suc} = 138 kPa; f = 50,60,70 Hz
A2	4	PR = 6; P_{suc} = 138 kPa; f = 50,60,70 Hz
A3	4	PR = 3; P_{suc} = 276 kPa; f = 50,60,70 Hz
A4	4	PR = 6; P_{suc} = 276 kPa; f = 50,60,70 Hz
B	9	PR = 5; P_{suc} = 138 kPa; f = 50-130 Hz
C	3	PR = 10; P_{suc} = 70 kPa; f = 50,60,70 Hz

3.4.2 LG linear compressor

Instead of having a large range of input frequency, the LG linear compressor is designed to operate over a much narrower range of frequencies between 50 Hz and 65 Hz and the motor inverter has 53 Hz as a nominal frequency. The test matrix

for compressor B in terms of different input frequencies and pressure ratios with a fixed suction condition is shown in Figure 3.11. Assuming an evaporator superheat for a refrigerator of 15 °C, the suction condition was fixed as 105 kPa and -5 °C corresponding to $T_{evap} = -20$ °C. Considering the effect of an equivalent pressure gas spring, the system was unsteady at high pressure ratios as discussed in Zhang et al [69] and therefore, the test matrix was divided into steady and unsteady operating conditions. The critical point for unsteady behavior is a pressure ratio of 9. Four pressure ratios and five frequencies were selected corresponding to a conventional refrigerator/freezer application, resulting in a total of 20 test points.
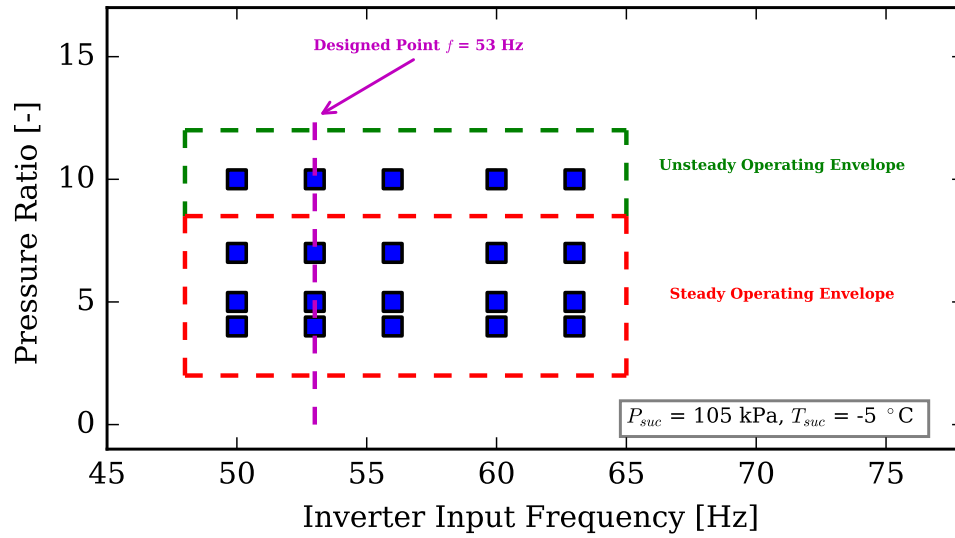
Fig. 3.11. LG linear compressor test envelope.

3.5   Experimental Results

3.5.1   Embraco Wisemotion linear compressor

Table 3.4 shows the experimental results obtained with the Embraco linear compressor using the hot-gas bypass test stand. As mentioned before, three sets of tests were chosen as the test matrix with different objectives of performance characterization. In test set A and C, three inverter input frequencies, *i.e.*, 50Hz, 60Hz, 70Hz,

were used as different operating conditions. Two pressures, 138 kPa and 276 kPa, were selected as the suction conditions which are based on the test envelope, shown as A1, A2 with 138 kPa and A3, A4 with 276 kPa in Figure 3.10.

Table 3.4.
Experimental results from Embraco linear compressor with uncertainties.

Test No.	P_{suc} (kPa)	$u(P_{suc})$ (kPa)	P_{dis} (kPa)	$u(P_{dis})$ (kPa)	PR (-)	$\dot{m}$ (g/s)	$u(\dot{m})$ (mg/s)	$\dot{W}_{in}$ (W)	$u(\dot{W}_{in})$ (W)	f (Hz)
	157.13	±0.35	1605.93	±4.27	10.22	0.76	±2.63	68.60	±0.07	70
A1	154.99	±0.35	1613.03	±4.27	10.40	0.62	±2.61	59.29	±0.06	60
	172.99	±0.35	1627.37	±4.27	9.41	0.55	±2.61	47.94	±0.05	50
	150.72	±0.35	1059.59	±2.96	7.03	1.01	±3.52	69.23	±0.07	70
A2	161.75	±0.35	1041.25	±2.96	6.44	0.89	±3.14	60.16	±0.06	60
	167.88	±0.35	1045.78	±2.96	6.22	0.75	±2.63	49.30	±0.05	50
	287.79	±0.69	1089.37	±2.96	3.78	1.58	±5.52	69.39	±0.07	70
A3	279.44	±0.69	1047.93	±2.96	3.75	1.36	±4.73	59.09	±0.06	60
	299.16	±0.69	1074.75	±2.96	3.59	1.17	±4.12	50.33	±0.05	50
	279.86	±0.69	1725.68	±4.27	6.17	1.04	±3.52	69.19	±0.07	70
A4	287.03	±0.69	1755.96	±4.27	6.05	0.87	±3.14	59.99	±0.06	60
	275.10	±0.69	1723.41	±4.27	6.26	0.70	±2.63	49.40	±0.05	50
B	175.82	±0.35	1005.25	±2.96	5.72	-	-	-	-	50-130
	76.95	±0.20	769.94	±2.07	10.00	0.76	±2.63	68.49	±0.07	70
C	77.01	±0.20	762.70	±2.07	9.90	0.66	±2.61	58.43	±0.06	60
	76.05	±0.20	750.22	±2.07	9.864	0.53	±2.61	49.29	±0.05	50

The Wisemotion linear compressor utilizes a linear variable capacity technology to modulate the mass flow rate and capacity. Instead of varying the electrical frequency/compressor speed in a conventional variable speed compressor, the controller adjusts the voltage and power to the linear motor and the displacement of the piston in the Wisemotion varies directly with power as well as the cooling capacity. The driving frequency to the piston is not related to the inverter input frequency but

maintained at/close to the design natural frequency, which results in steady running pace with less vibration and lower noise level, instead of conventional on/off switching logic.

Figure 3.12 shows the relationship between the inverter input frequency and motor power consumption, given by the manufacturer. It can be seen that there is no power output when the inverter input frequency is below 20 Hz and the maximum power is controlled to be 160 W, when the frequency is beyond 160 Hz. When the input frequency is in the range from 20 to 160 Hz, the motor power is a linear function of input frequency, which is related to the internal controller of the compressor for variable piston stroke.
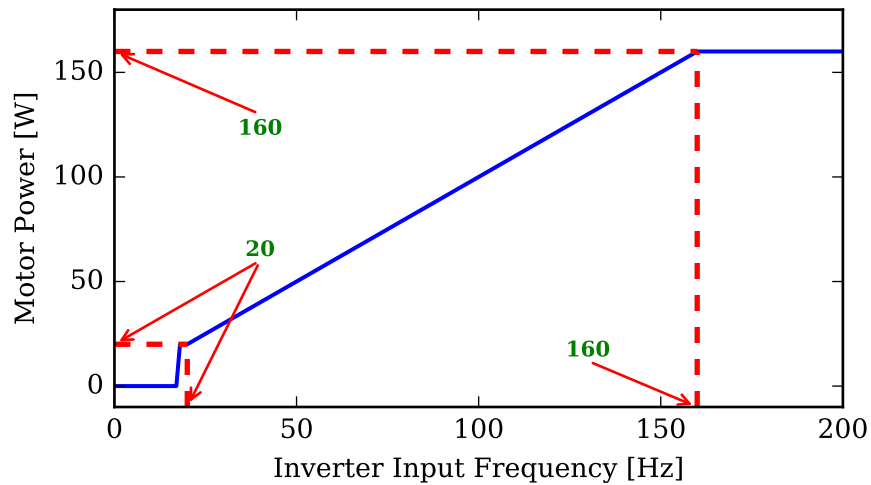
Fig. 3.12. Relationship between inverter input frequency and motor power in Wisemotion linear compressor.

The experimental results for three sets of tests will be presented in the following sections with respect to different performance aspects, including: power consumption, mass flow rate, heat rejection, overall isentropic efficiency and system COP. Each parameter was investigated as a function of pressure ratio and input frequency, respectively.

Test A

In this test set, four operation points, marked in Figure 3.10 were selected as the tested conditions with two suction pressures: 138 kPa and 276 kPa. For each test set, the compressor was tested with three different input frequencies receptively.

Figure 3.13 shows the measured power data as a function of pressure ratio. The variation of power is minimal with respect to different pressure ratio. It can be concluded that the motor power in the Embraco linear compressor is only a linear function of the frequency and does not depend on the imposed pressure ratio, which differs from the conventional reciprocating compressor where the condition with higher pressure ratio requires more power to drive the piston movement. Basically, this can be explained by looking at Figure 3.12. The motor power of the Wisemotion linear compressor is only a function of the input frequency, which is a very special feature.
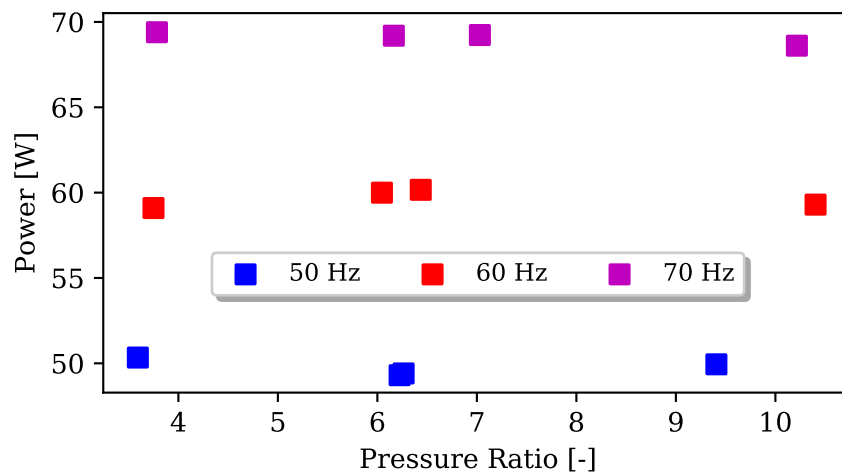
Fig. 3.13. Motor power as a function of pressure ratio in Wisemotion linear compressor.

Figure 3.14 shows the experimental mass flow rate as a function of pressure ratio at different operating frequencies of the compressor. It can be noted that the compressor delivered more mass flow rate with smaller pressure ratio. Moreover, for the same pressure ratio, the mass flow rate is not affected significantly by the suction pressure

(i.e. different compressor operating conditions). This fact can be seen by comparing the data points in the center of Figure 3.14 where suction pressures are 138 kPa and 276 kPa, respectively.
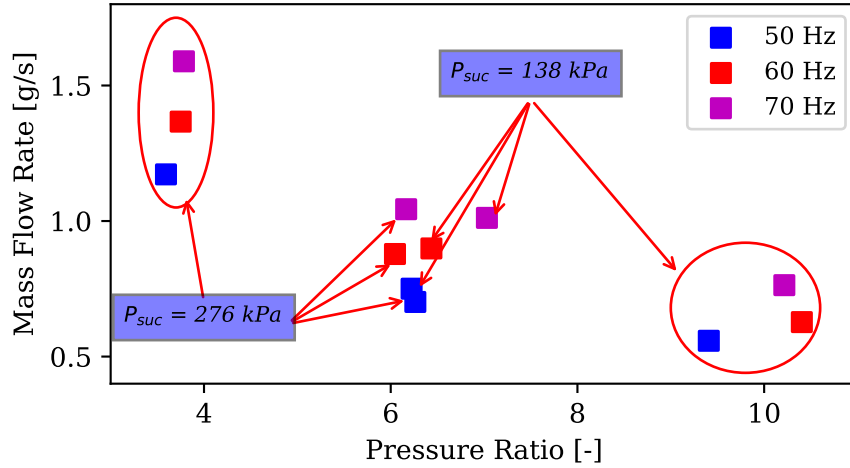
Fig. 3.14. Mass flow rate as a function of pressure ratio in Wisemotion linear compressor.

Figure 3.15 shows the variation of mass flow rate as a function of inverter input frequency for different pressure ratios and suction pressures. Higher mass flow rates can be obtained with higher input frequencies. Furthermore, the mass flow rate shows linear trends with respect to the input frequency at different operating conditions. From the Figure 3.15, it can still be noted that the measured mass flow rate points are overlapped with same pressure ratio which indicates the suction pressure has little influence on the mass flow rate variation.

The heat rejection rate is defined as the heat loss from the compressor to the surrounding, which is an indirect calculated factor to evaluate the performance of a compressor. This parameter shows the energy transfer difference between the input power and the work on the compression chamber, calculated by Equation 3.9.

$$\dot{Q}_{amb} = \dot{W}_{in,meas} + \dot{m}_{meas}(h_{suc} - h_{dis}) \tag{3.9}$$
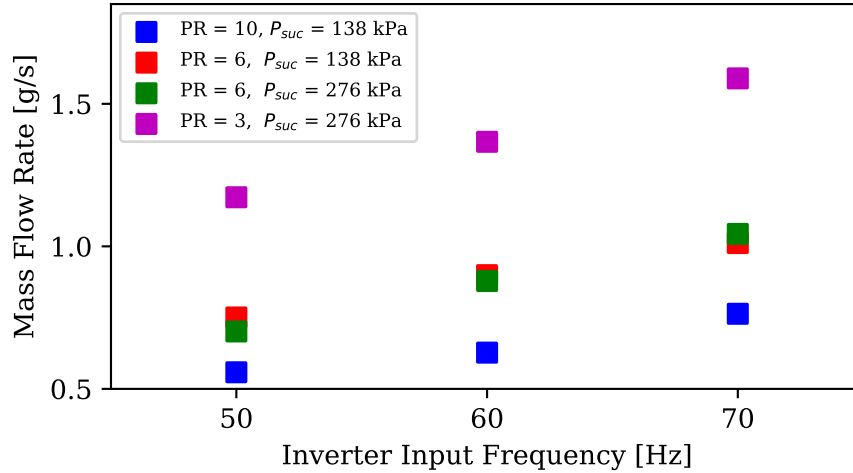
Fig. 3.15. Mass flow rate as a function of input frequency in Wisemotion linear compressor.

Figure 3.16 depicts the variation of heat rejection rate as a function of pressure ratio. It is seen that smaller pressure ratio is associated with less heat loss rate which means most of the input power was converted to the work on the refrigerant. Due to the fact that the input power is independent of pressure ratio, seen in Figure 3.13, it can be predicted that the compressor will have higher efficiency with smaller pressure ratio with less heat rejection with the same power consumption. In addition, it also can be observed that suction pressure now affects the heat rejection rate slightly in terms of the same pressure ratio and the condition with higher suction temperature rejects more heat to the surrounding.

From Figure 3.17, it can be observed that the heat loss increases by up to 40% under larger pressure ratio with the increase of input frequency. However, at low pressure ratios or at low suction pressures, the heat rejection is not significantly affected by the variation of input frequency which may lead to more steady operating conditions since the heat losses have negative impacts on the compressor performance.

Figure 3.18 and Figure 3.19 show the overall isentropic efficiency of the compressor as a function of pressure ratio and input frequency, respectively. The overall isentropic efficiency of the compressor is defined as Equation 3.10. In particular, the definition
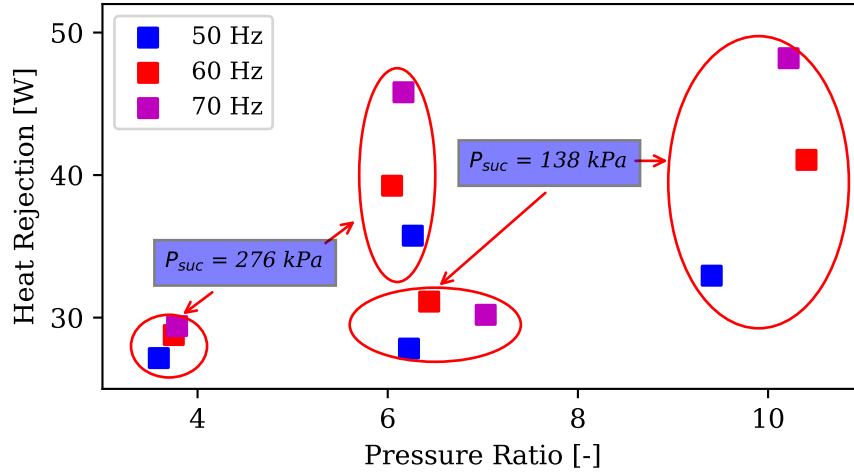
Fig. 3.16. Heat rejection as a function of pressure ratio in Wisemotion linear compressor.
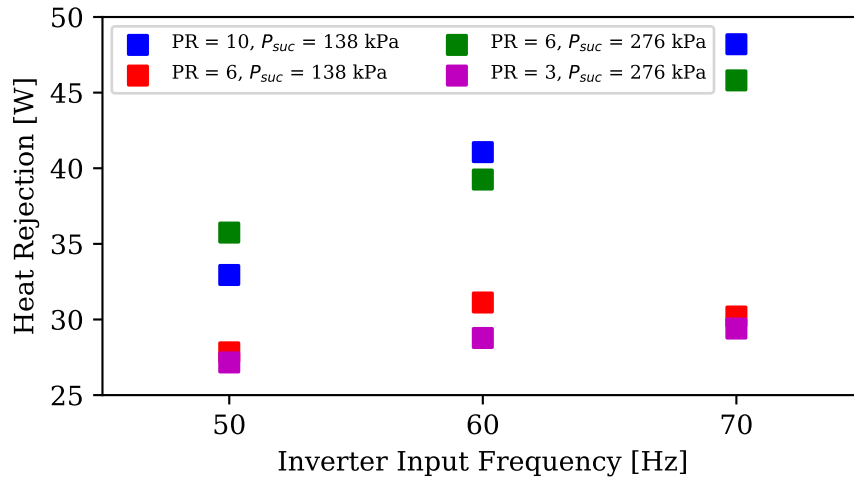
Fig. 3.17. Heat rejection as a function of input frequency in Wisemotion linear compressor.

for overall isentropic efficiency takes into account all the losses of the compressor and it is used as an overall performance metric for the compressor under investigation.

$$\eta_{o,is} = \frac{\dot{m}_{meas}(h_{dis,is}(T,P) - h_{suc}(T,P))}{\dot{W}_{meas}} \qquad (3.10)$$

where $\eta_{o,is}$ is the compressor overall efficiency , $\dot{m}$ is the compressor mass flow rate, h is the specific enthalpy of the gas. $\dot{W}$ denotes the compressor power input.
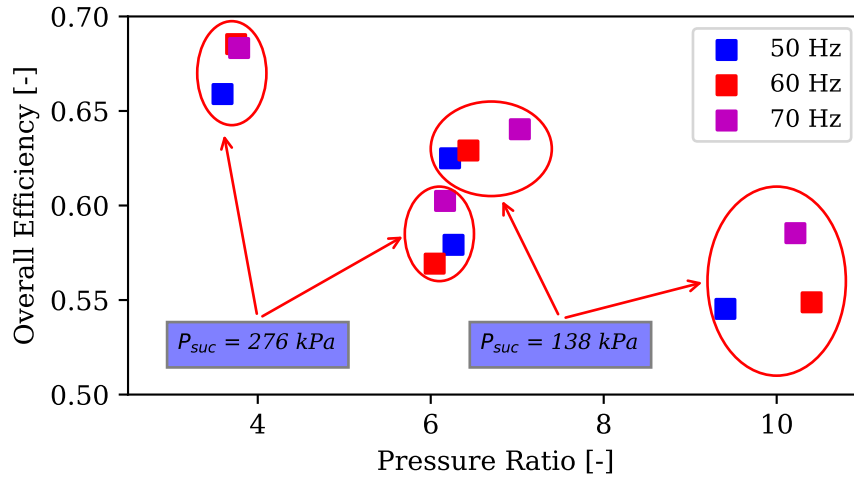
Fig. 3.18. Overall efficiency as a function of pressure ratio in Wise-motion linear compressor.

As is seen in Figure 3.18, the compressor shows better performance when the pressure ratio is small. The overall efficiency reaches value up to 0.67 for a pressure ratio of 4 and decreases down to approximately 0.55 for a pressure ratio of 10. Additionally, at the same pressure ratio, *i.e.*, pressure is 6 shown in the Figure 3.18, the condition with 138 kPa suction pressure has higher overall efficiency than the measured point with 276 kPa suction pressure. Basically, the results here are consistent with the data shown in Figure 3.16 and Figure 3.13. When system pressure ratio is small, there is less heat loss rate but with same power input compared with the condition under larger ration, resulting in the higher overall efficiency of the compressor.

Furthermore, different input frequencies have limited influence on the overall efficiency of the compressor which is seen from Figure 3.19. As discussed before, both power consumption and mass flow rate increase linearly as a function of input frequency, presented in Figure 3.15 and Figure 3.12 and this overall effect is to maintain the compressor operate at the steady running space with steady performance instead of being based on the variable input frequency.
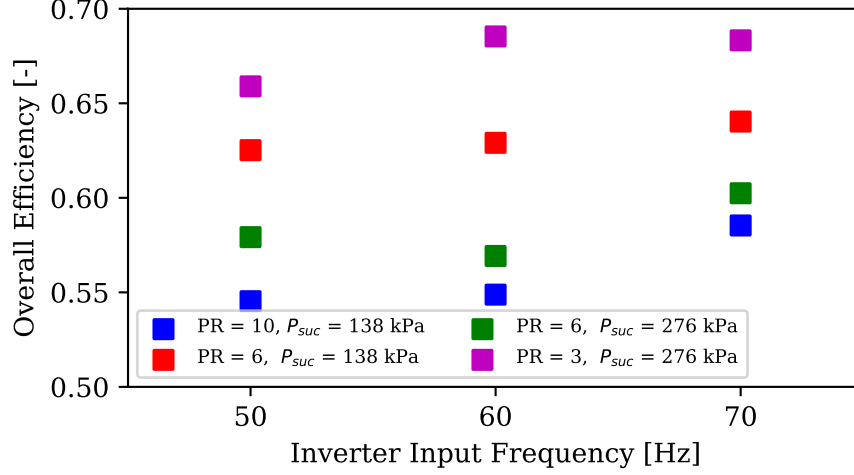
Fig. 3.19. Overall efficiency as a function of input frequency in Wise-motion linear compressor.

In order to have a better understanding of the performance of the tested linear compressor, the system COP has been used as an indicator to evaluate compressor performance based on the measured data. The system COP is defined by Equation 3.12 where $\dot{Q}_{cooling}$ is given by Equation 3.11. By assuming that the system operates under the fixed sub-cooling (5 K) and superheating temperatures (15 K), a simple vapor compression cycle can be generated to conduct a simple system COP analysis and the P-h diagram is created as Figure 3.20.

$$\dot{Q}_{cooling} = \dot{m}_{meas}(h_2 - h_7) \tag{3.11}$$

where h_2 denotes the enthalpy at compressor inlet and h_7 is the inlet enthalpy of the evaporator. The two points can be seen on the P-h diagram in Figure 3.20.

$$COP = \frac{\dot{Q}_{cooling}}{\dot{W}_{meas}} \tag{3.12}$$

As is shown in Figure 3.21, the compressor generates the higher system COP with smaller pressure ratio whose trend is similar to the overall isentropic efficiency in Figure 3.18. In particular, at the high pressure ratio 10, the system COP is relatively low which indicates that the compressor is not able to run efficiently. In addition,
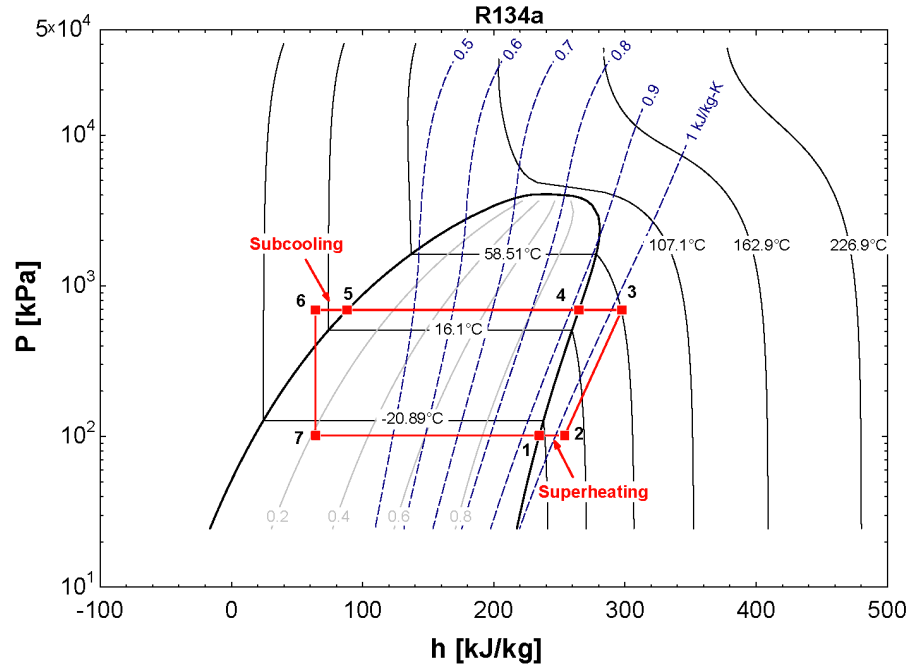
Fig. 3.20. P-h Diagram for System COP analysis.

the measured compressor with lower suction pressure but at the same pressure ratio would provide higher system COP which is approximately 2.5. It also can be observed that the calculated system COP is relatively constant for different compressor input frequencies, shown in Figure 3.22.

Based on the analysis above, it can be concluded that this linear compressor was designed to operate at low pressure ratio conditions where the system can provide a reasonably better performance. In addition, the motor power and mass flow rate are strongly affected and controlled by the input frequency which indicates that the control logic of this compressor is to maintain the compressor operation independent of the input frequency but only a function of pressure ratio.
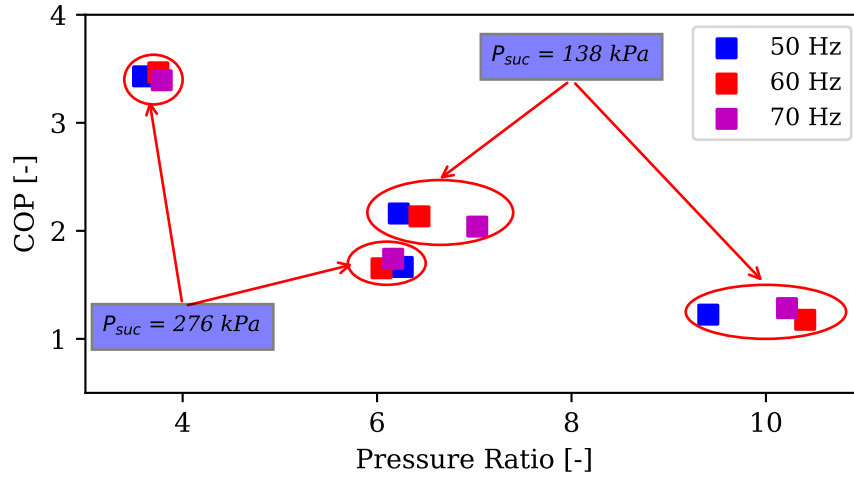
Fig. 3.21. System COP as a function of pressure ratio in Wisemotion linear compressor.
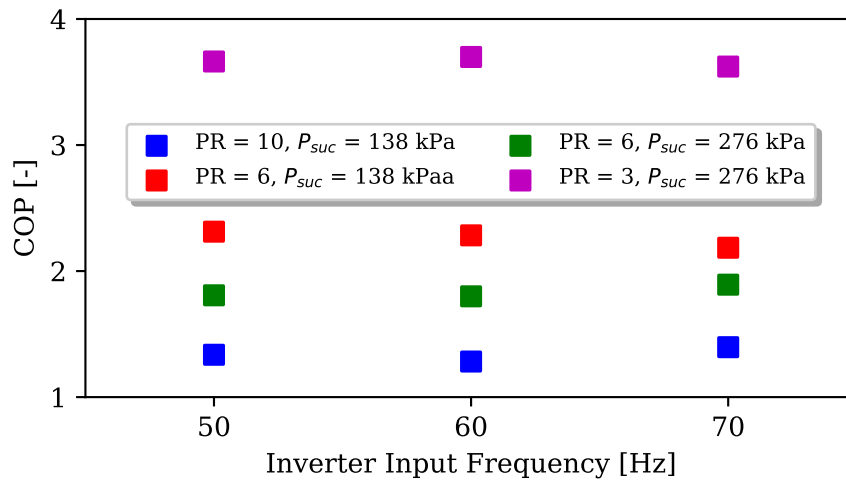
Fig. 3.22. System COP as a function of input frequency in Wisemotion linear compressor.

Test B

Since the Wisemotion linear compressor is designed with a linear variable capacity compressor technology, it is interesting to assess whether the compressor has different behaviors when the inverter input frequency is beyond normal frequency range. Based on the measured data shown in Figure 3.23, the power consumption varies linearly

with the mass flow rate of the linear compressor (capacity), by adjusting the piston stroke int the compressor rather than changing the compressor speed significantly. This results in the fact that the compressor performance, represent as efficiency, is independent of conditions and capacity. This feature promises the compressor work at very steady operation for all different operating conditions.
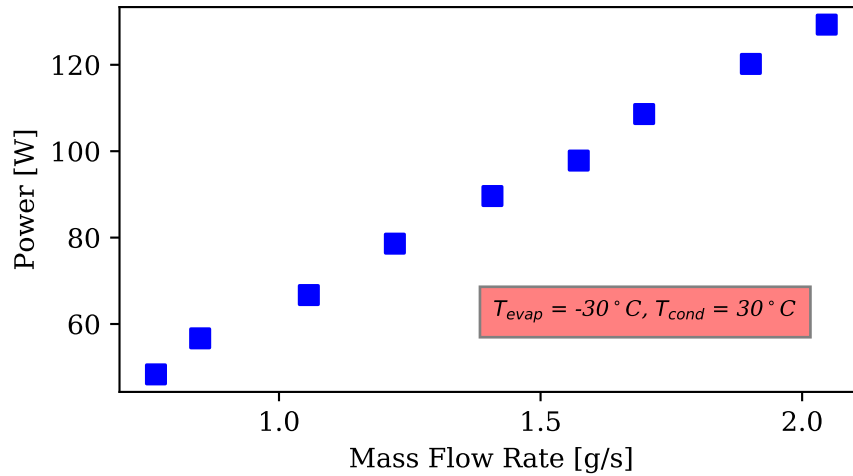
Fig. 3.23. Motor power as a function of mass flow rate (capacity) in Wisemotion linear compressor.

Based on the trend of mass flow rate and power consumption, the variation of overall efficiency shows minor change with increasing mass flow rate (variable cooling capacity). It can be concluded that the Wisemotion linear compressor can operate over a wide range of capacity modulation with variable piston stroke, instead of switching on and off, which results in smaller temperature variations and smaller vibration.

Test C

Three extra test points at the boundary of the operating envelope have also been considered with evaporating and condensing temperatures of -30 ℃ and 30 ℃, respectively. It can be observed that the compressor still works normally, but it runs
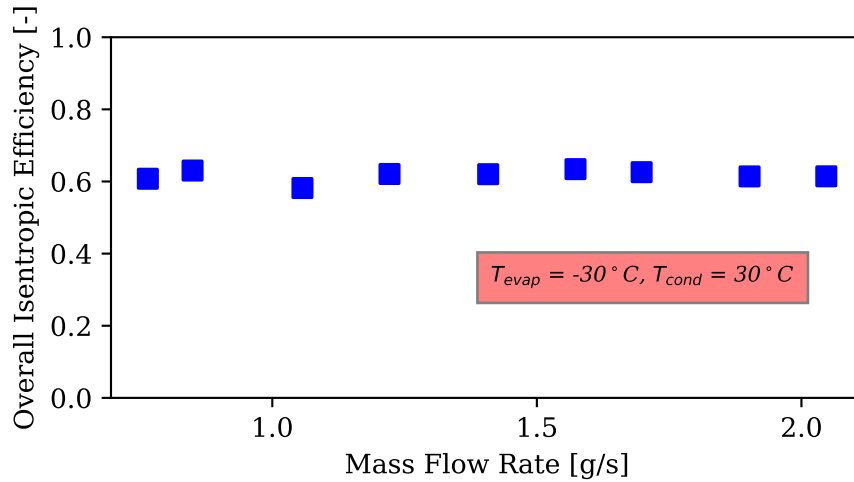
Fig. 3.24. Overall efficiency as a function of mass flow rate (capacity) in Wisemotion linear compressor.

with at slightly lower overall efficiency (approximately 0.6), compared to the previous analyzed operating points.

3.5.2 LG linear compressor

Table 3.5 shows the experimental results of the LG linear compressor. As discussed in Section 3.4, a 4×5 envelope with different pressure ratios and input frequencies was used for the experiments. 20 points were tested in total and analyzed to characterize the LG linear compressor performance. In particular, the input voltage and current of the motor in the LG linear compressor were measured and recorded. These parameters are very significant inputs for the future model validation.

Similar to the analysis of the Wisemotion linear compressor, the experimental results of the LG linear compressor are analyzed and discussed with respect to different performance aspects, including: power consumption, mass flow rate, overall efficiency and system COP. Each parameter is investigated as a function of pressure ratio and input frequency.

Table 3.5.
Experimental results from LG linear compressor with uncertainties.

Test No.	P_{suc} (kPa)	$u(P_{suc})$ (kPa)	P_{dis} (kPa)	$u(P_{dis})$ (kPa)	PR (-)	$\dot{m}$ (g/s)	$u(\dot{m})$ (mg/s)	$\dot{W}_{in}$ (W)	$u(\dot{W}_{in})$ (W)	f (Hz)	U (V)	I (A)
1	89.28	±0.21	373.00	±0.89	4.18	1.31	±4.58	80.15	±0.08	50	183	0.40
2	104.78	±0.28	404.72	±0.89	3.88	1.75	±6.13	105.42	±0.10	53	195	0.45
3	102.39	±0.28	402.24	±0.89	3.93	1.86	±6.51	181.54	±0.18	56	206	0.70
4	104.59	±0.28	390.45	±0.89	3.73	1.33	±4.58	119.31	±0.12	60	220	1.35
5	102.59	±0.28	370.52	±0.89	3.61	0.78	±2.73	90.20	±0.09	63	220	1.35
6	101.28	±0.28	535.86	±1.32	5.29	1.51	±5.28	97.81	±0.10	50	184	0.40
7	105.49	±0.28	517.73	±1.31	4.91	1.80	±6.51	133.91	±0.13	53	195	0.50
8	102.87	±0.28	549.93	±1.33	5.35	1.91	±6.68	209.20	±0.21	56	205	0.90
9	104.46	±0.28	548.62	±1.33	5.25	1.43	±5.00	133.56	±0.13	60	220	1.30
10	106.66	±0.28	563.58	±1.35	5.28	0.83	±2.87	100.70	±0.10	63	220	1.30
11	105.49	±0.28	743.87	±1.79	7.05	1.28	±4.58	98.69	±0.08	50	184	0.35
12	104.42	±0.28	691.41	±1.77	6.82	1.68	±5.88	131.55	±0.13	53	194	0.60
13	108.25	±0.28	722.02	±1.78	6.67	1.74	±6.13	174.52	±0.17	56	205	1.45
14	107.49	±0.28	743.46	±1.79	6.92	1.40	±4.86	136.18	±0.14	60	220	1.30
15	101.08	±0.28	689.48	±1.75	6.82	0.83	±2.87	103.98	±0.10	63	220	1.30
16	76.88	±0.14	843.23	±2.06	10.97	0.62	±2.87	72.07	±0.07	50	184	0.35
17	89.84	±0.21	963.96	±2.34	10.73	1.08	±3.78	109.48	±0.11	53	194	0.40
18	96.87	±0.28	1030.49	±2.55	10.64	1.39	±4.86	163.94	±0.16	56	205	1.40
19	106.94	±0.28	995.46	±2.48	9.31	1.35	±4.83	130.24	±0.13	60	220	1.30
20	98.25	±0.28	917.62	±2.34	9.34	0.58	±2.03	87.57	±0.08	63	220	1.30

Figure 3.25 shows the experimental mass flow rate as a function of pressure ratio at different operating frequencies of the compressor. It can be noted that the trend was not as linear as that on the Wisemotion linear compressor. It is seen that the mass flow rate increases gradually until it reaches to a peak and then drops significantly with the increasing pressure ratio under lower input frequency, i.e. 50 Hz, 53 Hz and 56 Hz. The peak occurs when the pressure ratio is approximately 5.5. However, when the input frequency equals 60 Hz or 63 Hz, the mass flow rate is relatively stable with

the variation of pressure ratio but still has a maximum flow rate approximately at pressure ratio 6.

One potential reason for this result is the resonant frequency of the system. It is observed that the maximum mass flow rate was delivered with the input frequency 56 Hz for all operating conditions, which indicates the system resonant frequency is close to 56 Hz when the maximum stroke can be obtained as well as the corresponding maximum mass flow rate. In addition, the gas pressure force depends on the pressure ratio. It dominates the piston movement when pressure ratio is small (i.e. less than 5.5) at low frequency input. In this case, a longer piston stroke can be achieved, which results in high mass flow rate. After the peak, the piston stroke is not significantly affected by pressure force but determined by the driving force associated with the input frequency. Especially at operating conditions with high frequency of 60 Hz and 63 Hz, the mass flow rate was relatively stable compared to the other three conditions.
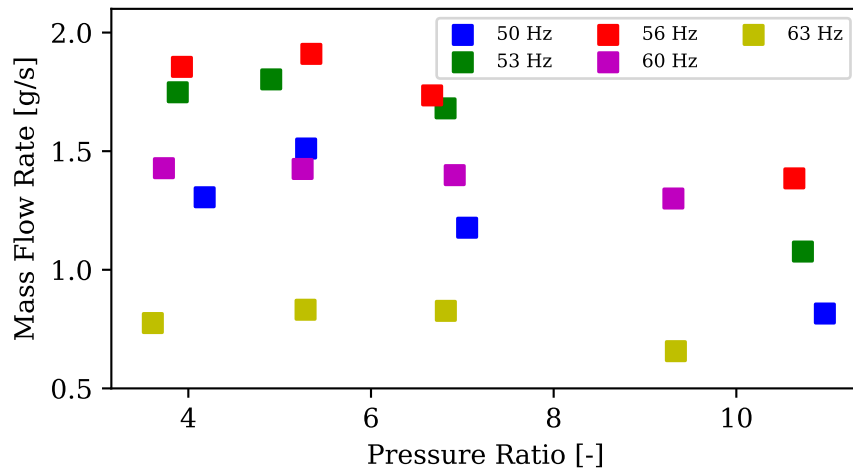
Fig. 3.25. Mass flow rate as a function of pressure ratio in LG linear compressor.

Variation of mass flow rate as a function of input frequency for different pressure ratios can be seen in Figure 3.26. It is noticed that there is a peak at the specific operating frequency of the system which is approximately at 56 Hz no matter how much the pressure ratio is for the system. It can be concluded that this operating point produces the maximum piston stroke as well as the mass flow rate. Besides,

green curve, i.e. PR = 5, always provides the highest flow rate which demonstrates that the gas pressure force dominates the piston stroke, as previously discussed. In addition, the mass flow rate in all operating points has a large variation range from 0.6 to 1.9 g/s.
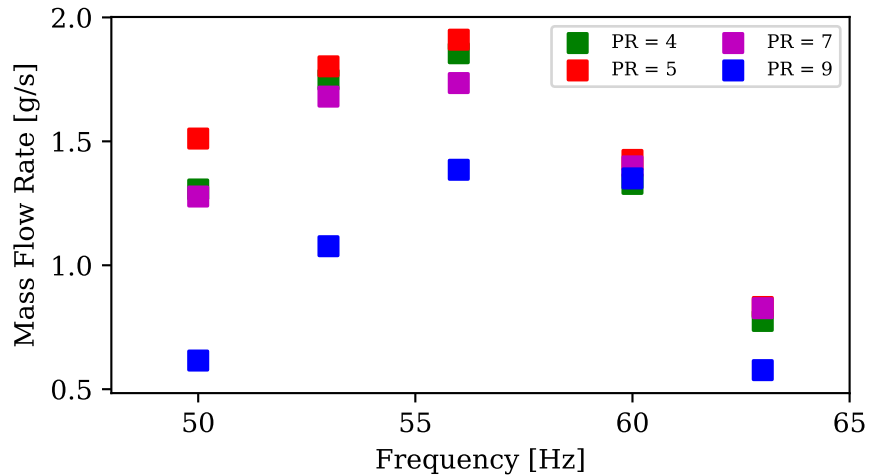
Fig. 3.26. Mass flow rate as a function of input frequency in LG linear compressor.

Figure 3.27 depicts the variation of power consumption as a function of pressure ratio. It is seen that the trend of power consumption shows very a similar pattern to the variation of mass flow rate. It can be explained by the fact that more flow rate needs more power consumption and the maximum power consumption of 210 W happens at an input frequency 56 Hz.

A dome shape performance can still be seen in Figure 3.28, which presents the variation of power consumption as a function of input frequency. Although more power is consumed at the resonant frequency, it can be predicted based on the simulation results that the motor runs more efficiency at the optimal point when the maximum amount of electrical energy can be converted to the mechanical energy and the maximum piston stroke as well as the mass flow rate can be obtained accordingly.

It can be seen from Figure 3.29 that the compressor overall efficiency increases slightly with increasing pressure ratio but this trend is not very clear. Based on the previous analysis, the system mass flow rate and power consumption are mainly deter-
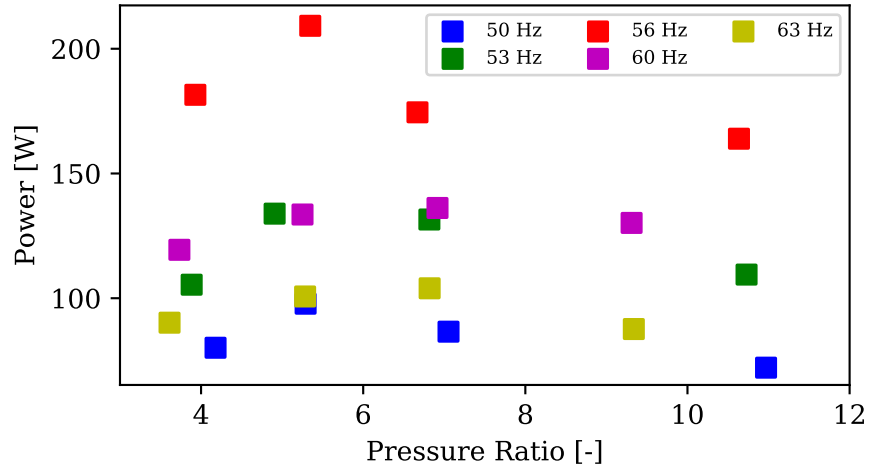
Fig. 3.27. Motor power as a function of pressure ratio in LG linear compressor.
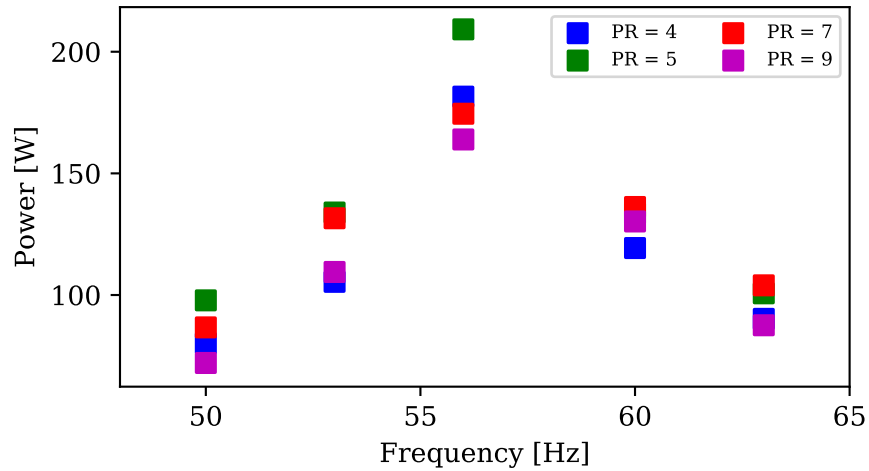
Fig. 3.28. Mass flow rate as a function of input frequency in LG linear compressor.

mined by the input frequency and only affected slightly by pressure ratio. Therefore, it can be concluded that the pressure ratio may not be a good indicator to investigate the overall efficiency of linear compressors. Therefore the variation of the overall efficiency of the compressor with different input frequency is analyzed in Figure 3.30. As is seen that the overall efficiency decreases with the increasing input frequency and the trend can be identified easily. The best overall efficiency of 0.6 was found with 50 Hz input frequency when the pressure ratio is close to 5.5. The lowest overall

efficiency is 0.25 at an input frequency of 63 Hz where the compressor shows very poor performance. Therefore, it can be concluded that different input frequencies put more limitations on the overall efficiency of the compressor and the frequency should be controlled carefully. Basically, the compressor runs more efficiently at lower input frequency.
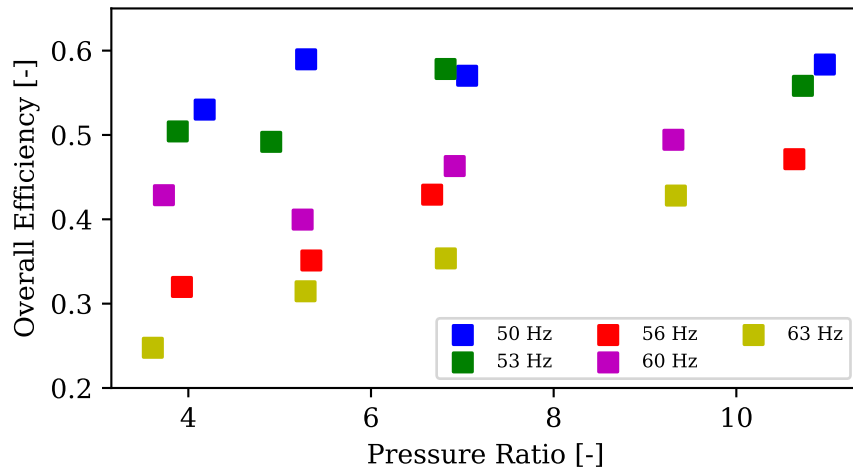
Fig. 3.29. Overall efficiency as a function of pressure ratio in LG linear compressor.
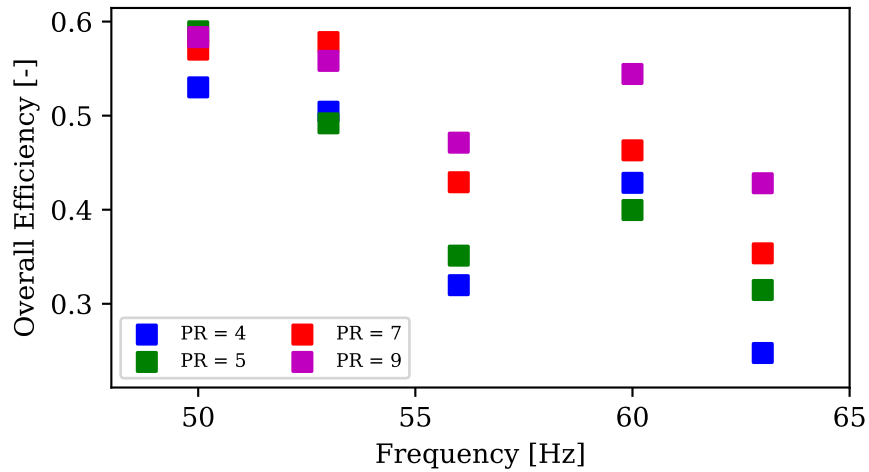
Fig. 3.30. Overall efficiency as a function of input frequency in LG linear compressor.

Figure 3.31 shows the system COP variation as a function of pressure ratio. The assumptions made for the COP analysis are exactly same as the analysis for the Wisemotion linear compressor in Section 3.5.1. As is shown, the compressor generates a higher system COP with smaller pressure ratio and the value goes down with increasing pressure ratio. In particular, the system COP is relatively low with higher pressure ratio which indicates that the compressor is not able to run efficiently. Furthermore, Figure 3.32 shows the relationship between system COP and input frequency. Better system performance can be obtained with lower input frequency. The trend is similar to the curves in Figure 3.31.
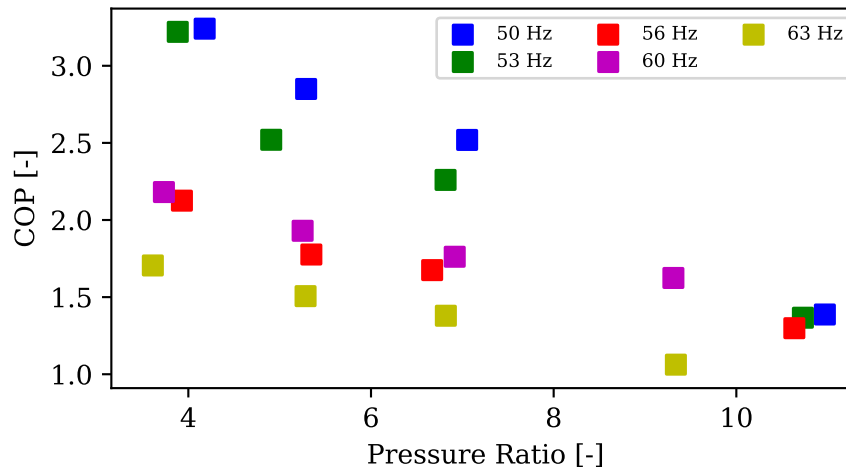
Fig. 3.31. System COP as a function of pressure ratio in LG linear compressor.

3.6   Experimental Performance Comparison

In this section, two types of performance comparison will be reported. First of all, based on the measurements data above, it is interesting to compare the performance data from two commercial linear compressors since each of them has different compressor design and lubrication method. In addition, since the compressor mechanical design of linear compressor is very similar to the conventional reciprocating
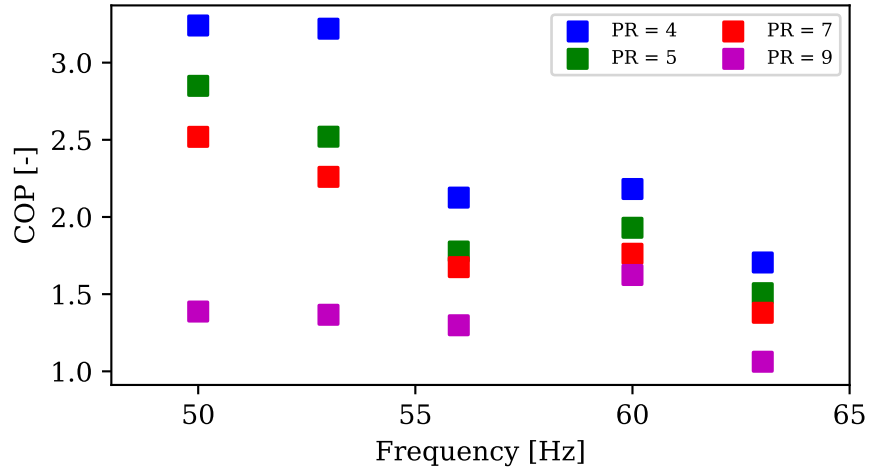
Fig. 3.32. System COP as a function of input frequency in LG linear compressor.

compressor, it is important to make a comparison between a linear compressor and a reciprocating compressor with similar design and target capacity.

3.6.1 Comparison between two commercial linear compressors

Two commercial linear compressors have been tested and characterized at different operating conditions. The measurements were used to characterize and evaluate their performances. Relatively little experimental data is reported in the literature with respect to linear compressor performance comparisons. In terms of these two commercial linear compressors used in this study, LG linear compressor uses synthetic POE oil for lubrication and the refrigerant gas itself is used to lubricate the Wisemotion linear compressor which is oil-free. In addition, the spring systems were designed very differently in these two compressors, which affects the contribution of spring force on piston movement. Furthermore, the tubular linear motor in the LG compressor may lead to different driving forces for piston, compared to the separated linear motor in the Wisemotion linear compressor. Therefore, it was decided to compare the performance of these two compressors based on their measurement data.

Based on all the measurements discussed in Section 3.5.1 and Section 3.5.2, the experimental results of these two compressors are compared. However, it's hard to compare their performance and draw any conclusions between direct if two compressors deliver different mass flow rate and consume different power even at similar operating conditions. It can be seen that linear compressor always delivers less flow with similar pressure ratio as well as power consumption. However, based on the analysis in Section 3.5.1 and plot in Figure 3.23, the power consumption varies linearly with the mass flow rate in Wisemotion linear compressor. Therefore, it would be helpful to use the mass flow from LG linear compressor as a target and interpolate the flow rate from Linear compressor Wisemotion linear compressor, the power consumption will be determined accordingly. Moreover, the overall isentropic efficiency is also a good parameter to show the difference between these two compressors. The modified tested results are shown in Table 3.6. In order to deliver the same flow rate, Wisemotion linear compressor will operate with longer piston stroke and consume more power. The relative power consumption difference to Wisemotion power between two compressors is also listed in the table. It is seen that the power consumption in Wisemotion linear compressor is almost half of the required power of the LG linear compressor to deliver same flow rate and with smaller pressure ratio. However, when operating at higher pressure ratio, the power difference between Wisemotion and LG is only up to 11.7%.

Figure 3.33 shows the variation of power consumption as a function of target flow rate for the two linear compressors. With the same target flow rate, Wisemotion linear compressor always consumes less power compared to LG linear compressor and the difference becomes larger when the target flow rate increases. In addition, pressure ratio also affects the differences between two compressors. It can be seen that power consumption of two compressors are close to each other when the pressure ratio is at 6.

The overall isentropic efficiency is determined by the combination effect of mass flow rate and power consumption as long as the same operating conditions were kept.

Table 3.6.
Modified experimental results for the LG and Wisemotion linear compressor power consumption comparison.

Type	LG	WM	Diff.
$\dot{m}$	$\dot{W}$	$\dot{W}$	$\dot{W}_{diff}$
(g/s)	(W)	(W)	$(\%)$
1.31	80.15	56.47	41.9
1.33	119.31	57.35	108.0
1.18	98.69	96.59	2.2
1.40	136.18	121.87	11.7
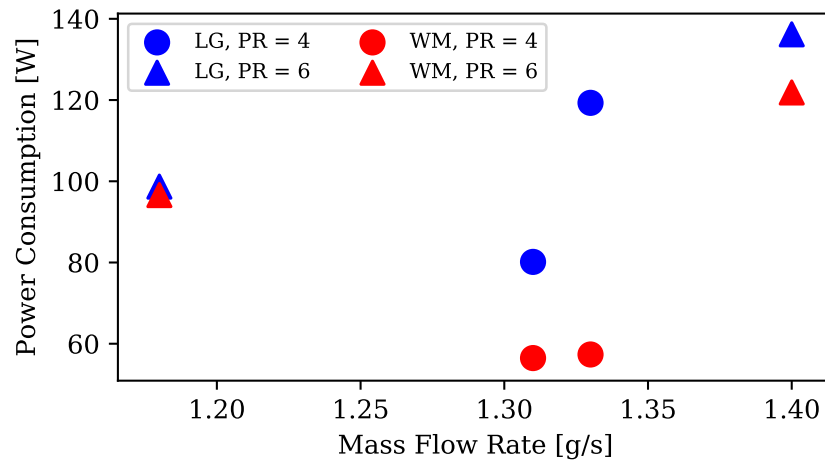
Fig. 3.33. Comparison of Motor power between Wisemotion (WM) and LG linear compressor.

It is expected that Wisemotion linear compressor has higher efficiency than that in LG compressor at smaller pressure ratio, where LG compressor consumed more power but delivered a similar flow rate. It can be seen from Figure 3.34 that all the red markers are above the blue markers at same frequency. Moreover, the overall efficiency of the Wisemotion compressor decreases with increasing pressure ratio while this trend in LG linear compressor is slightly reversed.
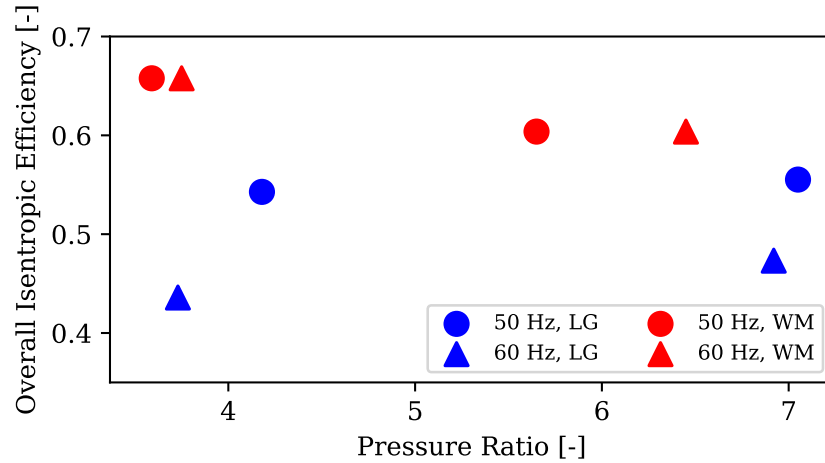
Fig. 3.34. Comparison of overall isentropic efficiency between Wise-motion and LG linear compressor.

3.6.2 Comparison between one linear compressor and one reciprocating compressors with similar geometry

Fundamentally, linear compressor and reciprocating compressor are very similar technologies, which are positive displacement piston-cylinder compressor. Due to the different driving mechanism and compressor design configuration, linear compressors show a good performance theoretically. Therefore, it is necessary to compare those two types of compressor experimentally to see the differences between their performance. One commercially available reciprocating compressor was also designed from Embraco, which is used for residential refrigerator. In order to conduct a reasonable comparison, the geometry and capacity of the tested reciprocating compressors are also very close to Embraco Wisemotion linear compressor, which is a very good benchmark for analysis. Table 3.7 shows a summary of the Embraco reciprocating compressor and Wisemotion compressor including all the geometry information, respectively. It can be found that two tested compressors have very similar geometry, *i.e.*, piston size, lubrication, valve type.

Table 3.7.

Summary of tested linear and reciprocating compressors for performance comparison.

Manufacturer	Embraco	Embraco
Type	Linear	Reciprocating
Basic Information		
Refrigerant	R134a	R134a
Motor	Tubular linear	Rotary
Lubrication	Refrigerant	Refrigerant
Vibration Absorption	No	Yes
Orientation	Horizontal	Vertical
Suspension system	Yes	No
Geometry		
Dimension (cm)	30/13/12	20/15/18
Piston diameter (cm)	1.95	1.85
Piston Length (cm)	5.17	2.18
Piston mass (kg)	0.05	0.02
Suction valve port diameter (cm)	7.6*2	6.82 (Ring)
Discharge valve port diameter (cm)	2.25*6	3.62*3
Suction valve type	reed valve	reed valve
Discharge valve type	reed valve	reed valve

Table 3.8 shows a summary of experimental results of the Embraco reciprocating and linear compressor and two compressors were tested at similar operating conditions with three driving frequencies. A total of 6 points were tested and used to compare their performance. Two compressors were tested with similar operating conditions and there were two input frequencies (50Hz and 60 Hz) for each condition. It can be seen that Wisemotion linear compressor always delivers less flow with similar pressure ratio as well as consume power consumption and it will be unfair to compare

the results and draw any conclusion between the direct comparison. With the same method used in Section 3.6.1, power consumption from Wisemotion linear compressor was interpolated in order to deliver the same mass flow rate from the tested reciprocating compressor for a consistent comparison. The modified results are shown in Table 3.9.

Table 3.8.
Experimental results for the reciprocating and linear compressor comparison.

Type	Recip.			LC.		
f	PR	$\dot{m}$	$\dot{W}$	PR	$\dot{m}$	$\dot{W}$
(Hz)	$(-)$	(g/s)	(W)	$(-)$	(g/s)	(W)
50	3.82	1.72	110.70	3.69	1.17	50.33
	5.92	1.64	132	6.26	0.71	49.4
60	3.89	2.00	136.40	3.75	1.36	59.09
	6.39	1.84	159	6.05	0.87	59.99
70	3.86	2.43	171.40	3.79	1.587	69.39
	6.59	1.96	181	6.17	1.04	69.19

It can be observed from Table 3.9 that with the same target flow rate, linear compressor always requires longer piston stroke, especially for higher pressure ratio. For example, when the pressure ratio is close 6, in order to deliver 1.84 g/s flow, the required piston stroke for Wisemotion linear compressor is 16.4 mm, which is 1.17 times of the piston stroke of reciprocating compressor. However, power consumption at this condition in linear compressor is 37.1 % less than the required power for the reciprocating compressor.

Figure 3.35 shows the variation of power consumption as a function of target flow rate for the comparison between the reciprocating and linear compressor. With the same target flow rate, Wisemotion linear compressor always consumed less power compared to the reciprocating compressor and the difference became smaller with

Table 3.9.
Modified experimental results for the reciprocating and linear compressor power consumption comparison.

Type	Recip. ($x_s = 14mm$)			LC. ($f = 60Hz$)			Diff.
$\dot{m}$	PR	f	$\dot{W}$	PR	x_s	$\dot{W}$	$\dot{W}_{diff}$
(g/s)	$(-)$	(Hz)	(W)	$(-)$	(mm)	(W)	$(\%)$
1.72	3.8	50	110	3.7	10.94	76	44.7
1.64	5.9	50	132	6.3	12.64	104	26.9
2.00	3.9	60	136	3.8	14.09	89	52.8
1.84	6.4	60	159	6.0	13.60	116	37.1
2.43	3.9	70	171	3.8	16.40	109	56.9
1.96	6.6	70	181	6.2	15.46	123	47.2

the larger pressure ratio. It can be observed from Figure 3.36 that linear compressor has higher overall isentropic efficiency than that from the tested reciprocating compressor, which is approximately around 0.7 and 0.6 when pressure ratio is at 4 and 6, respectively. However, the compared reciprocating compressor only showed up to 0.5 overall isentropic efficiency at the tested conditions. Moreover, it can be observed that the operating frequency play less influence on the performance of Wisemotion linear compressor and the efficiency showed relatively steady trend. Nevertheless, the efficiency in the compared reciprocating compressor goes down slightly when the operating frequency increases.

3.7   Conclusions

The experimental results of two commercial linear compressors were presented in this chapter. Compressor mass flow rate, suction and discharge temperatures, suction and discharge pressures, intermediate pressures and temperatures, and compressor power consumption were used to characterize the two compressors. Two experimental
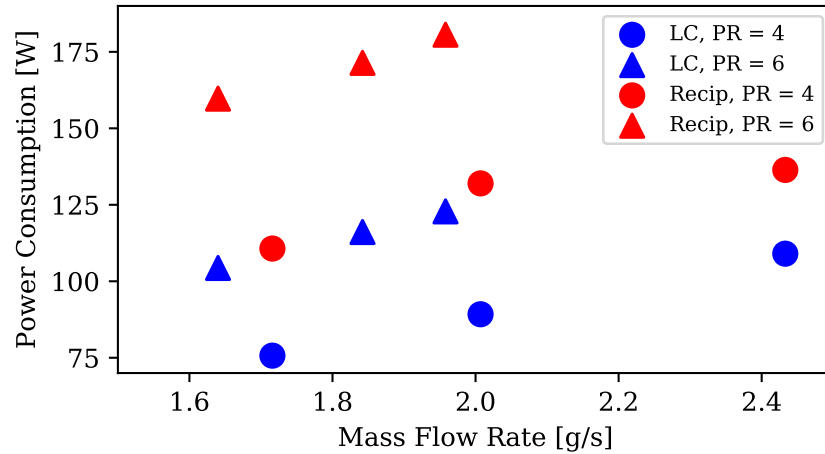
Fig. 3.35. Comparison of power consumption between Embraco linear compressor and Embraco reciprocating compressor.
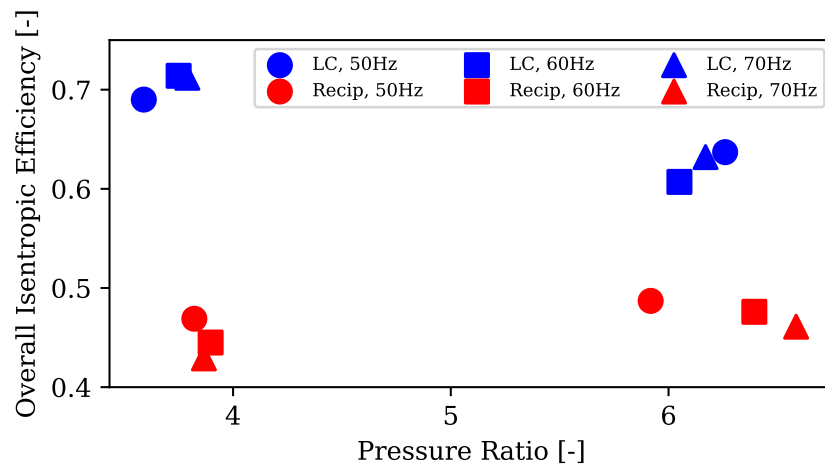
Fig. 3.36. Comparison of overall efficiency between Embraco linear compressor and Embraco reciprocating compressor.

comparisons between the two commercial linear compressors and between one linear and one corresponding reciprocating compressor were conducted to observe differences between each of them with respect to the experimental performance. Furthermore, a comprehensive table summarizes all main specifications and some special aspects

of all tested compressors. Several features were identified and the advantages and disadvantages of each design were discussed.

Based on a comparison between the Wisemotion and LG linear compressors, several conclusions can be made with respect to their performance as follows:

- The Wisemotion linear compressor is controlled more steadily with smaller power consumption. The control logic of the Wisemotion compressor allows the compressor to maintain a more steady operation and limits the sensitivity of the compressor to variations of the required capacity.

- At higher pressure ratio, the LG compressor is able to deliver more flow with respect to the Wisemotion compressor. A possible reason is that power consumption of the Wisemotion compressor is not a function of pressure ratio and there is not enough driving force to generate flow rate compared to the LG compressor.

- Overall, the LG compressor shows better performance at higher pressure ratio at the two analyzed input frequencies. However, the Wisemotion compressor runs more efficiently at lower pressure ratio. Since domestic refrigerators operate at small pressure ratios, the Wisemotion compressor may show better performance than the LG linear compressor.

Also, according to the comparison between the Wisemotion linear and Embraco reciprocating compressors, several conclusions also can be draw with respect to their performance and differences:

- The Wisemotion linear compressor consumes less power when delivering same flow rate, which is up to 56.9% power difference among all compared tested conditions. In terms of different pressure ratios, the difference of the required power for two compressors decrease and it can be concluded that linear compressor operates better at smaller pressure ratio, compared to reciprocating compressor.

- Among the analyzed conditions, linear compressor shows a better performance with higher overall isentropic efficiencies, which are approximately 1.6 times and 1.4 times of the reciprocating compressor efficiency at pressure ratio at 4 and 6, respectively.

- The overall isentropic of linear compressor is not as sensitive to the operating conditions as reciprocating compressor, which show a decrease of efficiency with the increasing compressor speed.

4. MODEL VALIDATION AND EVALUATION

The comprehensive compressor simulation model described in Chapter 2 is employed to analyze the dynamic behavior of linear compressors and to conduct sensitivity studies. Before exercising the model, a model validation is carried out by utilizing the experimental data obtained in Chapter 3 to assess the accuracy of the model and eventually identify the improvements required. The experimental results from both of two linear compressors were used for model validation. Moreover, the simulation results of two calculation modes are also reported in this chapter, which were used to investigate the transient and periodic-steady behavior of a linear compressor using the model inputs, listed in Table 4.1. The transient behavior of the linear compressor is analyzed first and then the periodic solution will be presented. In the end, the overall performance of the analyzed compressor is predicted and discussed. In order to understand the behavior of a linear compressor, the following aspects are investigated as a function of time:

- Piston motion
- Cylinder pressure and temperature
- Motor input current/power
- Cylinder vapor mass
- Valve motion
- P-V diagram
- Lumped temperature of main component

Table 4.1.
The model inputs for the dynamic simulation model based on LG linear compressor.

Description	Parameter	Value	Unit
Working Fluid	-	R134a	-
Suction Pressure	P_{suc}	111.81	kPa
Suction Temperature	T_{suc}	8.08	°C
Pressure Ratio	PR	5.5	-
Compressor Frequency	f	60	Hz
Piston Diameter	D_p	26.5	mm
Piston Length	L_p	79.6	mm
Suction Valve Diameter	$D_{\text{s,v}}$	5.21	mm
Suction Valve Length	$L_{\text{s,v}}$	18.48	mm
Suction Valve Thickness	$h_{\text{s,v}}$	0.152	mm
Discharge Valve mass	$m_{\text{d,v}}$	4	g
Piston Mass	M_p	0.632	kg
Spring Mass	M_s	0.164	kg
Spring Stiffness	k_s	45.66	Nmm^{-1}
Clearance Gap	g	5	μm
Motor factor	α	75	NA^{-1}
Motor Resistant	R	15.7	Ω
Motor Inductance	L	450	mH

4.1 Model Validation

A comprehensive linear compressor simulation model for both transient and periodic-steady behavior and energy flows of a linear compressor is described in Chapter 2 and was used to model the two commercial linear compressors tested in this study. Sev-

eral modifications to the model were necessary to allow consideration of different features of the two compressors, *e.g.*, lubrication method, spring configuration and motor driving approach.

Figure 4.1 presents comparisons of predicted and measured mass flow rates. The Mean Absolute Percentage Error (MAPE) is 2.7% for compressor A and 4.5% for compressor B with all calculated points within a relative error of ±9%. As a general observation, the proposed model tends to over-predict mass flow rate, but the overall mass flow rate distribution is reasonable. The results could undoubtedly be improved by implementing a more detailed model leakage across the piston for both oil-lubricated and oil-free operation.
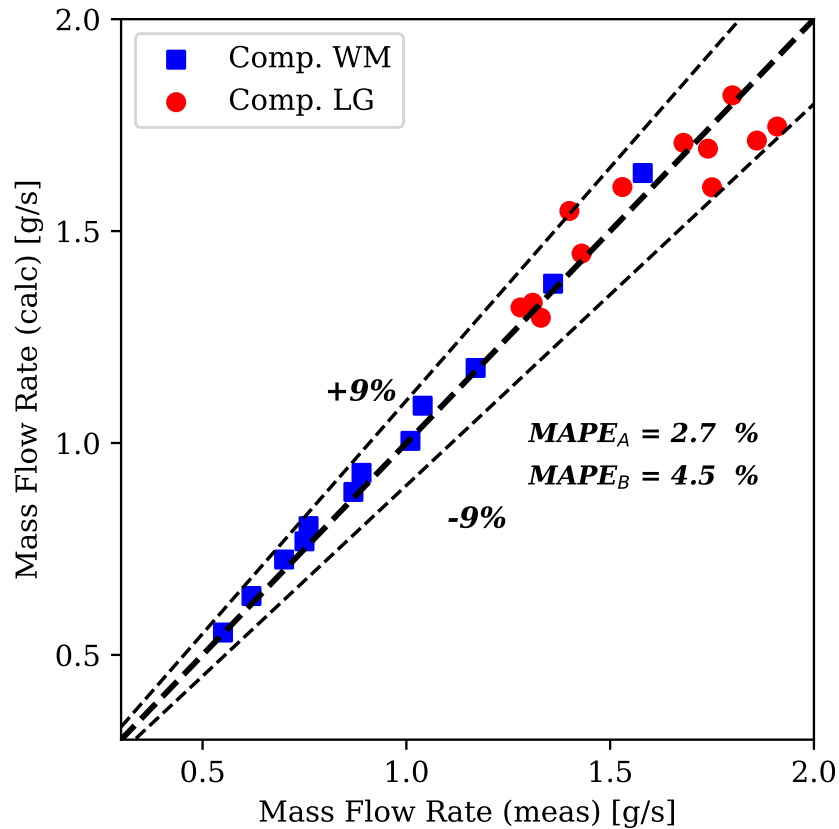
Fig. 4.1. Model validation results for the mass flow rate of two linear compressors.

The compressor power consumption was predicted within a relative error of $\pm 15\%$ and the MAPE value was 3.6% for compressor A and 9.3% for compressor B, as shown in Figure 4.2. Similar to the mass flow rate results, there are some deviations between the measurements and simulation results, but the agreement falls within a good range ($< 15\%$). These errors could be due to the use of a simplified motor and control model, which was not able to account for the real performance of the linear motor used in the commercial linear compressors. Limited information regarding the compressor motors and controls were available. The agreement for compressor A is better than that for compressor B, perhaps because of a lack of information needed to accurately model the power consumption of the oil pump for compressor B.
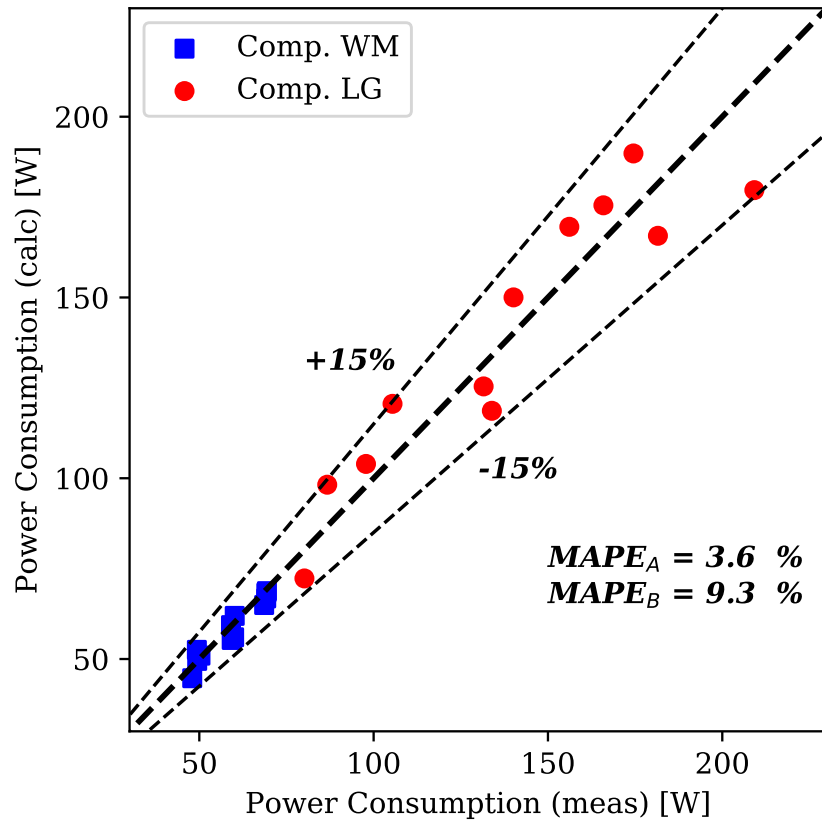
Fig. 4.2. Model validation results for the power consumption of two linear compressors.

It is seen in Figure 4.3 that the MAPE for overall isentropic efficiency with compressor A is 5.2% and 7.8% for compressor B within an overall relative error of $\pm 14\%$. Based on model validation results discussed above, although there is still room for additional model improvements, the model itself has a reasonable accuracy and can be used for further analysis of linear compressor performance. The simulation results are presented in next section.
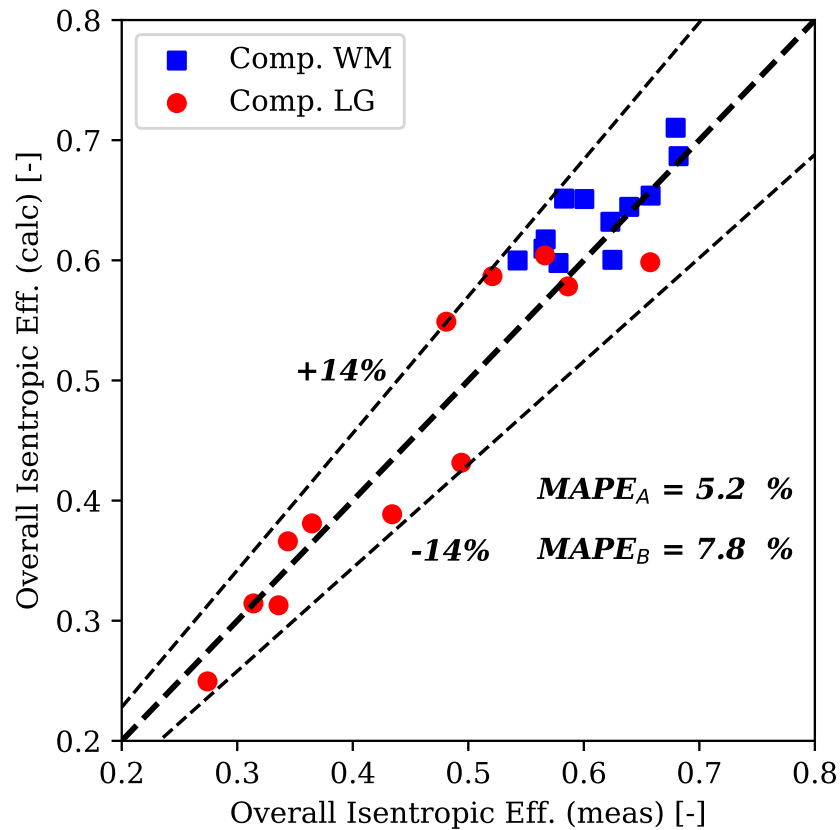
Fig. 4.3. Model validation results for the overall isentropic efficiency of two linear compressors.

4.2 Transient Results from Compressor Start-up

The transient behavior of the linear compressor is analyzed at first. In particular, the following aspects are investigated as a function of time from the compressor start-up:

- Piston motion
- Cylinder pressure
- Motor input current/voltage
- Motor power

Figure 4.4 shows the schematic diagram for a piston movement analysis and cyclic variation of the piston displacement can be seen from Figure 4.5 as a function of time. It is noted that the y-axis in Figure 4.5, $i.e.$, piston displacement, is consistent with the x direction in Figure 4.4. It can be seen from the curve that the simulated piston stroke is not fixed, unlike in conventional reciprocating compressors. A mechanical steady-periodic condition is achieved when the piston stroke is no longer changing and the compressor is working with a periodical cycle.
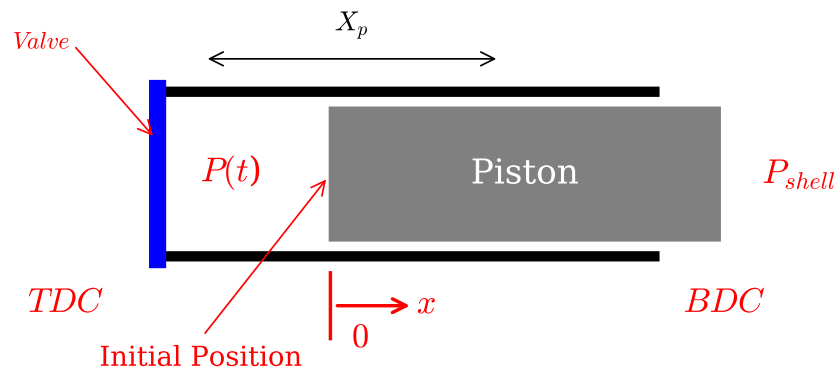
Fig. 4.4. Diagram of piston at initial position.
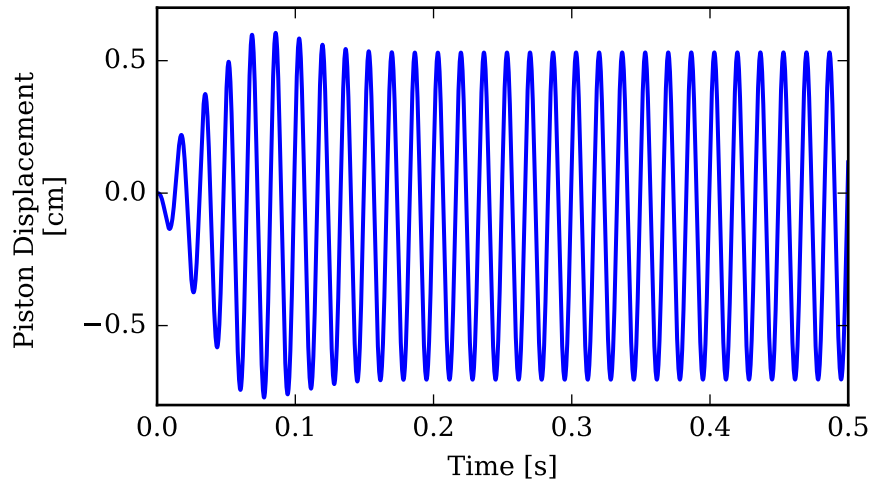
Fig. 4.5. Transient piston displacement variation over compressor running time.

Figure 4.6 shows the dynamic variation of the cylinder pressure as a function of time as well as the compressor shell pressure, which is the same as the compressor inlet pressure. The pressure inside the cylinder builds up during the first few cycles until it exceeds the target discharge pressure, which was set to 560 kPa, when the discharge valve is able to open. Once steady-periodical conditions are detected from the piston motion, the cylinder pressure shows cyclic steady performance. The results discussed above demonstrate the dynamic behavior of the compressor at start up and as it approaches a periodical steady state but prior to satisfying the overall energy balance. The results presented in Figure 4.5 and Figure 4.6 demonstrate the dynamic behavior of the compressor from compressor start-up as it approaches a periodical steady state but prior to satisfying the overall energy balance.

Figure 4.7 shows dynamic variation of the current in the electrical circuit as a function of time from start up. Note that there are irregular oscillations in the first few cycles, similar to the variation of piston movement. These oscillations have a significant effect on the motor efficiency as seen in Figure 4.8, where input power has a significant spike during the start-up process but only a portion of the power is converted as output to drive the piston. This can be seen from the deviation between the input power (red dashed line) and output power (blue solid line). It is also noted
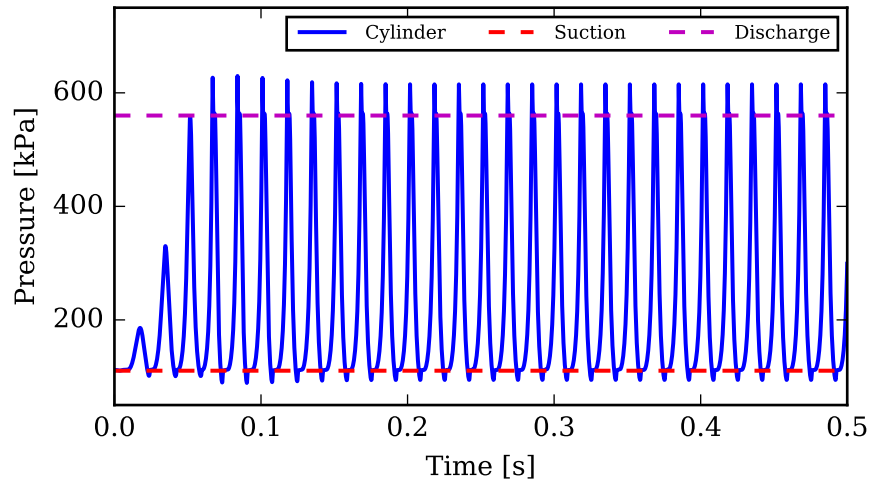
Fig. 4.6. Transient in-cylinder pressure variation over compressor running time.

that the transient power (similar to the driving force) has the largest value at start-up to initiate the motion of the piston and then decays over the running time as steady-periodic behavior is achieved.
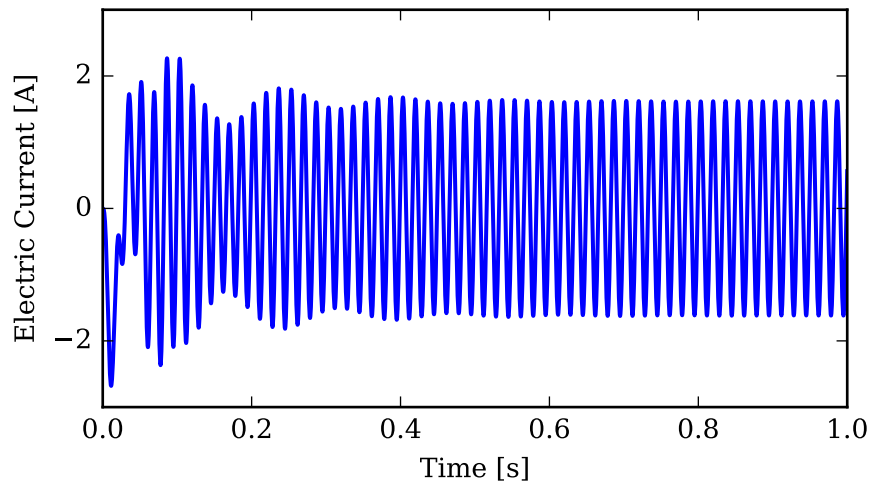
Fig. 4.7. Transient electric current variation over compressor running time.
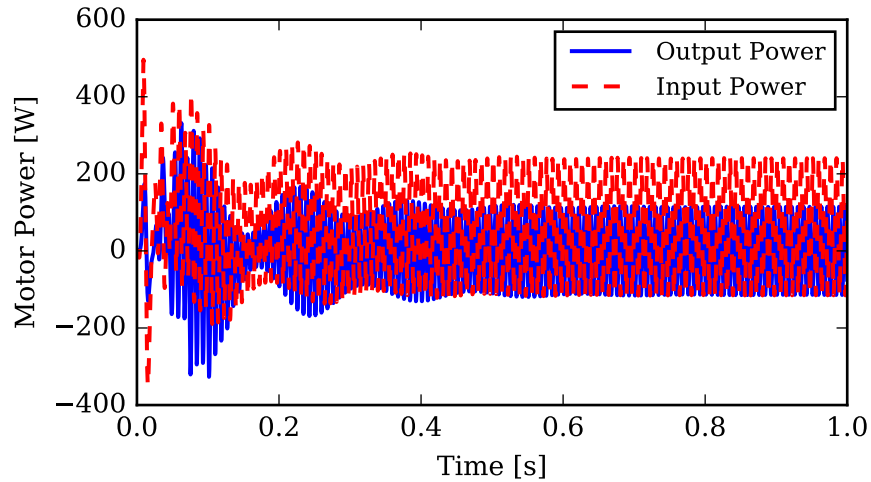
Fig. 4.8. Transient motor power variation over compressor running time.

4.3 Periodic Steady-State Results

After the initial transient behavior, the linear compressor establishes periodic steady-state operation for fixed boundary conditions. Using the steady-periodic mode of the model, a fully steady-periodic solution was identified and determined for the boundary conditions considered in the previous subsection. Figure 4.9 shows the dynamic behavior of the piston displacement at periodical steady-state conditions. The behavior is similar to the sinusoidal pattern of oscillation that occurs in conventional reciprocating compressors. The overall piston stroke was predicted to be approximately 13 mm, which is marked in green. It can also be noted that there is a displacement bias between the initial piston position and the final equilibrium position, which is a typical characteristic of a linear compressor discussed in Section 2.6.1. Black and red dashed lines denote the piston initial preset position and the new equilibrium position at periodical steady state, respectively. It is noted that the bias displacement is positive in this result, which is favorable motion for a linear compressor.

The in-cylinder pressure traced as a function of time can be seen in Figure 4.10. Four processes in a linear compressor can be identified, *i.e.*, suction, compression,
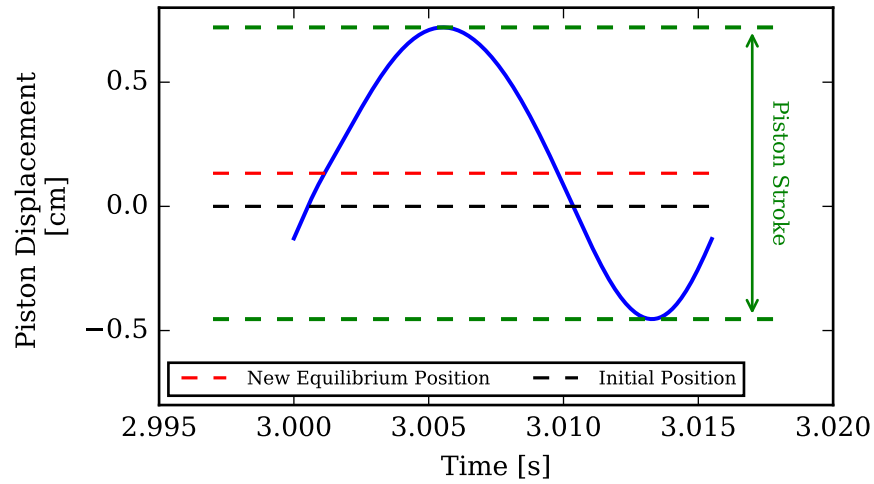
Fig. 4.9. Piston displacement and driving force at periodical steady state.

discharging, and expansion. Two different types of valves used in the modeled linear compressor lead to very different pressure fluctuations during suction and discharge processes, which can be distinguished in Figure 4.10. In particular, the plate valve on the discharge line produces more pressure drop than the reed valve used in the suction line.
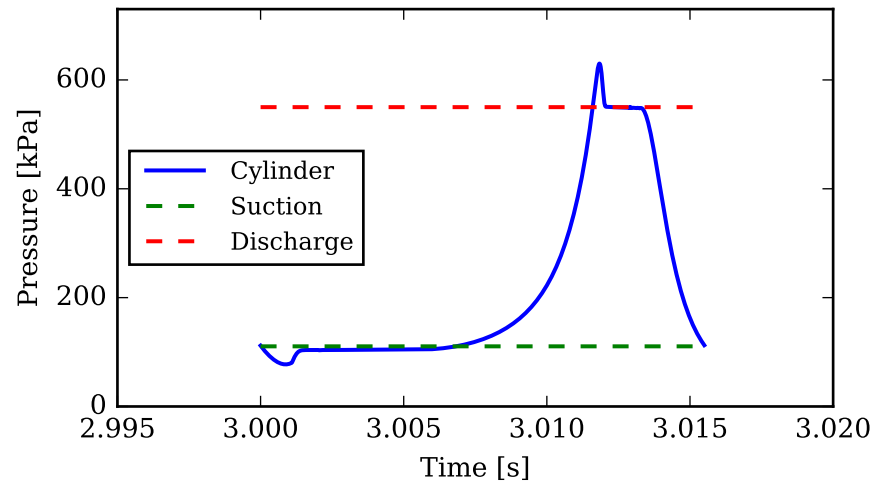
Fig. 4.10. Cylinder pressure variation at periodical steady state.

Figure 4.11 shows the variation of input voltage and current at periodical steady state. Compared to the performance during the start-up process shown in Figure 4.7, the current has very good steady behavior with a quarter period lag with respect to the voltage. It is noted that the power periodic variation only has the half of the period of current/voltage change due to the calculation of power consumption, shown in Equation 2.59 and Equation 2.60, which are a very typical feature of an AC motor. Besides, the amplitude of the output power is lower than that of the input power with a lag (approximately 90°) as expected, shown in Figure 4.12.
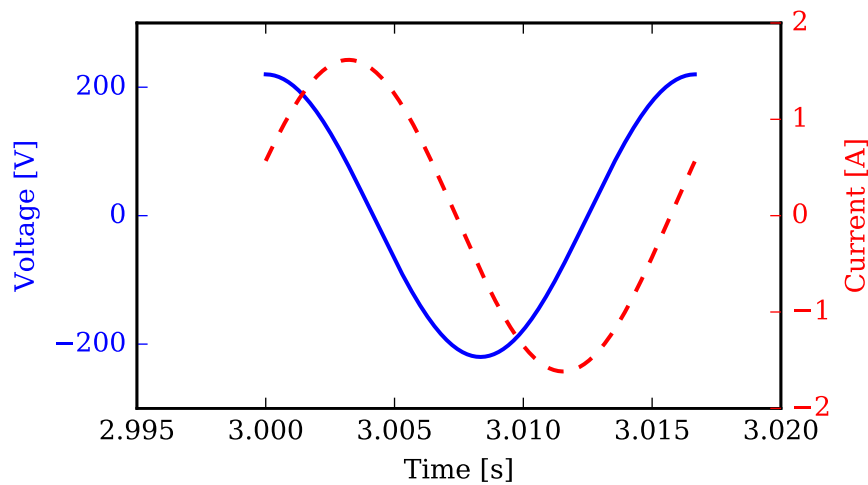
Fig. 4.11. Current variation at periodical steady state.

Figure 4.13 shows the temperature variation of the refrigerant within the cylinder, which has a similar pattern to the pressure change. It is noted that as is shown in Figure 9, three criteria, i.e., piston displacement, piston velocity, motor current, were used to identify periodic steady state. Based on the simulation results, the discharge temperature that is presented here satisfied the periodic steady-state criteria. The highest cylinder temperature was predicted to be approximately 330 K corresponding to conditions in the discharge tube.

The reed valve in the suction process leads to a longer opening time and smoother performance, as shown in Figure 4.14. In the modeled commercial linear compressor, a reed valve is located at the end of the piston, and three ports on the valve plate
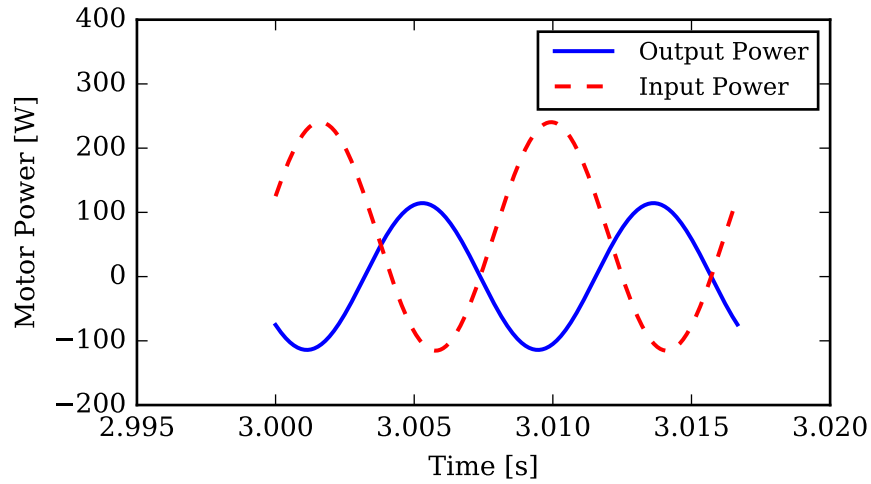
Fig. 4.12. Power variation at periodical steady state.
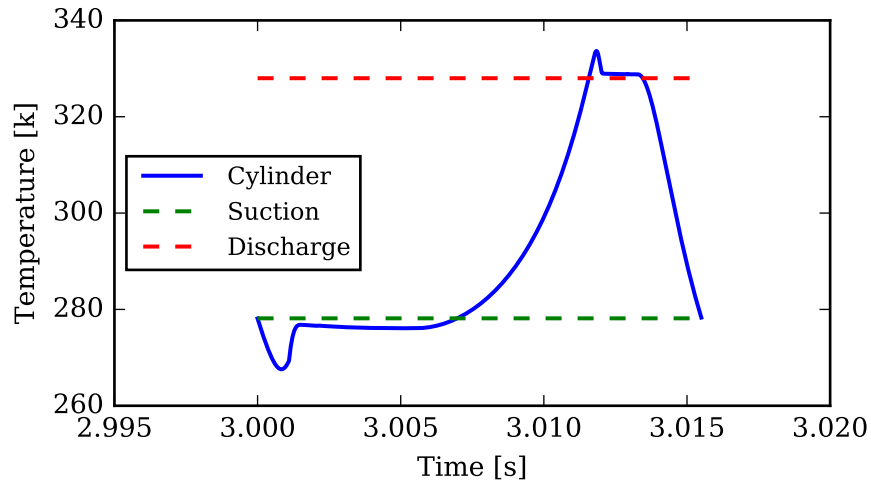
Fig. 4.13. Cylinder temperature variation at periodical steady state.

direct flow smoothly, which can be observed from pressure variation during the suction process in Figure 4.10. On the other hand, the plate valve with a single large discharge port installed on the discharge side produces a shorter discharging process. It is noted that no gas pulsation was considered in this analysis.

The variation of the in-cylinder vapor mass at periodical steady state as a function of time is reported in Figure 4.15. The opening and closing processes of the suction and discharge valves are clearly delimited by the dashed lines. The density of the
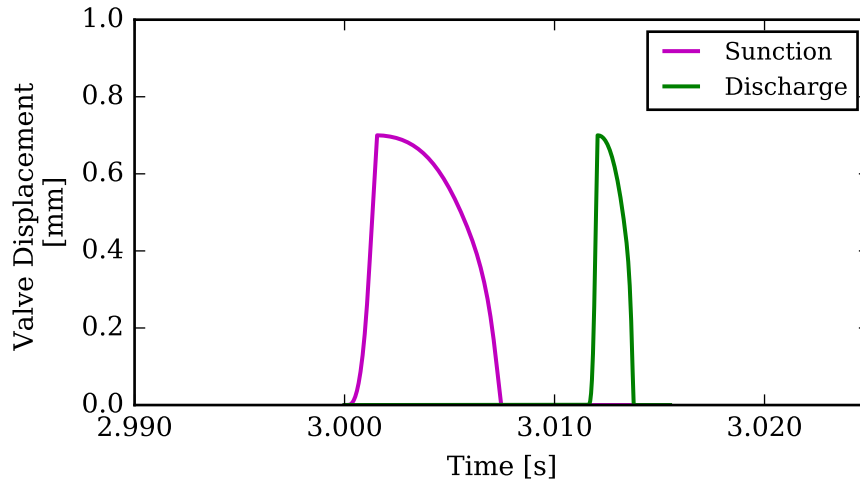
Fig. 4.14. Valve displacement at periodical steady state.

suction gas is lower than the discharged gas. As a result, the conservation of mass in the compression chamber dictates that the volumetric flow of the suction process is higher than that of the discharge process, which results in a larger valve opening time for the suction process, even though the discharge port has smaller cross-area. Therefore, the suction process takes more time, *i.e.*, longer opening time for the suction valve, while the discharging process is shorter, which is very consistent with the variation of the valve motions shown in Figure 4.14. However, at all other times, *i.e.*, when the two valves are closed, the cylinder vapor mass is almost constant because of mass conservation. Minor variations may occur due to small leakage flows between the compression cylinder and the shell.

The P-V diagram of the linear compressor at periodic steady-state condition, including the opening and closing of the valves, is shown in Figure 4.16. By analyzing the P-V diagram, it is seen that the linear compressor has a specific clearance volume, which affects the indicated work and both the volumetric and isentropic efficiencies and should also avoid metallic contact between the piston and valve seat. Due to the existence of a spring system in a linear compressor design, the expansion work from this clearance is stored inside the spring and released back during the compression process.
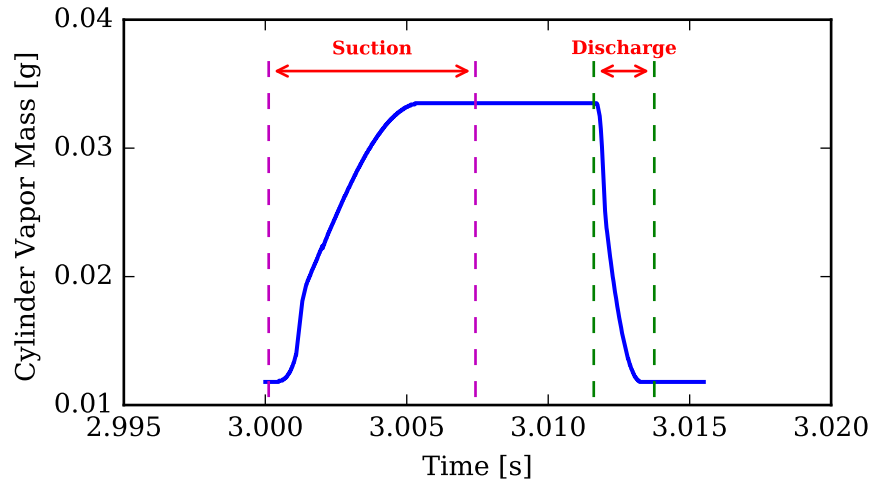
Fig. 4.15. Cylinder vapor mass at periodical steady state.
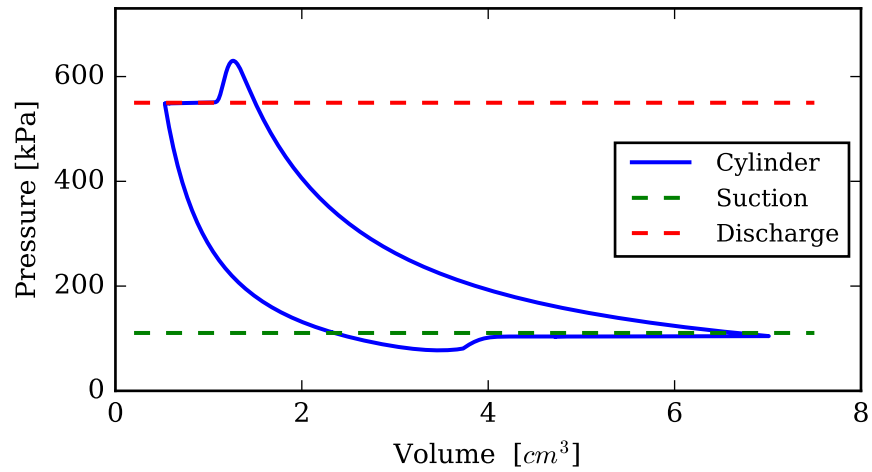
Fig. 4.16. PV Diagram at periodical steady state.

For the case shown in Figure 4.17, it takes about an hour for the compressor system to reach the steady-state temperature. Compared with the periodic-steady state results with respect to the mechanical part, it is time consuming to obtain the time history of the transient temperatures either from simulation model or experiment. As discussed in Section 2.9, the transient temperature of main elements in linear compressor can be calculated in current model by integrating the ODE shown in Equation 2.67, which is applied and coupled with the other sub-models. Besides,

it should be noted that, all thermal resistances were estimated and calculated by employing the appropriate heat transfer correlations listed in Section 2.2. These values will be updated accordingly once the thermal measurements will be available.
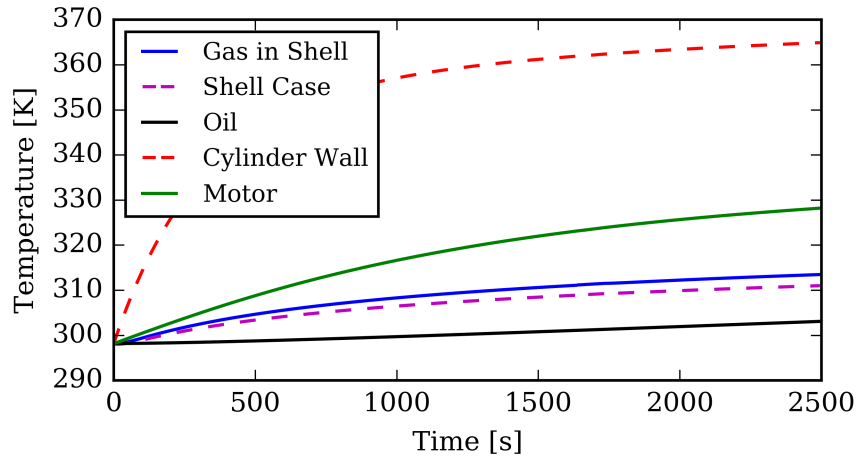
Fig. 4.17. Multi-lumped transient temperature of the main elements in linear compressor.

4.4 Overall Performance Predictions

In order to have a better understanding of the dynamic characteristics of linear compressors for the variable frequency, the proposed model was used to conduct and analyze overall performance predictions that are presented in this section.

Figure 4.18 depicts the variation of the predicted mass flow rates from the simulation model (theoretical results) as well as selected experimental data points (experimental results) for preliminary model validation. Because of preheat through the suction pipe as well as the suction passage within the piston assembly (see Figure 1.1) and the complicated leakage loss within piston clearance gap, the mass flow rates were not predicted very accurately by the model, which affects the agreement between the theoretical and experimental results. Overall, the model predicts the mass flow rate well and the effect of operating frequency. It can be observed that there is peak flow

at a frequency close to 56 Hz, which can be considered to be the resonance frequency of the piston motion.
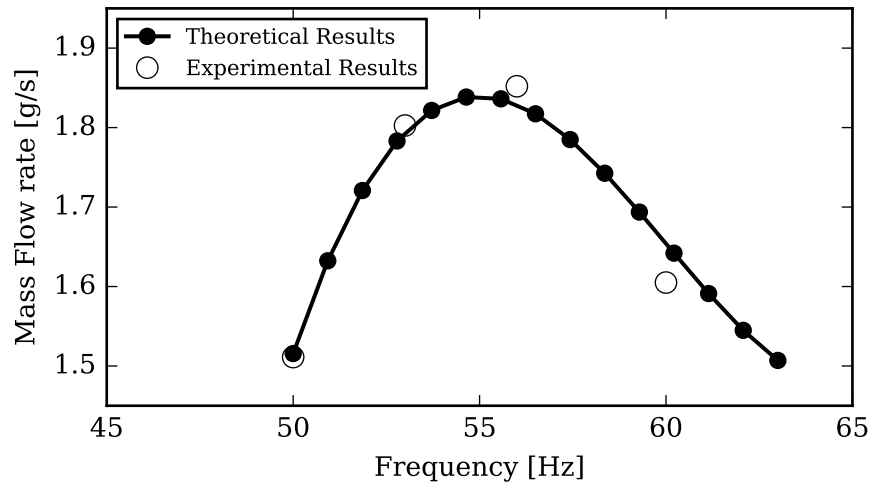
Fig. 4.18. Predicted and measured mass flow rate as a function of input frequency with pressure ratio 5.

In a positive displacement machine, the volumetric efficiency, defined in Equation 4.1, is generally used to characterize the compressor performance. As previously noted, the volumetric efficiency depends a clearance volume that can vary with operating characteristics of a variable stroke linear compressor. In a linear compressor, advanced control approaches have to be implemented to actively control the piston motion to avoid contact with the valve assembly, as it was previously mentioned in Section 2.6. Many research studies have been conducted to investigate this issue experimentally. One of the latest methods was reported by Liang et al. [38], where the clearance distance was fixed and controlled in a prototype linear compressor. However, this method may be difficult to implement when the piston stroke is long or the operating conditions are significantly different than the design operating conditions, because the clearance volume is very difficult to be fixed and controlled in a real design, especially for a larger linear compressor with longer piston stroke.

In this study, a dependent and variable clearance volume, as a function of piston stroke, has been enforced into the overall model. It is seen from Equation 4.2 that a

longer piston stroke leads to a larger clearance at a specific operating condition with respect to a predefined constant volume factor.

$$\eta_{vol} = \frac{\dot{m}}{\rho_{in}(x_s + x_{cl})f A_p} \qquad (4.1)$$

where $\dot{m}$ represents the delivered mass flow from the compressor, ρ_{in} is the density at suction condition, x_s denotes the piston stroke and A_p is the piston cross area. In particular, x_{cl} represents clearance distance between maximum piston stroke and TDC, defined as:

$$x_{cl} = F_{cl}x_s \qquad (4.2)$$

where F_{cl} is the fixed clearance volume factor.

Figure 4.19 shows the variation of the volumetric efficiency as a function of the input frequency with different pressure ratios. It is observed that smaller pressure ratio leads to a higher volumetric efficiency, similar to the performance in a conventional reciprocating compressor. However, the influence from the input frequency on the volumetric efficiency is limited and only slight decrease can be noticed from the figure with the increasing input frequency. It can be explained from the fact that the clearance volume is scaled with the stroke length, associated with variation of the mass flow rate [70] and the leakage loss is relatively small. However, it can also be predicted that the variation of mass flow rate and piston stroke may predominate on the influence of volumetric when the linear compressor is scaled up with the same numerical value of input frequency. Moreover, it is noted that due to the spring assembly in a linear compressor, the expansion work can be stored in the spring and released back to the piston during the compression process. Therefore, the overall isentropic efficiency is not low compared to the reciprocating compressor with similar geometry. However, the control approach may affect the isentropic efficiency in a linear compressor.

Figure 4.20 presents the variation of the motor efficiency as a function of input frequency. A peak occurs at an input frequency equal to the resonance frequency of
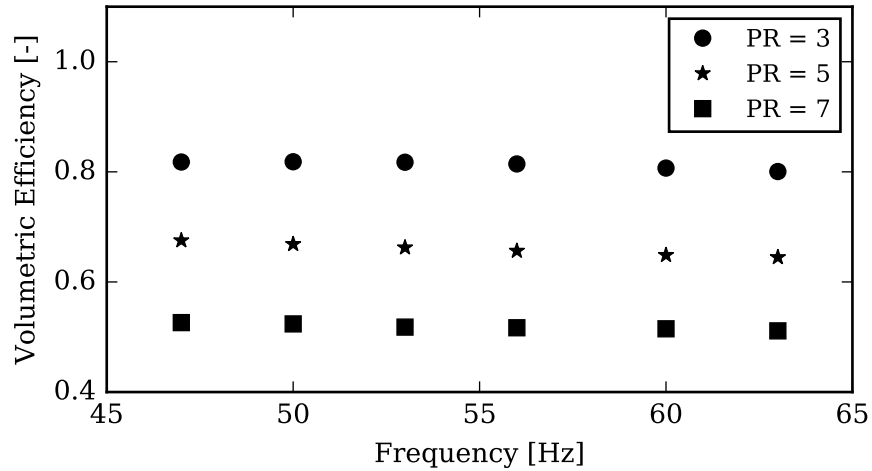
Fig. 4.19. Predicted compressor volumetric efficiency as a function of input frequency.

the system, which is very consistent with that in Figure 4.18. This operating point produces the maximum mass flow rate, and the best energy conversion ratio from electrical to mechanical energy. It is seen that the highest motor efficiency nearly 90 % at the peak and drops drastically away from the resonant frequency. It is clearly beneficial to control the compressor operation close to the resonant frequency.
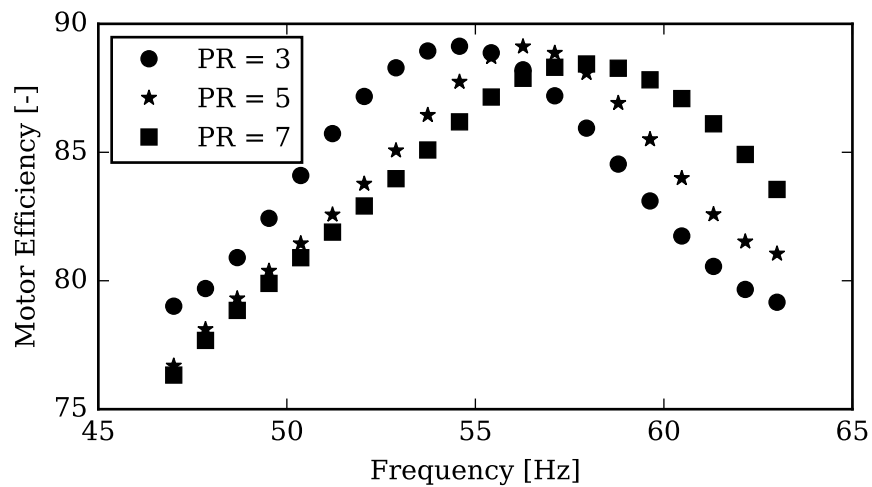
Fig. 4.20. Predicted motor efficiency as a function of input frequency.

4.5 Conclusions

The simulation results based on a commercial linear compressor have been obtained and reported in this section. A detailed validation was conducted utilizing experimental results from a commercial linear compressor for domestic refrigerators. The model predicted mass flow rate very well and the effect of operating frequency. Both transient and periodical state-state simulation results were presented and analyzed. The model demonstrated that the maximum mass flow rate and highest motor efficiency occur when the excitation frequency is at the resonance frequency of system and showed the penalties associated with operation away from resonance. A more detailed sensitivity study based on the developed model will be presented in next chapter.

5. SENSITIVITY STUDIES

The validated model was used to carry out sensitivity studies on key parameters affecting compressor performance with the goal of providing guidance for improving existing compressor designs and developing improved linear compressor designs. Only the oil-free compressor was analyzed in this section because of its greater performance potential and interest for development of future products. However, many of the conclusions from the sensitivity studies are valuable for any linear compressor design. The objectives of the sensitivity studies were to:

  (i) understand the major losses associated with leakage and friction in a linear compressor;

 (ii) develop a simulation model to analyze the characteristics of gas bearing;

(iii) investigate vibration behavior in a linear compressor and identify key factors in controlling compressor operation to achieve better performance; and

(iv) study piston eccentricity issues, which are particularly important for an oil-free linear compressor.

5.1 Leakage and Frictional Losses

Leakage and frictional losses are the two main sources of losses in a linear compressor and can have a significant effect on compressor performance. In order to study leakage and frictional losses, it is necessary to understand how cylinder pressure varies as a function of time, which can be obtained from the simulation model and four processes in a linear compressor, *i.e.*, suction, compression, discharging, and expansion. An example pressure versus time plot is shown in Figure 5.1(a) along with the suction and discharge pressure boundary conditions imposed on the compressor.

The in-cylinder pressure profile of Figure 5.1(a) and the constant shell pressure were used within a parametric study as the differential pressure force on the piston, which is a key parameter that affects losses in a linear compressor. Figure 5.1(b) shows a schematic of a linear compressor piston and cylinder assembly that depicts the location for leakage and frictional losses, *i.e.*, clearance gap (g) between the piston and cylinder wall, which is the similar to that in a conventional reciprocating compressor but without a piston ring assembly.

Figure 5.2(a) shows the gas film pressure variation as a function of time at different locations along the piston. Three locations that have been selected, *i.e.*, A, B, C, are labeled in Figure 5.1(b). By analyzing Figure 5.2(a), it can be seen that the gas film pressure at the top location (Point A) of the piston has a similar behavior as the in-cylinder pressure profile. However, the pressure at the middle location (Point B) does not fully correspond to the cylinder pressure variation and the peak value is almost half of the maximum cylinder pressure. This is most likely because there is a significant pressure drop along the piston and the pressure distribution cannot track the pressure within the compression chamber. With respect to the pressure at the end of the piston (point C), the gas pressure is approximately stable at 100 kPa, a little bit higher than the shell pressure. The gas film pressure profiles at the three locations have a more stable variation with longer piston length. Thus, it can be concluded that the pressure profile for a longer piston length has slightly less dependence on in-cylinder pressure changes, which is beneficial for reduction in leakage.

Figure 5.2(b) depicts a dynamic gas film pressure distribution along the piston length at four different times during periodic motion of the piston, 0, 0.25T, 0.5T, and 0.75T, where T is the period of the piston displacement such that the pressure profile at t = T is identical to the pressure distribution at t = 0. From Figure 5.2(b), it can be seen that except for the initial gas pressure at t = 0, which follows the in-cylinder pressure change, the gas film pressure at the other times shows a 'dome' shape, where the pressure increases along with the piston length first, then drops after a peak. The dynamic interactions are such that gas accumulates at the point

(a)

A: Piston Top
B: Piston Mid
C: Piston End

Valve **Piston**

$P_{cyl}(t)$

g $\dot{m}_{leak}$

L_p

A B C

P_{shell}

F_{fric}

TDC x BDC
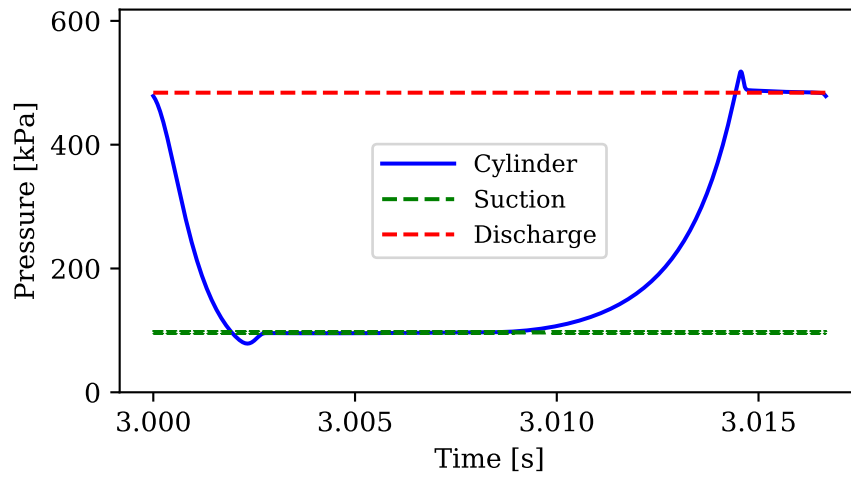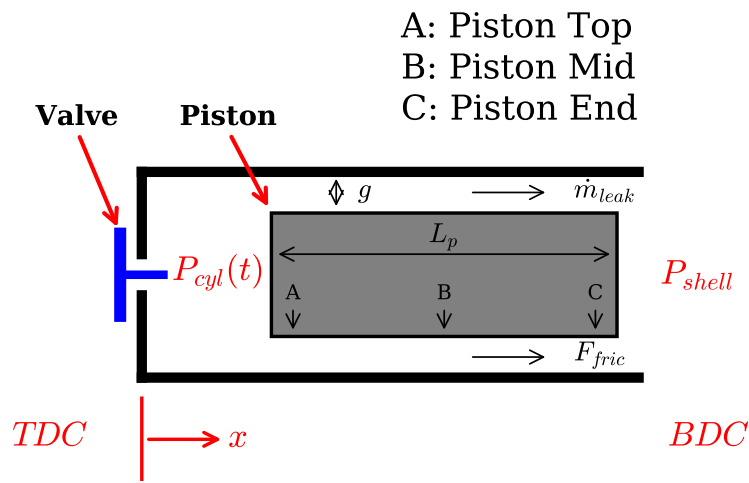
(b)

Fig. 5.1. (a) In-cylinder pressure variation profile over running time; (b) Schematic of a linear compressor piston and cylinder assembly (suction valve is not plotted).

along with leakage path where the pressure peak exists. It is also apparent that the gas pressure is higher with longer piston length.
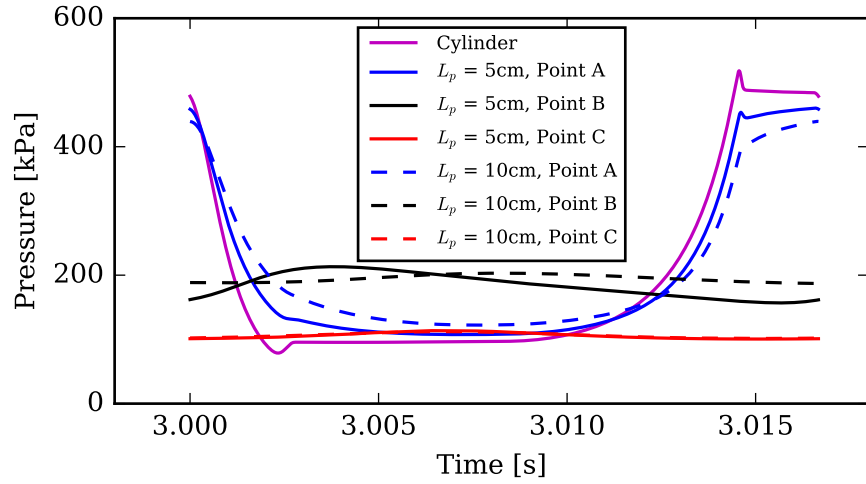
(a)
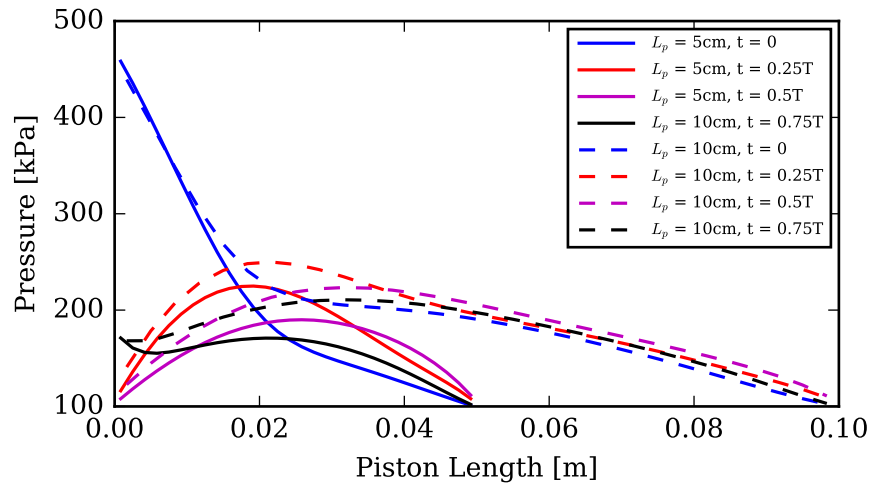
(b)

Fig. 5.2. Gas film pressure distribution in the clearance gap : (a) at different piston locations as a function of time; (b) with different piston length at different analyzed times.

After obtaining a gas film pressure profile, the leakage rate can be calculated using Equation 5.1. Integrated results for normalized leakage rate, defined as the ratio between the calculated leakage rate and a target delivery mass flow rate without the

leakage, are plotted in Figure 5.3(a) as a function of the piston length for different clearance gaps. It is seen that normalized leakage rate decreases with increasing piston length because of the greater flow resistance due to friction. If the piston length were reduced to 3 cm length, then the leakage flow would be almost half of the target flow rate. In addition to reduced overall compressor flow, this would lead to a significant energy loss associated with the need to recompress the leaked gas. In terms of the different clearance gaps, a larger gap provides more flow path area with less flow resistance leading to more leakage flow from the compression chamber to the shell. The leakage loss is minimal when the clearance gap is reduced to 2 μm. However, increasing the piston length and reducing the gap size leads to an increase in frictional losses. Thus, there is a tradeoff between leakage and friction losses with these changes that needs to be considered in determining an optimal design.

$$\dot{m}_{leak} = \int_0^T \left(\frac{\rho g^3}{12\mu} \frac{\partial P}{\partial x} + \frac{\rho g \dot{x}_p}{2} \right) \bigg|_{x=L_p} dt \tag{5.1}$$

where g is the clearance gap thickness with respect toe the piston radius, ρ is the gas density, μ is the dynamic viscosity of the gas, $\dot{x}_p(t)$ denotes piston movement velocity obtained from the linear compressor model, $\partial P/\partial x$ is the local pressure gradient, respectively.

The friction force between the cylinder and piston surface is the sum of the asperity contact force and gas viscous friction force of the gas flow. On the one hand, the viscous friction is determined by the pressure distribution within the clearance gap and the gas viscosity. On the other hand, the friction force due to the surface roughness, called the asperity contact force, depends on the relative ratio between clearance gap and surface roughness. An approach for determining the frictional loss has been reported by Zhang et al. [69]. Figure 5.3(b) shows normalized frictional loss, defined as the ratio between frictional loss and compression work, as a function of the piston length. Results using a clearance gap of 2 μm are not shown because the estimated frictional loss was unrealistically large, even higher than the total power consumption. This may be due to numerical solution problems occurring at clearance

gaps that are on the same order of surface roughness and that lead to a large asperity force that dominates the friction force. The results show a dramatic reduction in frictional loss for the larger clearance gap. In fact, the frictional loss is negligible for a clearance gap of 6 μm. In addition, frictional loss increases with piston length due to a larger frictional surface area. Overall, there is an optimal clearance gap and piston length that results from a trade-off point between leakage and frictional losses. In the analyzed case, the optimal clearance gap was determined to be 5 μm.

5.2   Gas Bearing Analysis

Linear compressor technology has received increasing attention due to its unique features. The absence of a crank mechanisms allows oil-free operation, which is highly desirable in terms of compressor design and selection of the working fluid. To achieve oil-free operation and control the trade-off between leakage flows and frictional losses in a linear compressor, Fuller [71] concluded that gas-lubricated bearings were one of the most suitable technologies. In order to investigate the characteristics and potential improvements of gas bearing designs, a number of simulation models have been developed and described in the literature. For instance, Pandian [72] proposed an accurate and reliable numerical scheme to predict pressure distributions and bearing loads within gas-lubricated slider bearings under high Reynolds numbers and reported results of parametric studies on the film-thickness ratio and the number of bearings. In 1994, a numerical study was conducted by Han et al. [73] to investigate the characteristics of externally pressurized air bearings in a rotor. The theoretical calculations were compared with experimental data and the maximum deviation was below 5%. After almost a decade, Arghir et al. [74] presented a finite-volume numerical solution of the Reynolds equation for a compressible fluid. In particular, both static and dynamic characteristics of cylindrical hydrodynamic and externally pressurized gas bearings were analyzed. Zhang et al. [75] proposed a linearized Reynolds equation applicable under the condition of small pressure variations within the gas film of a
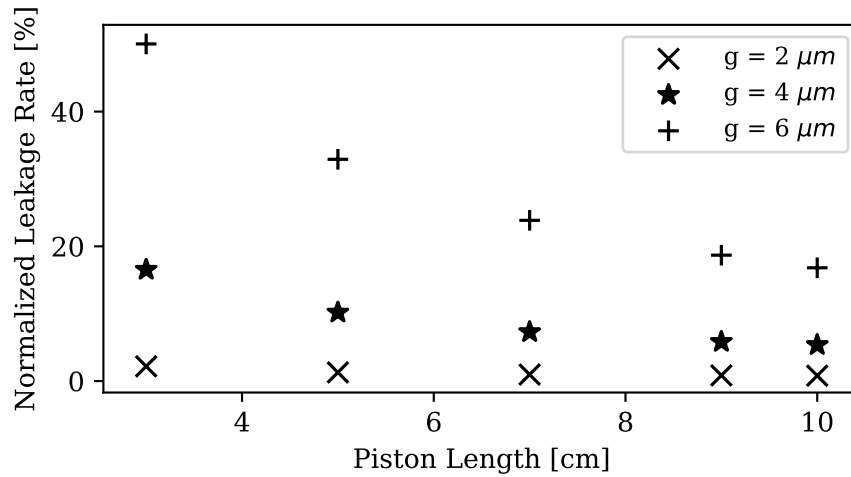
(a)
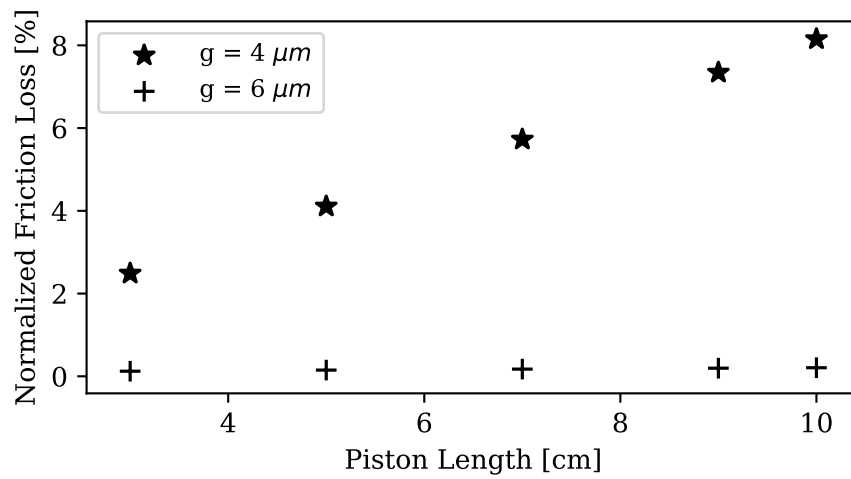
(b)

Fig. 5.3. (a) Variation of normalized leakage rate with different clearance gap as a function of piston length; (b)Variation of normalized frictional loss with different clearance gap as a function of piston length.

gas-lubricated bearing. The analysis showed that the approximating numerical solution gives an improved agreement with experimental results than the direct numerical solution and demands less computational time. It was found that eccentricity of the

piston led to significant effect on the stability of the numerical solution predicted by the model.

By surveying the literature, it can be concluded that most of the previous work focused on either gas bearings in a rotor supported by externally pressurized gas bearings or in orbiting journal bearings under rotating unbalanced forces. However, limited studies were conducted on gas bearings applied to linear motion. A few studies considered positive displacement compressors, but did not couple the fluid mechanics to the compression process.

Recently, Hulse and Prata [76] developed a 2-D numerical model to analyze a capillary compensated aerostatic bearing in a linear reciprocating compressor. However, the analysis focused on the injection hole size configuration of the gas bearings and neither the pressure distribution profile nor a detailed flow model of the injection flow were reported. In this section, a 1-D gas bearing model based on a Finite-Volume-Method (FVM) applied to a linear compressor is presented. The model considers the dynamic behavior of the pressurized gas film as well as the injection flow. The proposed model has been coupled with a detailed comprehensive linear compressor model to enable detailed analysis.

It is known that gas bearings have a number of advantages with respect to conventional liquid lubricated bearings in compressor applications [71]. First of all, the contamination caused by the typical lubricants, *e.g.*, oil, can be reduced, which eliminates refrigerant compatibility issues and enables the use of more environmentally friendly refrigerants. Secondly, the pressurized gas film can be used as a sealing method to prevent leakage from high to low pressures. Furthermore, the working fluid itself can act as a lubricant in the gap between the bearing and cylinder. The gas cushion carries the load without any contact between moving parts, which simplifies the design of the overall system and reduces costs compared to oil-lubricated compressors. Last but not the least, unlike conventional lubricants, gas bearings have more stable behavior, without issues of vaporization, cavitation, and decomposition

that can occur under severe conditions. This expands the operating conditions and life of the compressor.

Generally, gas bearings can be classified into two categories: aerostatic and aerodynamic bearings. Both types utilize a thin film of pressurized gas to avoid direct contact between surfaces in order to reduce friction, wear, and particulates within the load-bearing interface. Aerodynamic bearings create a gas cushion through the relative motion between static and moving parts, whereas aerostatic bearings rely on an external injection flow.

In this study, a hybrid bearing that combines the two aforementioned categories is considered and analyzed. The schematic of the system is shown in Figure 5.4. In particular, aerodynamic gas bearing results from the piston movement in a linear compressor, which establishes a pressurized gas film within the gap between the piston and cylinder wall surface. Due to the existence of a injection flow channel in the analyzed linear compressor, the injection pressurized gas leads to an aerostatic gas bearing. With the combination of these two types of bearings, the friction and leakage losses can be minimized, so as to improve the compressor performance.
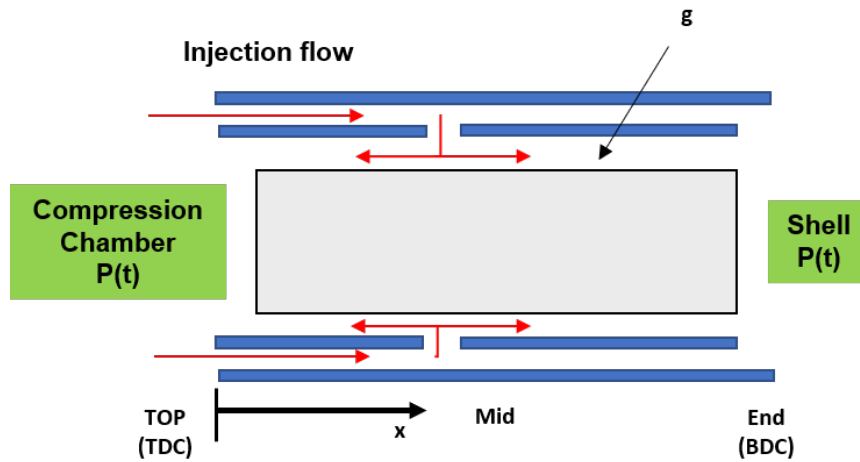
Fig. 5.4. Schematic of piston with injection flow channel in a linear compressor.

5.2.1 Pressurized gas film model

The pressurized gas flow through the clearance gap (g) between the piston and cylinder surfaces is governed by the Navier-Stokes (N-S) equations, in which inertia, body, pressure, and viscous terms are included. Based on lubrication theory proposed by Hamrock et al. [77], the gas flow condition within the clearance gap in a piston compressor is usually considered as "slow viscous motion", where the pressure and viscous terms are predominant and the full N-S equations can be simplified accordingly. The pressurized gas flow is modeled as a 1-D lubrication film with constant clearance gap, *i.e.*, no eccentricity, and the modified governing equation is given by Equation 5.2.

$$\frac{\partial}{\partial x}\left(\frac{\rho g^3}{12\mu}\frac{\partial P}{\partial x}\right) + \frac{\dot{m}_f}{A_f} = \frac{\dot{x}_p(t)}{2}\frac{\partial}{\partial x}(\rho g) + \frac{\partial}{\partial t}(\rho g) \tag{5.2}$$

where g is the clearance gap thickness with respect to the piston radius, ρ is the gas density, μ is the dynamic viscosity of the gas, $\dot{x}_p(t)$ denotes piston movement velocity obtained from the linear compressor model, $\dot{m}_{inj}$ and A_{inj} are the injection flow rate and injection port area, respectively.

The first term on the left-hand side (LHS) of the Equation 5.2 is referred to as the Poiseuille term and describes the net flow rates due to pressure gradients within the leakage path. The second term represents the injection flow rate, which produces an aerostatic bearing. The first term on the right hand side (RHS) is the Couette term representing the net entraining flow rate due to surface velocity, *i.e.*, piston velocity, for the aerodynamic bearing. The second term on the RHS denotes the transient change of the flow rate, coupled with pressure change profile, which represents the dynamic characteristics of the gas pressure distribution. In this study, the gas flow within the clearance gap is assumed to be isothermal and the fluid viscosity is treated as constant. It follows that the governing equation can be simplified by substituting the density term with the pressure term. Moreover, the dynamic pressures in the compression chamber and shell, calculated from the comprehensive linear compressor

model, are used as the boundary conditions, respectively. FVM has been applied with the discretization domain in the x direction, which is along the piston length. The pressure gradient in the domain can be determined at each time step by solving the governing equation and the gas film pressure distribution is then updated for the next time step.

5.2.2 Injection flow model

Supplying gas to the interface between moving elements of an aerostatic bearing can be accomplished in different ways: porous surface, discrete orifice injection, slot injection, and groove injection [78]. In the analyzed compressor design, the supplying pressurized gas is fed from the discharging chamber via one variable area nozzle and several small nozzles with constant areas. As show in Figure 5.5, the injection flow is modeled as a combination of an isentropic flow and a Fanno flow, where the effect of the friction is considered.
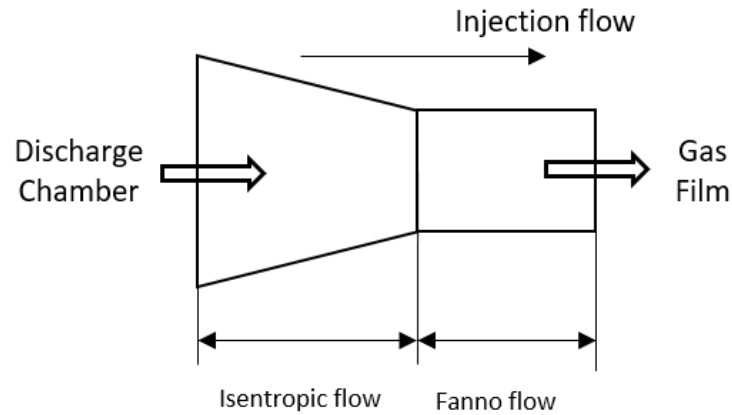
Fig. 5.5. Schematic of the flow path of the injection flow.

Isentropic flow.

An injection mass flow rate due to a pressure difference between the discharge chamber and inlet of the constant area nozzles is estimated using an isentropic flow model. The model assumes compressible flow with negligible friction and heat transfer effects. The thermodynamic parameters of the upstream condition, *i.e.*, temperature and pressure in the discharge chamber, are the inputs to this flow model. In order to compute the isentropic flow model, the local pressure ratio and the critical pressure ratio are needed and given by Equation 5.3 and Equation 5.4.

$$PR = \frac{P_{down}}{P_{up}}, \tag{5.3}$$

$$PR_{cri} = \left(\frac{2}{k+1}\right)^{k/(k-1)}, \tag{5.4}$$

where k is heat capacity ratio of the flow, subscript up means the upstream and $down$ means the downstream of the isentropic flow path.

These two pressures are compared to determine if a sonic condition exists at the exit of the flow path, *i.e.*, "choked flow", where the flow rate is maximum. The flow through the injection flow path is predicted according to two scenarios:

- Scenario I, $1 \geq PR \geq PR_{cri}$, flow is not choked and the mass flow rate is calculated by:

$$\dot{m}_{inj} = \frac{A_f P_{up}}{\sqrt{RT_{up}}} \sqrt{\frac{2k}{k-1} PR^{\frac{1}{k}} (1 - PR^{\frac{k-1}{k}})} \tag{5.5}$$

- Scenario II, $PR \leq PR_{cri}$, flow is choked and the mass flow rate is given by:

$$\dot{m}_{inj} = \frac{A_{inj} \rho_{up}}{\sqrt{kRT_{up}}} \left(1 + \frac{k-1}{2}\right)^{\frac{1+k}{2(1-k)}} \tag{5.6}$$

where subscript up denotes the parameters in upstream condition, A_{inj} are the total injection flow injection port area and R is the ideal gas constant.

Fanno flow.

The flow correlation proposed by Churchill [51] is used to determine the pressure drop associated with Fanno flow conditions due to the friction within the small injection nozzles. The expression for pressure drop is given in Equation 5.11.

$$A = \left(-2.457 \log \left[\left(\frac{7}{Re_D} \right)^{0.9} \right] \right)^{16} \tag{5.7}$$

$$B = \left[\frac{37530}{Re_D} \right]^{16} \tag{5.8}$$

$$f = 8 \left[\left(\frac{8}{Re_D} \right)^{12} + \frac{1}{(A+B)^{1.5}} \right]^{1/12} \tag{5.9}$$

where the Reynolds number is defined as:

$$Re_D = \frac{4\dot{m}_f}{\pi \mu D_f} \tag{5.10}$$

where D_f is the diameter of the injection port and $\dot{m}_f$ comes from the isentropic flow model. Finally, the pressure drop is given by:

$$\Delta P = \frac{-f G_f^2 L_p}{2 D_f} \tag{5.11}$$

where L_p is the length of the piston and the injection flow mass flux is defined as:

$$G_f = \frac{4\dot{m}_f}{\pi D_f^2} \tag{5.12}$$

5.2.3 Numerical algorithm and simulation results

The overall solution algorithm of the dynamic gas bearings simulation model is shown in Figure 5.6. Once the compressor geometry is defined and the boundary conditions are provided from the linear compressor mechanistic model, the simulation is initialized by discretizing the analyzed domain. Then, a guess value of initial gas

```
                      ┌─────────┐
                      │  Start  │
                      └─────────┘
                      ╱ Geometry ╱
                  ╱ Boundary Conditions ╱
                   ╱ Discretized Domain ╱
              ┌──────────────────────────┐
              │ Guess Initial Film Pressure│ ◄──────────┐
              │        P(x, t_start)       │            │
              └──────────────────────────┘            │
                      │ t=t_start │                    │
                          ●                            │
              ┌──────────────────┐                     │
              │ Guess Feeding Port│                    │
              │ Inlet Pressure P_f,in│                  │
              └──────────────────┘                     │
                  │ Obtain ṁ_f │                        │
              │ Feeding Pressure Drop ΔP │              │
              │ New P_f,in │                            │
   │ Update P_f,in │                                    │
                  ◇ |r_pin| < ε_pin ◇                   │
                      │ Yes                             │
              │ Feeding Flow ṁ_f │  │ Update Film Pressure│
              │ Gas Film Model │      │   P(x, t_start)    │
              │ Calculate ∂P(x,t)/∂t │                  │
   │ P(x,t+1) = P(x,t)+∂P(x,t)/∂tdt │                   │
              │ t = t + Δt │                            │
                  ◇ t ≥ t_end ◇                          │
                      │ Yes                             │
          ◇ P(x,t_start) − P(x,t_end) < ε ◇  ── No ─────┘
                      │ Yes
          │ Obtain Gas Film Pressure Profile │
                  │ Frictional Model │
                  │ Leakge Model │
                  ┌─────────┐
                  │  Stop   │
                  └─────────┘
```

Fig. 5.6. The flow chart of the gas bearing model.

film pressure is specified to begin the iterative solution process. The injection flow model is executed first to estimate the injection flow rate. The nozzle inlet pressure is solved iteratively by using the injection mass flow rate and pressure drop. By knowing the nozzle inlet pressure, the main pressurized gas film model is employed to calculate the film pressure distribution at the next time step. This procedure is repeated until the end of the working cycle. The final gas film pressure distribution is obtained when the residuals of the pressure distribution between the beginning and the end of the simulated cycle are within the convergence tolerance.

The in-cylinder pressure variation has been obtained from the compressor mechanistic model and it is shown in Figure 5.7. In particular, four main processes can be identified in a linear compressor similarly to a reciprocating compressor, *i.e.*, suction, compression, discharge, and expansion. The pressure profile determines the differential pressure force acting on the piston which is the key parameter that affects the linear compressor losses. The pressure profile reported in Figure 5.7 is used as input condition to the gas bearing model to carry on parametric studies.
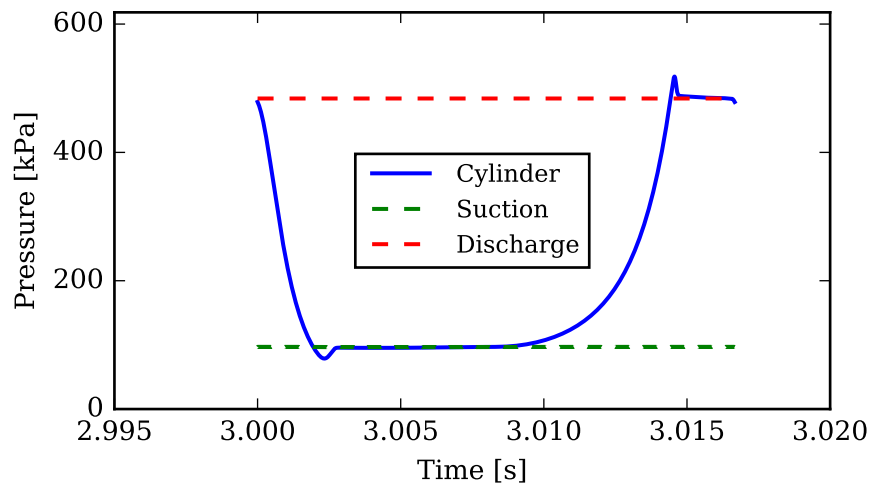
Fig. 5.7. In-cylinder pressure variation at periodical steady state.

Figure 5.8 shows the gas film pressure variation as a function of time at different locations along the piston. The three locations that have been selected, *i.e.*, top, mid, and end, are labeled in Figure 5.4. In addition, the gas film pressure distribution with

and without the gas bearing are also reported on the same figure with dashed and solid lines, respectively. By analyzing Figure 5.8, it can be seen that the gas film pressure at the top location of the piston has a similar behavior as the in-cylinder pressure profile. However, the pressure at the middle location does not fully correspond to the cylinder pressure variation and the peak value is almost half of the maximum cylinder pressure. The possible reason for this difference is that significant pressure drop exists along the piston and the distribution from the compressor chamber cannot arrive with the original pressure amplitude. With respect to the pressure at the end of the piston, the gas pressure is approximately stable at 100 kPa. It can be found that the pressure variation has been reduced significantly when the gas bearing is applied, particularly in the middle and the end of the piston. It follows that gas bearings can help to prevent the pressure propagation from the top to the end, which is beneficial in reducing leakage and friction losses.
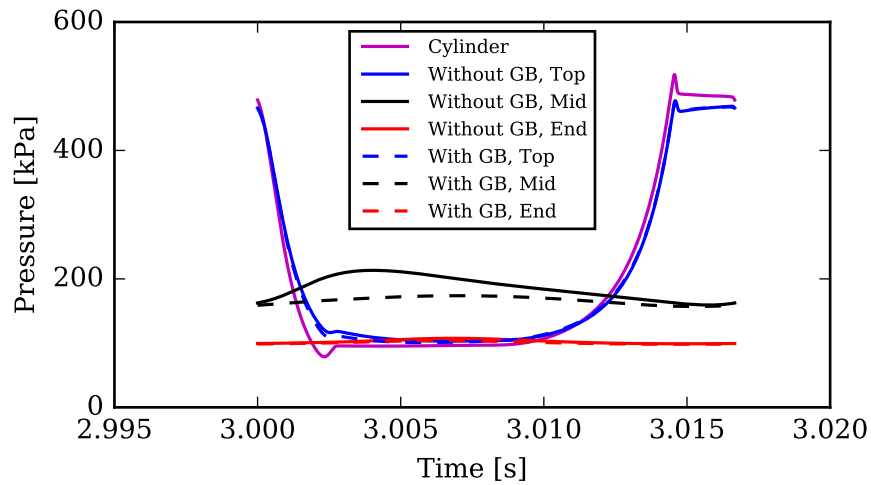
Fig. 5.8. Gas film pressure variation within the clearance gap (different piston locations) as a function of time.

Figure 5.9 depicts the gas film pressure distribution along the piston length at four time steps, 0, 0.25T, 0.5T, and 0.75T, where T is the period of the piston displacement such that pressure profile at t = T is identical to the pressure distribution at t = 0. The injection flow was injected at the 0.018 m from the piston top based on the

configuration of the analyzed compressor. From Figure 5.9, it can be seen that in the absence of the gas bearing, the gas film pressure increases and then decreases along the piston length except for t = 0. At t = 0, the fill pressure follows the in-cylinder pressure variation. This behavior can be explained by the fact that gas accumulates along the gas flow path. When the gas bearing is employed, the pressure profile is slightly lower than that without a gas bearing. Moreover, the pressure profile becomes more uniform after the injection point, whereas the pressure before the injection location follows the in-cylinder pressure variation. These results indicated that high pressurized injection gas can reduce the pressure propagation and, thus, provide a seal in the clearance gap.
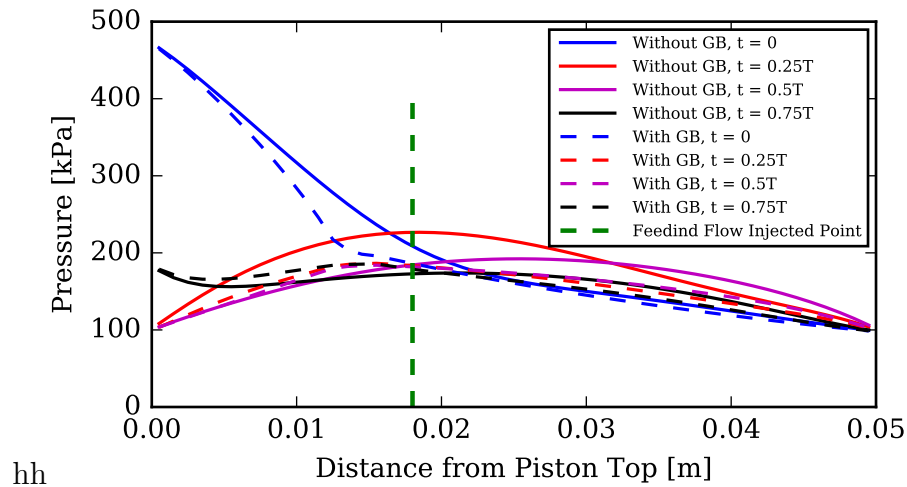
Fig. 5.9. Gas film pressure distribution along with piston location at different times.

Parametric studies were conducted to investigate the effects of the gas bearings on the leakage flow rates and frictional losses in the analyzed linear compressor. Figure 5.10 shows leakage flow rate as a percentage of the theoretical mass flow rate without leakage as a function of clearance gap and piston length for cases with and without the gas bearings. As expected, the leakage rate increases with decreasing clearance gap and decreasing piston length. Furthermore, the case with a gas bearing has a lower leakage flow rates due to lower pressure gradient. The differences in leakage

rates between the cases with and without gas bearings increase with increasing gap clearance. In order to have a better understanding of the system improvements by using gas bearings, the leakage reduction percentage between the two cases at the same operating conditions has been calculated and is also plotted in Figure 5.10. The gas bearings contribute significantly more to sealing the leakage at higher clearance gaps. For example, the leakage was reduced by about 60% when employing the gas bearing for piston length of 5 cm length and clearance gap of 6 μm.
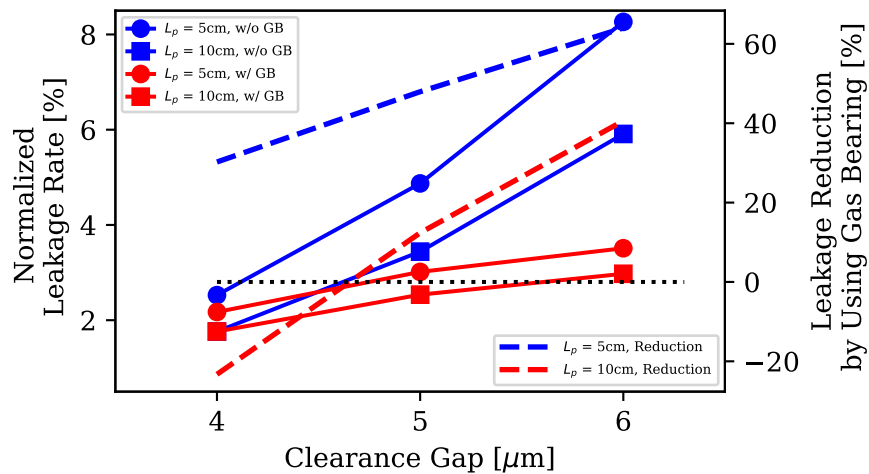
Fig. 5.10. Normalized leakage rate variation and improvements with gas bearings as a function of clearance gap.

Figure 5.11 shows the variation of frictional losses as a percentage of the compressor work input as a function of the clearance gap for the cases considered for Figure 5.10. First of all, it can be seen that the frictional losses change dramatically between a clearance gap of 4 and 5 μm. The 4 μm clearance gap is close to the surface roughness and the large asperity force dominates the friction force in this region with dramatic increasing frictional forces with decreasing gap. Furthermore, the frictional loss is negligible for clearance gaps larger than 5 μm. It is also clear that frictional losses increase with increasing piston length due to the increasing surface area. In terms of the integration of gas bearings, frictional losses are reduced due to the more uniform pressure film distribution, which dominates the viscosity force discussed in

Equation 2.41. However, the benefit is relatively small, especially as compared with the benefits for leakage.
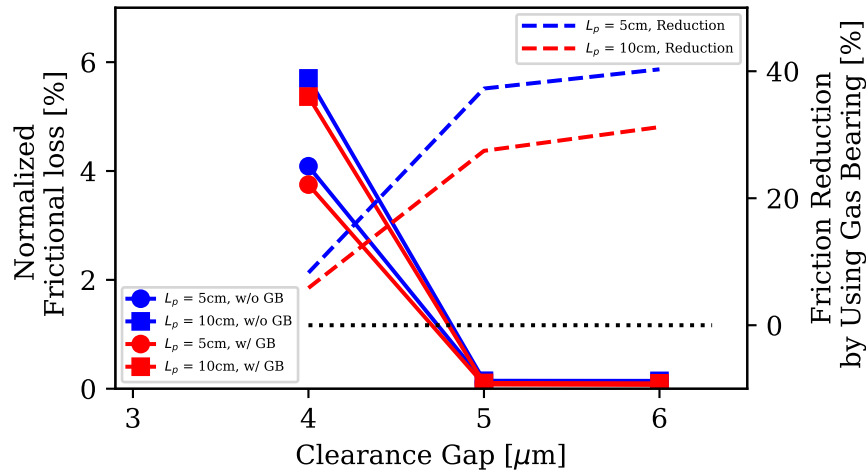
Fig. 5.11. Normalized frictional loss variation and improvements with gas bearings as a function of clearance gap.

5.3 Piston Vibration Analysis

A simplified piston stroke control model was developed in Section 2.6 to describe the dynamic piston movement in a linear compressor. However, the dynamic model does not consider vibration. During linear compressor operation, there are three important frequencies associated with the dynamic movement:

- driving frequency (Ω), generated from the linear motor;

- piston natural frequency ($\omega_{n,p}$), based on the piston, spring system, gas pressure and frictional forces; and

- system overall mechanical natural frequency ($\omega_{n,sys}$), which includes all components associated with the dynamic motion, including the piston, cylinder, shell, motor, magnet, *etc.*

The damping ratio (ζ), introduced to determine if the system is damped or un-damped, is calculated by Equation 5.13 and is a key factor for conducting the vibration analysis. Two natural frequencies, $\omega_{n,p}$ and $\omega_{n,sys}$, are defined by Equation 5.14 and Equation 5.15. The main difference between the two natural frequencies is related to the different equivalent masses and spring stiffnesses.

$$\zeta = \frac{c}{2\sqrt{k_s m_{eff}}} \tag{5.13}$$

$$\omega_{n,p} = \sqrt{\frac{k_{s,p}}{m_{eff,p}}} \tag{5.14}$$

$$\omega_{n,sys} = \sqrt{\frac{k_{s,sys}}{m_{eff,sys}}} \tag{5.15}$$

where k represents the equivalent spring stiffness, c denotes the system damping ratio, m is the effective mass.

In order to identify the best motor operating point, the input driving frequency, denoted as Ω, should operate at or close to the piston natural frequency ($\omega_{n,p}$). Operating the piston at or close to its resonant frequency maximizes the energy conversion from motor power output to fluid power input. The system overall natural frequency ($\omega_{n,sys}$) differs from the piston natural frequency ($\omega_{n,p}$) because of other elements inside the system. It is not favorable to drive the overall system close to its system overall natural frequency ($\omega_{n,sys}$) as it will bring very strong vibration and noise issues.

The transmissibility function $Tr(\Omega)$, proposed by Rao and Yap [79], is defined as the ratio between the transmitted force and input driving force. A mathematical function and graphical representation are presented in Equation 5.16 and Figure 5.12, respectively. This metric can be used for linear compressor vibration analysis, since the transmissibility relates the vibration response from a driving force in terms of the ratio between the driving and natural frequencies, and the natural frequency could be for the piston or system.

$$Tr(\Omega) = \frac{\sqrt{1 + (2\zeta\Omega/\omega_n)^2}}{\sqrt{[1 - \Omega/\omega_n)^2]^2 + (2\zeta\Omega/\omega_n)^2}} \tag{5.16}$$
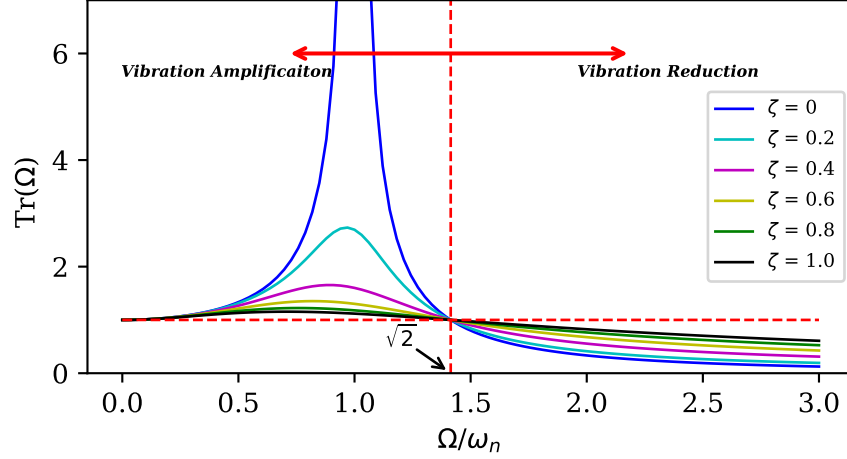
Fig. 5.12. Amplitude transmissibility function with different driving frequencies.

It is observed that when the excitation frequencies are small compared to the natural frequency, $i.e.,\Omega/\omega_n \ll 1$, the transmissibility function tends to unity regardless of the damping ratio. Furthermore, when the ratio becomes large, $i.e.,$ $\Omega/\omega_n \gg 1$, $Tr(\Omega)$ approaches zero. The maximum value of $Tr(\Omega)$ can be noted near $\Omega/\omega_n = 1$ and this maximum value decreases with increasing damping ratio ζ. In addition, there is a critical point, $\Omega/\omega_n = \sqrt{2}$, that divides the curve into two areas with the left section termed "vibration amplification" and the right section denoting "vibration reduction". In the left region, $Tr(\Omega)$ is always larger than unity and increases with decreasing damping ratio, whereas in the right section the opposite behavior occurs where $Tr(\Omega)$ drops with decreasing damping ratio and is always below unity.

The control and adjustment of input driving frequency should be based on the vibration characteristics of transmissibility in a linear compressor. With respect to the piston movement, it is favorable to control the ratio $\Omega/\omega_{n,p}$ close to 1 where the maximum piston stroke can be achieved. At the same time, it is also important to

keep $Tr(\Omega)$ below a prescribed value in terms of the overall system $\omega_{m,sys}$ to reduce vibration and noise.

The overall system natural frequency ($\omega_{n,sys}$) generally can be controlled easily by a using a soft suspension spring and maintaining a reasonable weight of the overall compressor unit. Thus, it is possible to operate in the vibration reduction region except when the compressor speed is extremely low. However, it can be challenging to control the vibration of the piston since the piston natural frequency ($\omega_{n,p}$) varies with operating conditions because of the varying gas pressure force (gas spring) and therefore the transmissibility will change with driving frequency. Therefore, it is necessary to conduct a preliminary model calculation to estimate the range of the piston natural frequencies when designing a linear compressor. In general, a strong mechanical spring is recommended to avoid the influence of in-cylinder pressure variation on the piston natural frequency in order to limit the variation of the transmissibility with different conditions. It is also beneficial to control the damping ratio (ζ) by adjusting the suspension system to achieve a target operating condition.

5.4 Piston Eccentricity Analysis

It has been reported by Liang [80] that an oil-free linear compressor will have higher leakage losses when there is an eccentricity between the piston and cylinder wall. There are two factors considered in this section that generally affect compressor eccentricity issues: spring assembly and piston rod elasticity.

Figure 5.13 shows two common compressor spring configurations used in a linear compressor. As illustrated in Figure 5.13a, the use of a single spring results in an eccentric spring force applied to the piston that inherently leads to spring eccentricity associated with the piston movement, as previously modeled by Bradshaw et al. [13]. If the rotating angle of the piston is large and the piston vertical displacement, estimated from Equation 5.17, is larger than the clearance gap, a metal contact

between the piston and cylinder will exist during compressor operation that will result in significant frictional losses and could potentially lead to compressor failure.

$$\epsilon_p = \theta_p * L_p \tag{5.17}$$

where ϵ_p denotes the piston displacement in vertical direction, also called piston eccentricity, θ_p represents the rotating angle due to the eccentric spring force and L_P is the piston length.

As a remedy, multiple springs can be used to provide the necessary spring force while minimizing the eccentricity. As shown in Figure 5.13b, multiple springs can balance the eccentricity forces if located such that there is an equal distance between the spring acting points and the center of the piston body. An individual spring in a multiple group will be smaller and softer than a single one in order to maintain the same required spring force. Moreover, a flexure (also called spiral disc) spring results in a more symmetric force on the piston body and is a good solution for avoiding eccentricity when a single spring is employed.
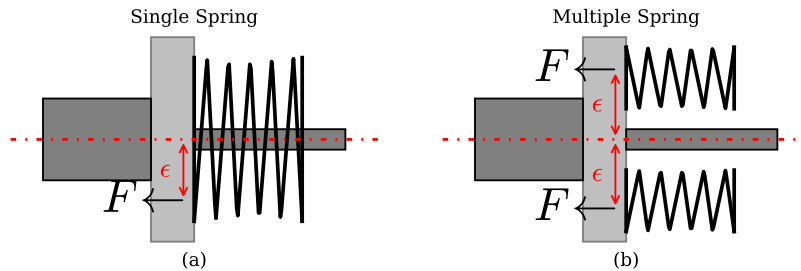
Fig. 5.13. Two type of compression spring configurations in a linear compressor: (a) single spring; (b) multiple spring.

In addition to spring configuration, piston rod elasticity can influence eccentricity. Flexural oscillations of a piston and piston rod system have been analyzed for a conventional reciprocating compressor by Graunke and Ronnert [81] and their approach can be used to analyze the piston oscillation in a linear compressor by removing the effects of the crank mechanism and cross head. Figure 5.14(a) depicts the dynamic

variation of piston relative eccentricity, defined as the ratio of the absolute piston eccentricity to the clearance gap, as a function of piston mass and rod length. Relative eccentricity tends to increase with increasing piston mass and rod length. However, a lighter piston and shorter piston rod have more oscillations but with smaller amplitude. Figure 5.14(b) shows the same results as Figure 5.14(a) but presents more details about the relationship between piston eccentricity and piston movement. Higher piston eccentricity occurs as the piston approaches Top Dead Center (TDC), where a high-pressure force is applied to the piston body as an excitation force in the piston oscillation. Piston eccentricity due to rod elasticity is more significant during the discharge than the suction process. To this end, it can be concluded that a shorter piston rod and lighter piston are preferred. In particular, a hollow piston body and tubular linear motor are one of the solutions to achieve this goal.
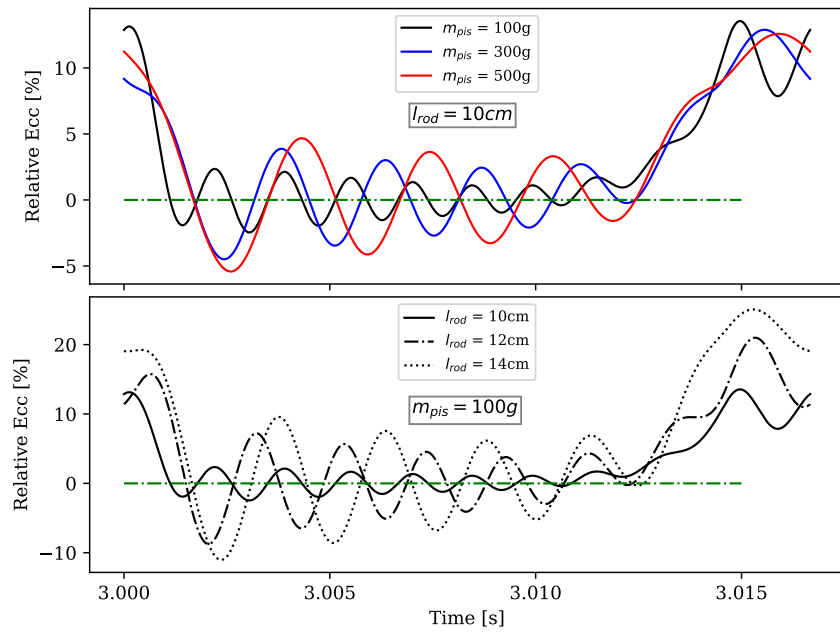
(a)
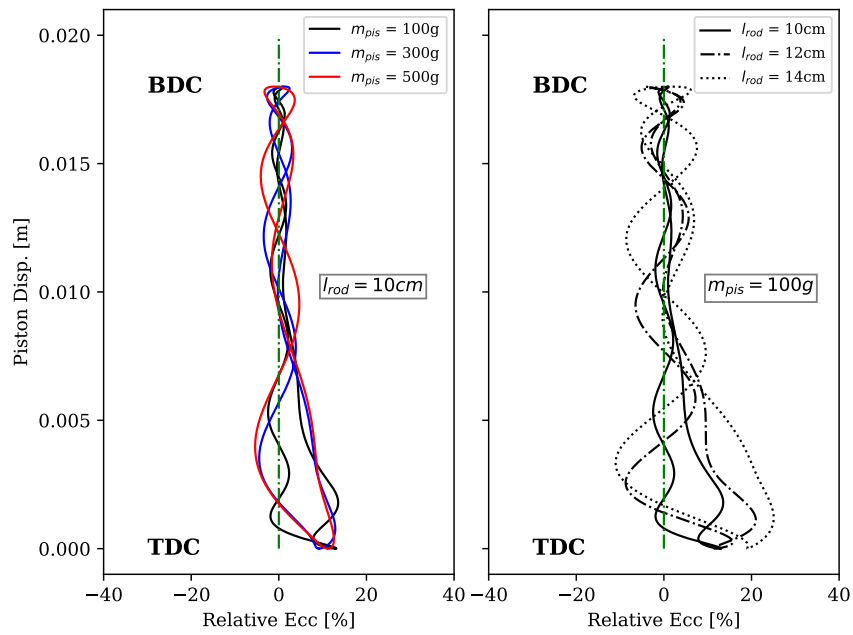
(b)

Fig. 5.14. (a) Relative piston eccentricity as a function of time with different piston mass and piston rod length; (b) Relative piston eccentricity as a function of piston stroke with different piston mass and piston rod length.

The design clearance gap between the piston and cylinder wall should be adjusted based on estimates of the piston eccentricity and is a function of the piston radius angle. It can be seen in Figure 5.15 that the piston is shifted from an original position to a new position with eccentricity ϵ. Then, based on the geometry and eccentricity, Equation 5.18 can be used to calculate the gap distance explicitly as a function of radius angle. This gap distribution could be used to more accurately determine leakage and frictional losses. However, this effect was not included in the model of this paper and will be part of future work.

$$h(\theta, t) = -R + \sqrt{\epsilon(t)^2 + (R + g)^2 - 2\epsilon(t)(R + g)cos(\gamma - \theta)} \qquad (5.18)$$

where g represents the designed constant clearance gap and h is the variable clearance gap as a function of radius angle θ and R is the radius of the piston, $\epsilon(t)$ is the piston eccentricity as a function of time and γ denotes the angle between the eccentricity and x axis.
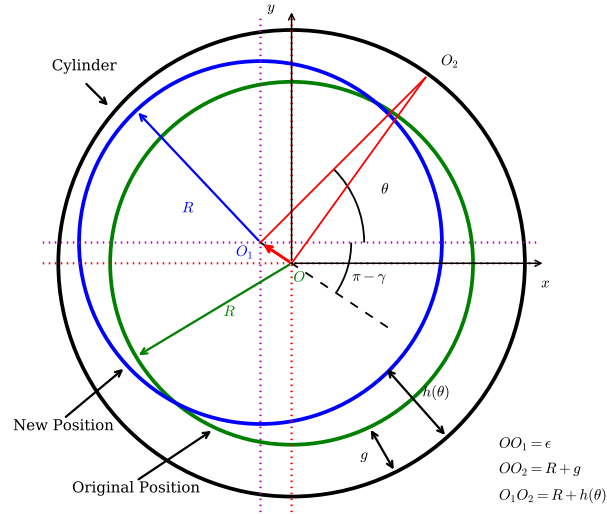
Fig. 5.15. Top view of cylinder and piston assembly with eccentricity in a linear compressor.

5.5 Conclusion

In this section, a comprehensive sensitivity study based on the validated simulation model was carried out, which was used to gain a better understanding of the behavior of linear compressors. Several conclusions can be drawn from the different analyses conducted in this work:

- A longer piston and smaller clearance gap are helpful in reducing leakage in an oil-free linear compressor but will increase frictional loss between the piston and cylinder wall. An optimal clearance gap and piston length has been determined using the model based on tradeoffs between leakage and frictional losses. For an oil-free linear compressor, a high-pressure gas bearing is one potential solution for reducing the leakage while limiting frictional losses.

- Based on the developed 1-D FEM simulation model, it can be found that gas bearings have a significant effect on reducing leakage flows, but a relatively small effect on reducing frictional losses. The benefits of gas bearings for sealing leakage compared to no gas bearings increase with larger clearance gaps between the piston and cylinder walls. Since frictional losses decrease dramatically with increasing leakage gap clearance, the use of gas bearings can enable the use of larger gap sizes where frictional losses are negligible. Moreover, the utilization of gas bearings can prevent pressure propagation from the piston top to the end and the pressure distribution is more uniform after the injection point.

- A vibration analysis should be conducted when designing and operating a linear compressor. For optimal compressor performance, the driving operating frequency should be close to the piston resonance frequency to have an amplified movement but should avoid the system mechanical natural frequency to limit mechanical vibration and noise. To this end, control and adjustment of the excitation frequency is important along with a good suspension system.

- Piston eccentricity is a significant issue in a linear compressor, particularly for oil-free linear compressors. To minimize the effects, the spring assembly should be carefully selected and installed to limit eccentric forces on the piston. Additionally, minimizing the piston mass and rod length can limit piston eccentricity due to rod elasticity.

6. VAPOR INJECTION WITH PISTON COOLING AND SCALABILITY ANALYSIS

This chapter describes a further analysis by using the proposed linear compressor simulation model considering the system level and design aspects. The objective of this study is two-fold: (i) investigate and characterize the performance of vapor injection technology with piston cooling from a theoretical analysis. (ii) identify the limitations of scale-up linear compressors by conducting a scalability analysis.

Vapor injection technology is of great interest, both academically and industrially, and it is interesting to numerically investigate the utilization of this approach in a linear compressor. In addition, the potential improvements from a system level perspective are also investigated (See Section 6.1). Challenges arise from the fact that it is relatively difficult to integrate an injection flow path within a typical linear compressor design. Therefore, several piston-cylinder concept designs are proposed and demonstrated to achieve the goal of absorbing the heat of compression as well as vapor injection (See Section 6.2). Generally, linear compressors are mainly implemented into small-scale refrigeration systems. However, it is interesting to explore the scalability of the linear compressor technology. To this end, a 14kW (4-ton) heat pump system (See Section 6.3.1) and a 45 kW air compressor (See Section 6.3.2) are used as examples of the analysis of scalability, which manifests the limitations of a scale-up linear compressor with respect to performance stability. The last section in this chapter is structured in a way that provides a detailed guidance of how to design/select each component for a prototype linear compressor (See Section 6.4).

6.1 Linear Compressor Vapor Injection and Regeneration

Compressor performance is often referenced to one of three ideal reference processes: adiabatic, polytropic, and isothermal. These different reference processes have been extensively investigated and compared [82]. It is well known that an adiabatic and reversible (isentropic) compression process requires more work input than an isothermal and reversible compression process for the same suction conditions and discharge pressure. As shown in Figure 6.1, the variation of total work on air is a function of polytropic index, where the process is isothermal when index is 1. It can be seen that when index is 1.4, the amount of heat transfer is zero, which is called as isentropic process. By comparing the three reference compression processes, the results show that isentropic compression requires the most work input and the isothermal compression consumes the least of work. In the isothermal process, the energy is removed from the system as heat at the same rate that it is added by the mechanical work of compression. In comparison to the other two processes, an isothermal process requires significant cooling.
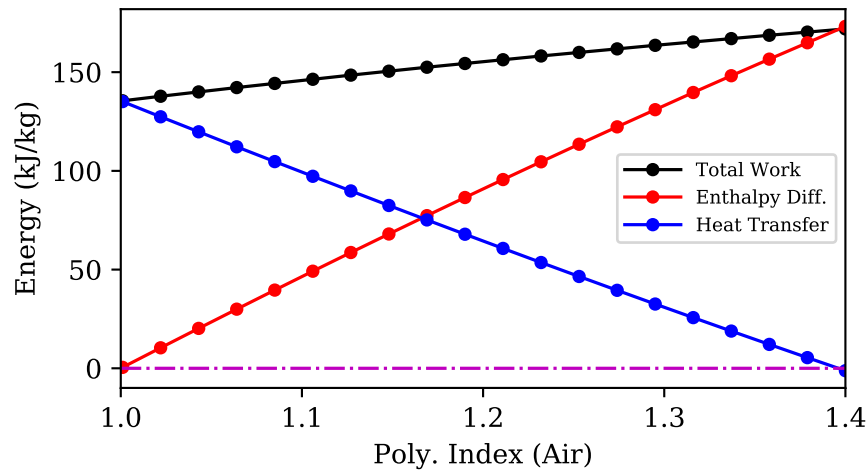
Fig. 6.1. Energy and polytropic index diagram comparing isentropic, polytropic, and isothermal compression processes.

However, in order to establish an isothermal process, the heat generated during the compression process must be removed from the system at the same rate that it is added by the mechanical work of compression. Isothermal compression processes are extremely difficult to achieve due to the fact that two opposing effects need to be balanced. On the one hand, the isothermal compression process needs to occur in small confined volumes at very high speeds in order to achieve high efficiencies. On the other hand, the heat transfer process needs to take place over large surfaces at very slow velocities to achieve high effectiveness. As a consequence, isothermal compression has not been approached in a real application. In the literature, different approaches have been investigated to approach an isothermal compression process. For instance, the use of multi-stage compression with inter-cooling could be used to remove the compression heat. However, this approach results in complex systems with high manufacturing costs. Heidari et al. [83] designed, manufactured, and analyzed a finned piston compressor and an equivalent electric analogy was used to simulate the transient heat transfer process inside the compressor. The results showed that the temperature rise during compression decreased by 33% in the proposed design compared to a conventional process. Penazzo [84] proposed an aqueous foam liquid compressor. In particular, a large heat transfer area as well as a high heat transfer coefficient were achieved with such design. It was reported that the proposed design reduced the discharged temperature approximately by 15 °C and improved the compressor efficiency by 4 to 8%. The challenging part of the aforementioned novel compressor designs are the high manufacturing and maintenance costs. In addition, the selection of the working fluids and the scale of application are also limited. Other popular techniques to achieve a quasi-isothermal compression process are fluid injection during the compression process and liquid-flooded compression. The injected fluid can be superheated, two-phase, or subcooled refrigerant. The most common fluid to flood the compression process is a lubrication oil. A detailed comparison of four different vapor compression cycle (VCC) performances using refrigerant injection was conducted by Heo et al. [85] by utilizing the combination of a sub-cooler and flash

tank. It was experimentally observed that the cycle configuration slightly improved the system capacity, but the system COP did not change significantly. Shuxue and Guoyuan [86] characterized the performance of a heat pump coupled with economized vapor injection. In this study, the optimal injection location and the injection ratio were discussed in-depth, and the system performance was improved by approximately 4%. Bell et al. [87] investigated the feasibility of achieving a quasi-isothermal compression by employing oil-flooding. The proposed cycle configuration included an internal regenerator. The theoretical and experimental analyses resulted in cycle efficiency improvements between 5% and 20% depending on the operating conditions. By surveying the literature, it is apparent that most of the researchers focused on scroll and screw-type compressors due to their favorable designs that allow an easier integration of the injection ports and their suitability for flooded compression. However, limited work was found related to vapor injected linear compressors. In this section, a novel cylinder cooling design in a linear compressor and its evaluation when integrated within a VCC are presented. A thermodynamic system model was developed in order to conduct parametric studies, which were further used to identify the key parameters and compare the designed system with a conventional VCC.

6.1.1   Vapor injection cycle with piston cooling

The absence of a crank mechanisms in a linear compressor allows for oil-free operation, which is possible to eliminate refrigerant compatibility issues and open up more options for environmentally-friendly working fluids. Besides, the appropriate working fluids can be selected to operate at higher temperatures and pressures. Due to its compactness and scalability, the linear compressor is an appealing technology for domestic and miniature-scale refrigeration systems, which have space constraints. The reduction of space occupied by the compressor enables of the use of additional components or modification in alternative system configurations that can improve overall efficiency for space-constrained systems.

The schematic of the proposed system architecture is shown in Figure 6.2. Two distinct system features can be noted: (1) a regenerator transfers heat from the liquid refrigerant exiting the condenser to the compressor suction line to ensure high superheat at the compressor inlet; (2) two-phase refrigerant at an intermediate pressure is injected into compressor cooling paths to enable a quasi-isothermal compression process. In this configuration, the sub-cooled refrigerant, exiting the condenser at state point 5 is divided into two flow paths, *i.e.*, injection line and evaporation line. The flow in the injection line is throttled to an intermediate pressure at state point 6 and passes through piston cylinder cooling paths absorbing the heat from the compression chamber to a superheated injected vapor at state point 7, also shown in Figure 6.3(a). The injected flow and the compressed vapor, already inside the compression chamber at state point 2, are mixed and compressed together from state point 3 to state point 4. On the other hand, the liquid to evaporator line enters the regenerator and exchanges heat with the refrigerant vapor exiting from the evaporator. Then, the liquid refrigerant with higher subcooling at state point 8 is throttled and passes through the evaporator to state point 10.

Figure 6.3 shows the cylinder-piston assembly that includes cooling paths and cylinder injection. The coolant inlet is the two-phase refrigerant that has been throttled from the liquid line to an intermediate pressure between condensing and evaporating pressures (state 6 in Figure 6.3). The coolant passes through cooling paths around the compressor chamber to absorb the heat from compression process, as shown in Figure 6.3(a), and is evaporated to a superheated vapor at the exit. The coolant flow can be controlled to maintain a desired exit superheat by a thermal expansion valve within the cycle. With the help of the connecting pipe (not shown in the schematic), the superheated vapor at state point 7 is injected into the compression chamber through the cylinder wall, as indicated in Figure 6.3(b). The timing of the vapor injection process is determined by the location of the reciprocating piston. For example, when the piston is at location A in Figure 6.3(b), the chamber pressure is below the intermediate injection pressure and the injection flow will be pushed into
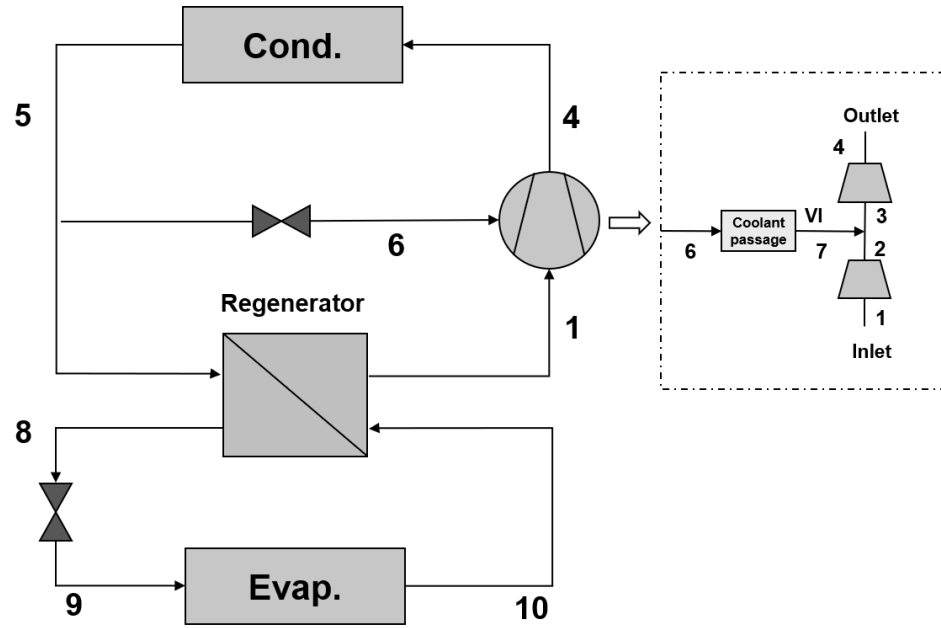
Fig. 6.2. Schematic of an integrated vapor injection and piston-cylinder cooling system.

the compressor chamber. However, if the piston moves over the injection port, *e.g.*, location B, the injection port will be blocked by the piston wall and there is no further vapor injection until the next cycle. However, some back-flow from compression chamber to the injection line could occur due to the differential pressure, and it may result in a small amount of internal leakage in the compressor. Therefore, the location of the vapor injection port should be chosen wisely.

The state points of the aforementioned thermodynamic cycle are shown in P-h and T-s diagrams in Figure 6.4. In particular, different solid line colors indicate different flow paths, and the dash black lines represent the thermodynamic process of a conventional VCC having the same compressor efficiency. It can be seen in Figure 6.5 that the compressor inlet temperature in the new design (point 1) is significantly higher than that of the conventional cycle, which is due to the use of the regenerator to achieve high superheat. The injection flow at the intermediate pressure is mixed
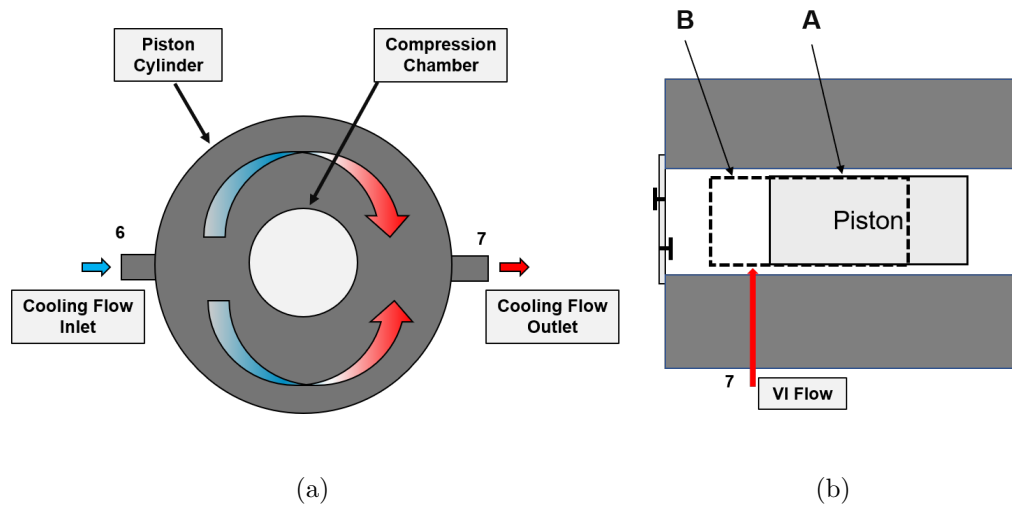
Fig. 6.3. Proposed piston-cylinder cooling assembly: (a) top view of the piston cylinder integrated with cooling paths; (b) side view of the piston with vapor injection port.

with compressed gas from state point 2 and then compressed together to state point 4 with lower discharge temperature compared to the conventional cycle.

6.1.2   Cycle modeling method and simulation results

A thermodynamic cycle model has been developed and was used to analyze the proposed system and predict its performance in comparison to the baseline system. For the baseline system, it is similar to that of standard vapor compression system with constant isentropic efficiency for compressor. As previously outlined, the primary differences between the baseline and proposed system are the vapor injection line, the regenerator, and the cylinder cooling design.

The compression process in the proposed system is modeled as a two-stage compression process with intercooling due to the injection process at the intermediate pressure. Since there is significant heat transfer during compression process, instead
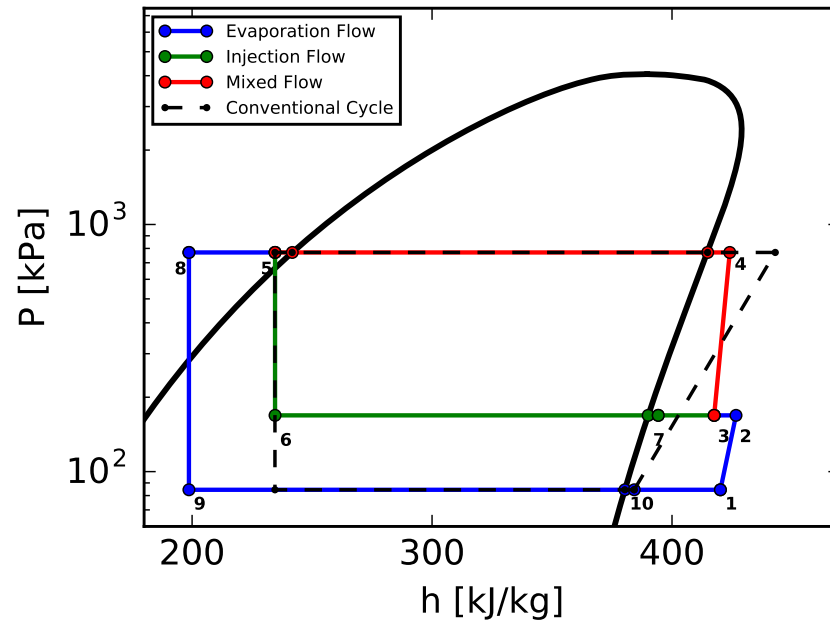
Fig. 6.4. P-h diagram for vapor injection cycle system with cylinder cooling design.
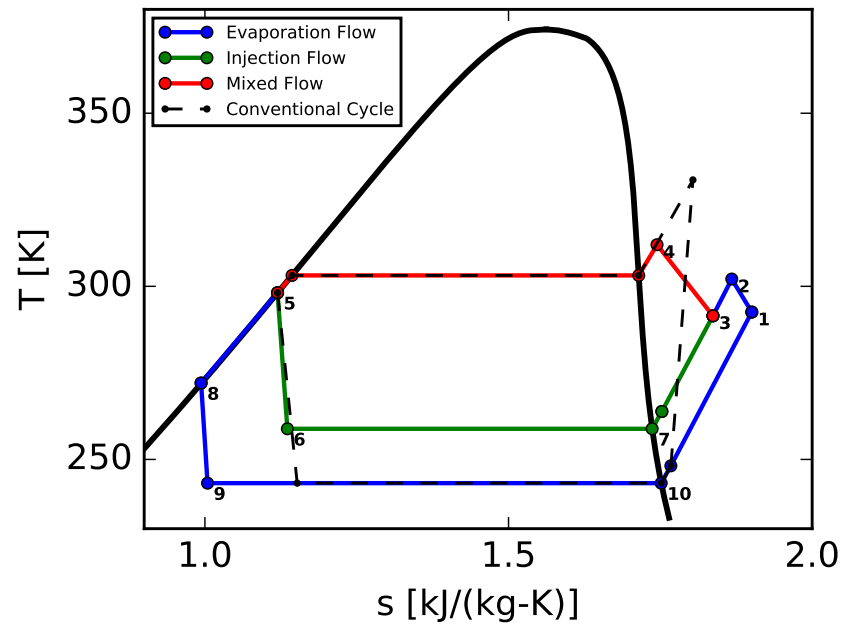
Fig. 6.5. T-s diagram for vapor injection cycle system with cylinder cooling design.

of using isentropic efficiency, polytropic efficiency is used to evaluate compressor performance, which is obtained from Equation 6.1.

$$\eta_{\mathrm{p}} = \frac{w_{\mathrm{p}}}{w_{\mathrm{ac}}} \tag{6.1}$$

where w_{ac} represents the actual work for the compression process and the polytropic work, w_{p}, is defined to quantify the work required for a reversible polytropic process occurring between the actual compressor inlet and outlet states with heat transfer, defined by Equation 6.2.

$$w_{\mathrm{p}} = P_{\mathrm{suc}} v_{\mathrm{suc}} \frac{n}{n-1} \left[\left(\frac{P_{dis}}{P_{suc}} \right)^{(n-1)/n} - 1 \right] \tag{6.2}$$

where P and v denote the pressure and specific volume, respectively; n is the polytropic index calculated by:

$$n = \frac{\ln\left(\frac{P_{\mathrm{dis}}}{P_{\mathrm{suc}}}\right)}{\ln\left(\frac{v_{\mathrm{suc}}}{v_{\mathrm{dis}}}\right)} \tag{6.3}$$

Once the actual work is obtained, compressor discharge state can be determined iteratively based on the first Law of Thermodynamics, which is shown in Equation 6.4:

$$w_{\mathrm{ac}} = q + (h_{\mathrm{dis}} - h_{\mathrm{suc}}) \tag{6.4}$$

where h denotes the specific enthalpy and the subscript dis and suc represent the exit and inlet of compressor, respectively.

Note that the cylinder cooling effects are considered in the proposed simulation model with a constant cylinder wall temperature, which is directly coupled to the heat transfer surface area. The instantaneous heat transfer process between cylinder wall and compression chamber is similar to that in a conventional reciprocating compressor. The heat transfer coefficient is determined by using the correlation proposed by Adair et al. [61] given by Equation 6.5.

$$\text{Nu} = \frac{\text{h}_\text{c}\text{D}_\text{p}}{\text{k}} = 0.053\text{Re}^{0.8}\text{Pr}^{0.6} \tag{6.5}$$

$$\dot{Q} = h_c L_\text{ht} x_p (T(t) - T_w(t)) \tag{6.6}$$

where h_c is the convective heat transfer coefficient, Dp is the diameter of the piston, k represents the thermal conductivity of the working fluid. $T(t)$ and T_w denotes the transient chamber vapor and cylinder wall temperature, respective and the wall temperature is determined by the coolant flow temperature. In particular, it is also worth pointing out that L_ht is defined as the wetted length for the piston, which allows for not only the cylindrical shape of the piston but other geometries, such as hollow concentric band and bean-shape piston.

The cylinder wall temperature and the in-cylinder heat transfer during the cooling process are significantly affected by the intermediate pressure (and the corresponding intermediate temperature) associated with State 6 on Figure 6.2. The detailed linear compressor model was used to analyze the relationship between the heat transfer from compression chamber with a constant wall temperature and the power consumption. In addition, the effect of different wetted length is also investigated. As shown in Figure 6.6, two processes, *i.e.*, before and after vapor injection (VI) process, are analyzed and it is observed that they have very different trends. In terms of the heat transfer before VI process, the ratio between heat loss and power consumption, defined as heat to work (HTW), decreases with the increasing of intermediate pressure ratio. In fact, the smaller intermediate pressure ratio indicates a lower cylinder wall temperature, resulting in a larger temperature difference, i.e. heat transfer rate, between the compression chamber and cylinder wall. When the intermediate pressure as well as the cylinder wall temperature (the corresponding intermediate temperature) increases, the heat transfer process for cylinder cooling is attenuated. Moreover, a larger pressure ratio yields more power consumption for the compression process, which also causes a drop of the HTW ratio.
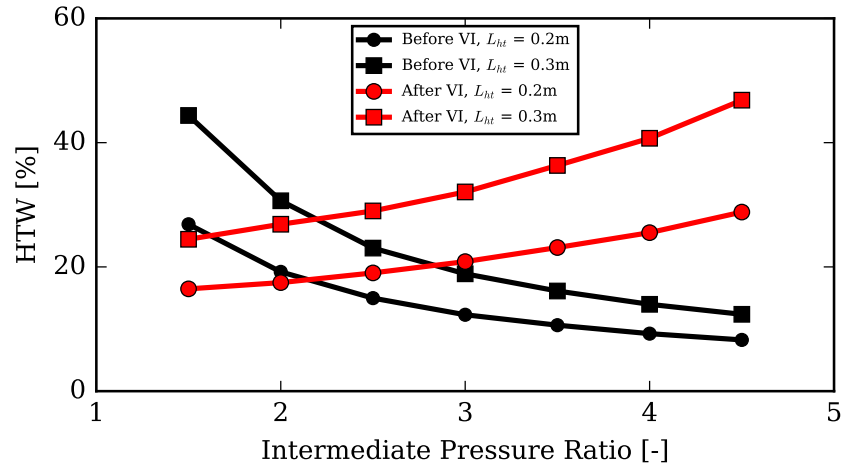
Fig. 6.6. HTW Ratio of as a function of intermediate pressure.

However, in terms of the compression process after VI, it is observed that the HTW ratio increases with increasing intermediate pressure ratio. This behavior can be explained by the following reasons. First of all, the temperature of compression chamber after VI is much higher than that in the process before VI, and the temperature difference for heat transfer is always very large such that heat loss is the dominant factor for the HTW ratio, although the cylinder wall temperature rises with the increase of the intermediate pressure ratio. Secondly, with the increasing of the intermediate pressure ratio, the pressure ratio for the second stage of the compression process after VI will be reduced accordingly, which also limits the increase of the power consumption. To this end, higher intermediate pressure ratios lead to a larger HTW ratios for the second stage of compression process. Moreover, it can also be seen from Figure 6.6 that longer wetted length of the piston results in higher HTW ratios since more heat transfer area is available. Based on the discussion above, the energy balance Equation 6.4 can be modified to Equation 6.7, which expedites the calculation of the cylinder cooling to determine the exit temperature for a polytropic compression process in the system model.

$$w(1 - HTW) = (h_{\text{dis}} - h_{\text{suc}}) \tag{6.7}$$

The VI mixing process between the injected flow and compressed flow is modeled by imposing a mixture energy balance and calculating the resulting mixture temperature, which is determined by:

$$\dot{m}_{\text{VI}} h_7 + \dot{m}_{\text{evap}} h_2 = \dot{m}_{\text{tot}} h_3 \tag{6.8}$$

where $\dot{m}_{\text{VI}}$, $\dot{m}_{\text{evap}}$, $\dot{m}_{\text{tot}}$ represent the mass flow rate from VI line, evaporation line and total mixed mass flow rate, respectively and h denotes the specific enthalpy of state point shown in Figure 6.2.

A simplified regenerator model with a constant effectiveness, given by Equation 6.10, is used to model the heat exchange process between the compressor suction line and liquid line after the condenser. In particular, the largest enthalpy change from the regenerator is chosen as the minimum enthalpy difference in Equation 6.9. As long as the enthalpy change within the regenerator has been obtained, the inlet conditions to evaporator and compressor are determined from Equation 6.11 and Equation 6.12.

$$\Delta h_{\text{reg,max}} = \min \begin{cases} h_5 - h(T_{10}, P_5) \\ h(T_5, P_{10}) - h_{10} \end{cases} \tag{6.9}$$

$$\eta_{\text{reg}} = \frac{\Delta h_{\text{reg}}}{\Delta h_{\text{reg,max}}} \tag{6.10}$$

$$h_8 = h_5 - \Delta h_{\text{reg}} \tag{6.11}$$

$$h_1 = h_{10} + \Delta h_{\text{reg}} \tag{6.12}$$

where all the state points are coherent with Figure 6.2.

It is also worth pointing out that a cylinder cooling efficiency is used to represent the heat transfer ratio between heat rejection from the compression chamber and heat absorption to the two-phase flow inside the coolant passage. The in-cylinder compression process is modeled as a two-stage compression process with intercooling due

to the injection process at the intermediate pressure. The cylinder wall temperature and therefore, the in-cylinder heat transfer during the cooling process is significantly affected by the intermediate pressure (and the corresponding intermediate temperature). Other components, including condenser, evaporator, throttling valve, are modeled with the similar approach to the conventional VCC system. Therefore, the proposed simulation system model described above was employed to investigate the system performance. The inputs to the model are listed in Table 6.1.

Table 6.1.
List of inputs used for the system simulation model.

Description	Parameter	Proposed Sys.	Baseline Sys.	Unit
Working Fluid	-	R134a	R134a	-
Evaporating Temperature	T_{evap}	-30	-30	°C
Condensing Temperature	T_{cond}	30	30	°C
Superheat Temperature	ΔT_{sup}	5	5	°C
Subcooling Temperature	ΔT_{sub}	10	10	°C
Compressor Efficiency	η_{com}	0.8	0.8	-
Cylinder Cooling Efficiency	$\eta_{hx,cyl}$	0.85	-	-
Regenerator Efficiency	ϵ_{re}	0.8	-	-
Intermediate Pressure Ratio	PR_{int}	2.5	-	-

Figure 6.7 and Figure 6.8 depict different injection processes at different intermediate pressures ratios. It can be seen that a smaller intermediate pressure ratio results in lower cylinder wall temperatures, which results in more heat removal from the compression chamber as a larger temperature difference exists for the in-cylinder heat transfer. In addition, larger cooling capacities can be obtained at lower intermediate pressures for the cylinder cooling, which is determined by the enthalpy change between state points 10 and 8. Therefore, with the decrease of the intermediate pressure ratio from 4.5 to 1.5, the compressor discharge temperatures decrease accordingly (state points 4c, 4b, 4a), which makes the overall two-stage compression process (1

to 4) closer to a quasi-isothermal process. For that reason, the polytropic index n approaches unity (isothermal process), which leads to a decrease in reversible polytropic and actual specific work. However, a lower intermediate pressure also leads higher bypass flow to the compressor and reduced refrigerant flow through the evaporator. Thus, there is an optimum intermediate pressure.
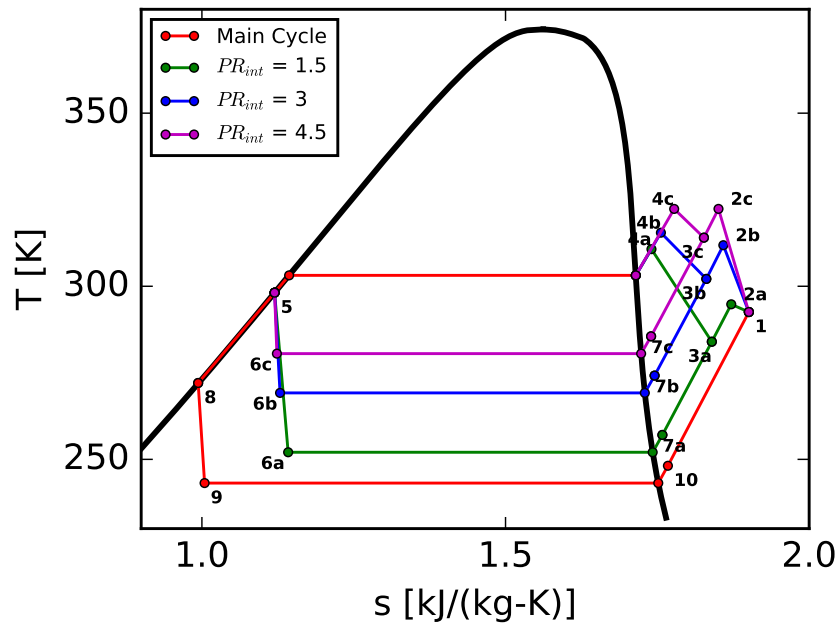
Fig. 6.7. T-s diagram of vapor injection cylinder cooling system with difference pressure ratios.

Figure 6.9 depicts the variation of the compressor temperature rise as a function of different intermediate pressure ratios for three different values of the regenerator efficiency. As previously discussed, decreasing intermediate pressure leads to a reduced temperature rise due to a lower coolant temperature. Moreover, it is also observed that a higher regenerator efficiency leads to a lower temperature rise since a higher inlet temperature allows for larger temperature difference for in-cylinder heat transfer.

However, the refrigerant flow to the evaporator decreases with increasing flow to the compressor as the intermediate pressure is reduced. This leads to a reduction in
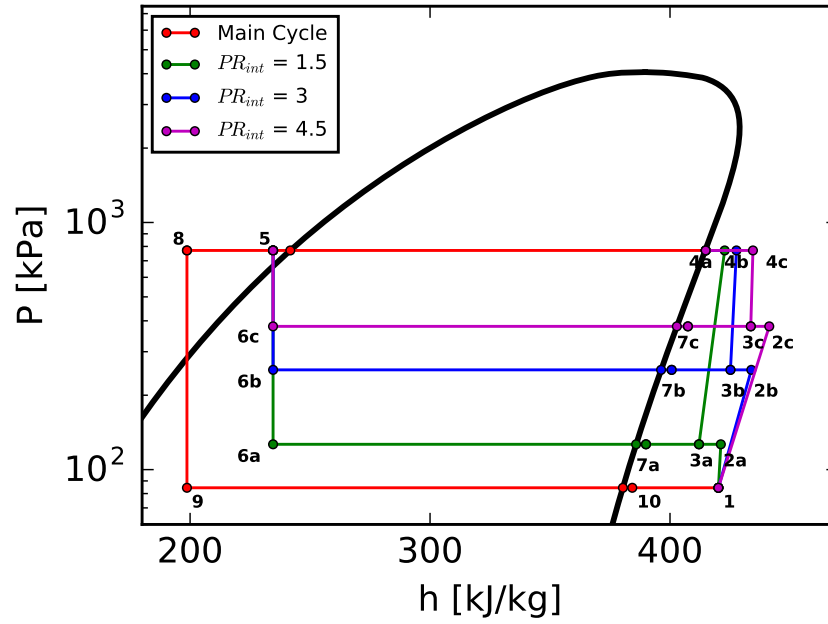
Fig. 6.8. P-h diagram of vapor injection cylinder cooling system with difference pressure ratios.
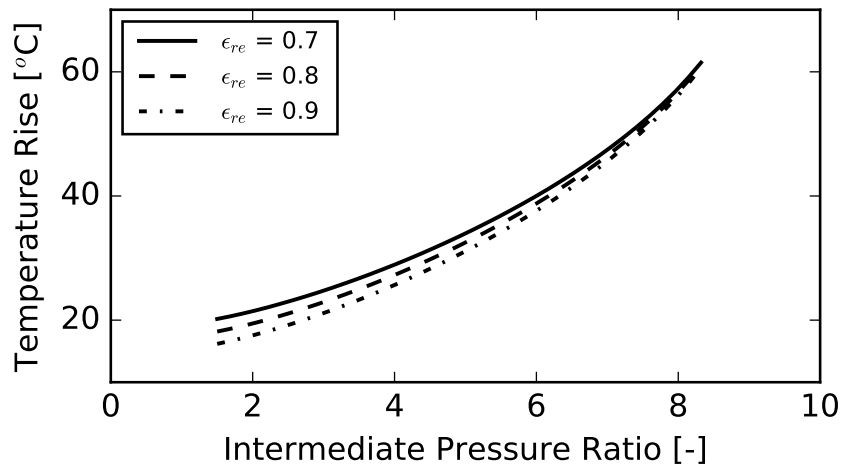
Fig. 6.9. Compressor temperature rise versus intermediate pressure ratio for different regenerator efficiencies.

system cooling capacity which counters the positive effect of reduced compressor specific work. Therefore, there is an optimal intermediate pressure for the best system

performance, which is very similar to a standard multiple-stage compression process. Figure 6.10 shows system COP as a function of intermediate pressure ratio for different regenerator efficiencies. The optimum intermediate pressure ratio is between about 5 and 6 for this case. COP increases with regenerator efficiency, but it has an insignificant effect on the optimum intermediate pressure that maximizes COP.
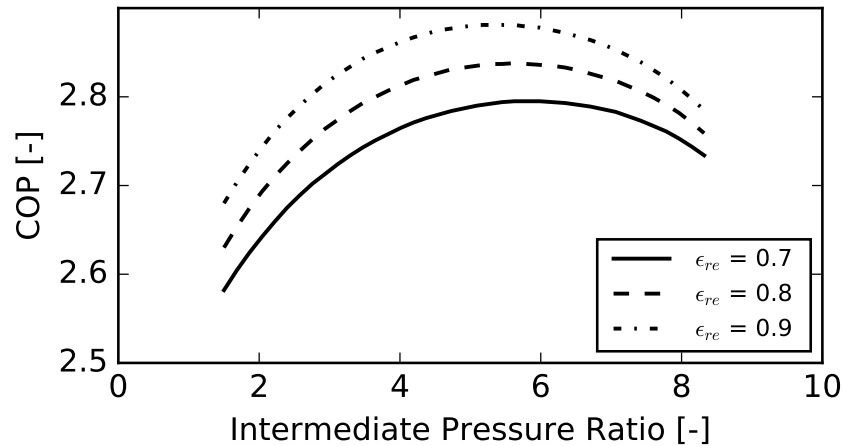
Fig. 6.10. System COP versus intermediate pressure ratio for different regenerator efficiencies.

To further investigate the benefits of the designed cylinder cooling and vapor injection system with respect to the conventional vapor compression system, the simulation model is exercised to account for different operating conditions. To ensure a consistent comparison, all selected operating conditions are imposed to both cycle architectures, and the COP improvements from the conventional cycle is used as the parameter to identify the differences. Additionally, some of the common working fluids are selected to quantify the effect of working fluid selection on the system performance. It is shown in Figure 6.11 that the designed system has higher COPs than that of the conventional vapor compression system for all four selected refrigerants. In particular, an improvement can be found with the use of refrigerant R1234yf operating at lower evaporating temperatures because the proposed system can reduce the desuperheating loss, which is a predominant loss in the conventional vapor com-

pression system when the evaporating temperature drops for a constant condenser temperature.
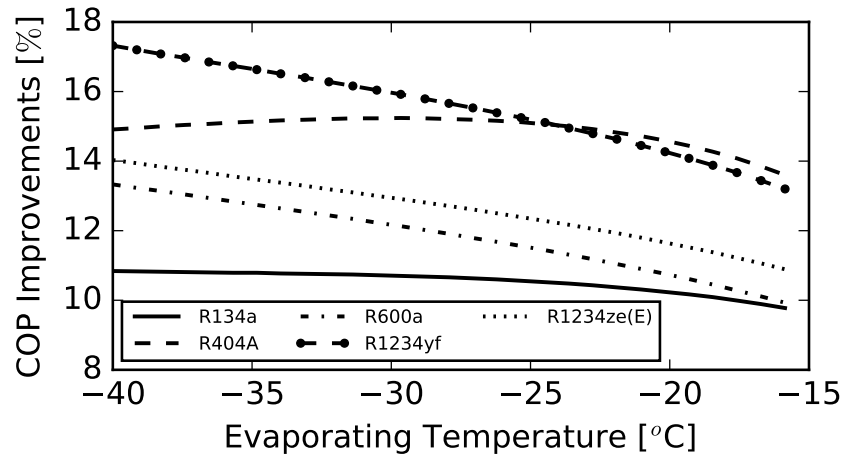
Fig. 6.11. COP improvements from a conventional VCR cycle versus evaporating temperature for different working fluids.

6.1.3   Conclusion

A new concept of an oil-free linear compressor with piston/cylinder cooling, vapor injection, and regeneration has been presented in this section. The performance of this technology was assessed for a number of different refrigerants and operating conditions using a system simulation model. Several conclusions can be drawn from the results as follows:

- The proposed system design can significantly reduce the compressor temperature rise compared to a conventional system, but the temperature rise depends on the intermediate pressure
- There is an optimum intermediate pressure for cylinder cooling and vapor injection in terms of achieving the best overall system COP.

- Although overall system performance is strongly dependent on the regenerator effectiveness, the optimum intermediate pressure is relatively insensitive to the regenerator effectiveness.

- The proposed system showed between 10% and 18% improvements in performance compared to the conventional system. The greatest improvements occurred with R1234yf as the working fluid, especially at larger temperature lifts.

6.2   Isothermal Piston-cylinder Concept Design

As is discussed in last section, isothermal compression processes are extremely difficult to achieve due to the fact that two opposing processes have to be satisfied. One of these processes is the compression process, which needs to occur in small confined volumes at very high speeds in order to achieve high efficiencies. The other process is a heat transfer process, which needs to occur over large surfaces at very slow velocities to achieve high effectiveness. Therefore, perfect isothermal compression has not been attainable in current commercially available compressors. It has been theoretically proved in last section that one way to approach isothermal compression is to add more heat exchange surfaces to the piston, which are challenging to be created and manufactured using conventional manufacturing techniques. However, these limitations may be overcome with the help of 3-D printing. Therefore, it is an objective of this proposed work to come up with some core piston-cylinder designs in linear compressors with heat exchange surface as large as possible by adding internal cooling paths. Once the designs are finalized, the core elements will be 3-D metal printed by the Advanced Manufacturing Group at Oak Ridge National Lab and the printed elements will be assembled into working linear compressor prototypes.

6.2.1   Preliminary piston-cylinder designs

Based on the proposed comprehensive linear compressor model as well as the general VRC system model, four concept designs will be discussed in the preceding

section. All designs have the same suction volume for a consistent comparison. For the sake of clarity, these designs are named as follows and all designed parameters are list in Table 6.2:

- Design A: one-piston design (baseline design)

- Design B: cylinder and center cooling

- Design C: three-pistons

- Design D: bean-shape pistons

Table 6.2.
List of parameters for each piston-cylinder concept design.

Design No.	Name	Outer Diameter	Wetted Perimeter
-	-	[m]	[m]
A	One-piston	0.025	0.079
B	Center-cooling	0.026	0.096
C	Three-piston	0.030	0.136
D	Bean-shape	0.035	0.264

Design A: baseline one-piston design

Figure 6.12 and Figure 6.13 show a schematic drawing and section view of Design A. Design A includes three main assemblies: piston, cylinder and valve set. Similar to the commercial LG linear compressor, the suction valve has been placed inside the piston and the discharge plate valve has been placed across the entire cylinder head. With this design, the suction gas travels from the shell of the compressor into the suction muffler, and then into the center of the piston. The gas pushes the suction
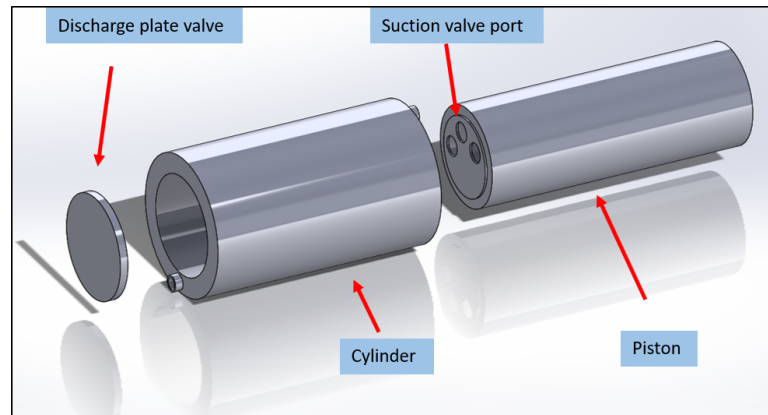
Fig. 6.12. Schematic drawing of isothermal core elements of compressor in Design A.
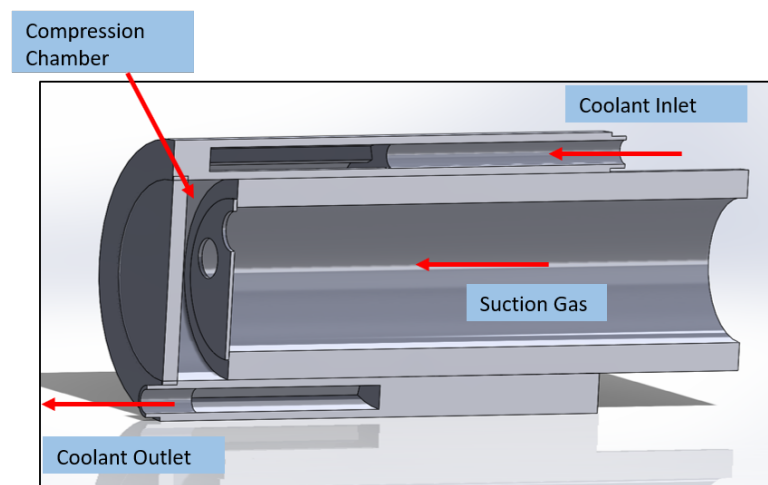
Fig. 6.13. Section view of isothermal core elements of compressor in Design A.

reed valve inside the piston on the piston down stroke and fills up the compression chamber with suction gas.

Instead of using solid cylinder walls, a cooling path has been added inside the cylinder walls with the coolant ports at the top and bottom of the cylinder, as shown in Figure 6.14. The coolant will be pumped into the cooling path inside the cylinder wall, which includes several parallel fins in order to increase the heat exchange surface and enhance the heat transfer process, as shown in Figure 6.15. The added cooling

path helps to approach an isothermal compression process. Since it is similar to the configuration of the commercial LG linear compressor, Design A will be treated as the baseline design in this study for comparison with the other three designs.
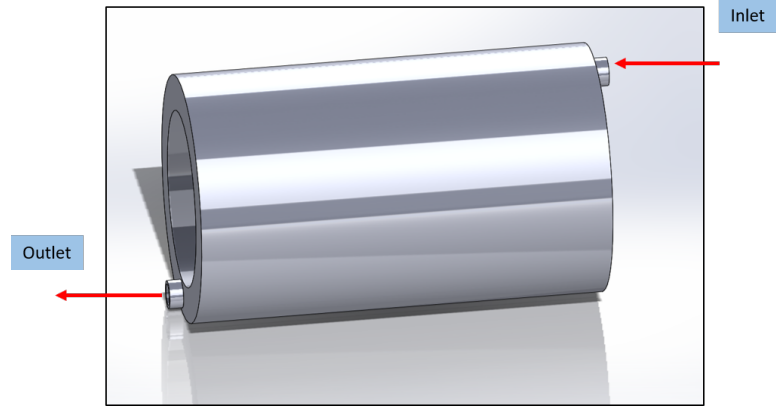
Fig. 6.14. Side view of cylinder assembly in Design A with internal cooling path.
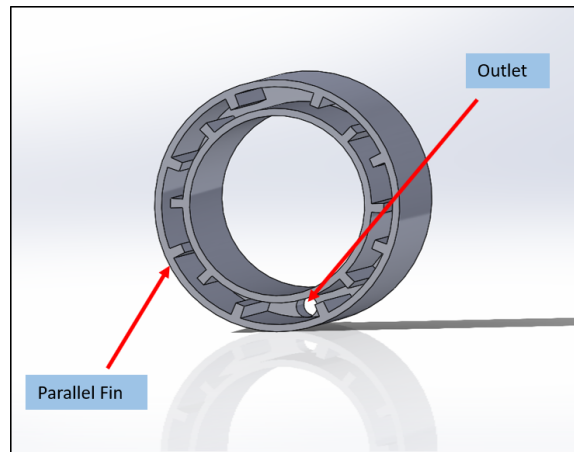
Fig. 6.15. Section view of cylinder assembly in Design A with internal cooling path.

Design B: cylinder and center cooling

Figure 6.16 shows a schematic drawing of Design B. Similar to the Design A, there are three main assemblies: piston, cylinder and valve set. However, instead of placing

the suction valve inside the piston, both suction valve and discharge valve have been installed on the same side across the cylinder head. By doing so, two cooling paths have been included in Design B. The first one is identical to the cooling path of Design A (see Figure 6.15). In addition, a second cooling pipe passes through the center of the entire piston with the coolant entering from one end and leaving from another end, as illustrated in Figure 6.17. It follows that a tubular-like compression chamber is created by the cylinder walls, piston, valve plate and center cooling pipe. Therefore, the gas inside compression chamber is cooled down by both the cylinder wall with internal cooling paths as well as by the center cooling pipe. With the combination of cooling paths inside cylinder wall and center cooling pipe, Design B is expected to show better performance compared to the baseline Design A. However, the eccentricity issue and leakage gap due to the center cooling pipe should be taken into account in this design.
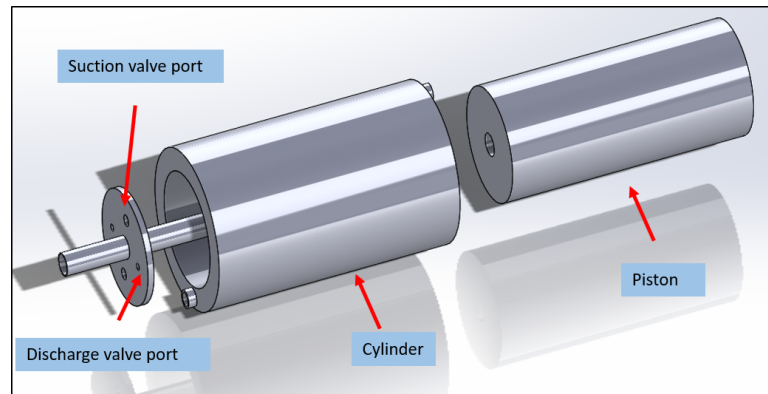
Fig. 6.16. Schematic drawing of isothermal core elements of compressor in Design B.

Design C: three-piston

A simple way to further increase the heat transfer surface area of the working chamber is to increase the area of the piston in contact with the cooling path. In Design C, the single piston assembly adopted in Design A and B has been replaced
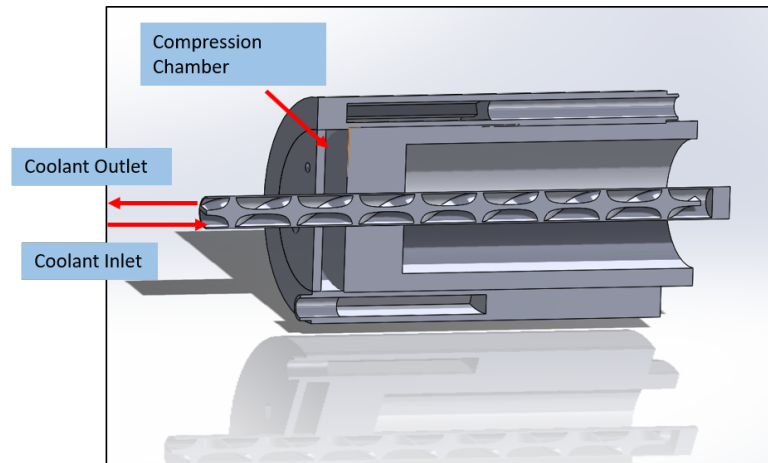
Fig. 6.17. Section view of isothermal core elements of compressor in Design B.

by three smaller pistons with three corresponding compression chambers inside the main cylinder assembly, as shown in Figure 6.18. Similar to Design B, both suction and discharge valves have been placed on the same side at the top of the cylinder with multiple valve ports.
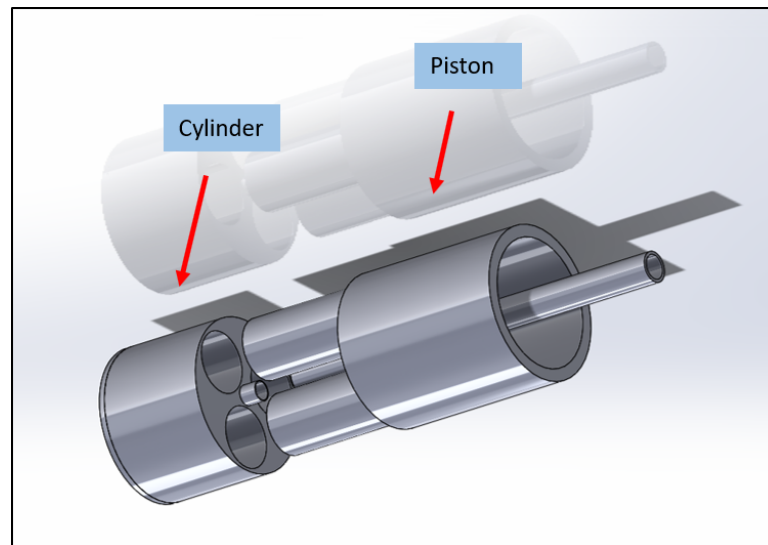
Fig. 6.18. Schematic drawing of isothermal core elements of compressor in Design C.

By referring to Figure 6.20, a special cylinder assembly has been designed with one common coolant inlet and one common coolant outlet. The total coolant flow enters through the cooling tube and is distributed among the three cooling chambers. Inside each cooling chamber, several baffles have been added to direct flow as well as increase the heat exchange surface area. At the end of the cooling chambers, the coolant flows are mixed together and leave the compressor core from the common outlet. To keep the displacement constant among all designs, the diameter of the cylinder in Design C would be larger than that of baseline Design A. The larger heat exchange surface area should result in an improved isothermal compression process.
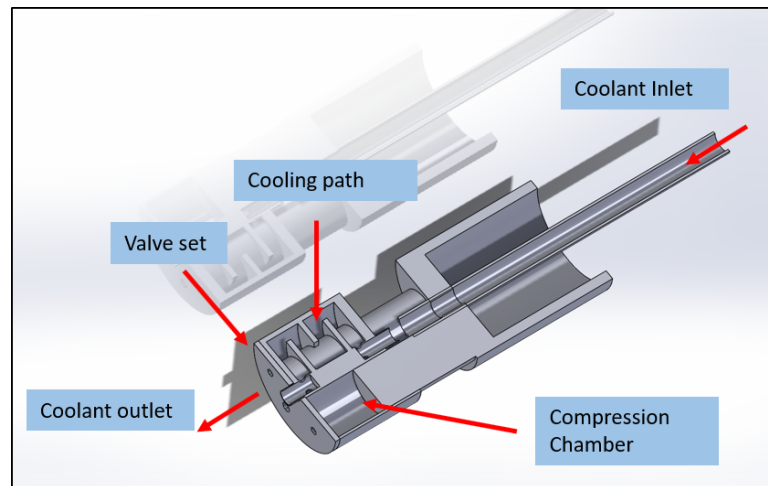
Fig. 6.19. Section view of isothermal core elements of compressor in Design C.

By considering the manufacturing point of view, the existence of multiple pistons leads to larger leakage gaps and therefore, the tolerance requirements are stricter. Particular care need to be taken with respect to the alignment between the cylinder assembly and the pistons. In fact, during the compression process, the tilting of the pistons has to be avoided because it would cause an increase in friction losses during the sliding of each piston inside the corresponding cylinder wall.
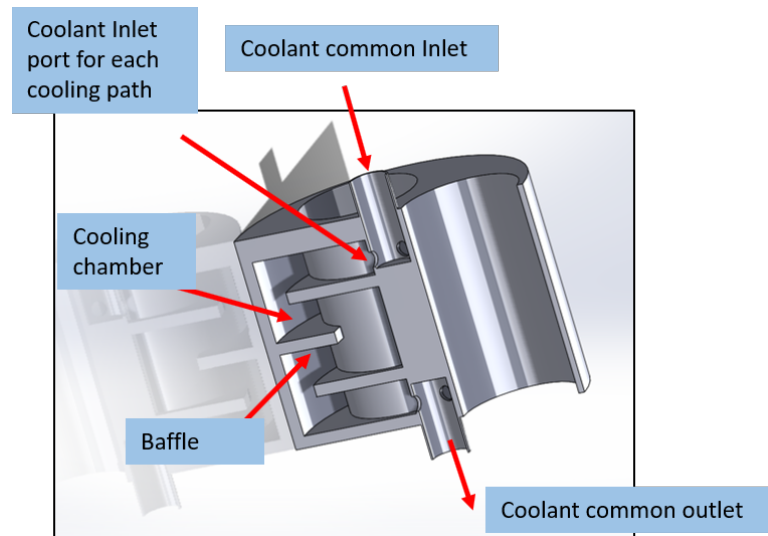
Fig. 6.20. Section view of cylinder assembly in Design C with internal cooling path.

Design D: bean-shape piston

In the case of Design D, the traditional cylindrical piston geometry has been replaced by a bean-shape geometry with larger surface area, as shown in Figure 6.21. As for the previous designs, there are three main assemblies: cylinder, valve set and bean-shape piston. In Design D, four compression chambers have been created inside the cylinder. For each compression chamber, suction port and discharge port on the valve set have different diameters.

Due to the characteristics of the bean-shape piston, there are two types of compressor chambers in this design defined as inner compression chamber and outer compression chamber, as denoted in Figure 6.22. The volume of the inner compression chamber is smaller than that of the outer chamber. Four cooling circuits have been added into cylinder assembly and coolant flows through each cooling circuit around the surface of the compression chamber, as shown in Figure 6.23. Each cooling circuit has one inlet and one outlet for the coolant flow and two circular fins have been used to direct flow and enhance the heat transfer rate for inner loop and outer loop, respectively.
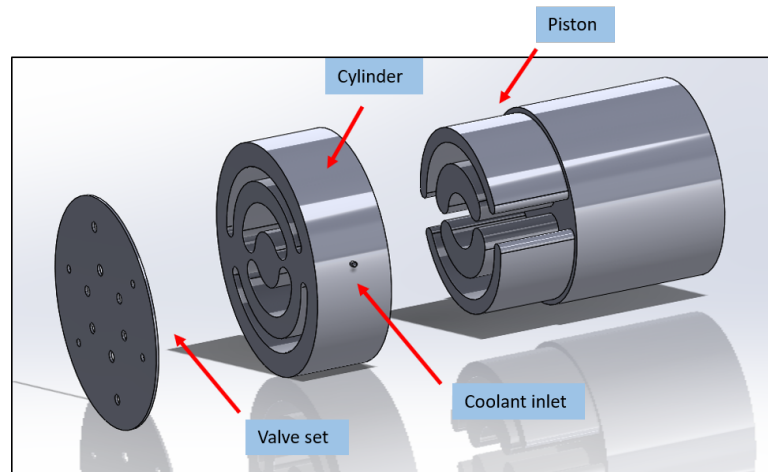
Fig. 6.21. Breakdown schematic drawing of isothermal core elements of compressor in Design.
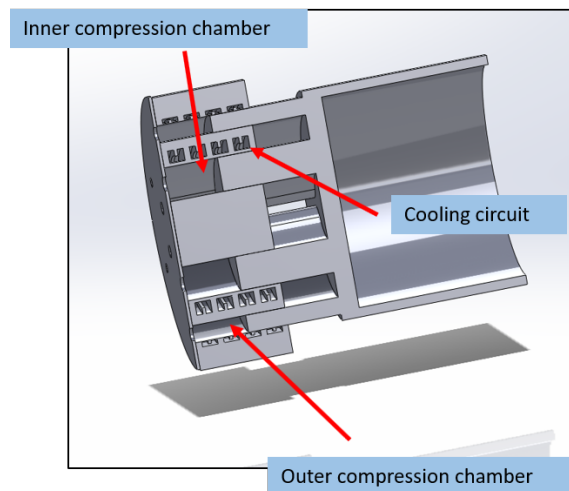
Fig. 6.22. Section view of isothermal core elements of compressor in Design D.

In terms of heat exchange surface, this design shows many advantages over the previous three designs. In addition, only one common inlet and one common outlet for coolant flow are necessary. To this end, two distributers will be used for all circuits as the inlet/outlet, as is the case in a conventional heat exchanger. Furthermore, to keep the balanced pressure force on each piston, all four pistons should have exactly the same cross-section area which leads to the larger wall thickness of the inner
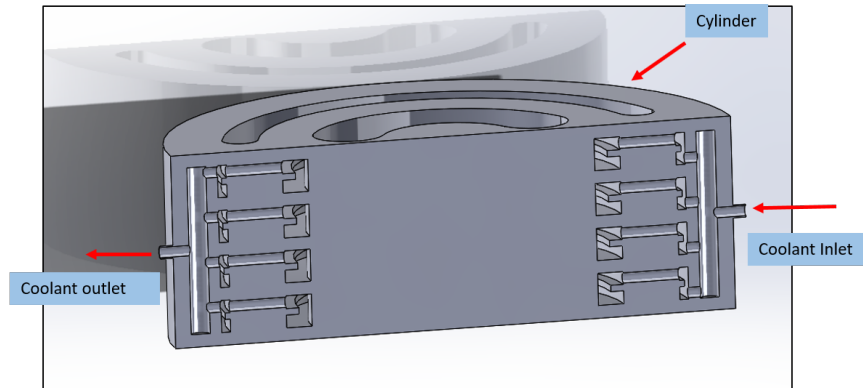
Fig. 6.23. Section view of cylinder assembly in Design D with internal cooling path.

bean-like piston. Therefore, parametric studies will be conducted to identify the best aspect ratio. On the negative side, surface areas for leakage and eccentricity are increased compared to the other designs and special care need to be taken during the manufacturing phase.

6.2.2 Isothermal prototype core element manufacturing attempt

Aforementioned, enhanced heat exchange may benefit from adding cooling path into piston cylinder and in order to prove this concept, one-piston cylinder design with cooling channels for isothermal prototype compressor design has been finalized and the overview drawing is shown in Figure 6.24. It is seen that the previous vertical solid cylinder side was perforated with cross-shape structures marked as blue colored inside the cylinder wall, which is used to support the entire assembly as well as reduce the total weight of the component for manufacture material cost consideration.

Figure 6.25 gives another view of the volume reduction. The new structure has a special trapezoid shape that will enhance the design strength. In addition, this type of design is also good for future implementation of all bolt holes, internal tubes, etc., where 4 mm minimum thickness is promised. In terms of the internal cooling channels, some modifications were also made within the latest design, as shown in Figure 6.26. The trunk and all the branches of the tree support, located at the end
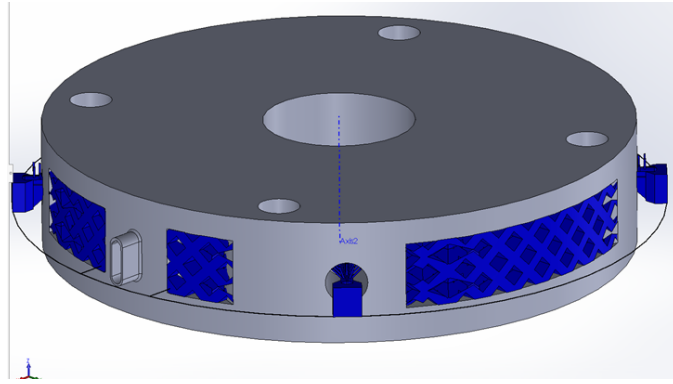
Fig. 6.24. Overview of cylinder with cooling channels in isothermal prototype design.

of each circuit, have 0.25 mm square pins. Besides, the flow passages are triangular and gable ceilings shape as required for the strength consideration.
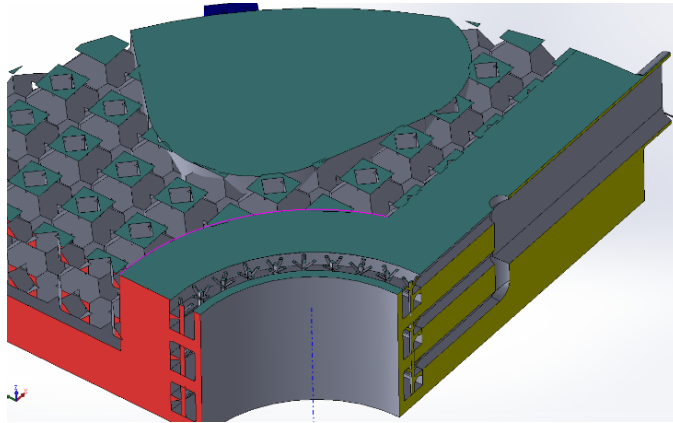
Fig. 6.25. Partial view of the reduced volume structure inside isothermal prototype design.

Figure 6.27 shows the first manufacturing attempt of the isothermal prototype one-piston cylinder design by employing 3D metal printing. During the first trial, Hastelloy X was used as the printing material, although it is not a suitable material for the actual application. The cooling passages have been tested by the Advanced Manufacturing Group at Oak Ridge National Laboratory (ORNL) to ensure their functionality and resistance under high pressure. A vacuuming process will be con-
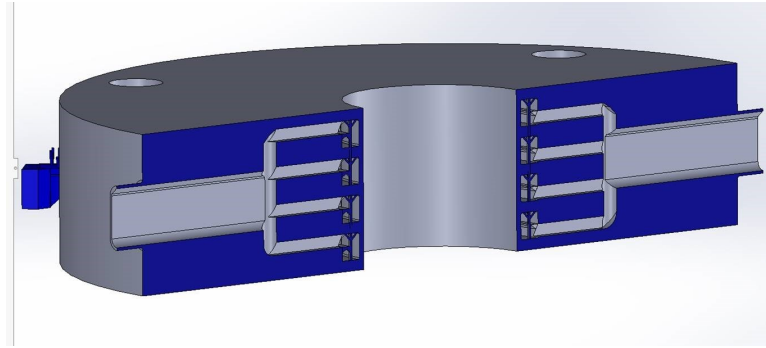
Fig. 6.26. Cross-section view of cylinder with cooling channels in isothermal prototype design.

ducted to remove the sintered powder inside. As the next step, the contact surfaces will be polished and minor machining processes will be done to thread holes, milling out spring pockets to finalize the component design and also improve the component appearance and performance.
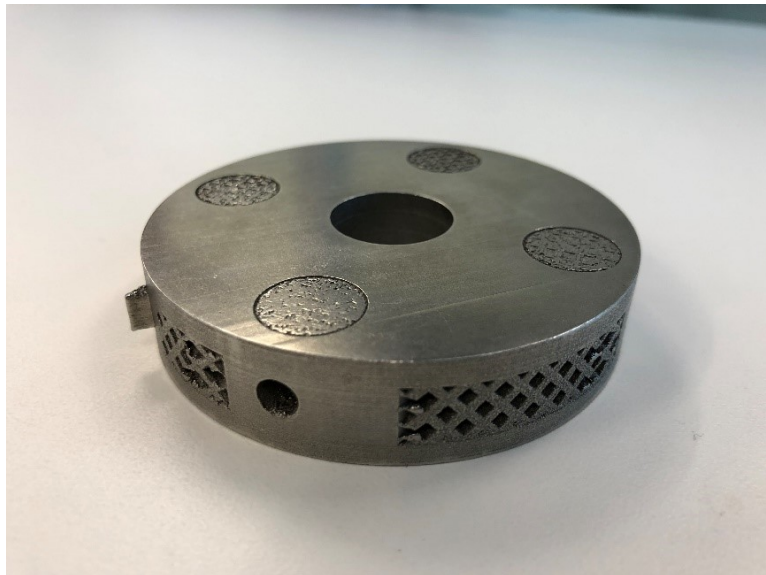
Fig. 6.27. Picture of first 3D printing build of compressor cylinder with cooling channels.

6.3   Scalability Analysis of Linear Compressors

Unlike other types of positive displacement compressors, linear compressor technology has been drawn attention for small-scale domestic refrigeration due to lower friction and power losses with respect to conventional reciprocating compressors as well as their compactness and reduced noise and vibrations. To author's knowledge, there have never been a scale-up linear compressor, used for other applications with higher capacity and the questions may arise in what are the limitations of designing a bigger linear compressor. It would be extremely interesting to numerically analyze the scalability of a linear compressor with the help of the proposed simulation model and some in-depth sensitivity were also carried out to characterize the performance of the scale-up compressors. As will be reported in the following section, two scenarios were used as the examples of the analysis, *i.e.*, heat pump system and air compression system. To the end, a preliminary concept design will be given for each case.

6.3.1   14 kW (4-ton) heat pump system

In order to size the scale-up linear compressor, the required mass flow rate should be determined from the vapor compression cycle model first. A simplified 4-ton heat pump system model has been developed in Engineering Equation Solver (EES) and R410A is used as the working fluid. Two operating conditions have been considered to exercise the simulation model and have been reported in Table 6.3 and the corresponding P-h diagram is shown in Figure 6.28. It is noted that Point 1 is a normal condition for heat pump application, whereas Point 2 is used as a critical condition with higher pressure ratio for this analysis, where the compressor was assumed with a higher superheat but lower isentropic efficiency. For a standard 4-ton capacity heat pump unit, it can be obtained from the system model that the minimal required mass flow delivered from the scale-up compressor should be 55 g/s, considered as a design objective in the compressor model. Note that the mass flow rate will vary with

respect to different operating conditions but this calculated flow rate (55 g/s) should be the lower limit throughout the entire analysis.

Table 6.3.
List of the inputs value for the simplified system model.

Parameter	Point 1	Point 2	Unit
Refrigerant	R410A		-
Capacity	14 kW (4-ton)		-
Evaporating Temperature	-20	-25	°C
Condensing Temperature	40	55	°C
Superheat Temperature	10	15	°C
Subcooling Temperature	10	10	°C
Pressure Ratio	6	10	-
Compressor Efficiency	0.75	0.7	-
Target Flow Rate	56	55	g/s

A preliminary study is proposed here to tackle this problem. After determining the target mass flow rate, the validated comprehensive linear compressor model was exercised to understand the size requirements to achieve the target mass flow rate from the system model and more further sensitivity studies were also conducted to have a better understanding of the scalability of linear compressors. However, this analysis is an open problem with many undetermined boundary conditions, and the assumptions employed for the analysis are as follows. Note that the following analysis is simplified in order to demonstrate the design limitations of a scale-up linear compressor, the addition of sub-models is significant but beyond the scope of current discussion, which can be implemented later once the design has been finalized.

(i) no valve model was applied into the compressor analysis since the geometry information is undetermined but significant on the simulated results;
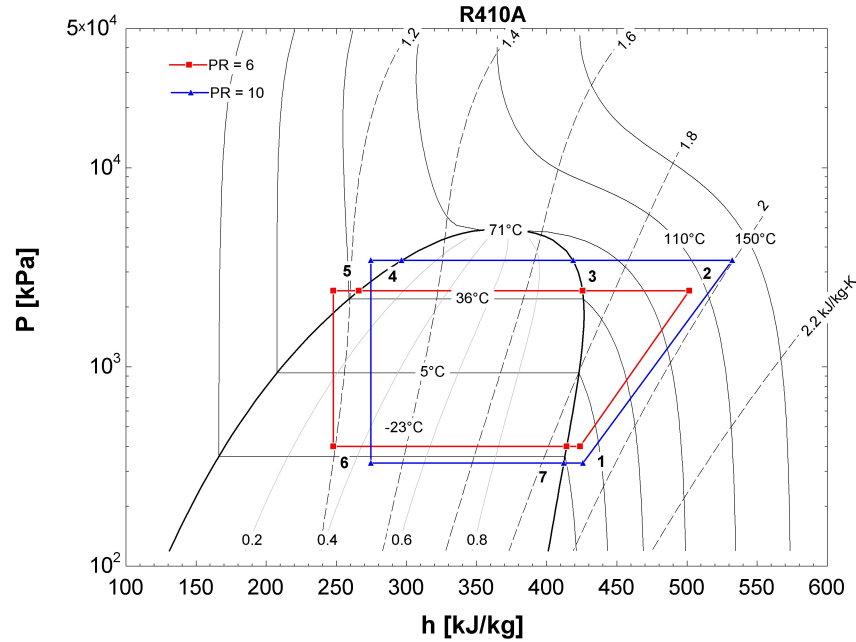
Fig. 6.28. COP improvements from a conventional VCR cycle versus evaporating temperature for different working fluids.

(ii) one simplified leakage flow model, *e.g.*, Couette flow, is used to predict the leakage flow from the compression chamber to the shell side;

(iii) required compression work is calculated based on a constant motor efficiency.

In order to satisfy the design requirements and achieve the target flow, piston geometry has to be determined first. Equation 6.13 represents the calculation of the mass flow rate from a compressor and three key parameters, *i.e.*, piston diameter, piston stroke and operating frequency, would affect the delivered flow rate. In this study, 60Hz and 55 g/s were used as the analyzed operating frequency and the target flow rate. Higher operating frequency will be involved in the section of sensitivity study. Volumetric efficiency, η_v, manifests as a key parameter affecting the compressor flow rate significantly. In generally, this value is in range between half to unity for a reciprocating compressor. With a smaller η_v, longer piston stroke is needed with the same piston diameter to maintain the same target flow rate. Figure 6.29 describes how

the piston stroke changes with respect to the piston diameter, where two dash lines denote the theoretical minimum and maximum piston stroke by defining volumetric efficiency as 0.5 and 1, respectively. These two curves were treated as the boundary conditions for this scalability study.

$$\dot{m} = \eta_v \dot{m}_{th} = \frac{1}{4} \eta_v \rho \pi D^2 x_{s,th} f \qquad (6.13)$$

where $\dot{m}_{th}$ represents the theoretical mass flow rate from the compressor and D is piston diameter, x_s is piston stroke determined by the force balance on the piston, f is operating frequency and η_v denotes the volumetric efficiency, determined from top clearance volume and leakage loss.

As linear compressor is considered as a typical oscillating system, it is favorable to operate the compressor at/close to its resonance frequency. It has been previously reported by Zhang et al. [69] that selecting a mechanical spring with higher stiffness can address this issue due to the fact that the spring force dominates the piston reciprocating motion as well as the resonance frequency. As a result, the effect of the non-linearity of cylinder gas pressure is also minimized. Therefore, in this study, gas spring stiffness is limited up to be half of mechanical spring stiffness and the calculation of piston natural frequency can be modified from Equation 6.14 to Equation 6.15. In the case of 60 Hz, the minimum mechanical spring stiffness can be calculated as 140 N/mm, where the corresponding maximum gas spring stiffness would be 70N/mm Equation 6.16 shows a mathematical calculation of gas spring stiffness, which is a function of pressure ratio, piston diameter and the corresponding piston diameter. It is seen that higher pressure ratio and larger piston diameter lead to a 'stronger' gas spring. Oppositely, longer piston stroke is favorable if 'softer' gas spring is needed. A critical piston stroke line therefore can be drawn in terms of different piston diameters and pressure ratios when the gas spring with the maximum stiffness is generated.

Figure 6.29 describes the variation of critical piston stroke as a function of piston diameter at two pressure ratios, *i.e.*, 6 in green dash line and 10 in blue dash line.

These two lines were also utilized as the boundary conditions, where a preferred piston stroke should be designed with a value beyond. It can be also observed that longer critical piston stroke is required with the increasing piston diameter and with the same piston stroke, the boundary line with pressure ratio 10 lifts up compared to the pressure ratio 6 condition.

$$f_n = \frac{1}{2\pi}\sqrt{\frac{k_{\text{gas}} + k_{\text{me}}}{m_{\text{eff,p}}}} \tag{6.14}$$

$$f_n = \frac{1}{2\pi}\sqrt{\frac{3k_{\text{me,cri}}}{2m_{\text{eff,p}}}} \tag{6.15}$$

$$k_{\text{gas,max}} = \frac{\pi P_s (PR - 1) D_p}{4x_{s,cri}} = \frac{1}{2}k_{\text{me,cri}} \tag{6.16}$$

where P_s is the suction pressure, PR is pressure ratio.

In this study, five piston diameters, *i.e.*, 3 cm, 3.5 cm, 4 cm, 4.5 cm, 5 cm, were selected as the analyzed points and with the objective of the target flow rate, the corresponding required piston stroke were then calculated from the linear compressor model with respect to two pressure ratios and each piston diameter, respectively. It is seen that all the calculated piston stroke from the left three piston diameters, *i.e.*, 3 cm, 3.5 cm, 4 cm, are higher above the critical blue dash line, which indicates that the non-linearity of cylinder gas pressure can be minimized no matter of the pressure ratios. In the case of 4.5 cm piston diameter, the calculated piston stroke meets the requirement for each analyzed pressure ratio, while the gas spring stiffness will increase and beyond the limit if the pressure ratio rises still with the same shorter designed stroke. Regarding to the largest piston diameter, both of two analyzed points are below the critical lines, which means that the gas spring will be too high at this design and bring larger non-linearity to the system. Additionally, the selection of linear motor and control approach is largely market availability dependent and more issues may be involved if the piston stroke is designed too long (compared to the piston diameter and piston length), another maximum boundary of the designed

piston stroke was therefore limited as 12.5 cm, which is 2.5 times of the largest piston diameter. With all the criteria listed above, piston diameter 3 cm will no longer be a good point as the calculated stroke are 13.3 and 19.5, respectively.
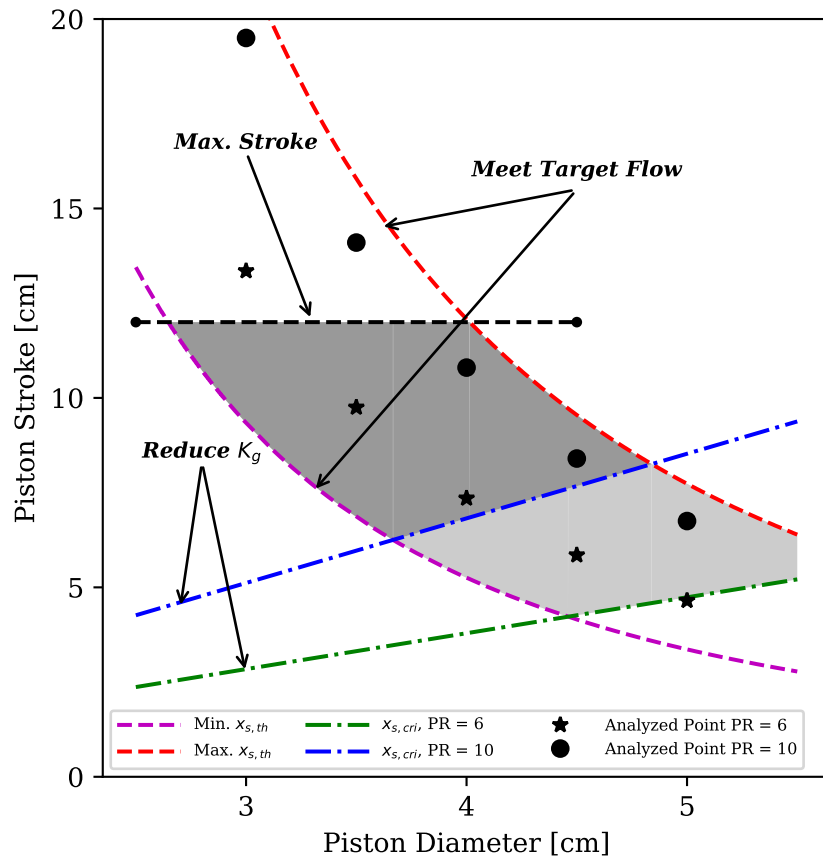
Fig. 6.29. Variation of piston stroke as a function of piston diameter.

In order to have a better understanding of the relationship between the mechanical spring and gas spring stiffness in all proposed designs, the relationship between two spring stiffness versus piston diameter is plotted in Figure 6.30. Note that the gas spring stiffness was calculated by the selected piston diameter, the simulated piston stroke and pressure ratio, and the mechanical spring stiffness was determined by Equation 6.14 with the calculated gas spring stiffness. It can be observed that gas spring stiffness with 5 cm piston diameter are much larger than half of the stiffness of mechanical spring and 4.5 cm piston diameter just across the border, where two

gas spring stiffness at two pressure ratios are almost same to the half of mechanical spring stiffness. For other three points, there are no any issues from the design of spring stiffness, which are consistent to the results in Figure 6.29. Moreover, Figure 6.30 also depicts the relationship between the normalized change of system natural frequency, defined in Equation 6.17, and piston diameter. It can be found out that larger piston diameter will have an increasing variation of natural frequency when the pressure ratio changes, from less than 1 % up to 7 %, and this trend also explains the need to select a stronger mechanical spring to dominate the piston motion with a smaller change of resonance frequency.

$$\Delta f_n = \frac{f_{n,10} - f_{n,6}}{f_{n,6}} \tag{6.17}$$

where $f_{n,10}$ and $f_{n,6}$ represent the natural frequency at pressure ratio 10 and 6, respectively.
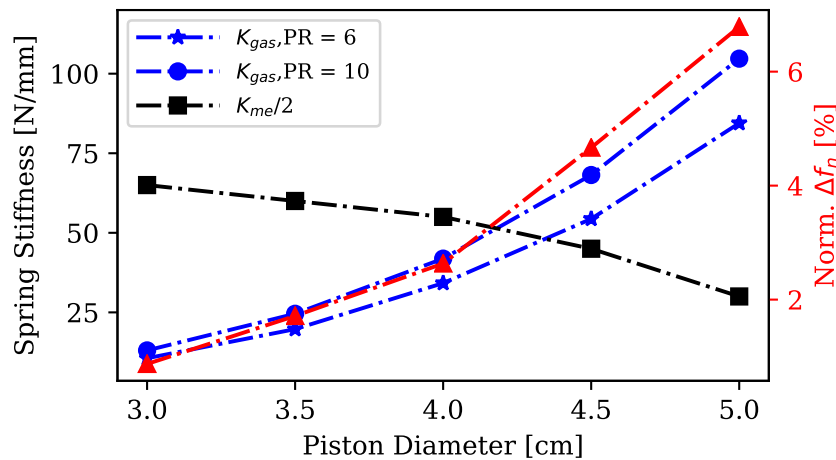
Fig. 6.30. Variation of spring stiffness and normalized natural frequency difference as a function of piston diameter.

To this end, the domain to design a scale-up linear compressor has been determined from the discussion above and three piston diameters were selected: 3.5 cm, 4 cm, 4.5 cm. The geometry of chosen piston size will be implemented as the inputs into the comprehensive linear compressor and more sensitivity studies were conducted to

investigate the compressor performance. The simulation results are listed in Table 6.4 with respect to two pressure ratios and three driving frequencies. It has to be noted that in the case of each piston size, the mechanical spring stiffness was assumed to be same and the designed piston stroke is a function of piston size and pressure ratio, which is not frequency dependent though. In preceding discussion, the mass flow rate at 60 Hz has been set up as a target of minimum value of 55 g/s for all designs to determine the required piston stroke and at the other two frequencies, the mass flow rate will be calculated through the model with the calculated piston stroke from 60Hz.

Figure 6.31 shows the variation of mass flow rate as a function of the piston stroke. It can be seen that although only the mass flow rate at 60 Hz was setup as the target flow, the mass flow rates are almost constant at 70 Hz and 80 Hz in terms of different piston stroke, piston diameter and pressure ratio. It is extremely interesting to conclude that the mass flow rate shows a linear trend with respect to the driving frequency once the design and condition are fixed. Additionally, with the same delivery of mass flow, longer piston stroke is required either with smaller piston diameter at the same pressure ratio or larger pressure ratio with same size of piston.
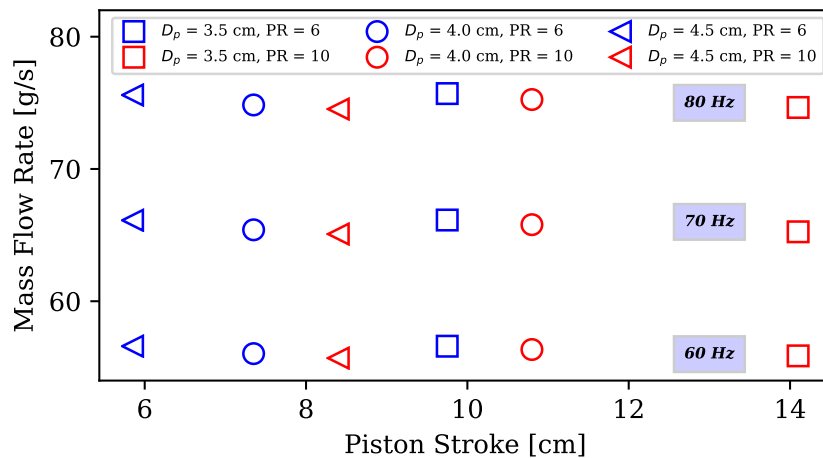
Fig. 6.31. Variation of mass flow rate in terms of different piston stroke at different operating frequency.

Table 6.4.
List of the simulated results for scale-up linear compressor.

PR	D_p	k_{me}	x_s	k_{gas}	$\dot{m}$	f
-	[cm]	[N/mm]	[cm]	[N/mm]	[g/s]	[Hz]
					56.60	60
	3.5	120	9.75	19.74	66.14	70
					75.71	80
					56.04	60
6	4.0	110	7.35	34.19	65.40	70
					74.84	80
					56.60	60
	4.5	90	5.85	54.37	65.12	70
					75.59	80
					55.87	60
	3.5	120	14.10	24.56	65.25	70
					74.65	80
					56.35	60
10	4.0	110	10.80	41.88	65.79	70
					75.25	80
					55.70	60
	4.5	90	8.40	68.16	65.08	70
					74.53	80

Variation of compressor power consumption with different piston sizes and pressure ratios is reported in Figure 6.32. More power is consumed with higher pressure ratio and increasing operating frequency, which is consistent to the performance of a conventional reciprocating compressor. It can be also observed that power consumption rises with a increase of piston diameter, however, the difference is limited when

pressure ratio at 6 but more disparity with pressure ratio 10, which is approximately 27 % increase when piston size increase from 3.5 cm to 4.5 cm.
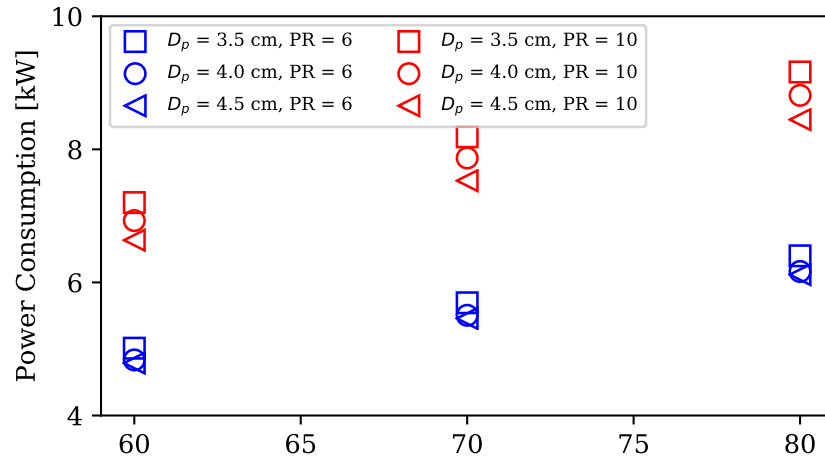
Fig. 6.32. Variation of compressor power consumption as a function of operating frequency.

Figure 6.33 depicts the variation of the overall isentropic efficiency with the designed piston size in terms of different operating frequency and pressure ratio. First of all, it can be seen that compressor performs better when pressure ratio is at 6 and a increase of operating frequency can also improve the overall isentropic efficiency. For instance, in the case of 60 Hz and piston diameter 3.5 cm, the improvements between the overall isentropic efficiency from pressure ratio 6 to pressure ratio 10 can be approximately 6.5 %. In addition, higher overall isentropic efficiency can be obtained from the compressor with a larger piston diameter. For example, in the case of 4.5 cm piston diameter at 60 Hz, its efficiencies are 4.7 % and 8.2 % higher than that of piston diameter 3.5 cm at pressure ratio 6 and 10, respectively.

Figure 6.34 shows the simulated $P - x_p$ diagram of the analyzed linear compressor in terms of different mechanical spring stiffness (or piston diameter) and pressure ratio. Larger clearance volume is found in the design with stronger spring, which will restrict the compressor volumetric efficiency. Emphasis is also placed on the pressure
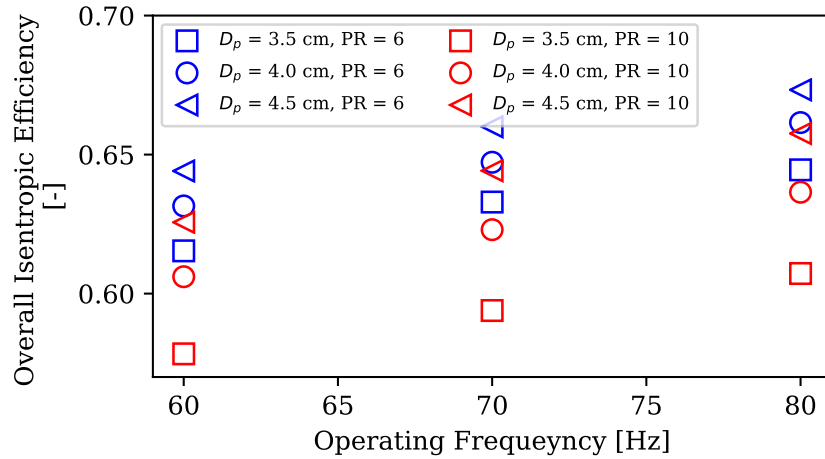
Fig. 6.33. Variation of compressor overall isentropic efficiency as a function of operating frequency.

ratio and it's not favorable to have a large clearance from the higher effective pressure force at higher pressure ratio.
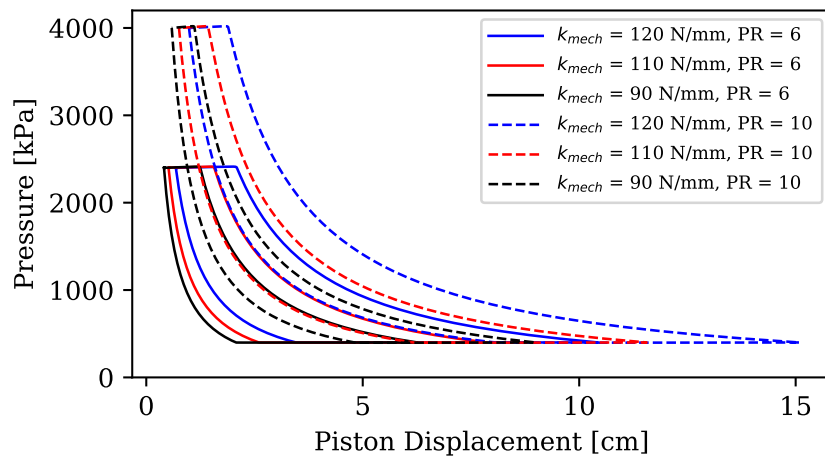
Fig. 6.34. $P - x_p$ diagram with different mechanical spring stiffness and pressure ratio.

Integrated results for normalized leakage rate, defined as the ratio between the calculated leakage rate and a target delivery mass flow rate without the leakage, are plotted in Figure 6.35. Since higher pressure ratio condition has larger pressure

difference between the cylinder and shell side in a linear compressor, it is seen that PR 10 condition has leakage loss, compared to the results from the PR 6 condition. Regarding the size of piston, a larger piston diameter gives larger perimeter length of the piston, as well as more flow path, which allows for more leakage flow from the compression chamber to the shell side. Moreover, it is also found that increasing compressor speed also helps to reduce the leakage loss slightly.
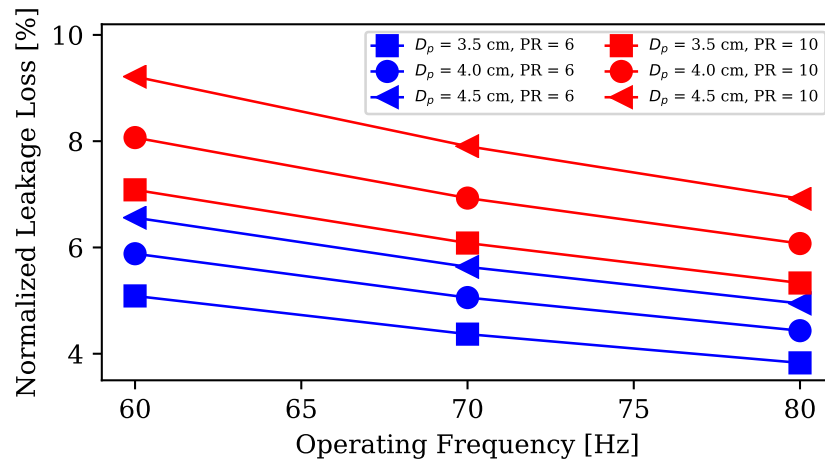
Fig. 6.35. Variation of normalized leakage loss as a function of operating frequency.

Figure 6.36 shows normalized frictional loss, defined as the ratio between frictional loss and compression work, as a function of the operating frequency. It has been known that a smaller piston diameter has a longer required piston stroke, resulting in more surface area for the frictional loss during compressor operation. Therefore, larger piston diameter has less frictional loss, compared to the results from the smaller piston size. As friction between the cylinder wall and piston cylinder mainly comes from gas viscosity in the gap, which highly depends on the pressure gradient as well as the compressor speed, it can be observed that higher pressure ratio condition will lose more energy and increasing the operating frequency also results in a rise of frictional loss.

Based on the analysis above, several conclusions can be drawn as follows:
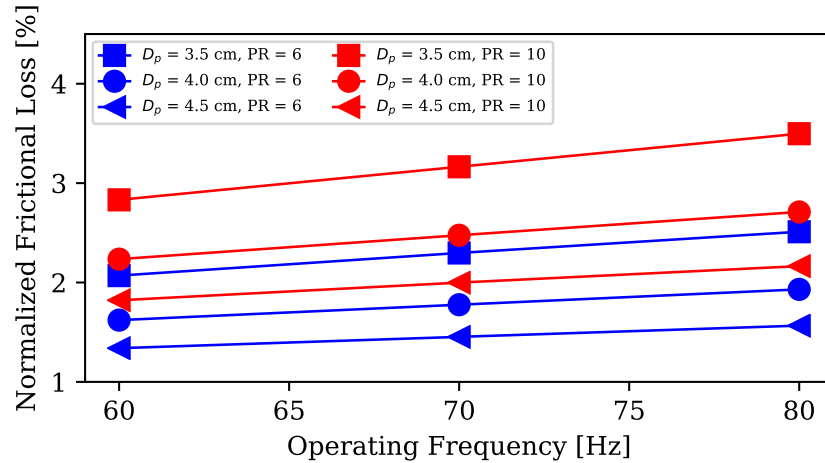
Fig. 6.36. Variation of normalized frictional loss as a function of operating frequency.

- The mechanical spring should be chosen wisely to ensure the dominance of the stable piston motion as well as the designed system natural frequency. Stiffer mechanical spring is beneficial for the resonance frequency control, but it increases the manufacturing cost, compressor weight and component configuration within the shell. Additionally, more analysis should be conducted to investigate the availability of small size of mechanical spring but with higher stiffness.
- It is favorable to maintain the effective gas spring stiffness with a limited value, which is recommended up to half of selected mechanical spring stiffness. There is a trade off between a good gas spring stiffness, piston size and required stroke.
- A good selection of piston diameter should be analyzed and determined based on the target flow, limit of linear motor stroke and a reduction of effective gas spring.
- Higher pressure ratio designed condition has significant effects on the selection of piston size and piston stroke.

Therefore, a preliminary design has been finalized based on all the analysis above and it is noted that the piston length was selected as twice of the piston stroke. All the key parameters are listed in Table 6.5.

Table 6.5.

List of parameters in a scale-up linear compressor design used for 4-ton heat pump.

Parameter	Unit	Valve
Piston Diameter	[cm]	4.0
Piston Length	[cm]	15.0
Compressor Stroke	[cm]	7.35
Mechanical Spring	[N/mm]	110
Design Natural Frequency	[Hz]	60

6.3.2   45 kW air linear compressor

In this section, a numerical analysis is reported on the feasibility of a scale-up linear air compressor with 45 kW total input power. First of all, a simplified air compression system model was also developed to determine the target flow delivered from the compressor. In addition, the feasibility of single stage and multi-stage air compressor were discussed based on the operating condition. In the end, several potential designs were proposed and discussed. Furthermore, a sensitivity study was conducted to understand the trade-off between the losses and performance to provide a design guidance for a scale-up air linear compressor. Based on the application of a typical air compressor, Table 6.6 lists the designed operating conditions.

Similar to the approach used in Section 6.3.1, the piston geometry should be determined based on the stroke length analysis. To simplify the analysis process, 60Hz, pressure ratio 10 and 115 g/s were used as the analyzed operating frequency, analyzed pressure ratio and target flow rate. Figure 6.37 shows the variation of piston stroke as a function of piston diameter, where two dash lines denote the theoretical minimum and maximum piston stroke, which were used as a boundary conditions for this scalability study, respectively. Also, a critical piston stroke line is also plotted in terms of different piston diameters to reduce the effective spring stiffness. Moreover,

Table 6.6.
Designed conditions for a 45kW scale-up air linear compressor.

Parameter	Design Point		Unit
Working Fluid		Air	-
Inlet Temperature		25	°C
Operating Frequency		60	Hz
Pressure Ratio	10	8.5	-
Target Volumetric Flow	200	225	CFM
	340	375	m^3/h
Target Mass Flow		115	g/s

due to the market availability of a linear motor, the maximum stroke was limited to 20 cm, which is marked a horizontal black dash line in the plot. Three piston diameters were selected as the analyzed points, *i.e.*, 12 cm, 14 cm, 16 cm, which were used as the inputs for the linear compressor model to calculate the required piston stroke with a target of flow rate.

Unlike the results shown in Figure 6.29, there is only limited dark grey area in Figure 6.37 suitable for the selection of piston diameter. It is seen that the calculated piston stroke with 12 cm diameter is too large than the maximum stroke limit, whereas the required stroke with 16 cm diameter piston is below the critical stroke line, which denotes that a large gas spring may be generated in this design. Even for the design with 14 cm as the piston diameter, the calculated stroke is just across the boundary, which also may not a good design point. This trend can be also observed from Figure 6.38, which presents the relationship between the calculated gas spring stiffness and the required mechanical spring stiffness. It is seen that only when the piston is approximately smaller than 13.5 cm, the effective gas spring stiffness could be smaller than half of mechanical spring, which is a requirement for a good scale-up linear compressor design. Compared to the curve in Figure 6.37, the required piston stroke
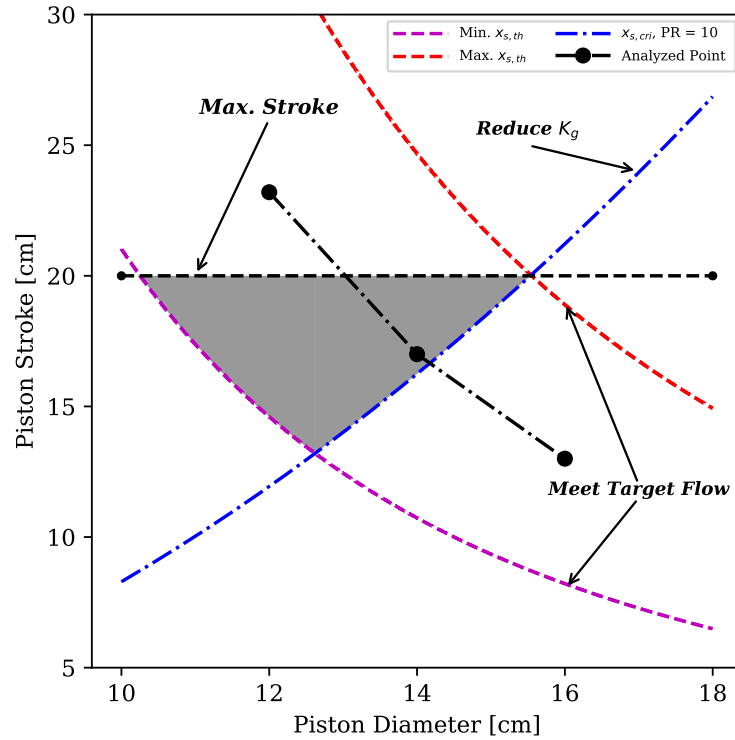
Fig. 6.37. Variation of piston stroke as a function of piston diameter for a single stage air compressor.

may be beyond the maximum stroke when the piston diameter is larger than 13.5 cm. Additionally, the simulated discharge temperature from the proposed single stage air compressor design is relatively high, up to 320 °C, which is also a limitation on the selection of piping materials and other components in the system. Therefore, if no further knowledge is available, it can be concluded that it is not favorable to design a single stage air compressor to achieve the target capacity at the designed condition.

In order to satisfy the requirement of capacity for a scale-up air linear compressor, multi-stage compression will be a good option with an intercooler to maintain a good efficiency as well as overcome the design limitations. Two types of multi-stage air linear compressor were considered in this study: one is two separate scale-up linear compressors to consist of a two-stage compression system with an intercooler, whose schematic is shown in Figure 6.39. Another option is to design a double-acting linear
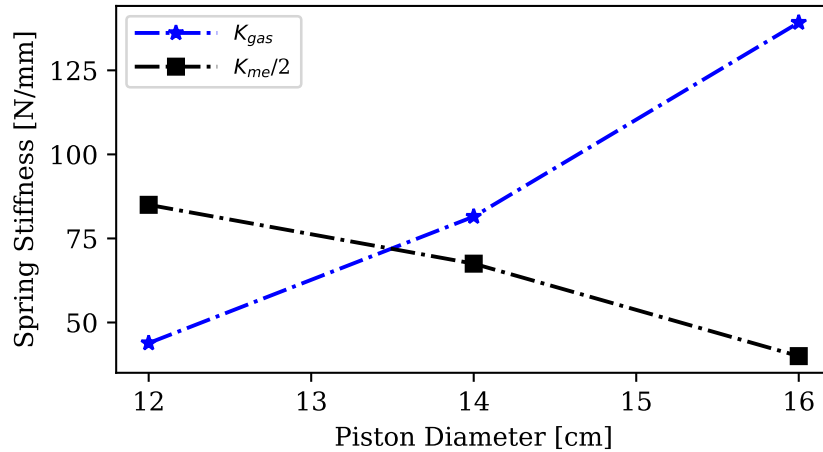
Fig. 6.38. Variation of spring stiffness as a function of piston diameter for a single stage air compressor.

compressor with internal piping and intercooler between two stages and the linear motor is shared for both of stages. The schematic is shown in Figure 6.40. It can be seen that the air coming out of the first-stage discharge valve is compressed to the intermediate pressure, which travels through an intercooler to cool down the air and goes to the second-stage shell. Note that the piston stroke in both of two type multi-stage air linear compressors were assumed to be same for two stages, which is beneficial for the preceding analysis in this study and make the conclusions general enough for both two types of multi-stage air compressors.

Unlike a single domain in the analysis in previous sections, two domains to design a two-stage scale-up air linear compressor have been determined for each stage, shown in Figure 6.41. Due to the mass flow conservation and consistent piston stroke for two stages, it is seen that the design domain (dark grey area) for first stage is in the right hand side (RHS) of that for second stage, which denotes piston diameter in the first stage should be larger than that in second stage with the same stroke. Note that the mechanical spring stiffness and the required piston stroke were assumed to be same for two stages in a single design. Three piston diameters were selected for each of stage based on the design domain. The geometry of chosen piston size was
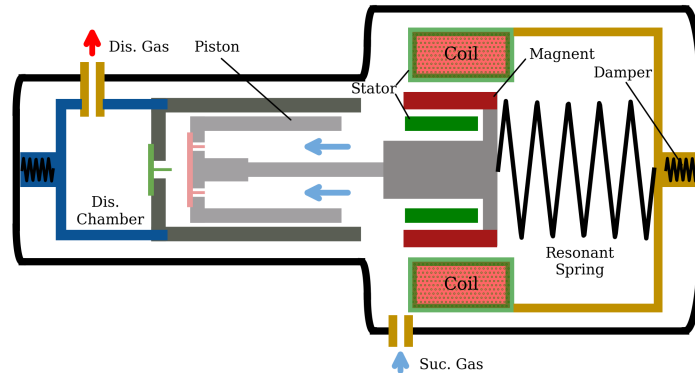
Fig. 6.39. Schematic of a scale-up linear compressor in one of stages for separate two-stage air compression.
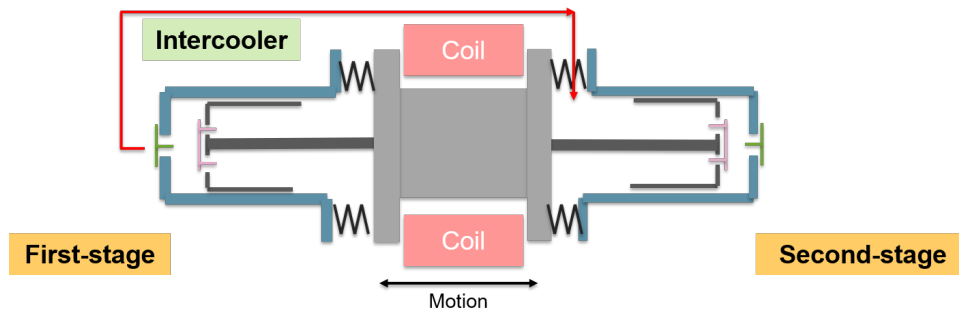
Fig. 6.40. Schematic of a double-acting linear compressor used for two-stage air compression.

used as the inputs into the comprehensive linear compressor and the required spring stiffness and piston stroke can be calculated, accordingly. The parameters used in the proposed designs are listed in Table 6.7 and three designed are label as A, B, C for the following discussion. It is seen that all six required piston strokes (three for each stage) fall into the designed domain, where only the piston stroke of Design A is close to the maximum stroke limit. It is possible to further analyze the gas spring and mechanical spring stiffness in three designs based on Figure 6.42. Unlike the trend
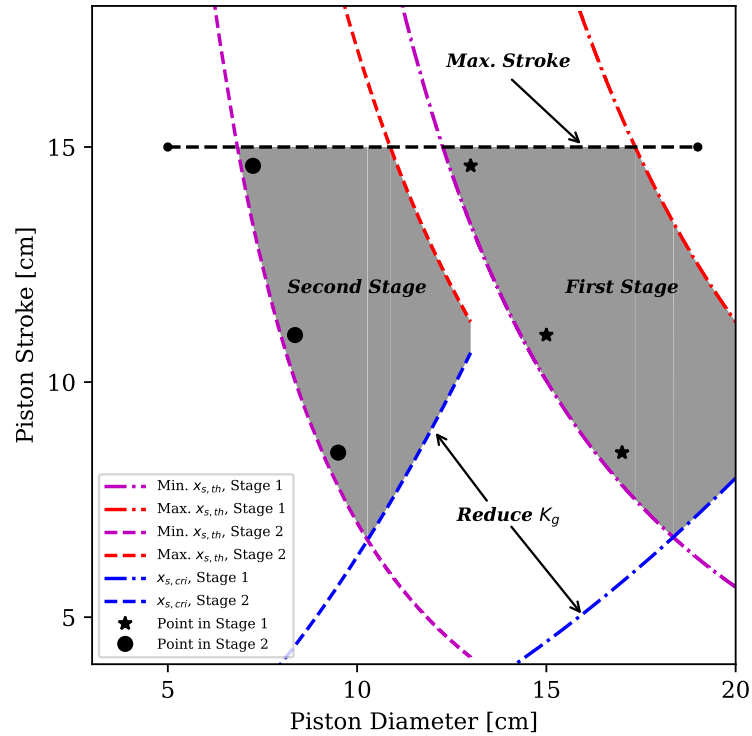
Fig. 6.41. Variation of piston stroke as a function of piston diameter for a two-stage air linear compressor.

shown in Figure 6.38, the gas spring stiffness in both of two stages are below half of the required mechanical spring stiffness for all three designs, which is beneficial to maintain the stability of the system. To this end, it is of great interest to use all three designs as the examples for the following sensitivity study.

The simulation results are listed in Table 6.8 and in the case of each design, three driving frequencies were used as analyzed additional operating conditions. With respect to each piston size, the mechanical spring stiffness was assumed to be same, as shown in Table 6.7 and the designed piston stroke is only the function of piston size and not driving frequency dependent. In this simulation, the mass flow rate at 60 Hz has been set up as a target of minimum value of 115 g/s for all designs to determine the required piston stroke and at the other two frequencies in the same

Table 6.7.
List of the parameters used in the proposed designs.

Design No.	PR	Stage	D_p	k_{gas}	k_{me}	x_s
-	-	-	[cm]	[N/mm]	[cm]	
A	10	1	13.0	19.64	200	14.6
		2	7.25	19.30		
B	10	1	15.0	34.7	180	11.0
		2	8.36	34.06		
C	10	1	17.0	57.68	160	8.50
		2	9.50	56.92		
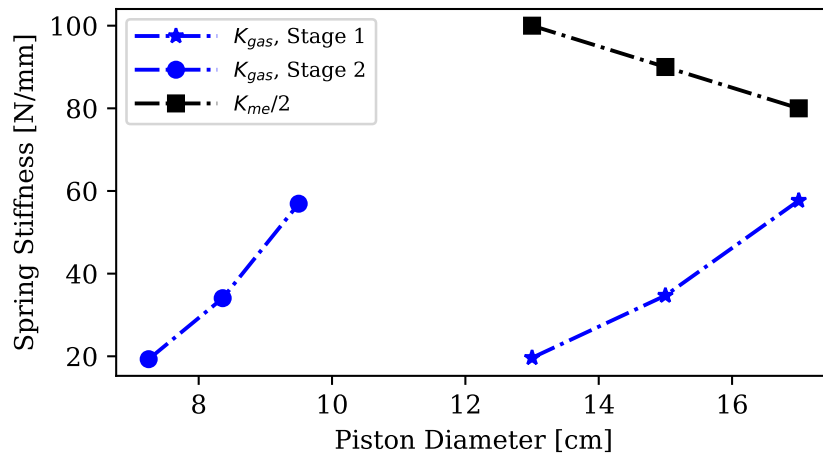
Fig. 6.42. Variation of spring stiffness as a function of piston diameter for a two-stage air linear compressor.

design, the mass flow rate will be calculated through the model with the calculated piston stroke at 60 Hz accordingly.

Figure 6.43 shows the variation of the overall isentropic efficiency for three designs as a function of different operating frequency. In terms of two stages in a single design, compressor at stage 2 always performs better than the first stage compressor, which

Table 6.8.

Summary of the simulated results for scale-up two-stage air linear compressor.

Design No.	f	Stage	Power	Total Power	$\dot{m}$	Flow Rate	Flow Rate
-	[Hz]	-	[kW]	[kW]	[g/s]	[SCFM]	[m³/h]
A	60	1	22.6	43.5	116.2	225.7	384
		2	20.9				
	70	1	26.8	50.9	134.6	261.5	445
		2	24.1				
	80	1	31.3	58.7	152.6	296.4	503
		2	27.4				
B	60	1	22.5	43.1	116.8	226.9	386
		2	20.6				
	70	1	26.7	50.6	135.3	262.8	447
		2	23.9				
	80	1	31.1	58.2	153.3	297.8	506
		2	27.1				
C	60	1	22.2	42.7	116.2	225.7	384
		2	20.5				
	70	1	26.4	50.0	134.5	261.3	444
		2	23.6				
	80	1	30.9	57.7	152.5	296.2	503
		2	26.8				

benefits from the use of intercooler with a relatively low suction temperature at the intermediate pressure. With the increasing of the driving frequency, the discrepancy of the overall isentropic efficiency between two stages increases, where the efficiency

of first stage drops but slightly rises for second stage compressor. For example, in the case of Design C, the difference of overall isentropic efficiency between two stages can be found as higher as 18% at 80Hz. When comparing the performance between each design, it can be seen that Design C always reveals a best efficiency for both of two stages and all three analyzed frequencies. In particular, at 70 Hz, the efficiency of Design C is 1.52 % and 0.68 % in first stage, 2.78 % and 1.07 % in second stage higher than that in Design A and Design B, respectively.
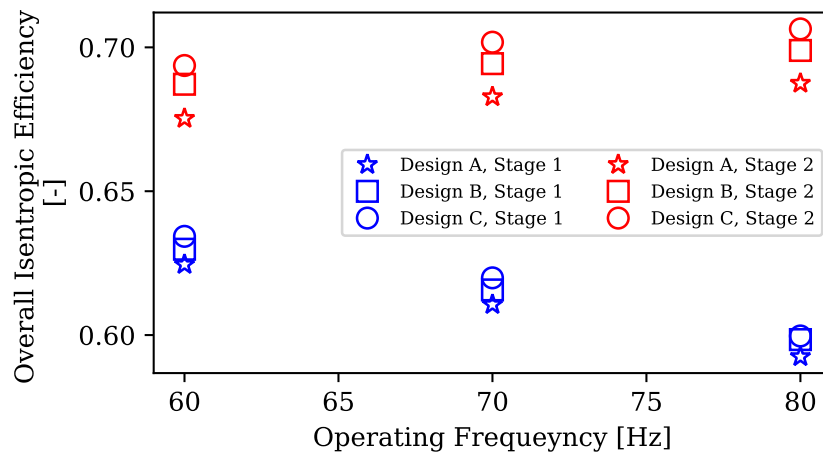
Fig. 6.43. Variation of compressor overall isentropic efficiency as a function of operating frequency of two stages in three proposed designs.

From Table 6.7, it can be seen that Design C has the softest mechanical spring but with largest piston diameters in both of stages, which leads to a shortest required piston stroke in all of three designs. Figure 6.44, simulated $P - x_p$ diagram of the analyzed multi-stage air linear compressors, can be utilized to demonstrate the influence from this difference. First of all, it is seen that stronger spring (*e.g.*, Design A) will lead to a larger clearance volume, which diminishes the compressor volumetric efficiency, while some of the energy can be recovered from the spring system during the expansion process. However, it also needs to be noticed that the effects from the mechanical spring stiffness on the clearance volume is limited at stage 2. Moreover,

significant over-shot pressure can be found in the first stage, which may result from the inappropriate sizing of the discharge pipe or the discharge ports and it should be considered carefully in the final prototype design.
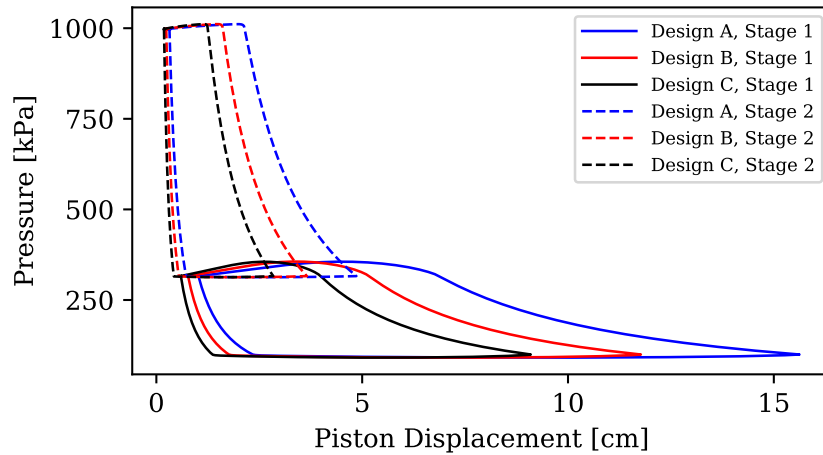
Fig. 6.44. P-x diagram of two stages in three proposed designs.

Integrated results for normalized leakage loss in all three designs, defined as the ratio between the calculated leakage rate and a target delivery mass flow rate without the leakage, are plotted in Figure 6.45 as a function of the operating frequency. It is seen that Design A has least leakage loss, compared with the other two designs, because its smaller piston diameter in each stage will provide less leakage flow path area through gap between the piston and cylinder wall. Particularly, when the driving frequency is at 60 Hz, the normalized leakage loss in Design C and Design B are 1.82 % and 0.9 % higher than that in Design A. Similar to the previous analysis, increasing compressor speed also helps to reduce the leakage loss.

Figure 6.46 shows normalized frictional loss in all three designs, defined as the ratio between frictional loss and compression work, as a function of the operating frequency. It has been known that smaller piston diameter has longer required piston stroke, leading to more surface area for the frictional loss during the compressor operation. Therefore, larger piston diameter (Design A) has less frictional loss, compared to the
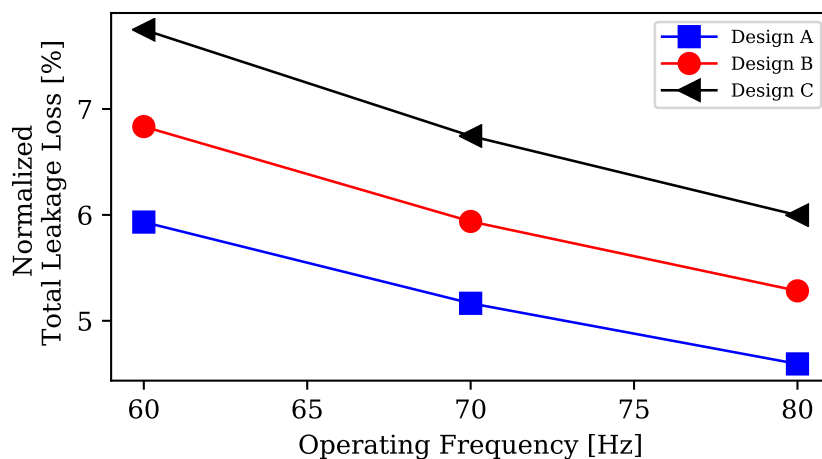
Fig. 6.45. Variation of normalized leakage loss as a function of operating frequency.

results from the smaller one (Design C), where the difference can be found as 3.15 % and 4.08 % when the driving frequency is at 60 Hz and 80 Hz, respectively. As friction between the cylinder wall and piston cylinder mainly comes from gas viscosity in the gap, which highly depends on the pressure gradient as well as the compressor speed, it can be observed that higher operating frequency results in a rise of frictional loss.
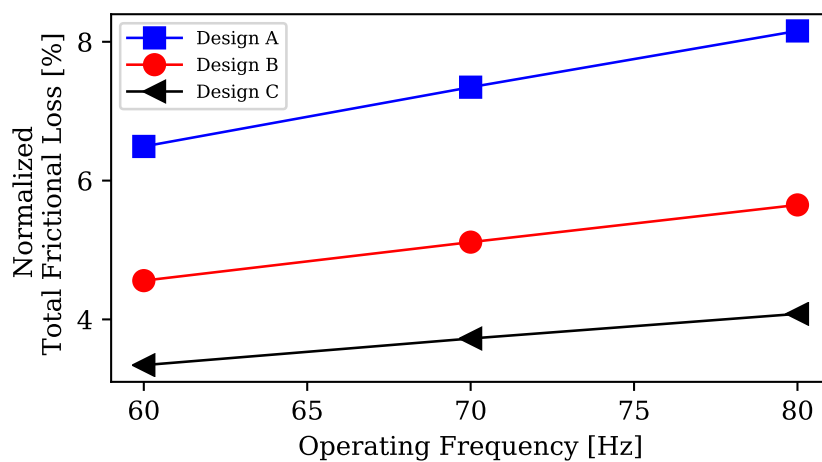
Fig. 6.46. Variation of normalized frictional loss as a function of operating frequency.

In this section, the feasibility of both single and multi-stage scale-up air linear compressor has been discussed and analyzed. In addition, a sensitivity study has been conducted on the proposed designs to investigate and identify the key parameters affecting the compressor performance with the goal of providing guidance for developing improved scale-up air linear compressor designs. Based on the above analysis, some of conclusions are same as the discussion in Section 6.3.1 and some specific conclusions for scale-up air linear compressor are as follows:

- The potential of single stage scale-up air linear compressor is limited by the selection of piston, system stability, *etc.*. However, the feasibility of multi-stage scale-up air linear compressor has been proved and analyzed in this study.
- Three two-stage air linear compressor designs have been proposed, which were also used for further sensitivity study. Based on the analysis, a preliminary design has been finalized and it is noted that the piston length was selected as twice of the piston stroke. All key parameters are listed in Table 6.9.
- Mechanical spring has less effects on compressor in the second stage and it is possible to place more emphasis on the first stage when designing the spring assembly.

Table 6.9.
List of parameters in a scale-up air linear compressor design.

Parameter	Value	Unit
First Stage D_p	17.0	[cm]
Second Stage D_p	9.5	[cm]
Piston Length	35.0	[cm]
Compressor Stroke	8.50	[cm]
Mechanical Spring	160	[N/mm]
Design Natural Frequency	60	[Hz]

6.4 Linear Compressor Prototype Design

In parallel to the isothermal prototype linear compressor design that will be manufactured using 3D printing processes, a new prototype linear compressor design without internal cooling paths has been developed, which is also beneficial to help experimentally analyze the characteristics and scalability of linear compressors. This compressor will be also used as the baseline for comparison to the design of the isothermal compressor later on. Currently, a version of the baseline linear compressor has been finalized, which was built by employing conventional CNC machines. The overall schematic drawing of the updated baseline linear compressor prototype design is shown in Figure 6.47.
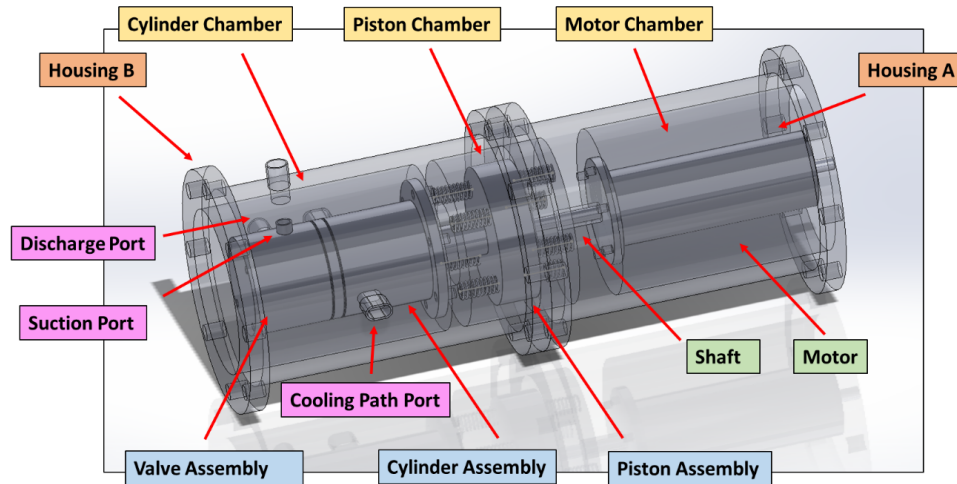
Fig. 6.47. Schematic drawing of the updated linear compressor prototype design.

In order to simplify the compressor assembly, a semi-hermetic design with two housings is used to split the entire compressor shell into three chambers, *i.e.*, cylinder chamber, piston chamber and motor chamber by adding two flanges on each side, which are used for the fixation of motor, springs and cylinder, respectively. As aforementioned, in this baseline prototype design, no cooling circuits were added inside the cylinder wall and the piston follows the conventional cylindrical shape as well. However, the cooling path port on the housing still exists because the housing cham-

ber will be used as the shared part for different designs whose key elements inside are interchangeable. In order to expedite the prototyping process and improve the performance of the design, several key components can be selected either off-the-shelf or obtained from other suppliers based upon our specifications. These components include the linear motor, compression springs and valve assembly. Each component will be discussed in detail in the following sub-sections.

6.4.1 Motor selection

Linear motors play a key role in determining the linear compressor performance. In recent years, linear motor technology has improved significantly, especially in the transportation area. Generally, there are two types of direct drive DC linear motor, which consists of a permanent magnetic field assembly and a coil assembly. The electric current flowing through the coil assembly interacts with the permanent magnetic field and the driving force can be generated and reversed by adjusting the polarity of current. Figure 6.48 shows a general schematic of those two types of motors and some typical specifications are listed in Table 6.10.

(a)   (b)
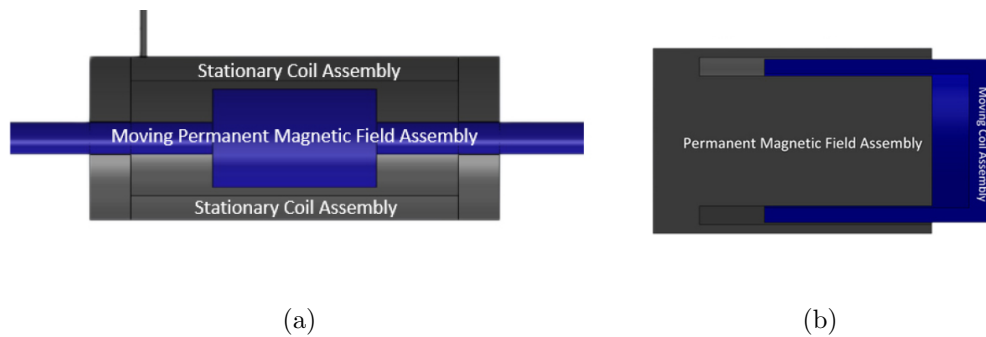
Fig. 6.48. Schematic of two direct drive DC linear motor: (a) Moving magnet type; (b) Moving coil type.

A typical moving magnet linear motor features a tubular shape and the internal shaft is connected to the moving magnet surrounded by a stator with a single coil

Table 6.10.
Summary of parameters in a scale-up air linear compressor design.

Type	Max. Stroke	Peak Force	Max. Moving Mass	Max. Diameter
-	[cm]	[kN]	[kg]	[cm]
Moving Coil	13.5	7	6.5	25
Moving Magnet	10	1.8	4.5	16

winding. As the coil is powered by the excitation current, the driving electro-magnetic force is generated on both the magnet and the shaft pole to drive the piston motion. It can be seen in Table that moving magnet linear motors has relatively smaller geometry and less weight but short designed stroke and smaller peak driving force. However, due to its configuration, it has lower reliability concerns, less cost, which justify their use as the driving motor for our baseline linear compressor prototype, which is designed for a residential refrigerator. However, if larger capacity is required as discussed in Section 6.3, moving coil type linear motor will be recommended or other bigger linear motor, *e.g.*, linear servo motors, which are ideal for long stroke. Moreover, the selected linear motor is also equipped with an integrated sliding contact linear bearing, which can significantly improve the stability of the linear motion and reduce the eccentricity simultaneously. Figure 6.49 shows the picture of the selected commercially available motor.

6.4.2   Spring selection

As discussed in Section 5.4, multiple springs should be utilized to reduce the piston eccentricity. In this proposed prototype design, two sets of spring systems are used to provide the spring force for piston movement as well as stabilize the vibration and avoid piston rotation. In order to achieve this goal, a series of compression springs

Fig. 6.49. Picture of the selected linear motor.

were selected based on the spring rate of each spring as well as the resonant frequency of the overall system. One picture of the spring configuration in the prototype is reported in Figure 6.50.
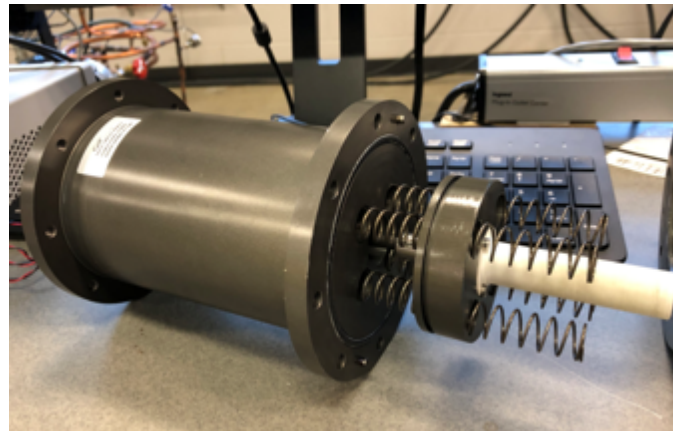
Fig. 6.50. Picture of the spring configuration in the prototype design.

Moreover, a flexure (also called spiral disc) spring, shown in Figure 6.51, results in a more symmetric force on the piston body and is a good solution for avoiding eccentricity when a single spring is employed. Besides, flexure spring is also famous for its with compact design and high stiffness (multiply assembly), which may be a better option for scale-up linear compressor.

Fig. 6.51. Picture of a commercially available flexture spring [14].

6.4.3 Valve assembly design

Valve port sizing

In a linear compressor, the valve design will affect the compressor performance and the valve port size should be sized correctly and accurately. In this section, the port size of two valves was sized to ensure that the Mach number of the incoming or outgoing fluid remains at approximately 0.3 or lower, in order to treat the flow as incompressible. As is shown in Figure 6.52, in order to lower the Mach number, the total flow area ratio between design port area and critical flow area should be larger than 2 and the corresponding port diameter can be calculated then: suction port should be larger than 1.98 mm and discharge port is larger than 0.68 mm when there are two ports applied for each valve.

In addition, the valves geometries are collected by measuring some commercial products and measurements, which are listed in Table 6.11. Three commercial piston compressors, *e.g.*, Embraco reciprocating compressor, Embraco WM linear compressor and LG linear compressor, were selected as the reference for the reed valve design in the prototype linear compressor and all of them have a similar target cooling capacity for consistence comparison. It can be observed that our prototype linear com-
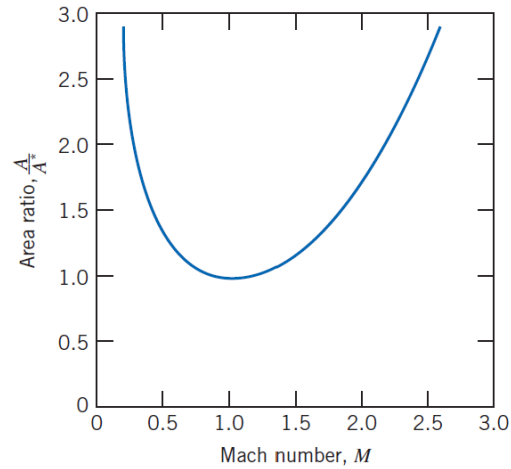
Fig. 6.52. Relationship between flow area and flow Mach number (obtained from [88]).

pressor will be equipped with similar port size as other commercial linear compressor after calculating the flow Mach number to promise the enough flow rate.

Table 6.11.
Valve measurements on three commercial compressors and valve design in prototype linear compressor.

Parameter	Embraco Recip.	Embraco WM	LG Linear	Prototype
Designed Capacity [W]	150	150	200	150
Piston Diameter [mm]	18.4	19.5	26.5	20.5
Suc. Port Dia. (Single) [mm]	6.85	7.6	5.2	5.0
Suc. Port Area [mm^2]	36.5	90.7	63.7	39.3
Dis. Port Dia. (Single) [mm]	3.62	2.25	27	3.5
Dis. Port Area [mm^2]	10.2	23.8	67.8	19.3

Valve reed design

As is shown in Figure 6.53, the schematic of a typical reed valve, the reed length and the port distance to the anchor needs to be designed accurately and the reed

thickness will be determined by the material selection. The valve dynamic performance is highly affected by the valve design, which has been discussed in Section 2.4.2.
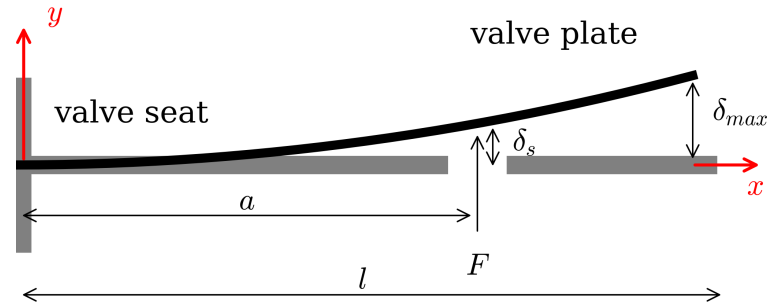
Fig. 6.53. Schematic of a typical reed valve.

Based on the valve sizing model calculation, the variation of the effective mass and spring rate as a function of piston length can be found in Figure 6.54(a) and Figure 6.54(b). It is seen that the effective spring rate will decrease with the increasing reed length, leading to a higher effective mass though. Basically, the higher effective mass of the valve reed can produce higher inertia force on the valve dynamics, therefore the valve needs longer time to open and close. According to the research and measurement conducted on the commercial products, the reasonable design region has been marked with the red rectangle. Figure 6.55 shows the schematic of the final valve design in the prototype linear compressor. In particular, the suction valve reed has special shape for the manufacture convenience.

6.4.4 Overall prototype linear compressor design

The overall prototype linear compressor design has been finalized and the overview is shown in Figure 6.56. The compressor assembly has three housings, *i.e.*, valve, piston, motor, regarding with the convenience of the parts assembly and operation
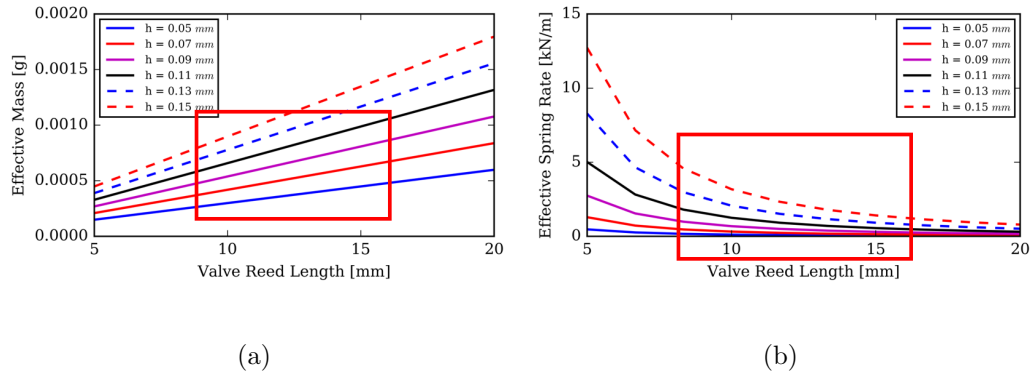
Fig. 6.54. Valve reed design as a function of valve reed length : (a) Effective spring rate; (b) Effective mass.
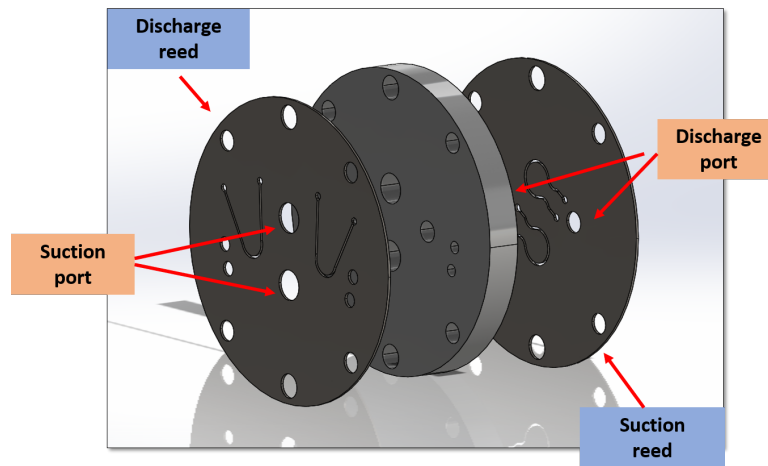
Fig. 6.55. Drawing of the final valve assembly design in the prototype linear compressor.

stability. In addition, two measurement ports are added on two ends of the housing, which will be used for the internal measurements cable and power strips. Similar to the Embraco WM linear compressor, two suspension system are designed on the center of two sides, which will absorb the vibration during the compressor running. For this baseline prototype design, the piston cylinder will be solid-structure without any internal cooling channels but the piston housing is still designed with the coolant

ports and the 3-D printed cylinder with cooling channels will replace the baseline cylinder but connect to the same housing.
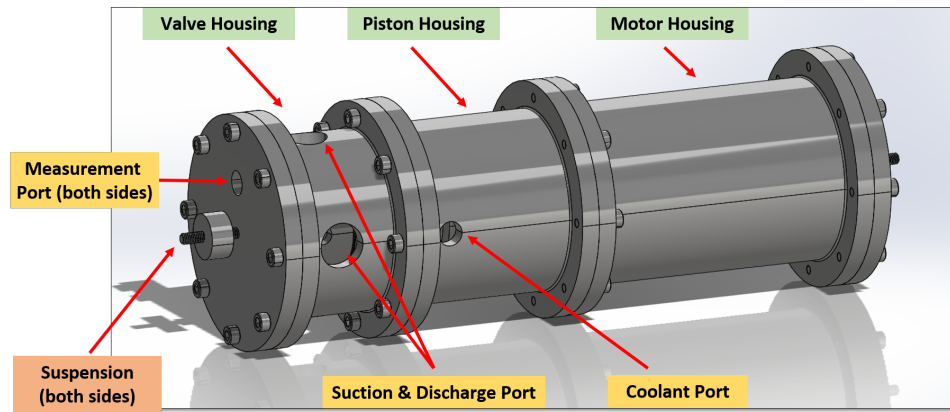
Fig. 6.56. Schematic drawing of the final linear compressor prototype design (overview).

Figure 6.57 depicts the transparent view of the final prototype linear compressor design. More space is added inside the piston housing in terms of the convenience of the spring assembly. One compatible grease will be selected and used for lubrication between the piston seat and housing inner surface. In fact, this add-on lubrication won't affect the oil free operation condition at all because the grease does not mix with refrigerant when compressor in operation. As a part of future work, the gas groove channels will be added into the piston seat, which acts as the external gas bearing to reduce the friction while the piston is reciprocating.

More details of components can be seen from Figure 6.58. In addition to the main parts, *i.e.*, valve, piston, motor, several auxiliary parts are considered as well. Two dowel pins are used for a better alignment when connecting different housings. Three O-rings are utilized to seal each connection surface and avoid the metal direct contact as well. Figure 6.59 depicts the drawing of the piston and the cylinder assembly. One interchange PTFE coating sleeve is used to reduce the metal contact between the piston and cylinder surface and other materials will be analyzed to find the optimal coating material. One two-part secondary coupling improves the connection
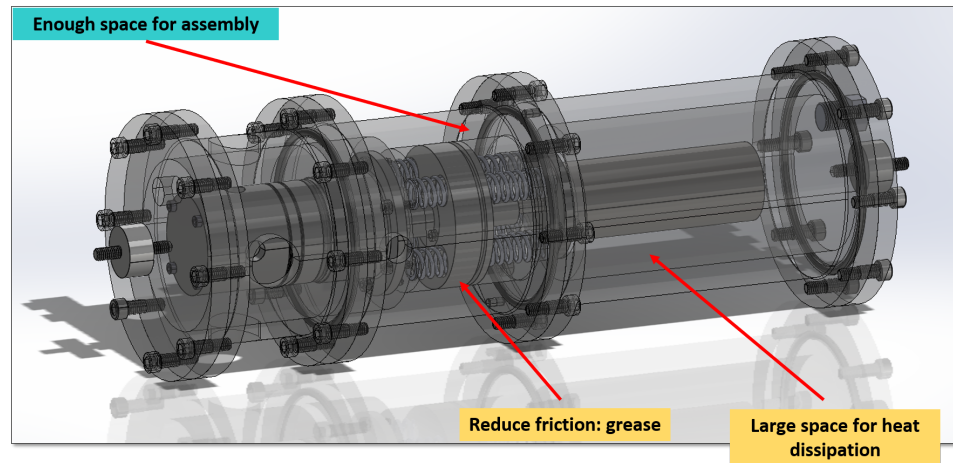
Fig. 6.57. Schematic drawing of the final linear compressor prototype design (transparent view).

and alignment between the motor shaft and piston assembly to reduce the piston eccentricity as much as possible, which will reduce the leakage and frictional based on the previous analysis. To the end, the picture of the final version of the prototype linear compressor design is shown in Figure 6.60.
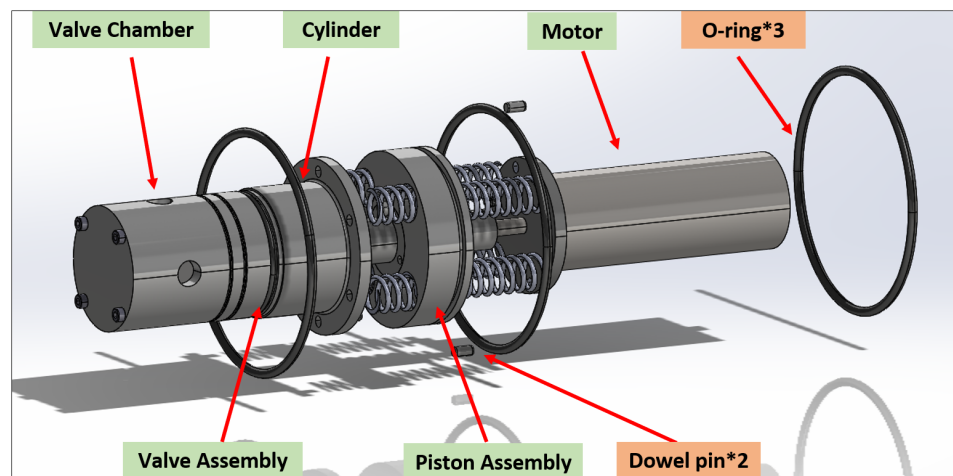
Fig. 6.58. Schematic drawing of the main components in prototype linear compressor.
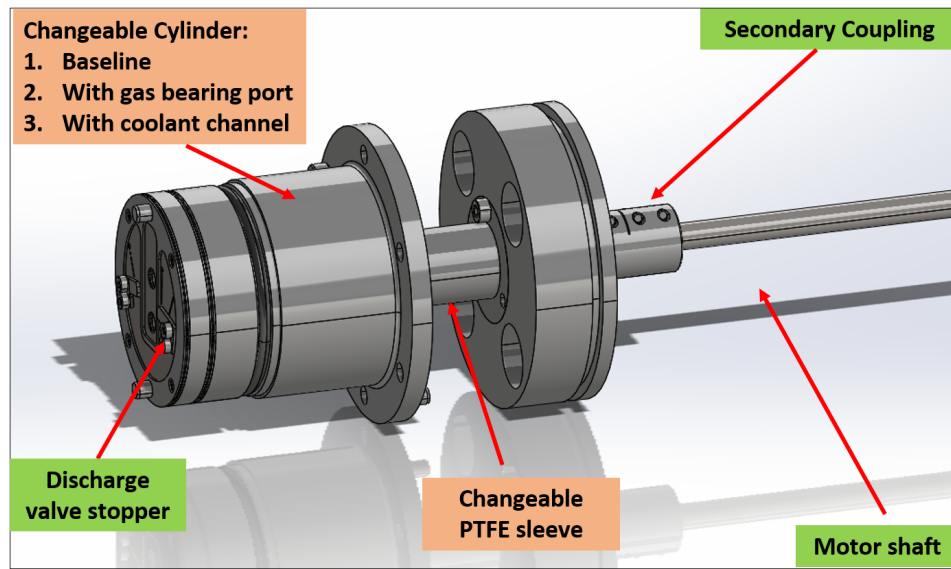
Fig. 6.59. Schematic drawing of the piston and changeable cylinder assembly in prototype linear compressor.

Fig. 6.60. Picture of the final version of the prototype linear compressor.

7. CONCLUSIONS AND FUTURE WORK

7.1 Conclusions

Motivated, primarily, by the need of understanding the dynamic characteristics of linear compressors and their potential applications in HVAC&R, a comprehensive and generalized simulation model that is used to simulate the dynamic performance of a linear compressor has been developed in the present work. The compressor model consists of several sub-models including a piston dynamic model, an electrical motor model, a valve dynamic model.

To characterize the performance of linear compressors, two commercially available linear compressors have been carried on performance testing to understand and compare their behaviors. Moreover, a detailed model validation has been conducted and the biases between the experimental data and simulation results have been identified. Once validated, the model has been exercised to investigate the characteristics of linear compressor by analyzing both transient and periodic steady-state results.

In-depth sensitivity studies were carried out on key parameters affecting linear compressor performance with the goal of providing guidance for improving existing compressor designs and developing improved linear compressor designs. Several key findings were obtained regarding to these aspects: (i) optimal piston diameter/length and clearance gap can be determining based on the trade-off between leakage and frictional losses; (ii) gas bearing can reduce the leakage loss significantly by minimizing the pressure propagation within the clearance gap; (iii) by maintaining a good range of piston and system resonance frequency with respect to the driving frequency, the piston vibration issues can be attenuated; and (iv) more symmetry spring configuration, lighter piston body and shorter piston rod are favorable to reduce the piston eccentricity issue.

A novel cylinder cooling design integrated within a vapor compression cycle was reported to realize the utilization of vapor injection technology in a linear compressor, which is beneficial to reduce the the compressor discharge temperature and achieve a better system COP at an optimal intermediate pressure. A general system model was developed to analyze the process and predict the system performance. Additionally, four linear compressor component designs in terms of their potential for approaching an isothermal compression process have been proposed. Each of the designs utilizes internal cooling paths that are integrated into the piston-cylinder design but with different geometries. A range of unique geometries are enabled through the use of 3D printing and the baseline component has been manufactured as the first attempt. A scalability analysis has been conducted in terms of two common applications and the limitations for building a scale-up linear compressor were identified about the determination of piston diameter and piston stroke and a preliminary design was proposed for each case. Finally, a guidance of designing a prototype linear compressor was reported, including the selection and calculation of the components.

7.2 Future Work

Although many researchers have focused on linear compressors for many years and technological progresses have been made in the past few years, there are still many challenges associated with the operation of linear compressors and some unexpected issues are still unsolved in their applications. Based on the methodologies and results presented in this document and the recent review work by Liang [59], some suggestions of possible future work are discussed here that could further improve the results or extend the applications. The followings are some areas that should be investigated to extend beyond the present study:

1. In Chapter 3, the experimental performance of two commercial compressors was compared and discussed. However, due to the potential manufacture variation, the conclusions may not be general enough for other commercial designs. There-

fore, the performance comparison between two types of compressors, *i.e.*, linear and reciprocating, could be conducted numerically by a validated model in the future, where not only the geometry data can be perfectly consistent but also the uncertainty from the design and manufacture process can be minimized.

2. In-depth sensitivity studies were reported in Chapter 5 and piston vibration issue was discussed. However, the discussion was only from the mechanical design point of view and limited control methodology was involved. Therefore, one of a promising future work is to propose a control method or design a controller based on the dynamic characteristics to solve the vibration issues in a linear compressor. Moreover, the improvements on the linear motor design and control could also be investigated in the future.

3. The isothermal compression process has been discussed extensively in Chapter 6 either from modeling aspect or from a design point. Unfortunately, no performance testing was conducted to prove the concept of the design and identify the potential limitations, which will be an extremely interesting direction as a future work in this area.

4. A thorough analysis and a guidance have been report in Chapter 6 with respect to the scalability of linear compressors. It would be very significant to design and build a scale-up linear compressor based on the recommendations in this document and the findings from the performance testing will contribute a lot to the development of linear compressors.

REFERENCES

REFERENCES

[1] D. H. O. Herrmann, "Small electric refrigerating machine," Jun. 1 1954, patent 2,679,732.

[2] R. V. Cadman, "A technique for the design of electrodynamic oscillating compressors," Ph.D. dissertation, Purdue University, 1967.

[3] R. Cohen, "Electrodynamic oscillating compressors: Part 1 design based on linearized loads," *Journal of Fluids Engineering*, 1969.

[4] E. Pollak, W. Soedel, R. Cohen, and F. Friedlaender, "On the resonance and operational behavior of an oscillating electrodynamic compressor," *Journal of Sound and Vibration*, vol. 67, no. 1, pp. 121–133, 1979.

[5] N. R. Van der Walt and R. Under, "The simulation and design of a high efficiency, lubricant free, linear compressor for a domestic refrigerator," in *1992 International Compressor Engineering Purdue Conference*, 1992, p. 787.

[6] ——, "Linear compressors-a maturing technology," in *Proceedings 45th International Appliance Technical Conference*, 1994, pp. 239–246.

[7] H. Hasegawa, A. Okaichi, H. Shintaku, M. Ikoma, and F. Nishiwaki, "A study of a linear compressor with a gas spring," in *2002 International Compressor Engineering Purdue Conference*, 2002, p. 1604.

[8] D.-Y. Koh, Y.-J. Hong, S.-J. Park, H.-B. Kim, and K.-S. Lee, "A study on the linear compressor characteristics of the stirling cryocooler," *Cryogenics*, vol. 42, no. 6-7, pp. 427–432, 2002.

[9] S.-J. Lee, "Linear compressor," Patent US 20 040 120 834A1, 10 29, 2002.

[10] LG, "LG's Linear Compressor Refrigerators: Technology that Preserves," http://www.lg.com/za/press-release/lgs-linear-compressor-refrigerators-technology-that-preserves, 2002, [Online; accessed 19-July-2002].

[11] J. Park, "Linear compressor with external vibration-absorbing structure," Patent US 20 050 175 482A1, 01 06, 2004.

[12] Embraco, "Embraco claims oil-less compressor breakthrough," http://www.acr-news.com/embraco-claims-oil-less-compressor-breakthrough, 2008, [Online; accessed 19-July-2002].

[13] C. R. Bradshaw, "A miniature-scale linear compressor for electronics cooling." Ph.D. dissertation, Purdue University, 2012.

[14] K. Liang, R. Stone, M. Dadd, and P. Bailey, "A novel linear electromagnetic-drive oil-free refrigeration compressor using r134a," *International Journal of Refrigeration*, vol. 40, pp. 450–459, 2014.

[15] A. Bijanzad, A. Hassan, and I. Lazoglu, "Analysis of solenoid based linear compressor for household refrigerator," *International Journal of Refrigeration*, vol. 74, pp. 114–126, 2017.

[16] X. Zhang, D. Ziviani, J. Braun, and E. Groll, "Numerical analysis of gas bearings in oil-free linear compressors," in *IOP Conference Series: Materials Science and Engineering*, vol. 604, no. 1. IOP Publishing, 2019, p. 011008.

[17] R. Cadman and R. Cohen, "Electrodynamic oscillating compressors: Part 2—evaluation of specific designs for gas loads," *Journal of Basic Engineering*, vol. 91, no. 4, pp. 664–670, 1969.

[18] C. Minas, "Nonlinear dynamics of an oilless linear drive reciprocating compressor," *Journal of Vibration and Acoustics*, vol. 116, no. 1, pp. 79–84, 1994.

[19] N. Chen, Y. Tang, Y. Wu, X. Chen, and L. Xu, "Study on static and dynamic characteristics of moving magnet linear compressors," *Cryogenics*, vol. 47, no. 9-10, pp. 457–467, 2007.

[20] D. Howe and J. Wang, "A novel linear drive for next-generation reciprocating vapor compressors," *IEEJ Transactions on Electrical and Electronic Engineering*, vol. 3, no. 5, pp. 455–463, 2008.

[21] S. Zhang, L. Norum, and R. Nilssen, "Oscillatory motion application of tubular linear permanent magnet machine," in *Industrial Electronics, 2009. IECON'09. 35th Annual Conference of IEEE*. IEEE, 2009, pp. 1223–1227.

[22] T. Ibrahim, "Short-stroke, single-phase tubular permanent magnet motors for refrigeration applications." Ph.D. dissertation, University of Sheffield, 2009.

[23] J. Wang, D. Howe, and Z. Lin, "Design optimization of short-stroke single-phase tubular permanent-magnet motor for refrigeration applications," *IEEE Transactions on Industrial Electronics*, vol. 57, no. 1, pp. 327–334, 2010.

[24] N. Tsai and C. Chiang, "Innovative linear compressor by magnetic drive and control," *Proceedings of the Institution of Mechanical Engineers, Part I: Journal of Systems and Control Engineering*, vol. 225, no. 5, pp. 623–639, 2011.

[25] M. Xia and X. Chen, "Analysis of resonant frequency of moving magnet linear compressor of stirling cryocooler," *International Journal of Refrigeration*, vol. 33, no. 4, pp. 739–744, 2010.

[26] H. Dang, L. Zhang, and J. Tan, "Dynamic and thermodynamic characteristics of the moving-coil linear compressor for the pulse tube cryocooler. part a: Theoretical analyses and modeling," *international Journal of Refrigeration*, vol. 69, pp. 480–496, 2016.

[27] ——, "Dynamic and thermodynamic characteristics of the moving-coil linear compressor for the pulse tube cryocooler: Part b–experimental verifications," *International Journal of Refrigeration*, vol. 69, pp. 497–504, 2016.

[28] J. K. Kim and J. H. Jeong, "Performance characteristics of a capacity-modulated linear compressor for home refrigerators," *International Journal of Refrigeration*, vol. 36, no. 3, pp. 776–785, 2013.

[29] M. Heidari, S. Wasterlain, P. Barrade, F. Gallaire, and A. Rufer, "Energetic macroscopic representation of a linear reciprocating compressor model," *International Journal of Refrigeration*, vol. 52, pp. 83–92, 2015.

[30] M. Lamantia, A. Contarini, and S. Giovanni, "Numerical and experimental analysis of a linear compressor," in *2002 International Compressor Engineering Purdue Conference*, 2002, p. 1602.

[31] X. You, L. Qiu, C. Duan, X. Jiang, C. Huang, and X. Zhi, "Study on the stroke amplitude of the linear compressor," *Applied Thermal Engineering*, vol. 129, pp. 1488–1495, 2018.

[32] H. Kim, C.-g. Roh, J.-k. Kim, J.-m. Shin, Y. Hwang, and J.-k. Lee, "An experimental and numerical study on dynamic characteristic of linear compressor in refrigeration system," *International Journal of Refrigeration*, vol. 32, no. 7, pp. 1536–1543, 2009.

[33] P. Bailey, M. Dadd, and C. Stone, "Cool and straight: linear compressors for refrigeration," *Proceedings of Institute of Refrigeration*, 2011.

[34] G. F. Davies, I. W. Eames, P. Bailey, M. W. Dadd, A. Janiszewski, R. Stone, G. G. Maidment, and B. Agnew, "Cooling microprocessors using vapor compression refrigeration," in *Thermal and Thermomechanical Phenomena in Electronic Systems (ITherm), 2010 12th IEEE Intersociety Conference on*. IEEE, 2010, pp. 1–8.

[35] K. Liang, R. Stone, W. Hancock, M. Dadd, and P. Bailey, "Comparison between a crank-drive reciprocating compressor and a novel oil-free linear compressor," *International Journal of Refrigeration*, vol. 45, pp. 25–34, 2014.

[36] K. Liang, M. Dadd, and P. Bailey, "Clearance seal compressors with linear motor drives. part 1: Background and system analysis," *Proceedings of the Institution of Mechanical Engineers, Part A: Journal of Power and Energy*, vol. 227, no. 3, pp. 242–251, 2013.

[37] ——, "Clearance seal compressors with linear motor drives. part 2: Experimental evaluation of an oil-free compressore," *Proceedings of the Institution of Mechanical Engineers, Part A: Journal of Power and Energy*, vol. 227, no. 3, pp. 242–251, 2013.

[38] K. Liang, R. Stone, M. Dadd, and P. Bailey, "The effect of clearance control on the performance of an oil-free linear refrigeration compressor and a comparison between using a bleed flow and a dc current bias," *International Journal of Refrigeration*, vol. 69, pp. 407–417, 2016.

[39] K. Liang, R. Stone, G. Davies, M. Dadd, and P. Bailey, "Modelling and measurement of a moving magnet linear compressor performance," *Energy*, vol. 66, pp. 487–495, 2014.

[40] H. Jiang, K. Liang, and Z. Li, "Characteristics of a novel moving magnet linear motor for linear compressor," *Mechanical Systems and Signal Processing*, vol. 121, pp. 828–840, 2019.

[41] H. Dang, J. Li, J. Tan, Y. Zhao, R. Zha, T. Zhang, B. Zhao, Y. Zhao, H. Tan, and R. Xue, "Theoretical modeling and experimental verification of the motor design for a 500 g micro moving-coil linear compressor operating at 90–140 hz," *International Journal of Refrigeration*, 2019.

[42] Z. Li, K. Liang, and H. Jiang, "Thermodynamic analysis of linear compressor using r-1234yf," *International Journal of Refrigeration*, 2019.

[43] I. H. Bell, V. Lemort, E. A. Groll, and J. E. Braun, "Development of a generalized steady-state simulation framework for positive displacement compressors and expanders," in *International Conference on Compressors and their Systems 2013*, 2013.

[44] D. Ziviani, "Theoretical and experimental characterization of single-screw expanders for orc applications," Ph.D. dissertation, Ghent University, 2017.

[45] Python, "Python Program Language," https://www.python.org/, 2001, [This page was last edited on 15 November 2017, at 08:15.].

[46] Cython, "C extensions for Python," http://cython.org/, 2017.

[47] D. Ziviani, I. H. Bell, X. Zhang, V. Lemort, M. De Paepe, J. E. Braun, and E. A. Groll, "Pdsim: Demonstrating the capabilities of an open-source simulation framework for positive displacement compressors and expanders," *International Journal of Refrigeration*, vol. 110, pp. 323–339, 2020.

[48] I. H. Bell, J. Wronski, S. Quoilin, and V. Lemort, "Pure and pseudo-pure fluid thermophysical property evaluation and the open-source thermophysical property library coolprop," *Industrial & Engineering Chemistry Research*, vol. 53, no. 6, pp. 2498–2508, 2014. [Online]. Available: http://pubs.acs.org/doi/abs/10.1021/ie4033999

[49] I. H. Bell, D. Ziviani, V. Lemort, C. R. Bradshaw, M. Mathison, W. T. Horton, J. E. Braun, and E. A. Groll, "Pdsim: A general quasi-steady modeling approach for positive displacement compressors and expanders," *International Journal of Refrigeration*, vol. 110, pp. 310–322, 2020.

[50] C. Colebrook and C. White, "Experiments with fluid friction in roughened pipes," in *Proc. R. Soc. Lond. A*, vol. 161, no. 906. The Royal Society, 1937, pp. 367–381.

[51] S. W. Churchill, "Friction-factor equation spans all fluid-flow regimes," *Chemical Engineering*, vol. 84, no. 24, pp. 91–92, 1977.

[52] D. Taler and J. Taler, "Simple heat transfer correlations for turbulent tube flow," in *E3S Web of Conferences*, vol. 13. EDP Sciences, 2017, p. 02008.

[53] G. O. Brown, "The history of the darcy-weisbach equation for pipe flow resistance," in *Environmental and Water Resources History*, 2003, pp. 34–43.

[54] A. Z. Szeri, *Fluid film lubrication*. Cambridge University Press, 2010.

[55] R. Singh and W. Soedel, "Fluid dynamic effects in the multicylinder compressor suction and discharge cavities," in *1976 International Compressor Engineering Purdue Conference*, 1976, p. 202.

[56] J.-H. Kim, "Analysis of a bowtie compressor with novel capacity modulation," Ph.D. dissertation, Purdue University, 2005.

[57] N. Wood, C. R. Bradshaw, J. Orosz, G. Kemp, and E. A. Groll, "Dynamic modeling of a poppet valve for use in a rotating spool compressor," in *2016 International Compressor Engineering Purdue Conferences*, 2016, p. 2468.

[58] J. Greenwood and J. Tripp, "The contact of two nominally flat rough surfaces," *Proceedings of the Institution of Mechanical Engineers*, vol. 185, no. 1, pp. 625–633, 1970.

[59] K. Liang, "A review of linear compressors for refrigeration," *International Journal of Refrigeration*, vol. 84, pp. 253–273, 2017.

[60] J. Kauzlarich, "Viscosity times density equations for five classes of lubricants," *Proceedings of the Institution of Mechanical Engineers, Part J: Journal of Engineering Tribology*, vol. 212, no. 3, pp. 235–239, 1998.

[61] R. Adair, E. Qvale, and J. T. Pearson, "Instantaneous heat transfer to the cylinder wall in reciprocating compressors," in *1972 International Compressor Engineering Purdue Conference*, 1972, p. 86.

[62] T. L. Bergman, *Introduction to heat transfer*. John Wiley & Sons, 2011.

[63] Z. Liu, "Simulation of a variable speed compressor with special attention to supercharging effects," Ph.D. dissertation, Purdue University, 1993.

[64] Y. Chen, "Mathematical modeling of scroll compressors," Ph.D. dissertation, Purdue University, 2000.

[65] J. Holman, "Heat transfer, 1986," *Mc Gran–Hill Book Company, Soythern Methodist University*, 1986.

[66] T. H. Kuehn and R. Goldstein, "An experimental study of natural convection heat transfer in concentric and eccentric horizontal cylindrical annuli," *Journal of Heat Transfer*, vol. 100, no. 4, pp. 635–640, 1978.

[67] L. C. Burmeister, *Convective heat transfer*. John Wiley & Sons, 1993.

[68] R. Puff, D. E. Lilie, M. Knies, and M. G. Bortoli, "Linear compressor suction valve optimization," in *2016 International Compressor Engineering Purdue Conferences*, 2016, p. 2399.

[69] X. Zhang, D. Ziviani, J. E. Braun, and E. A. Groll, "Theoretical analysis of dynamic characteristics in linear compressors," *International Journal of Refrigeration*, vol. 109, pp. 114–127, 2020.

[70] ——, "A numerical study on dynamic characteristics of linear compressor for electronics cooling," in *2018 International Compressor Engineering Conference at Purdue*, 2018, p. 1667.

[71] D. D. Fuller, "A review of the state-of-the-art for the design of self-acting gas-lubricated bearings," *Journal of Lubrication Technology*, vol. 91, no. 1, pp. 1–16, 1969.

[72] M. Pandian, "A new method for the numerical solution of the reynolds equation for gas-lubricated slider bearings," *Journal of Engineering Mathematics*, vol. 19, no. 1, pp. 3–19, 1985.

[73] D.-c. Han, S.-s. Park, W.-j. Kim, and J.-w. Kim, "A study on the characteristics of externally pressurized air bearings," *Precision Engineering*, vol. 16, no. 3, pp. 164–173, 1994.

[74] M. Arghir, S. L. Lez, and J. Frene, "Finite-volume solution of the compressible reynolds equation: linear and non-linear analysis of gas bearings," *Proceedings of the Institution of Mechanical Engineers, Part J: Journal of Engineering Tribology*, vol. 220, no. 7, pp. 617–627, 2006.

[75] H. Zhang, C. Zhu, and Q. Yang, "Approximate numerical solution of hydrodynamic gas journal bearings," in *International Conference on Intelligent Robotics and Applications*. Springer, 2008, pp. 260–268.

[76] E. R. Hulse and A. T. Prata, "Numerical modeling of capillary compensated aerostatic bearing applied to linear reciprocating compressor," in *2016 International Compressor Engineering Conference at Purdue*, 2016, p. 2410.

[77] B. J. Hamrock, S. R. Schmid, and B. O. Jacobson, *Fundamentals of fluid film lubrication*. CRC press, 2004.

[78] Specialtycomponents, "Air bearing fundementals," http://www.specialtycomponents.com, 2013.

[79] S. S. Rao and F. F. Yap, *Mechanical vibrations*. Prentice Hall Upper Saddle River, 2011, vol. 4.

[80] K. Liang, "Analysis of oil-free linear compressor operated at high pressure ratios for household refrigeration," *Energy*, vol. 151, pp. 324–331, 2018.

[81] K. Graunke and J. Ronnert, "Dynamic behavior of labyrinth seals in oilfree labyrinth-piston compressors," 1984.

[82] M. Heidari, S. Lemofouet, and A. Rufer, "On the strategies towards isothermal gas compression and expansion," in *2014 International Compressor Engineering Purdue Conference*, 2014, p. 2285.

[83] M. Heidari, M. Mortazavi, and A. Rufer, "Design, modeling and experimental validation of a novel finned reciprocating compressor for isothermal compressed air energy storage applications," *Energy*, vol. 140, pp. 1252–1266, 2017.

[84] V. Patil, P. Acharya, and P. Ro, "Experimental investigation of aqueous foam based heat transfer in liquid piston compressor for improvement in compression efficiency," in *2018 International Compressor Engineering Purdue Conference*, 2018, p. 2636.

[85] J. Heo, M. W. Jeong, C. Baek, and Y. Kim, "Comparison of the heating performance of air-source heat pumps using various types of refrigerant injection," *International Journal of Refrigeration*, vol. 34, no. 2, pp. 444–453, 2011.

[86] X. Shuxue and M. Guoyuan, "Research on air-source heat pump coupled with economized vapor injection scroll compressor and ejector," *International Journal of Refrigeration*, vol. 34, no. 7, pp. 1587–1595, 2011.

[87] I. H. Bell, E. A. Groll, and J. E. Braun, "Performance of vapor compression systems with compressor oil flooding and regeneration," *International Journal of Refrigeration*, vol. 34, no. 1, pp. 225–233, 2011.

[88] P. J. Pritchard and J. W. Mitchell, "Fox and mcdonald's introduction to fluid mechanics," 2016.

VITA

VITA

Mr. Xinye Zhang was born in Xi'an, China on December 12th, 1990 and is the son of Mrs. Yahong Wei and Mr. Tianle Zhang. He received his Bachelor of Science in Energy and Power Automation Engineering from Xi'an Jiaotong University in 2013. As part of his undergraduate period, he went to University of Michigan - Dearborn as an exchange student in Mechanical Engineering in 2012. Xinye received his Master of Science in Mechanical Engineering from Purdue University and continued his Ph.D. studies in May of 2015 at Ray W. Herrick Laboratories. As a part of his graduate studies, Xinye went to Tokyo, Japan and worked as a research fellow at Waseda University in the Fall of 2018. By the end of 2019, Xinye had an intern as a senior engineer at Buffalo Research Lab in Honeywell and finished the requirement for a Ph.D. in the spring of 2020 with a dissertation titled 'Theoretical and Experimental Analysis of Dynamic Characteristics in Linear Compressors'.